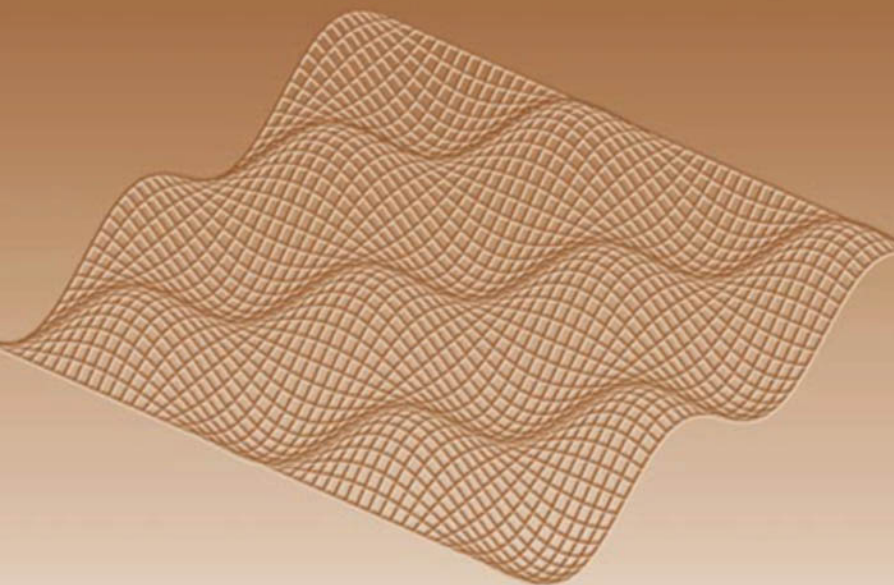


Almudena Suárez

Raymond Quéré

*Stability Analysis of
Nonlinear Microwave Circuits*



Stability Analysis of Nonlinear Microwave Circuits

For a listing of recent titles in the *Artech House Microwave Library*,
turn to the back of this book.

Stability Analysis of Nonlinear Microwave Circuits

Almudena Suárez
Raymond Quéré



Artech House
Boston • London
www.artechhouse.com

Library of Congress Cataloging-in-Publication Data

Suárez, Almudena.

Stability analysis of nonlinear microwave circuits/Almudena Suárez, Raymond Quéré.

p. cm. — (Artech House microwave library)

Includes bibliographical references and index.

ISBN 1-58053-303-5 (alk. paper)

1. Microwave circuits. I. Quéré, Raymond. II. Title III. Series.

TK7876 .S76 2003

621.381'32-dc21

2002038278

British Library Cataloguing in Publication Data

Suárez, Almudena

Stability analysis of nonlinear microwave circuits. — (Artech House microwave library)

1. Microwave integrated circuits—Design 2. Stability

I. Title II. Quéré, Raymond

621.3'8132

ISBN 1-58053-303-5

Cover design by Gary Ragaglia

Chapters 1, 2, 4, 5, 6 by Almudena Suárez

Chapter 3 by Raymond Quéré

© 2003 ARTECH HOUSE, INC.

685 Canton Street

Norwood, MA 02062

All rights reserved. Printed and bound in the United States of America. No part of this book may be reproduced or utilized in any form or by any means, electronic or mechanical, including photocopying, recording, or by any information storage and retrieval system, without permission in writing from the publisher.

All terms mentioned in this book that are known to be trademarks or service marks have been appropriately capitalized. Artech House cannot attest to the accuracy of this information. Use of a term in this book should not be regarded as affecting the validity of any trademark or service mark.

International Standard Book Number: 1-58053-303-5

Library of Congress Catalog Card Number: 2002038278

10 9 8 7 6 5 4 3 2 1

Contents

	Preface	<i>xī</i>
	Acknowledgments	<i>xv</i>
1	Steady-State Solutions of Nonlinear Circuits	1
1.1	Autonomous and Nonautonomous Dynamical Systems	2
1.2	Oscillations in Linear and Nonlinear Systems	10
1.3	Phase-Space Representation of Solutions	16
1.3.1	Transient Trajectories and Limit Sets	16
1.3.2	Limit Cycles	19
1.3.3	Invariant Sets	21
1.4	Stability of Limit Sets	29
1.4.1	Concept of Stability	29
1.4.2	Stability Types	31
1.4.3	Coexisting Stable Solutions	42
1.4.4	Qualitative Variations in the Stability Properties	43
1.5	Poincaré Map	44
1.5.1	Definition of the Poincaré Map	44
1.5.2	Poincaré Maps of Limit Sets	48

1.5.3	Chaotic Solutions	50
1.6	Entrainment: Phase-Locked Solutions in the Torus	52
	References	57
2	<u>Nonlinear Analysis Techniques</u>	61
2.1	Time-Domain Simulation	62
2.2	Harmonic Balance for Nonautonomous Circuits	66
2.2.1	Harmonic-Balance Equations	67
2.2.2	Numerical Resolution of the Harmonic-Balance Equations	71
2.2.3	Continuation Technique for High Amplitude of the RF Generators	73
2.3	Harmonic Balance for Autonomous and Synchronized Circuits	75
2.3.1	Analysis of Free-Running Oscillators	78
2.3.2	Analysis of Synchronized Circuits	86
2.3.3	Analysis of Self-Oscillating Mixers	89
2.4	Envelope Transient	91
2.5	Continuation Technique for Tracing Solution Curves Versus a Circuit Parameter	96
2.6	Analysis of Autonomous and Synchronized Circuits in Closed Harmonic-Balance Programs	99
2.6.1	Autonomous Circuits	100
2.6.2	Synchronized Circuits	104
2.6.3	Continuation Method Based on the Use of Auxiliary Generators	106
	References	111
3	<u>Local Stability Analysis</u>	117
3.1	Stability Concept for Linear and Nonlinear Circuits	118
3.1.1	Stability of Linear Circuits	119
3.1.2	Stability of Nonlinear Circuits	128

3.2	Derivation of the Characteristic System in the Harmonic-Balance Formulation	131
3.2.1	Expression of the Characteristic System	132
3.2.2	Stability Analysis of Lumped Circuits	135
3.2.3	Stability Analysis of Distributed Circuits	142
3.2.4	Characteristic Loci	147
3.2.5	The Negative Impedance Approach	151
3.3	The Open-Loop Approach	152
3.3.1	The Bode, Platzker Approach for Linear Circuits	153
3.3.2	Extension of the Method for Multibias Circuits	160
3.3.3	Extension of the Approach to Large-Signal Periodic Steady-State Regimes	161
3.3.4	Large-Signal Stability Analysis Using a Simplified Filter	168
	References	171
	Appendix 3A	172
4	<u>Bifurcation Analysis of Nonlinear Circuits</u>	177
4.1	Local Bifurcations	178
4.1.1	Local Bifurcations from the DC Regime	179
4.1.2	Local Bifurcations from the Periodic Regime	188
4.2	Bifurcations of the Poincaré Map	196
4.2.1	Flip-Type Bifurcations	201
4.2.2	Direct-Type Bifurcations	204
4.2.3	Hopf-Type Bifurcations	209
4.3	Global Bifurcations	211
4.3.1	Saddle Connection	212
4.3.2	Saddle-Node Local/Global Bifurcation	213
4.4	Analysis of Bifurcations from the Harmonic-Balance Characteristic System	216
4.4.1	Bifurcations from the DC Regime	217
4.4.2	Bifurcations from the Periodic Regime	219
4.5	Harmonic-Balance Analysis of Bifurcations with the Aid of an Auxiliary Generator	228

4.5.1	Autonomous Periodic	230
4.5.2	Periodic Regime with External Excitation	231
4.5.3	Autonomous Quasiperiodic Regime	233
	References	240
5	Global Stability of Microwave Circuits	243
5.1	Global Behavior of Free-Running Oscillators	244
5.2	Global Behavior of Synchronized Oscillators	247
5.3	Global Behavior of Frequency Dividers by Two	252
5.3.1	Design Concepts and Applications of Frequency Dividers	252
5.3.2	Parametric Stability Analysis of Frequency Dividers by Two	255
5.3.3	Improvement in the Frequency-Divider Design	262
5.4	Global Behavior of Self-Oscillating Mixers	266
5.4.1	Design Concepts and Applications of Self-Oscillating Mixers	266
5.4.2	Steady State of the Self-Oscillating Mixer	268
5.4.3	Parametric Analysis of the Self-Oscillating Mixer	269
5.5	Global Behavior of Frequency Doublers	273
5.5.1	Design Concepts of Frequency Doublers	273
5.5.2	Parametric Analysis of Frequency Doublers	273
5.6	Global Behavior of Phase-Locked Loops	278
5.6.1	General Equations of the Phase-Locked Loop	279
5.6.2	Parametric Analysis of the Phase-Locked Loop	281
5.6.3	Use of the Poincaré Map to Determine the Operating Bands of the Phase-Locked Loop	290
	References	292
6	Bifurcation Routes to Chaos	295
6.1	Homoclinicity	296
6.2	Quasiperiodic Route to Chaos	302
6.3	Period-Doubling Route to Chaos	305

6.4	Torus-Doubling Route to Chaos	311
6.5	Intermittence	315
	References	320
	About the Authors	323
	Index	325

Preface

The increasing use of high-frequency integrated circuits *monolithic microwave integrated circuits* (MMICs) in modern communications systems requires an accurate prediction of their response at the simulation stage because this technology does not allow any circuit modification after manufacturing. The microwave circuits are often designed using frequency-domain techniques, like harmonic balance. With this technique, only the steady state is analyzed, and the experimental solution may be very different from the simulated one. In nonlinear circuits, two or more steady-state solutions of same or different types may coexist for a given set of circuit-parameter values. The solutions may be stable (physically observable) or unstable. Because the transient is not simulated, harmonic balance can provide a solution towards which the system never evolves in time. Thus, it requires complementary stability analysis tools.

The main purpose of the book is to give a deep insight into the dynamics of the most common nonlinear microwave circuits without losing track of the practical-designer objectives. It gives explanation of the operation principles of circuits like tuned and synchronized oscillators, analog frequency dividers commonly employed in high-frequency phase-locked loops, and other circuits with complex behavior, like the self-oscillating mixers employed in the design of small, low-consuming frequency converters. The book tackles many instability problems encountered by circuit designers at the measurement stage. The emphasis here is the understanding and practical usefulness of the different stability concepts and the provision of stability-analysis techniques. More descriptions and demonstrations are given in the mathematical references of the book.

Chapter 1 presents the different kinds of solutions that the nonlinear circuits may have, together with the essential concepts of local stability, global stability, and bifurcation. The “safe” design and the design correction of nonlinear circuits require general knowledge about their potentially very complex behavior. The chapter presents detailed explanations about the mechanism of the oscillation startup and the self-sustained oscillation or limit cycle. Other common types of solutions are studied, like the self-oscillating mixing solutions and the subharmonic and the chaotic solutions. Practical examples are shown.

The harmonic-balance technique is very efficient for the simulation of circuits in forced regime (i.e., at the fundamental frequencies delivered by the input generators, like amplifiers and mixers). However, its application to circuits with self-oscillations and subharmonic components is more demanding. On the one hand, there is a need for the user specification of the Fourier-frequency basis. On the other hand, the physical circuit solution always coexists with a trivial solution without self-oscillations or subharmonic components. Unless special strategies are employed, convergence to the latter (and much simpler) solutions will be obtained. The harmonic-balance technique, presented in the Chapter 2, is oriented to circuits with autonomous, synchronized, or subharmonic behavior. The proposed algorithms can be employed by the user of commercial harmonic-balance software.

Especially when using harmonic balance, the physical observation of the simulated solution must be verified through a complementary stability analysis. In Chapter 3, a new open-loop technique for the stability-analysis of large-signal regimes is presented. Objectives have been the accuracy and rigor and the generality of application to circuits containing many nonlinear elements. The techniques can also be externally implemented by the user in commercial harmonic-balance programs. Although most of these programs provide tools for the stability analysis of direct current (dc) solutions and linear regimes, they do not usually include tools for the stability analysis of nonlinear large-signal steady-state regimes, like that of a power amplifier or an analog frequency divider.

The microwave-circuit designer usually requires knowledge about the behavior of the circuit in a certain input frequency band or versus a bias voltage, like in *voltage-controlled oscillators* (VCOs). Generator amplitudes or frequencies and linear-element values are examples of circuit parameters. The solution of a nonlinear circuit may undergo qualitative variations, or *bifurcations*, when a parameter is modified. There are different types of bifurcations, which are responsible for many commonly observed phenomena, such as undesired hysteresis in VCOs or the onset of natural frequencies in power amplifiers. In other cases, the bifurcations are necessary for obtaining a particular kind

of operation, as in the case of analog frequency dividers, whose operating frequency bands are determined by bifurcation phenomena. Chapter 4 presents the different types of bifurcation from dc regimes, periodic regimes, and quasi-periodic regimes. Different techniques for their detection from harmonic-balance software are provided and illustrated with practical examples. The techniques can be implemented in commercial harmonic balance. The aim of the chapter is to help the reader prevent undesired solutions at the design stage or to increase the parameter ranges with the desired behavior.

Because bifurcations delimit the operation bands of many nonlinear circuits, the capability to detect them through simulation offers new possibilities for an accurate and efficient design. Chapter 5 presents a parametric analysis of complex circuits like self-oscillating mixers, analog frequency dividers, and phase-locked loops. The parameters that are most likely to vary in design or measurement are used in each case. The aim is to show what can generally be expected in terms of operating ranges, stability problems, and undesired solutions. Techniques for this parametric analysis, implementable on commercial software, are provided.

Chaos is a kind of steady-state solution giving rise to continuous spectra, at least for some frequency intervals. Due to this characteristic, it is often mistaken, at the measurement stage, for an anomalous increase of the noise level. Chaotic solutions are generally undesired by the microwave-circuit designer. Due to the continuity of the spectra, they cannot be simulated through harmonic balance. However, harmonic balance can be used to simulate the bifurcations in the circuit solution that usually precede the chaotic behavior. Chapter 6 presents a detailed description of chaotic solutions and of the most common bifurcation sequences leading to chaotic behavior. Detection techniques for harmonic-balance programs are also proposed. The aim is to increase the designer's knowledge of the mechanisms leading to chaotic solutions and to provide some tools to prevent these solutions at the design stage.

Acknowledgments

Almudena Suárez would like to thank Dr. Juan Mari Collantes for invaluable advice and support, Dr. Sergio Sancho, Dr. Samuel Ver Hoeye, Franco Ramírez, Dr. Jose Morales, Dr. Joaquín Portilla, and her colleagues from DICOM at the University of Cantabria, especially Dr. Juan Pablo Pascual, Dr. José Angel García, Dr. Tomás Fernández, and Professor José Luis García. She would also like to thank her family for their continuous support.

Raymond Quéré acknowledges all of the members of the High Frequency Electronic Nonlinear Circuits and Subsystems group of IRCOM–LIMOGES for their help in performing research on nonlinear circuit modeling and design.

1

Steady-State Solutions of Nonlinear Circuits

The main objective of this first chapter is to give an introductory insight into the nonlinear dynamics of electronic circuits. It deals with the different types of steady-state behavior and with the concepts of stability (as a need for the physical observation of the solutions) and phase locking, or entrainment.

Nonlinear circuits can be described by means of a system of nonlinear differential equations [1–6], with their behavior, which may be very complex, being given by the solutions of these equations. A major classification of nonlinear-differential equations distinguishes the two possible cases of autonomous (self-oscillating) and nonautonomous (forced) systems. The two cases will be studied in this chapter, together with the different types of solutions that may be obtained, from a qualitative point of view.

Two ways of representing the solutions of a nonlinear system are going to be shown: the phase-space representation, which helps with understanding circuit dynamics, and the Poincaré map [7–9]. The latter reduces the dimension of the solution and proves very useful for analyzing variations in dynamics versus in a system parameter. To familiarize the reader with these representations, simple circuit examples that can be easily simulated [using *Simulation Program with Integrated Circuits Emphasis* (SPICE)] are presented.

1.1 Autonomous and Nonautonomous Dynamical Systems

An electronic circuit can be described by a minimal set of variables called *statevariables*. The knowledge of these variables, along with the excitations, is enough to define the state of the circuit or system at any time t . In circuits containing resistors, inductors, and capacitors (RLC circuits, for example) the set of state variables can be given by the capacitor voltages and the inductor currents [7]. Because any circuit can be described through a system of differential equations, the terms *circuit* and *system* will be used interchangeably in this book. The term *circuit* refers to the physical device; the term *system* refers to the equations of the mathematical model [7].

Formally, the state variables are the smallest set of variables, such that their knowledge at a time, $t = t_0$, together with that of the system input for $t \geq t_0$, determines the system behavior for $t \geq t_0$. Let $\bar{x} \in R^n$ be the vector containing the system state variables, where the components of \bar{x} may represent voltages across capacitors or currents through inductors. The circuit equations, in terms of the state variables, are best formulated as an n -dimensional differential equation of the first order in vector form. Two cases are possible, depending on the presence or absence of time-varying generators. In the former case, the circuit is forced or nonautonomous; in the latter (with only dc generators) the circuit is said to be autonomous. The differential equation is

$$\frac{d\bar{x}}{dt} = f(\bar{x}, t) \quad \bar{x}(t_0) = \bar{x}_0 \quad \text{Nonautonomous circuit} \quad (1.1a)$$

$$\frac{d\bar{x}}{dt} = f(\bar{x}) \quad \bar{x}(0) = \bar{x}_0 \quad \text{Autonomous circuit} \quad (1.1b)$$

where $\bar{x}(t) \in R^n$ is the system state vector at time t . The function f is called the *vector field*. The dynamics of (1.1) are linear if the vector field f is linear in \bar{x} . Otherwise, the system is nonlinear. The vector field depends on time in the case of nonautonomous systems (1.1a), in which case $f: R^n \times R \rightarrow R^n$. In the case of an autonomous system (1.1b), f is independent of time. Then $f: R^n \rightarrow R^n$. The particular case of f defined only in a subset $U \subset R^n \times R$ (in a nonautonomous system) or $U \subset R^n$ (in an autonomous system) can also be considered [9], although it will not be treated in this book.

In a nonautonomous system, the presence of at least one time-varying generator gives rise to a differential equation of the form (1.1a), in which the

function f depends explicitly on time. Any forced circuit with a *radio frequency* (RF) generator $A_g \cos(\omega_g t)$ is an example of a nonautonomous system because the existence of this generator makes time explicitly appear in the function f . For periodic forcing, the function f will be periodic. In the case of an autonomous system [of the form (1.1b)], the vector field f does not depend explicitly on time. This is the case of a free-running oscillator for which there are no external RF generators.

System (1.1) provides by itself some information about the system. Actually, in the nonautonomous system (1.1a), it assigns a vector $f(\bar{x}, t)$ to every point (t, \bar{x}) . In the case of the autonomous system (1.1b), it assigns the vector $f(\bar{x})$ to every point (\bar{x}) . The vector provides the velocity of variation of \bar{x} with respect to t (i.e., $\frac{d\bar{x}}{dt}$) at the particular point (t, \bar{x}) (or (\bar{x}) in an autonomous system).

Considering the case of a nonautonomous system, a grid can be defined as $R \times R^n$ in terms of t and \bar{x} , discretizing the time t and the components of \bar{x} . Then, for the representation of the vector field, a vector \bar{v}_f of arbitrarily small length l is attached to each point [1] of the grid (t, \bar{x}) , with its tail at the particular point (t, \bar{x}) . The orientation of the segment, different at each point of the grid, is given by the value of $f(\bar{x}, t)$ at the particular point (t, \bar{x}) (i.e., $\bar{v}_f = l \frac{\dot{\bar{x}}}{|\dot{\bar{x}}|}$). This indicates the direction and sense of variation of the system

solution at each point (t, \bar{x}) . This representation is, of course, only possible for low-dimension systems with $n = 1$ or $n = 2$. However, its meaning can conceptually be extended to systems of any dimension.

As an example, the particular case of an autonomous system in which the state-variable vector is one-dimensional, that is, $x \in R$, has been considered. In Figure 1.1, the slope of the small segment, at each point (t, x) , is $f(x, t)$. The resulting diagram shows why f is called the *vector field*. By observing the vector field of Figure 1.1, it can be gathered that it corresponds to an autonomous system, since points located on the same parallel line to the time axis have the same slope. Thus, f must be independent of time.

An *isocline* of the differential equation is the locus of points with the same value of the vector field [1, 9] defined by the condition $f(\bar{x}, t) = \bar{c}$. In the case of the one-dimensional autonomous system of Figure 1.1, the isocline equation is $f(x, t) = c$, obtaining parallel lines to the time axis. All the segments in each isocline have the same slope c . Sometimes it is useful to determine the isoclines before obtaining the vector field. Once the isoclines are known, several small segments with the same slope are traced along each isocline.

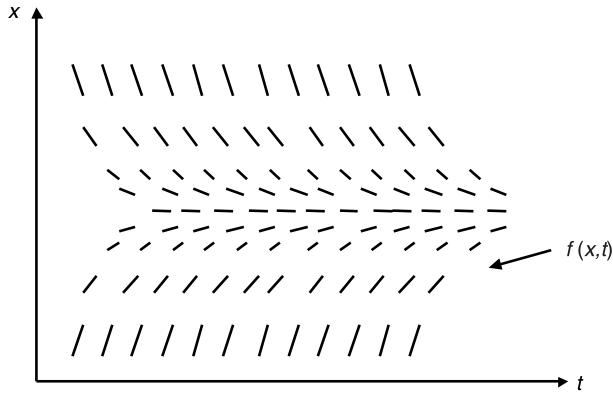


Figure 1.1 Vector field for an autonomous system with a single state variable $x \in R$. A short vector $f(x, t)$ is assigned to every point (t, x) .

If the nonlinear system (1.1) is solved for $\bar{x}(t)$, and \bar{x} is represented versus t , the resulting curve is necessarily tangent to the vector field because $\frac{d\bar{x}}{dt} = f(\bar{x}, t)$. This is clearly seen in the one-dimensional system of Figure 1.1. Thus, by joining together all the small segments in the direction indicated by the vector field, it is possible to obtain the solution curve for each initial value (t_o, x_o) . The accuracy is only limited by the length l of the segments employed in the representation. In the case of a first-order system, the vector field provides by itself valuable information about the system behavior. The problem is that obviously the application of the vector-field representation is limited to systems of very low order.

It is now time to indicate what is understood by solution of (1.1) and what the conditions are for the existence and uniqueness of this solution [2, 9, 10]. The case of a nonautonomous system of the form (1.1a) is initially going to be considered. A solution of the nonautonomous system (1.1a) is a function $\bar{x}(t) = \bar{u}(t)$, defined in a given time interval $I_t = (a, b) \in R$, fulfilling (1.1a) for all t belonging to I_t . Mathematically, $\left. \frac{d\bar{u}}{dt} \right|_{t=\tau} = \bar{f}(u, \tau)$, $\bar{u}(t_o) = \bar{x}_o$, for any

I_t . A similar definition is used in the case of an autonomous system (1.1b). The specification of the time interval $I_t = (a, b)$ in this general statement comes from the fact that time function $\bar{u}(t)$ might not be defined for all t (it might have discontinuity points). However, as already pointed out, because we are dealing with electronic circuits, only solutions defined for all t will be considered [i.e., $I_t = (-\infty, \infty)$].

It is also necessary to know whether a solution $\bar{u}(t)$ passing through a given point (t_o, \bar{x}_o) does exist and if this solution is unique. The theorem of Existence and Uniqueness [9] allows us to answer this by just examining function f . If function f is continuous and has continuous partial derivatives with respect to each variable x_i , with $i = 1$ to n , then the solution $\bar{x}(t) = \bar{u}(t)$, fulfilling $\bar{u}(t_o) = \bar{x}$, exists and is unique. Both the initial value of state vector $((\bar{x}_o))$ and the initial time (t_o) determine the circuit solution. Owing to this fact, solution curves cannot intersect. If two solutions curves with the same time origin intersected at the point (t_y, \bar{x}_y) , assuming the initial value $(t_o, \bar{x}_o) = (t_y, \bar{x}_y)$, the solution would not be unique.

In the case of an autonomous system (1.1b), the vector field f does not depend explicitly on time. Then, if $\bar{x}(t)$ is a solution of (1.1), $\bar{x}(t + \tau)$, with τ being an arbitrary time shift, is a solution too. Actually, the time-shifted solution can be replaced into (1.1) and the equation is fulfilled. This is not true in the nonautonomous system, due to the explicit dependence on time of the vector field f . The difference between the two systems is mathematically shown in the following:

$$\begin{aligned}
 & \frac{d \bar{x}(t)}{dt} = f(\bar{x}(t)) \\
 \text{Autonomous system} & \quad \frac{d \bar{x}(t + \tau)}{dt} = f(\bar{x}(t - \tau)) \\
 & \frac{d \bar{x}(t)}{dt} = f(\bar{x}(t), t) \\
 \text{Nonautonomous system} & \quad \frac{d \bar{x}(t + \tau)}{dt} \neq f(\bar{x}(t + \tau), t)
 \end{aligned} \tag{1.2}$$

Thus, the solutions of an autonomous system are invariant to time-domain translations $t \rightarrow t + \tau$. If a particular time value is specified, $t_o = 0$ for instance, the solution based at $(0, \bar{x}_o)$ is unique for each \bar{x}_o . If a different time value $t_o = t'$ is specified, the solution based at (t', \bar{x}_o) is the same solution based at $(0, \bar{x}_o)$ with a time shift $\tau = -t'$.

The solution curve of a nonautonomous system is often expressed $\bar{x}(t) = \bar{\varphi}_t(t_o, \bar{x}_o)$, with the initial point (t_o, \bar{x}_o) explicitly shown in brackets, and the evolving time appearing as a subindex. Since in the autonomous system, any arbitrary time displacement provides a valid solution, in the expression φ_t of a particular solution, it is not necessary to specify the time origin. For simplicity, the initial value $t_o = 0$ is generally assumed. The solutions of the

autonomous system are written $\bar{x}(t) = \varphi_t(\bar{x}_o)$. Thus, the explicit dependence of φ_t on t_o vanishes.

It is possible to formally express a nonautonomous system like an autonomous one. This can be done by considering the time t as a new state variable that is added to the set of state variables \bar{x} [7, 9]. This allows a more compact notation and can be advantageous in the system resolution because only one set of variables is employed, instead of using both \bar{x} and t . If the vector field of the nonautonomous system (1.1) is time periodic, with period $T > 0$ [i.e., $f(\bar{x}, t) = f(\bar{x}, t + T)$], then it is possible to use the variable $\theta = \frac{2\pi t}{T}$. The transformation is shown in the following:

$$\begin{aligned} \frac{d\bar{x}}{dt} &= f\left(\bar{x}, \frac{\theta T}{2\pi}\right) & \bar{x}(0) &= x_o \\ \frac{d\theta}{dt} &= \frac{2\pi}{T} & \theta(0) &= \frac{2\pi t_o}{T} \end{aligned} \quad (1.3)$$

Because f is periodic in time with period T , the new system (1.3) is periodic in θ with period 2π . The solution of (1.3) is defined in the cylindrical space $R^n \times S$, with $S = [0, 2\pi)$. The results for autonomous systems can thus be applied to the case of nonautonomous systems, periodic in time. If the nonautonomous system is nonperiodic, the transformation into an autonomous system is still possible [7]. However because of the lack of periodicity, the variations in θ cannot be restricted to the interval $[0, 2\pi)$. It is necessarily unbounded with $\theta \rightarrow \infty$ when $t \rightarrow \infty$.

In an autonomous system (1.2), it is generally possible to impose $\frac{d\bar{x}}{dt} = 0$ and solve $f(\bar{x}) = 0$. The resulting solutions are, of course, constant solutions and are called *equilibrium points*. Only a finite number of such points will generally exist. These constant solutions do not exist in nonautonomous systems owing to the explicit dependence on time of the vector field $f(\bar{x}, t)$. In an autonomous circuit (without forcing RF generators), the equilibrium points are the dc solutions of the circuit. An example of equilibrium point is the dc solution of an oscillator circuit that fails to oscillate in the experiment. The state variables of the circuit have constant values [instead of time-varying values $x_i(t)$] and the solution is an equilibrium point $\bar{x} = \bar{x}_{dc}$. When the circuit oscillates, a time-varying (generally periodic) solution is obtained $\bar{x} \equiv \bar{x}(t)$. However, the dc solution also exists for circuit element values for which the circuit actually oscillates. The reason is that the equations of the oscillator circuit can

always be solved for $\frac{d\bar{x}}{dt} = 0$. The constant solution \bar{x}_{dc} coexists with the actual oscillating solution $\bar{x}(t)$, although it is generally not observable (unstable).

To clarify all the above concepts, the analysis of a free-running oscillator circuit will be presented in Example 1.1. The nonlinear differential equations of the circuit are going to be obtained and compared with those of the general autonomous system (1.1b). The equilibrium point \bar{x}_{dc} and the periodic oscillating solution $\bar{x}(t)$ will be determined.

Example 1.1: Nonlinear differential equations of a cubic nonlinearity oscillator

The circuit in Figure 1.2 behaves as an autonomous system for a zero value of the voltage generator. The function $i_n(v)$ is the nonlinear transfer characteristic of the diode. In this example, the cubic relationship $i_n(v) = av + dv^3$ is used, with $a < 0$ and $d > 0$. The circuit parameter values are in the caption of Figure 1.2. The resistance value is $R = 0.75$ Ohm. The chosen state vector \bar{x} is composed of the current through the inductor i_L and the voltage across the capacitor v_C [i.e., $x \equiv (i_L, v_C)$]. This choice is very well suited for the application of Kirchoff's laws, although other state vectors are also possible, like $\bar{x} \equiv \left(i_L, \frac{di_L}{dt}\right)$ or $\bar{x} \equiv \left(v_C, \frac{dv_C}{dt}\right)$. With $x \equiv (i_L, v_C)$, the circuit is ruled by the following system of two nonlinear differential equations of the first order:

$$\begin{aligned} \frac{di_L}{dt} &= -\frac{R}{L}i_L - \frac{1}{L}v_C \\ \frac{dv_C}{dt} &= \frac{1}{C}i_L - \frac{1}{C}i_{nl}(v_C) = \frac{1}{C}i_L - \frac{1}{C}(av_C + dv_C^3) \end{aligned} \quad (1.4)$$

As compared with (1.1), system (1.4) is an autonomous system because time does not explicitly appear in the functions on the right-hand side. The vector field is independent of time. Because the vector field f is a continuous function

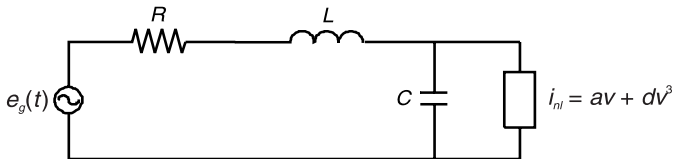


Figure 1.2 Diode oscillator: Linear element values are $L = 0.224 \mu\text{H}$, $C = 37.29 \text{ nF}$. Different values of the resistance R are considered in the text. The parameter values of the cubic nonlinearity are $a = -0.2 \text{ A/v}$, $d = 0.0375 \text{ A/v}^3$.

of v_C and i_L , and its partial derivatives with respect to v_C and i_L are continuous, the conditions for existence and uniqueness are fulfilled. Thus, for each initial point $(0, \bar{x}_o)$, with $\bar{x}_o = (v_c^o, i_L^o)$, a solution will exist, and it will be unique.

Before proceeding to analyze the system, note that the negative value of the parameter a makes the nonlinearity exhibit a negative value of incremental conductance about $v_C = 0$ (i.e., $\left. \frac{di_{nl}}{dv_C} \right|_{v_C=0} = a$). In practice, dc generators are

physically necessary to obtain negative resistance or conductance because nonlinearities with sections of negative slope require the presence of external energy sources. However, the idealization used here enables simpler equations.

The system is first solved for its constant solutions or equilibrium points, that is for solutions points fulfilling $\frac{d\bar{x}}{dt} = 0$. In this case, the resulting equilib-

rium point is $(v_C, i_L) = (0, 0)$. However, the numerical time-domain integration of the system (for the same circuit-element values) can provide a different solution. If this integration is performed from an initial value $x_o \neq (0, 0)$, a time-varying solution is also obtained $[v_C(t), i_L(t)]$. This is shown in Figure 1.3(a), where two different initial conditions, $\bar{x}_o = (0.01, 0)$ and $\bar{x}'_o = (1.1, 0)$, at the time $t_o = 0$ have been used. The solutions apparently intersect, but this is because only one state variable has been represented. Because it is a two-dimensional system, the solution curve must be traced in the complete space $[t, v_C(t), i_L(t)]$ as has been done in Figure 1.3. This shows that the two solutions do not intersect, which is in agreement with the Existence-Uniqueness theorem [9, 10]. On the other hand, because of the time invariance of autonomous solutions, any time shift of this helicoidal solution would give another solution, based at (t_o, \bar{x}_o) , with $t_o \neq 0$.

In the two solution curves of Figure 1.3, two different states can be distinguished: the transient and steady states. The transient state leads the solution $\bar{x}(t)$ from the initial point $\bar{x}(t_o) = \bar{x}_o$ to its asymptotic state $\bar{x}_s(t)$ obtained for $t \rightarrow \infty$. In Figure 1.4 this asymptotic state is a periodic oscillation reached after a transient whose duration depends on the initial value \bar{x}_o . The asymptotic behavior obtained for $t \rightarrow \infty$ is called the steady state $\bar{x}_s(t)$. In Figure 1.3, the different initial values give rise to a time shift of the steady-state solution. However, the amplitude and frequency of the oscillation do not depend on the initial conditions. As will be shown, this independence is only possible in nonconservative nonlinear systems.

Coming back to the difference between the transient and steady states, the behavior obtained for $t \rightarrow -\infty$, $\bar{x}_u(t)$ is also called steady state. Actually, in

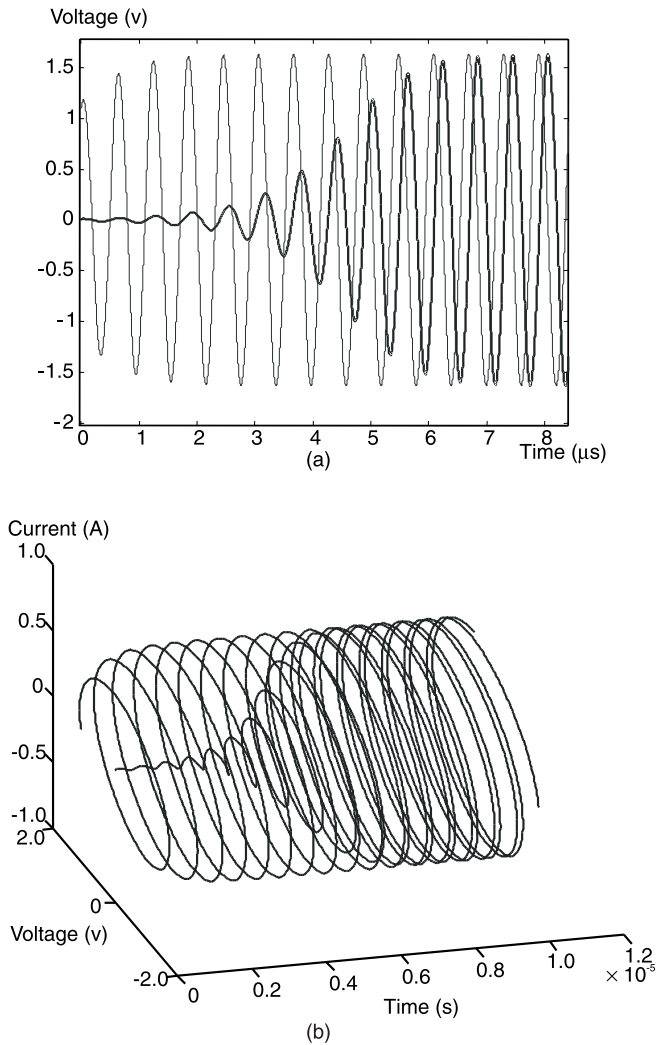


Figure 1.3 Solution of the cubic nonlinearity oscillator. Two different initial conditions have been considered. (a) Solution curves in the plane (t, v_C) . The coexisting equilibrium point lies on the horizontal axis ($v_C = 0$). (b) Solution curves in the complete space defined by (t, v_C, i_L) . Oscillation frequency: $f_o = 1.6$ MHz.

Example 1.1, when solving (1.4) with an initial condition $\bar{x}_o \neq 0$ for $t \rightarrow -\infty$, the equilibrium point $\bar{x}_{dc} = (0, 0)$ is obtained, which is the other system solution. Both the periodic solution $\bar{x}_i(t)$ and the constant solution $x_{dc} = (0, 0)$ are

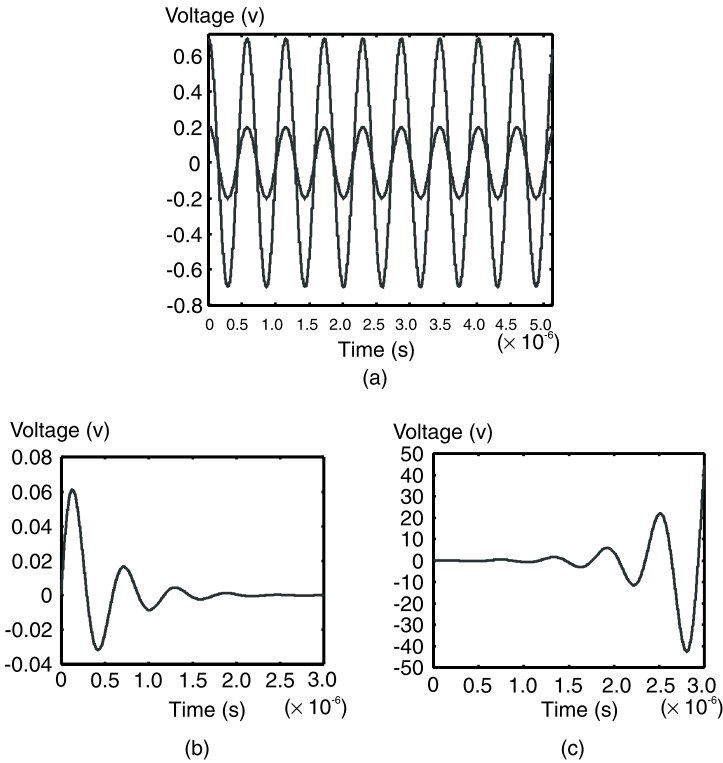


Figure 1.4 Linear oscillator: (a) undamped, (b) with positive damping, and (c) with negative damping.

steady states. For each initial condition $\bar{x}_o \neq 0$, the dc solution is obtained for $t \rightarrow -\infty$. Thus, this solution is unobservable in practice. This will be shown more clearly in the following sections.

1.2 Oscillations in Linear and Nonlinear Systems

Unlike forced or parametric oscillations, the self-oscillation of a given linear or nonlinear system is not due to the effect of an external periodic force or a periodic variation of the system parameters. A linear RLC circuit exhibits a self-oscillation under any external perturbation [11, 12]. However, the oscillation of the linear system decays in time. In contrast, the physically observed steady-state oscillation (in a free-running oscillator circuit, for example) has constant amplitude and period, and both are independent of the initial condition

(unless there is coexistence of oscillating solutions). Example 1.1 showed one steady-state oscillation (see Figure 1.3). Other types of oscillations (with amplitude growing ad infinitum or with amplitude, period, or both depending on the initial conditions) can be mathematically obtained in some equation systems, but are the result of an incomplete modeling of the system and are not physical.

To have a steady-state oscillation, the net energy loss per period must be zero and thus, the net damping per period must be zero [8]. In physical systems there is always dissipation, so, to compensate this, a source of energy must be present in the system. In an electronic circuit, a negative resistance will constitute this energy source. In the circuit of Figure 1.2 [described through the second-order system (1.4)], the nonlinear element, with its negative conductance about $v = 0$, constitutes the energy source. If the negative resistance were linear (which is physically impossible), the damping would always be negative (energy delivery) and the oscillation amplitude would grow ad infinitum. Thus for a *self-sustained* oscillation, the damping must be nonlinear, and thus, sensitive to the variable magnitude. The nonlinear active element provides amplitude sensitivity, which together with the presence of interactions (or feedback) in the system itself, controls the energy consumption. Thus, self-sustained oscillations are only possible in nonlinear, nonconservative systems. In a conservative oscillator, different oscillation amplitude is obtained for each initial condition, as in a pendulum with no friction, in which all the level curves, with constant energy, are solution curves. This is in contrast with the experimentally observed oscillations of electronic circuits, in which the oscillation amplitude and frequency are independent of the initial conditions.

The requirements for self-sustained oscillations are easily understood using a second-order oscillator system like the one in Example 1.1. Thus, taking the circuit in Figure 1.2 as the starting point, two examples are going to be presented in the following. Example 1.2 shows the case of a linear oscillator. Example 1.3 analyzes the sustained oscillation of the circuit in Figure 1.2 with nonlinear damping.

Example 1.2: Linear oscillator with and without damping

A linear system cannot have self-sustained oscillations. To see this, a linear RLC circuit will be considered. This may come from the circuit in Figure 1.2 after elimination of the nonlinear current $i_n(v)$. The following second-order differential equation is obtained:

$$\frac{d^2 i_L}{dt^2} + \frac{R}{L} \frac{di_L}{dt} + \omega^2 i_L = 0 \quad (1.5)$$

where ω is the resonance frequency $\omega = \frac{1}{\sqrt{LC}}$. Equation (1.5) can also be written in the form of the system (1.1), through the variable change $x_1 = i_L; jx_2 = \frac{di_L}{dt}$.

The damping term of (1.5) is the term affecting the time derivative $\frac{di_L}{dt}$. Initially, the case of a linear undamped oscillation will be considered by taking $R = 0$. A conservative system with no energy dissipation is obtained. It must, however, be emphasized that all physical systems are dissipative, so we are dealing with an ideal situation. The conservative system has the following equation:

$$\frac{d^2 i_L}{dt^2} + \omega^2 i_L = 0 \quad (1.6)$$

The solution of the former equation is given by

$$i_L(t) = c_1 e^{j\omega t} + c_2 e^{-j\omega t} \quad (1.7)$$

where the constants c_1 and $c_2 = c_1^*$ depend on the initial values of i_L and $\frac{di_L}{dt}$.

Thus, the solution of the linear system is an oscillation whose amplitude depends on the initial value \bar{x}_o of the state variables. This is shown in Figure 1.4(a). For each \bar{x}_o value, the oscillation has different amplitude, contrary to what happened in Example 1.1.

Now the case of an oscillator with linear damping will be considered. For $R \neq 0$, $\lambda_{1,2} = \frac{-R}{2L} \pm \frac{1}{2} \sqrt{\left(\frac{R}{L}\right)^2 - 4\omega^2} \equiv \alpha \pm j\beta$, where $\lambda_{1,2}$ are the eigenvalues associated with the linear equation (1.5). Then, the solution of the linear differential equation (1.5) is given by

$$i_L(t) = c_1 e^{(\alpha + j\beta)t} + c_2 e^{(\alpha - j\beta)t} \quad (1.8)$$

For $R > 0$, the oscillation at the frequency β will exponentially decay in time [Figure 1.4(b)], as it happens in real-life *inductor-capacitor* resonant circuits, in which resistances, due to material loss, are always present. On the other hand, for $R < 0$, the amplitude exponentially increases in time [Figure 1.4(c)], which is

physically impossible. In physical systems the negative resistance (conductance) of the active element always decreases with the amplitude of the current through it (or the voltage across its terminals). The case $R > 0$ [Figure 1.4(b)] provides an oscillating transient leading to the equilibrium point $\left(i_L, \frac{dv_C}{dt}\right) = (0, 0)$. The case $R < 0$ provides a transient ad infinitum [Figure 1.4(c)].

Example 1.3: Nonlinear oscillator with nonlinear damping

The circuit of Figure 1.2 is an example of nonlinear system in which a steady-state oscillation is possible. The oscillation mechanism of the circuit can be seen more clearly by using a single differential equation of the second order:

$$\frac{d^2 v_C}{dt^2} + \left[\frac{R}{L} + \frac{1}{C} (a + 3d v_C^2) \right] \frac{d v_C}{dt} + \omega^2 [(1 + Ra)v_C + R d v_C^3] = 0 \quad (1.9)$$

where ω is the resonance frequency $\omega = \frac{1}{\sqrt{LC}}$. The equation is nonlinear in

both the damping term, affecting $\frac{d v_C}{dt}$, and the independent (restoring) term.

Inspecting the nonlinear damping, its value will be negative for small $v_C(t)$ (because of the negative coefficient a) and energy will be delivered to the system. For big value of $v_C(t)$, the damping will be positive (because of the influence of the term $3d v_C^2$) and energy will be taken from the system. Thus, the presence of self-sustained oscillations can be expected.

The oscillation of Figure 1.3 can be predicted through a classical check-up for the possible fulfillment of oscillation start-up conditions in the frequency domain. To do so, the nonlinear function $i_n(v) = av + dv^3$ is linearized about the dc point ($v_C = 0$), obtaining the small-signal conductance:

$$G_N(0) = \left. \frac{\partial i_{nl}}{\partial v} \right|_{v=0} = a. \text{ Because } a < 0, \text{ the nonlinear element behaves like a}$$

source of energy about $v_C = 0$. The total admittance at the diode terminals Y_T is given by

$$Y_T(v_C \cong 0, \omega) = a + \frac{R}{R^2 + (L\omega)^2} + j \left(C\omega - \frac{L\omega}{R^2 + (L\omega)^2} \right) \quad (1.10)$$

The Y_T function is plotted versus frequency in Figure 1.5. The familiar conditions $\text{Re}[Y_T(f)] < 0$ and $\text{Im}[Y_T(f)] = 0$ are fulfilled at $f_o \cong 1.6$ MHz. These conditions indicate an imbalance between the energy delivered by the nonlinear element and the dissipation at the load resistor R . The energy excess is employed in the growth of an oscillation $x(t) = (v_c(t), i_L(t))$ at the resonance frequency (Figure 1.3).

Steady-state oscillations can only be analytically obtained from nonlinear differential equations in a few simplified cases. Numerical simulations in the time or frequency domain are usually necessary. In Example 1.4, a very approximate calculation of the oscillation in the circuit of Figure 1.2 will be carried out. The calculation will be made in the frequency domain, replacing the instantaneous model of the nonlinear element with its describing function.

Example 1.4: Approximate calculation of the steady-state oscillation of the cubic nonlinearity oscillator through the use of the describing function

In the describing function approach a sinusoidal solution (which may include a dc component) is assumed. The circuit of Figure 1.2 is considered here. Due to the absence of bias generators and the cubic nonlinearity, it is easily seen that the voltage across the nonlinear element will have no dc component. This voltage is assumed: $v_c(t) = V_o \cos(\omega_o t)$. The oscillator solution could equally have been expressed $v_c(t) = V_o \cos(\omega_o t + \phi)$. However, owing to the irrelevance of

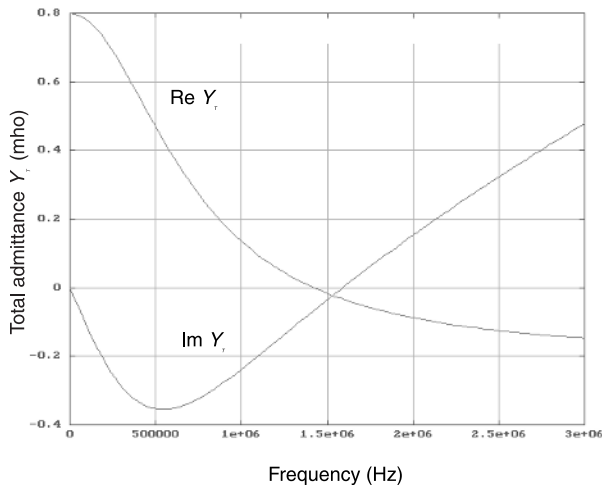


Figure 1.5 Verification of oscillation start-up conditions from an admittance analysis in small signal. The oscillation conditions are fulfilled for $f \cong 1.6$ MHz.

the time origin t_o in the autonomous system, any phase value provides a solution; so, for simplicity, the value $\phi = 0$ is chosen. Then, the describing function is associated to $i_{nl}(v_o)$ calculated as the complex ratio between the first harmonic of the output signal and the sinusoidal amplitude [11]:

$$G_D(V) = \frac{i_{nl}(V \cos(\omega t))|_{1st \text{ harmonic}}}{V} = a + \frac{3}{4}dV^2 \quad (1.11)$$

The describing function provides a very approximate model for the nonlinearity and is only valid for sinusoidal input $v(t)$. The model shows how, in agreement with physical requirements, the nonlinear conductance decreases with the voltage across the element terminals because $a < 0$, $d > 0$. The instantaneous model of the nonlinearity $i_{nl}(v)$ is thus replaced by its (very approximate) describing function. Applying Kirchoff's laws at the first (and only) harmonic component, the following equation is obtained:

$$Y_T(V_o, \omega_o)V_o = \left\{ \begin{array}{l} a + \frac{3}{4}V_o^2 + \frac{R}{R^2 + (L\omega)^2} + \\ j\left(C\omega - \frac{L\omega}{R^2 + (L\omega)^2}\right) \end{array} \right\} V_o = 0 \quad (1.12)$$

Compared to (1.10), (1.12) establishes the equality (in magnitude) of positive and negative conductance at the resonance frequency. Thus, the net energy consumption per period is equal to zero.

As can be seen, one of the solutions of (1.12) is $V_o = 0$, that is, a solution having no sinusoidal component. This solution corresponds, in fact, to the dc solution $v_c = 0$, $i_L = 0$ that had already been obtained in Example 1.1. The oscillating solution $R = 0.75\Omega$ is given by the following values:

$$V_o = \sqrt{\frac{-RC - La}{\frac{3}{4}Ld}} = 1.63v \quad ; \quad \omega_o = \sqrt{\frac{1}{LC} - \frac{R^2}{L^2}} = 104210^7 s^{-1} \quad (1.13)$$

The current calculation is straightforward. Its expression will be $i_L(t) = I_o \cos(\omega_o t + \phi)$, with $I_o = \frac{V_o}{\sqrt{R^2 + (L\omega_o)^2}}$ and $\phi = \arctg\left(\frac{-L\omega_o}{R}\right)$.

Thus, a perfect sinusoidal oscillation is obtained (because it was assumed this

way). For low-quality factors, the actual waveform will differ greatly from a sinusoidal waveform, invalidating the describing-function approach.

Compared to the time-domain integration of Example 1.1, the above resolution directly tackles the oscillator steady state (as in any frequency-domain analysis). There is no transient analysis, and this is a high risk. The obtained solution might be an unobservable solution to which the system never evolves. The physical observability of a solution can only be verified through the stability analysis of this solution. In the above example, the dc solution $\bar{x}_{dc} = 0$ is an example of an unobservable solution. It is only obtained for initial condition $\bar{x}_o = 0$, while for any other value $\bar{x}_o \neq 0$, the system evolves to the oscillating solution (Figure 1.3). But the condition $\bar{x}_o = 0$ is impossible in practice because of the unavoidable presence of perturbations in physical systems (coming from noise or from a slight fluctuation of the bias sources, for instance).

The checkup for oscillation start-up conditions of Figure 1.5 is, in fact, a stability analysis of the equilibrium point $(v_C, i_L) = (0, 0)$. The nonlinear element is linearized about $v_C = 0$, and this linearization is sufficient to determine the evolution of the solution versus perturbations because of their smallness. The energy unbalance makes this solution point unstable, and, thus, physically unobservable. In contrast, the periodic oscillation is robust versus perturbations and will be obtained in the experiment.

1.3 Phase-Space Representation of Solutions

1.3.1 Transient Trajectories and Limit Sets

When dealing with the solutions of a nonlinear system, a distinction is sometimes made between the solution curve and the solution trajectory. In the case of an autonomous system, the solution curve is traced versus time, as in Figure 1.3, while the *solution trajectory* is the projection of the solution curve on the space defined by the state variables x_i , with $i = 1$ to n , that is, the space obtained by assigning a coordinate axis to each state variable x_i . This space is known as the *phase space* [7–9]. Thus, in the case of an autonomous system with $\bar{x} \in R^n$, the phase space will have n dimensions. As will be shown, all the time-shifted solutions of the same autonomous system (based on $\bar{x}_o, t_o = \tau$ with τ being an arbitrary time value) give rise to the same trajectory in the phase space. In the case of a nonautonomous system, time can be considered a state variable, as shown in (1.3). Then, the phase space is the space defined by $t \times R^n$ and its dimension will be $n + 1$.

For the phase space representation of solutions, any choice of state variables can be used, provided it is a complete set. As has already been said, the

representation of the solution on the phase space gives rise to a *trajectory*. It shows the sequence of points through which the solution passes as time evolves. When carried out up to order three, this representation helps understand the system behavior. In a system with n variables and $n > 3$, the phase-space representation of the solution is not possible. However, projections of these solutions in lower-order spaces can still be carried out with the subsequent loss of information. The projection of different trajectories in a lower order space may lead to an apparent intersection of these trajectories. In spite of this, the projection will still provide good insight into the system behavior in most cases.

The trajectories in a phase space of order $n = 2$ can be classified as *ordinary* or *singular*. Equilibrium points and closed trajectories are examples of singular trajectories [8] (see Figure 1.6). Isolated steady-state solutions give rise to bounded sets called *limit sets*. Open semitrajectories that tend to a bounded set (e.g., a point or a closed trajectory) for either $t \rightarrow \infty$ or $t \rightarrow -\infty$ and behave as separatrixes (or borders between different regions) are also singular. The singular trajectories divide the phase space into cells (see Figure 1.6). The cells contain ordinary trajectories, all of which have the same qualitative behavior. Thus, to have the whole portrait of the system, only the knowledge of its singular trajectories and their behavior will be necessary.

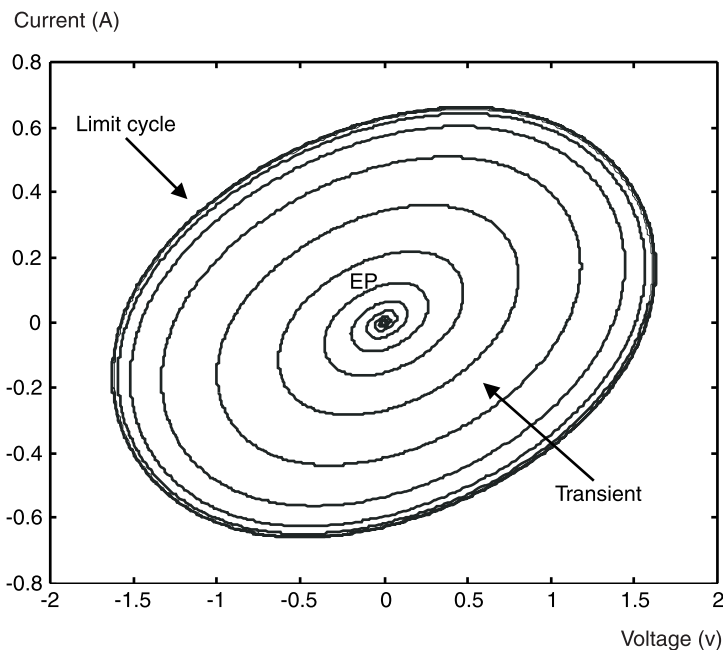


Figure 1.6 Solutions of the cubic nonlinearity oscillator; trajectory in the phase space.

When representing the solutions of a given system in the phase space, steady states are bounded sets and transients lead from one bounded set to another. The bounded nature of limit sets in nonautonomous systems is more difficult to understand owing to the necessary inclusion of time as one of the variables in the phase-space representation. However, in the usual case of periodic forcing at a frequency ω_g , the time axis can be replaced with the phase axis $\phi = \omega_g t$. Then, the hyperplanes $\phi = 0$ and $\phi = 2\pi$ are identified and the limit sets are bounded.

In Example 1.5, a phase-space representation of the solutions of the circuit of Figure 1.2 will be carried out.

Example 1.5: Phase-space representation of the solution of the cubic nonlinearity oscillator

To represent the solution curve (versus time) of the cubic-nonlinearity oscillator of Figure 1.2, a three-dimensional space is necessary, since the corresponding system has two state variables. This representation was shown in Figure 1.3(b), where the constant solution $(v_C, i_L) = (0,0)$ was given by the straight line $v_C(t) = 0, i_L(t) = 0$.

Because (1.4) is an autonomous system, the corresponding phase space will have the dimension $n = 2$ and will be the plane defined by v_C and i_L . Thus, to obtain the solution trajectory, a projection of the solution on this plane is carried out in Figure 1.6. When doing so, the constant solution $v_C(t) = 0, i_L(t) = 0$ becomes a point $(v_C, i_L) = (0,0)$ located at the plane origin. In turn, the oscillating solution obtained for $\bar{x}_o \neq 0$ becomes a spiral plus a closed curve. Note that all the possible time-shifted solutions of the autonomous system overlap in this representation, giving rise to the same trajectories. Like the point $(0,0)$, the closed curve is a singular trajectory of this phase space. The spiral is an ordinary trajectory corresponding to the transient observed in Figure 1.3(b). The system only follows the spiral trajectory once until it reaches the cycle. Once in the cycle, it turns in it endlessly because this is the behavior obtained for $t \rightarrow \infty$. For other initial conditions $\bar{x}_o \neq 0$, a different spiral trajectory (with the same qualitative behavior) would have been obtained. The point at the origin is the dc solution, and the closed curve, or cycle, is the steady-state oscillation. Note that in the periodic steady state, the values of the system variables are repeated after exactly one period T . Then, the solution fulfills $\bar{\varphi}_{kT}(\bar{x}_o) = \bar{x}_o$ for integer k and \bar{x}_o belonging to the oscillating steady state. The resulting closed trajectory is called a *limit cycle*, discussed in Section 1.3.2. For a different selection of the state variables (e.g., v_C and $\frac{dv_C}{dt}$), the qualitative result would be the same. The

phase-space representation is used for the better understanding of the nonlinear dynamics of the circuit, so the particular choice of the state variables (provided that it is a complete set) is irrelevant.

1.3.2 Limit Cycles

As shown in Example 1.5, the phase-space representation of a self-sustained oscillating solution of an autonomous system provides a limit cycle. It is an isolated closed trajectory in the phase space in a manner similar to the equilibrium points, which are also isolated. In a two-dimensional system no trajectory interior or exterior to a limit cycle ever crosses the cycle. Thus, the limit cycle can be considered the border (or limit) between two different regions of the plane: the region inside the cycle and the region outside the cycle. All the trajectories inside the cycle evolve qualitatively in the same way, converging toward the limit cycle or diverging from it, and so do all the trajectories outside the cycle.

In Figure 1.7 the behavior of trajectories in the neighborhood of the limit cycle of Example 1.5 is analyzed. As can be seen, for all the possible initial values \bar{x}_o (smaller or bigger in amplitude than the limit cycle) trajectories evolve so as to join the limit cycle. As an illustration, three different initial

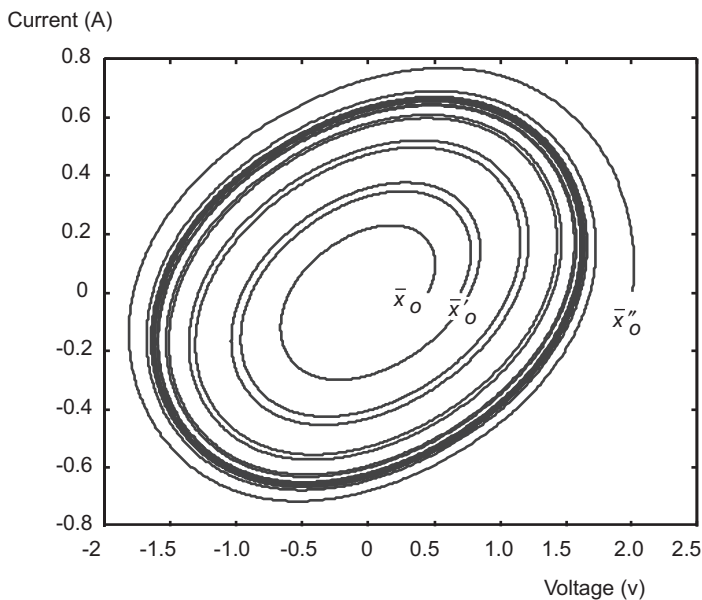


Figure 1.7 Different solution trajectories for different initial conditions. The trajectories never intersect, and the limit cycle is isolated.

values have been used. Note that due to the *Existence-Uniqueness* theorem, trajectories in the phase space do not intersect. All the ordinary trajectories evolve in the same way. Thus, in order to predict the system evolution for all the possible initial conditions \bar{x}_o , only the knowledge of its singular trajectories and their behavior (with respect to the neighboring trajectories) is required. As will be shown later, a given nonlinear system may have more than one limit cycle, with different behavior.

Not all the closed trajectories in the phase space are limit cycles. Cycles in conservative systems are not isolated and are not limit cycles [8]. The limit cycle is the trajectory associated with a self-sustained oscillation, so it can only exist in nonlinear, nonconservative systems, having net damping equal to zero. To show an example of cycles that are not limit cycles, the oscillating solutions of the linear circuit of Example 1.2 (an LC resonant circuit without resistance) are represented in Figure 1.8. Three different initial conditions \bar{x}_o have been used and a different cycle obtained for each. The phase space consists of a continuous family of nesting cycles, forming something similar to a continuous disk. This is due to the fact that each initial value gives rise to an oscillation with different amplitude [see (1.7)]. The cycles composing the disk are not limit cycles because they are not isolated cycles. In a conservative system, periodic solutions are never isolated and they are not robust, that is, capable of recovering from perturbations, because the solution moves from one to another under any perturbation.

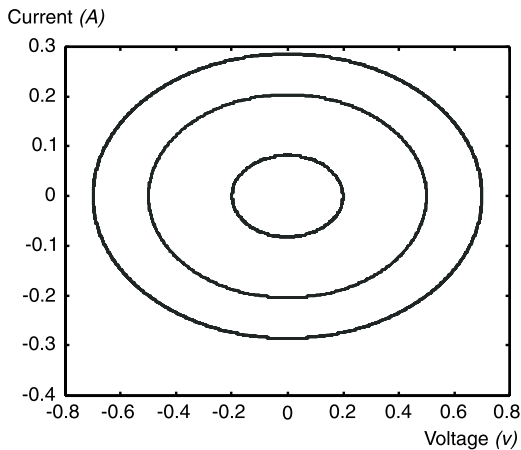


Figure 1.8 Solution cycles of an ideal LC resonant circuit with no resistance. They are not isolated, and they are not limit cycles.

1.3.3 Invariant Sets

It has been shown in Section 1.1 that, in the case of an autonomous system, the solution can be expressed as $\bar{x} = \varphi(\bar{x}_o)$. Now, when \bar{x}_o varies, a function can be defined $\varphi_t : R^n \rightarrow R^n$. This function is called *system flow* [9]. This has been represented in Figure 1.9, where a subset X_o of \bar{x}_o values is transformed into the subset X after the precise time interval t through the action of the system flow. For other time value t' , the flow would provide a different image subset X' . It is assumed that for any finite t , the inverse function φ_t^{-1} exists; also, both the Jacobian matrix $[D\varphi_t] = \frac{\partial \varphi_t}{\partial x}$ and the inverse $[D\varphi_t]^{-1}$ exist and are continuous. In the case of a nonautonomous system, with periodic forcing (with a periodic input generator), the solution can be expressed $\bar{x}(t) = \varphi_t(\bar{x}_o, \theta_o)$ with $(\bar{x}, \theta) \in R^n \times S$. Then the flow is defined as $\varphi_t : R^n \times S \rightarrow R^n \times S$.

The concept of system flow is essential for the characterization of a given nonlinear system. The sets that remain invariant under the application of the flow are very special sets. Two examples have already been seen. One of them is the equilibrium point or dc solution because $\bar{x}_o = \varphi_t(\bar{x}_o)$ for all t . Another invariant set is the limit cycle because once the solution is in the cycle, it remains there for all t . Points and closed orbits are invariant sets under the flow action. However, any set consisting of trajectories extending to $t \rightarrow -\infty$ or to $t \rightarrow \infty$ would also be invariant under the action of the flow. Some of these invariant sets are essential to define the structure of the phase space, since they behave as separatrixes of different regions in the phase space. We will come back to this when dealing with stability problems. For the moment, attention will only be paid to the bounded invariant sets or limit sets.

Two types of limit set have been studied: the equilibrium point (or constant solution) and the limit cycle (or periodic oscillation). However, these are

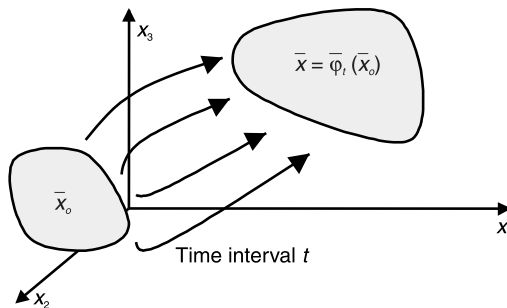


Figure 1.9 Flow $\varphi_t(R^n) \rightarrow R^n$ in an autonomous system.

not the only types of limit sets that can be observed in a nonlinear system. Other types are possible, in correspondence with the different types of steady-state solutions that can be obtained. These solutions can roughly be classified into four types: constant, periodic, quasiperiodic, and chaotic. Each one gives rise to a different type of limit set when represented in the phase space. The corresponding bounded sets (or limit sets) will be the next object of our study. Although the equilibrium point and the limit cycle are already known, they will be included in the comparison for completeness.

1.3.3.1 Equilibrium Point or DC Solution

The dc solutions or equilibrium points of an autonomous system are obtained by equating $\frac{d\bar{x}}{dt} = 0$. When represented in the phase space, each one gives rise to a single point. The point is a geometric figure of zero dimensions. One example of observable equilibrium point is the dc solution of a free-running oscillator circuit that fails to oscillate.

1.3.3.2 Limit Cycle or Periodic Solution

As has already been shown, when the periodic oscillation of a nonconservative system is represented in the phase space, an isolated closed orbit, named a *limit cycle*, is obtained. Any well-behaved free-running oscillator circuit gives rise to a limit cycle.

1.3.3.3 Limit Torus or Quasiperiodic Solution

Quasiperiodic solutions are obtained in nonlinear systems having two or more nonharmonically related fundamentals. This kind of solution is observed, for instance, in frequency mixers having two input sinusoidal signals: the RF (or IF) carrier and the local-oscillator signal. This kind of solution is also easily obtained when a RF generator is connected to a free-running oscillator. For most of the input power and input frequency values, the autonomous frequency and generator frequency coexist, giving rise to a two-fundamental solution. Both frequencies mix, and the circuit behaves like a self-oscillating mixer [13]. One of the two fundamental frequencies is externally introduced, and the other is autonomous. This is the case we will deal mostly with in the book.

For two independent fundamentals (ω_1 and ω_2), the circuit steady-state solution can be expanded in a Fourier series as

$$\bar{x}(t) = \sum_{k,l} \bar{X}_{kl} e^{j(k\omega_1 + l\omega_2)t} \text{ with } k, l \in Z \quad (1.14)$$

where Z is the set of integer numbers and \bar{X}_{kl} is the vector containing the spectral component $k\omega_1 + l\omega_2$ of all the state variables. In the phase-space, the existence of two independent fundamentals gives rise to two independent rotations (see Figure 1.10), one provided by ω_1 and the other by ω_2 . The ratio r between the two fundamental frequencies is called the *rotation number* [8, 14]:

$$r = \frac{\omega_1}{\omega_2} \quad (1.15)$$

To understand the name *rotation number*, one can see what happens with the phase θ_1 associated with the fundamental frequency ω_1 after a period of the second fundamental $T_2 = \frac{2\pi}{\omega_2}$. Let the initial value of this phase be $\theta_1 = \theta_{1o}$. After the time $t = T_2$, the phase θ_1 will be

$$\theta_1 = \theta_{1o} + \omega_1 t \Big|_{t=\frac{2\pi}{\omega_2}} = \theta_{1o} + 2\pi \frac{\omega_1}{\omega_2} = \theta_{1o} + r 2\pi \quad (1.16)$$

Thus, the rotation number indicates the fraction of 2π ($r 2\pi$) rotated by the angle associated with one of the fundamentals after exactly one period of the second fundamental. The rotation number agrees, as is shown in (1.15), with the ratio between the two fundamental frequencies.

If r is irrational, that is, $r \neq \frac{m}{n}$, with m and n positive integers, there is no common period for ω_1 and ω_2 , and the solution (1.14) is quasiperiodic. The

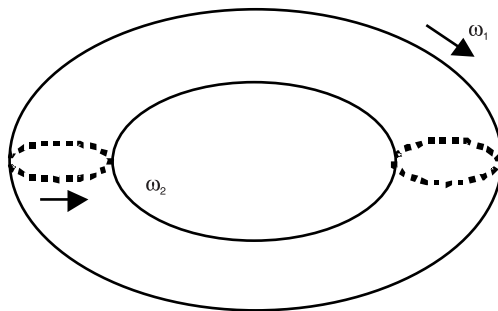


Figure 1.10 Quasiperiodic regime with two fundamental frequencies. 2-torus. There are two independent rotations, and the trajectory eventually fills the torus surface.

two frequencies are incommensurate. Note that in the opposite case, for $r = \frac{m}{n}$, it would be possible to write $n\omega_1 = m\omega_2$. For $m < n$, both frequencies would be integer multiples of $\omega_o = \frac{\omega_2}{n}$ because $\omega_2 = n\omega_o$ and $\omega_1 = m\omega_o$. Thus, the solution would be periodic with the period $T_o = \frac{2\pi}{\omega_o}$. This calculation is not possible for $r \neq \frac{m}{n}$.

When representing any state variable x_i of a quasiperiodic solution versus time, the resulting waveform $x_i(t)$ looks like a modulated waveform [see Figure 1.11(a)]. A periodic motion at ω_1 is modulated by a second motion at ω_2 , which is also periodic, but with an incommensurate period. The two independent fundamentals of the quasiperiodic signals give rise in the nonlinear system to intermodulation products, and the frequency spectrum looks like the spectrum of a frequency mixer [Figure 1.11(b)].

Considering a nonlinear system with periodic forcing (e.g., an injected oscillator), the phase space representation of the solutions can be carried out by using the variable $\theta = \frac{2\pi}{T_g}t$, with T_g being the period of the forcing signal.

A two-fundamental solution of this system could be due to the existence, in addition to the forced fundamental ω_g , of a self-oscillation frequency ω_o . For rotation number $r \neq \frac{m}{n}$, the solution is not periodic, and the trajectory in the phase space cannot return to the same point \bar{x} after a specific time T . Thus, the phase-space representation of the quasiperiodic solution cannot be a cycle. However, as shown in Figure 1.11, the solution curve is bounded in terms of \bar{x} for all t . When representing a quasiperiodic solution in the phase space (considering the variable $\theta = \frac{2\pi}{T_g}t$), the trajectory fills the surface of a 2-torus, as

shown in Figure 1.12. This limit set can be understood as the result of the two independent rotations in the two-fundamental solution (Figure 1.10). It is a hollow figure, so the 2-torus limit set is a two-dimensional set. A single trajectory will eventually fill the whole surface of the 2-torus (Figure 1.12). In the case of n fundamental frequencies without rational relationship, there would be n independent rotations. An n -torus would be obtained, giving rise to an n -dimensional figure. The n -torus, with $n > 2$, is also called a *hypertorus* [7].

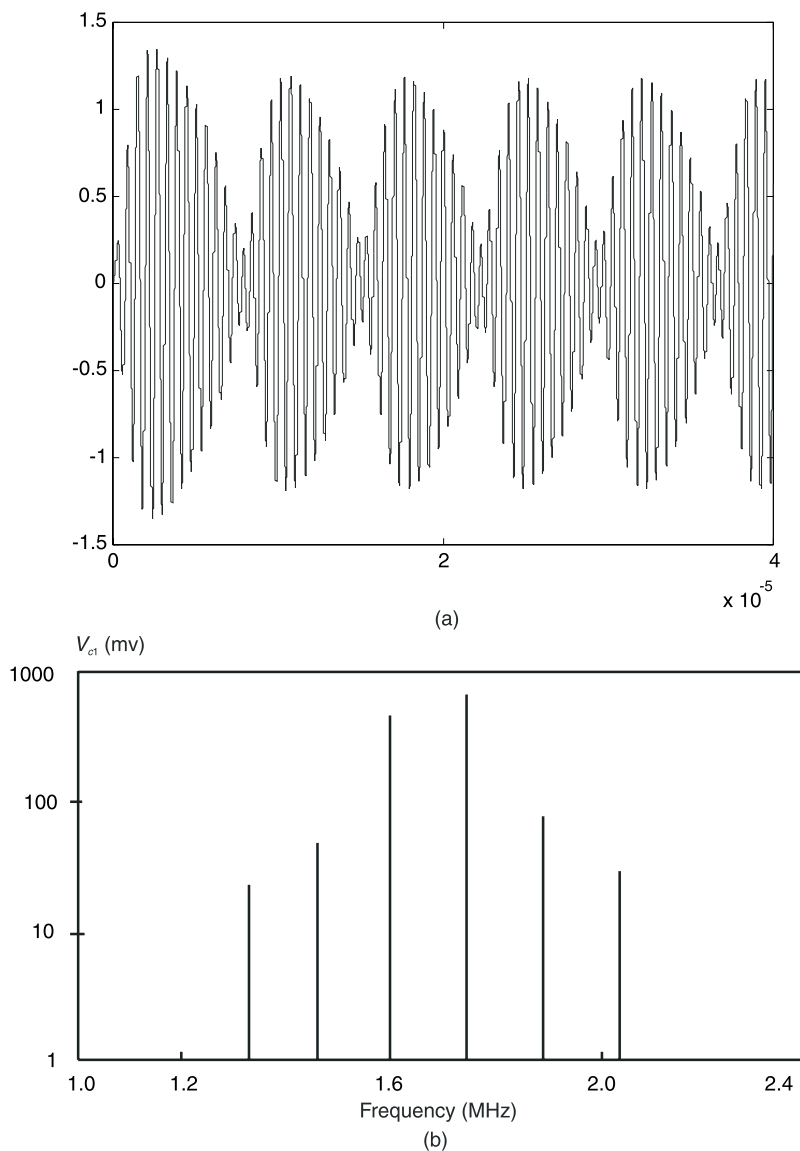


Figure 1.11 Quasiperiodic solution of the cubic nonlinearity oscillator analyzed in Example 1.6; generator values are $E_g = 0.13v$, $f_g = 1.74$ MHz: (a) time-domain waveform and (b) spectrum.

To clarify the above ideas, Example 1.6 analyzes a quasiperiodic solution of the oscillator circuit in Figure 1.2, under the presence of an input RF generator.

Example 1.6: Quasiperiodic solution of the cubic nonlinearity oscillator

When a sinusoidal voltage source $e_g(t) = E_g \cos(\omega_g t)$ is introduced in the circuit of Figure 1.2 in series with the resistor R (with value $R = 1$ Ohm), the following equation system is obtained:

$$\begin{aligned} \frac{di_L}{dt} &= -\frac{R}{L} i_L - \frac{1}{L} v_C + \frac{1}{L} E_g \cos(\omega_g t) \\ \frac{dv}{dt} &= \frac{1}{C} i_L - \frac{1}{C} (av_C + d v_C^3) \end{aligned} \quad (1.17)$$

As can be seen, time explicitly appears on the right-hand term. Thus, the vector field f explicitly depends on time, and the system is nonautonomous [see (1.1a)]. It is a periodic vector field.

For $E_g = 0$, (1.4) had an oscillating solution at frequency $\omega_o = 2\pi \cdot 1.6 \cdot 10^6 \text{ s}^{-1}$. Now, in the presence of the input generator, for some values of this generator, the two frequencies, ω_g and ω_o , will coexist. With the connection of the generator $e_g(t)$, the value of the self-oscillating frequency ω_o is not the same as in free-running situation (although it is generally very close). The external generator $e_g(t)$ has an influence over the frequency and amplitude of the self-oscillation. Their values must adapt the new forced condition of the circuit.

In Figure 1.11(a), the solution corresponding to the input-generator values $E_g = 0.13v$ and $f_g = 1.74$ MHz has been represented. It is a quasiperiodic solution that, versus time, looks like a modulated waveform. The spectrum [Figure 1.11(b)] is the result of the intermodulation of the two fundamental frequencies $k\omega_g + l\omega_o$. The circuit operates like a self-oscillating mixer. In the spectrum, the envelope of the frequency components $k\omega_o$ often has a triangular shape [Figure 1.11(b)]. In Figure 1.12 the same solution has been represented in the phase space defined v_C, i_L and $e_g(t)$. Note that $e_g(t)$ is a function of the phase $\theta(t)$, $\theta(t) = \omega_g t$ which must be included as a phase-space variable in the case of periodic forcing [i.e., $e_g(\theta) = E_g \cos(\theta)$]. Thus, $e_g(t)$ plays the same qualitative role. The trajectory is no longer a cycle because the solution is not periodic. It is a 2-torus.

The self-oscillating mixing regime is often exploited in practical design. It enables a very compact and low-power-consumption mixer circuit because the same nonlinear device (transistor or diode) acts as oscillator and mixer. In other circuits, the quasiperiodic regime is undesired. An example is an unstable power amplifier. In this circuit, the spurious oscillation gives rise to a second fundamental frequency, nonrationally related with that of the input generator.

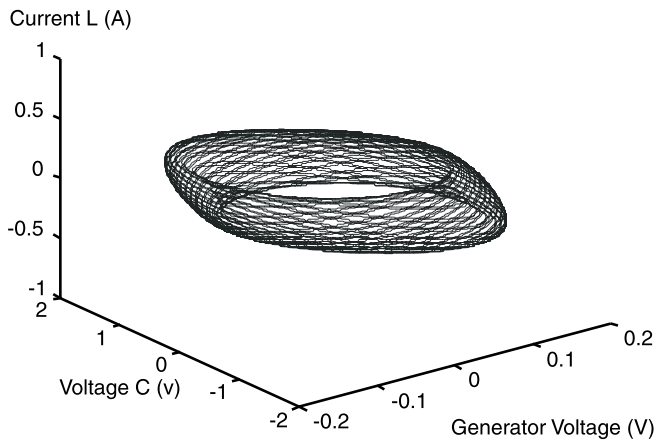


Figure 1.12 Phase-space representation of the quasiperiodic solution of the cubic nonlinearity oscillator; generator values are $E_g = 0.13\text{v}$, $f_g = 1.74\text{ MHz}$; resistance is $R = 1\text{ Ohm}$.

1.3.3.4 Chaos

The chaotic solutions can be defined in a general way as steady-state solutions that are neither constant, nor periodic, nor quasiperiodic [15–21]. A chaotic solution is shown in Figure 1.13(a). These solutions show a sensitive dependence on the initial conditions. This means that two solutions with an

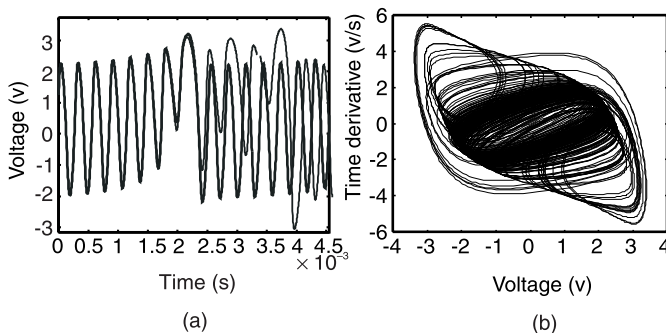


Figure 1.13 Chaos: (a) typical chaotic waveform where two trajectories have been traced with slightly different initial conditions, and (b) phase-space representation.

arbitrarily close initial value, \bar{x}_o, t_o , diverge exponentially in time. In Figure 1.13(a) the circuit has been solved twice for the same parameter values with slightly different initial conditions. Initially the two trajectories overlap. However, as time evolves, they separate from each other and diverge. Since the initial conditions cannot be known with infinite accuracy, the time evolution of the circuit variables $\bar{x}(t)$ is unpredictable. It is thus an unpredictable behavior that, contrary to noise and random signals, is deterministic.

In the phase space, chaotic solutions give rise to a bounded geometric figure with a fractal dimension [see Figure 1.13(b)]. The fractal dimension is related to the fact that the trajectory, unlike the case of cycles or tori, does not fill the whole figure, which seems to lack pieces [Figure 1.13(b)]. The divergent trajectories are uncorrelated versions of the same underlying pattern. The divergence is due to stretching and folding of the bundle of trajectories onto itself, as will be explained in Section 1.5, in more detail. Different chaotic limit sets have been obtained in the literature, corresponding to different types of nonlinear systems. They are surprisingly well structured and generally very beautiful.

Because the chaotic solution is neither periodic nor quasiperiodic, it has a continuous spectrum (at least in some frequency intervals). Thus, it is often mistaken for an anomalous noise increase when observed in a spectrum analyzer. Figure 1.14 shows the spectrum of the chaotic solution of Figure 1.13. Chaotic solutions are very common in electronic circuits of any frequency

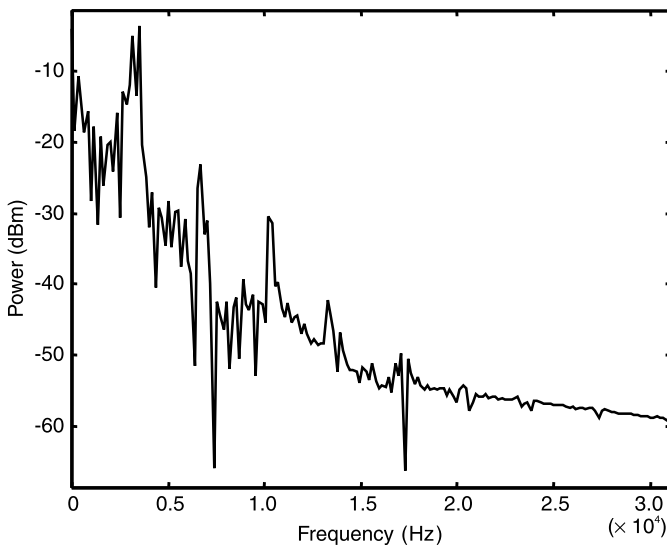


Figure 1.14 Chaotic spectrum of the solution of Figure 1.13.

range. At microwaves, the usual measurement in the frequency domain (with a spectrum analyzer) has made more difficult its identification by the circuit designer. They just provide a broadband spectrum that can be mistaken with noise or interference. When using an oscilloscope, the x - y mode provides a planar projection of the phase space, and thus, a projection of the chaotic limit set. Its fractal quality and special geometric structure are generally observable.

1.4 Stability of Limit Sets

1.4.1 Concept of Stability

As shown in Examples 1.1 and 1.5, in typical nonlinear systems, two or more limit sets may coexist for the same parameter values. In Example 1.5, the equilibrium point $\bar{x}_o = (v_C, i_L) = (0,0)$ coexists with the periodic oscillating solution or limit cycle $\bar{x}(t) = (v_C(t), i_L(t))$. However, only the periodic solution is physically observed. The dc solution does not recover from small perturbations, while the periodic oscillation does. Small perturbations are always present in physical systems. These may come from noise, from a small fluctuation in the generators, or from a small mechanical vibration, for instance.

To see the effect of perturbations on each of the two solutions (the dc solution and the oscillating solution), both of them are going to be perturbed in simulation. The perturbation can be considered as a small amplitude impulse taking place at a certain time t_o . In the representation of Figure 1.15, the two solutions are the dc solution $v_C = 0$ (lying on the horizontal axis) and the oscillating solution $v_C \equiv v_C(t)$. In Figure 1.15(a), two small perturbations are, respectively, applied at $t = 0$ and $t = 20 \mu\text{s}$. The perturbation applied at $t = 0$ makes the solution leave the steady state $v_C = 0$ and start a transient leading to the steady-state oscillation. Once the solution is in the oscillating steady state, a new perturbation is applied at $t = 20 \mu\text{s}$. Now, instead of moving to a different steady state, the solution comes back (exponentially in time) to the original oscillating state. The steady-state oscillation can regenerate itself in the presence of perturbations and, thus, is physically observable. Note that the reaction to perturbations of a given steady state is independent of the particular value of the applied small perturbation.

Without its initial perturbation, the system of the example keeps at the dc solution $\bar{x}_o = (v_C, i_L) = (0,0)$. To see this, in Figure 1.15(b), the perturbation is not applied until the time value $t = 20 \mu\text{s}$. It is clear that in this case the dc solution will be physically unobservable.

In order for a solution to be observable, it must be robust under perturbations. To be robust, the solution must be asymptotically stable [9, 22]. In the

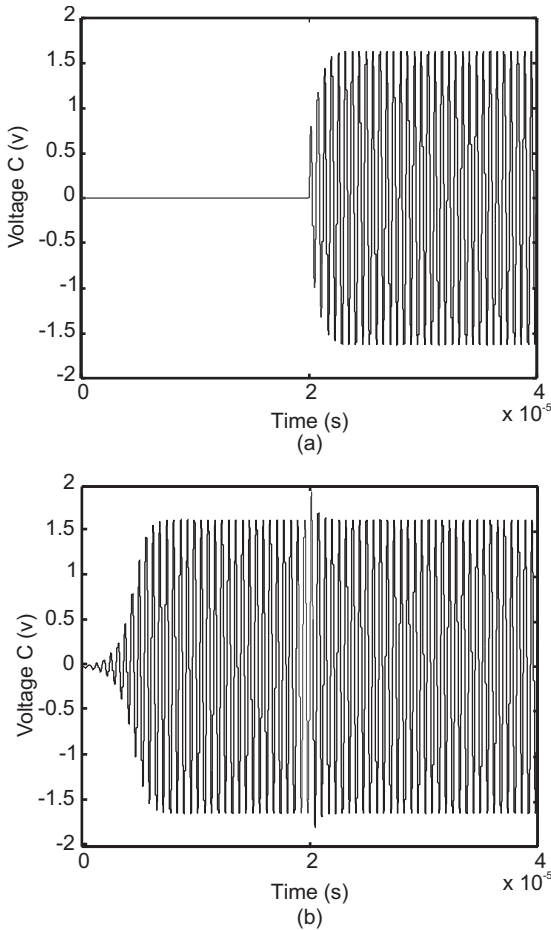


Figure 1.15 Stability verification of the solutions of the oscillator circuit of Figure 1.2. The resistance is $R = 1 \text{ Ohm}$: (a) two perturbations are applied at $t = 0$ and $t = 20 \mu\text{s}$, respectively, and (b) a perturbation is applied at $t = 20 \mu\text{s}$.

phase space, a limit set is asymptotically stable if all the neighboring trajectories lead to it as $t \rightarrow \infty$. Note that these neighboring trajectories are, in fact, all the transient trajectories that may be initiated by the small perturbations. The more general term *stable* refers to solutions whose neighboring trajectories always remain nearby, but do not necessarily approach the solution as $t \rightarrow \infty$. An example of a solution that is stable, but not asymptotically stable, is any of the cycles of Figure 1.10, which are solutions of the ideal LC circuit. If perturbed, the original solution in one of the cycles moves to another cycle and,

thus, remains nearby. An example of an asymptotically stable solution is the limit cycle of Figure 1.6. All the neighboring trajectories approach the limit cycle as $t \rightarrow \infty$. The solutions that are stable, but not asymptotically stable, do not have much physical interest. Thus, in this book, by stable we will always mean asymptotically stable.

The stable limit set behaves as an attractor of the neighboring trajectories. A clear example is the limit cycle of Figure 1.6, which attracts all the trajectories around it. In contrast, the equilibrium point of Example 1.2 (and Example 1.5) behaves as repellor. A *repellor* is a limit set such that all the neighboring trajectories lead to it as $t \rightarrow -\infty$. Thus, all neighboring trajectories diverge from it.

The two above definitions can be rewritten more formally in the following manner [11]. A limit set L is attracting for a given set U if $\lim_{t \rightarrow \infty} \varphi_t(\bar{x}_0) = L \forall \bar{x}_0 \in U$ with φ_t being the system flow. In general, there may be several separate sets U for which the limit set L is attracting. The basin of attraction of L is the union of all the sets U . For a limit set L to be stable, it has to be attracting for all the neighboring points (not just for one set). Stable solutions are also called attractors. A limit set L is an attractor if it is attracting for all its neighboring points \bar{x}_0 . Formally, the limit set L is an attractor if it is an attracting set containing a dense orbit (i.e., an orbit that can come arbitrarily close to every point in the attractor). In the same way, a limit set L' is a repellor if for all its neighboring points \bar{x}_0 , $\lim_{t \rightarrow -\infty} \varphi_t(\bar{x}_0) = L'$. The repellors can be obtained through integration by negatively increasing the time variable.

Up to now we have analyzed the two cases of an attractor limit set and a repellor limit set. In the case of a stable solution (attractor), all its neighboring points belong to its basin of attraction. A repellor does not have a basin of attraction. However, there is a third essential type of limit set, which is the limit set of the saddle type. This kind of limit set is only attracting for a subset of its neighboring points. The basin of attraction of a saddle limit set does not contain all its neighboring points. Thus, the limit set is unstable and unobservable. In spite of this, saddle-type limit sets have an essential role in the phase space because they give rise to open invariant sets that (together with the attractors and repellors) divide the phase space into different cells with identical qualitative behavior. This will be seen more clearly in the next section, dealing with the different types of stability. The simplest case of an equilibrium point behaving as attractor, repellor or saddle will be analyzed.

1.4.2 Stability Types

To illustrate the different types of stability, the simplest case of a limit set consisting of an equilibrium point \bar{x}_{dc} will be considered [1, 8]. To reduce the

formulation complexity, a two-dimensional system is analyzed, which is also convenient for the visualization of the results. Thus, the nonlinear system is given by

$$\begin{aligned}\dot{x}_1 &= f_1(x_1, x_2) \\ \dot{x}_2 &= f_2(x_1, x_2)\end{aligned}\quad (1.18)$$

The equilibrium points of the above system, which can be one or more (generally a limited number), are obtained by solving the following:

$$\begin{aligned}0 &= f_1(x_{1dc}, x_{2dc}) \\ 0 &= f_2(x_{1dc}, x_{2dc})\end{aligned}\quad (1.19)$$

Now the stability of one of the equilibrium points, given by (x_{1dc}, x_{2dc}) , is going to be analyzed. In the case of more than one equilibrium point, the stability of each point is analyzed in an identical way. Each stability analysis is an individual analysis.

For the stability analysis of the point (x_{1dc}, x_{2dc}) , a small perturbation is considered in the system, the perturbation being given by $[\xi_1(t), \xi_2(t)]$. In the presence of this perturbation, the state variables are written as follows:

$$\begin{pmatrix} x_1(t) \\ x_2(t) \end{pmatrix} = \begin{pmatrix} x_{1dc} + \xi_1(t) \\ x_{2dc} + \xi_2(t) \end{pmatrix}\quad (1.20)$$

For stability, the perturbation must vanish in time. This would lead the solution back to the original equilibrium point (x_{1dc}, x_{2dc}) . The purpose of the stability analysis carried out here is to determine the time evolution of this perturbation, independently of its particular initial value (provided that it is a small value). From the stability analysis, we must know whether any small perturbation will grow or decay in time.

Replacing (1.20) into (1.18) returns the following:

$$\begin{pmatrix} \dot{\xi}_1(t) \\ \dot{\xi}_2(t) \end{pmatrix} = \begin{pmatrix} f_1(x_{1dc} + \xi_1(t), x_{2dc} + \xi_2(t)) \\ f_2(x_{1dc} + \xi_1(t), x_{2dc} + \xi_2(t)) \end{pmatrix}\quad (1.21)$$

Owing to the smallness of the perturbation, the above nonlinear system can be expanded in a Taylor series about the equilibrium point $\bar{x}_{dc} = (x_{1dc}, x_{2dc})$. It will

generally be sufficient to use a Taylor series of the first order. The exceptions are explained later. Then, it is possible to write

$$\begin{pmatrix} \dot{\xi}_1(t) \\ \dot{\xi}_2(t) \end{pmatrix} = \left(\begin{array}{cc} \frac{\partial f_1}{\partial x_1} & \frac{\partial f_1}{\partial x_2} \\ \frac{\partial f_2}{\partial x_1} & \frac{\partial f_2}{\partial x_2} \end{array} \right)_{\substack{x_1=x_1 dc \\ x_2=x_2 dc}} \begin{pmatrix} \xi_1(t) \\ \xi_2(t) \end{pmatrix} \equiv \begin{bmatrix} Jf_{11} & Jf_{12} \\ Jf_{21} & Jf_{22} \end{bmatrix} \begin{pmatrix} \xi_1(t) \\ \xi_2(t) \end{pmatrix} \quad (1.22)$$

The above system can be rewritten in the following compact form:

$$\dot{\bar{\xi}}(t) = [Jf]_{dc} \bar{\xi}(t) \quad (1.23)$$

where $[Jf]_{dc}$ is the system Jacobian matrix evaluated at the equilibrium point. Because the equilibrium point is constant, it is a constant matrix. The linear system (1.23) defines a linear flow $[J\varphi]_{dc}$, which is given by

$$\begin{pmatrix} \xi_1(t) \\ \xi_2(t) \end{pmatrix} = [J\varphi]_{dc} \begin{pmatrix} \xi_{1o} \\ \xi_{2o} \end{pmatrix} = \left[e^{[Jf]t} \right] \begin{pmatrix} \xi_{1o} \\ \xi_{2o} \end{pmatrix} \quad (1.24)$$

with (ξ_{1o}, ξ_{2o}) being the initial value of the perturbation. The linearized flow that has just been defined will be essential in the stability analysis of the equilibrium point. In this analysis, we will look for the (unbounded) sets that are invariant to the application of this flow.

The advantage of the linearization is that (1.23) is a linear differential system of the first order with constant matrix coefficients, which has a well-known standard solution of the form

$$\bar{\xi}(t) = c_1 e^{\lambda_1 t} \bar{v}_1 + c_2 e^{\lambda_2 t} \bar{v}_2 \quad (1.25)$$

where \bar{v}_1 and \bar{v}_2 are the eigenvectors of the Jacobian matrix $[Jf]_{dc}$ and c_1 and c_2 are constants depending on the initial value. The eigenvalues are the roots of the characteristic equation:

$$\det \left\{ \lambda \begin{bmatrix} 1 & 0 \\ 0 & 1 \end{bmatrix} - \begin{bmatrix} Jf_{11} & Jf_{12} \\ Jf_{21} & Jf_{22} \end{bmatrix} \right\} = 0 \quad (1.26)$$

with *det* meaning “determinant.” Thus, the equation is

$$\lambda^2 - (Jf_{11} + Jf_{22})\lambda - Jf_{12}Jf_{21} + Jf_{11}Jf_{22} \equiv \lambda^2 + b\lambda + c = 0 \quad (1.27)$$

The roots (or eigenvalues) are given by

$$\lambda_{1,2} = \frac{-b \pm \sqrt{b^2 - 4c}}{2} \equiv \frac{-b \pm \sqrt{D}}{2} \quad (1.28)$$

The equilibrium point $(x_{1,d}, x_{2,d})$ is classified according to the nature of the eigenvalues λ_1, λ_2 . The points of a given type have, in the phase space, a common behavior of the neighboring trajectories, so this classification will be of great interest. At this moment, only equilibrium points having associated eigenvalues with real parts different from zero $\text{Re}(\lambda_i) \neq 0 \quad \forall i = 1 \text{ to } n$, will be considered. Points satisfying this condition are called *hyperbolic fixed points*. When the equilibrium point is nonhyperbolic, higher-order terms must be considered in the Taylor-series development of the vector field for the determination of its stability [9]. However, in many cases, the nonhyperbolic points are between a stable and an unstable situation (see Section 1.4.4).

According to the value of D in (1.28), the two eigenvalues associated with the equilibrium point will be real (for $D > 0$) or complex-conjugate (for $D < 0$). The different situations are analyzed in the following [1, 9].

Node Point—Real and Different Eigenvalues with the Same Sign

When the eigenvalues of the linearized system of dimension two, given by (1.23), are real and different with the same sign (either positive or negative), the corresponding equilibrium point is called a *node equilibrium point*. The real and different eigenvalues will be given by $\lambda_1 = \gamma_1$ and $\lambda_2 = \gamma_2$. Then the solutions of (1.24) are expressed

$$\bar{\xi}(t) = c_1 e^{\gamma_1 t} \bar{v}_1 + c_2 e^{\gamma_2 t} \bar{v}_2 \quad (1.29)$$

As can be seen, there is one independent solution in the direction of the eigenvector \bar{v}_1 and another independent solution in the direction of \bar{v}_2 . All the rest of solutions are linear combinations of the two, with coefficients c_1 and c_2 . These coefficients depend on the initial value and thus, on the initial perturbation. If the two real eigenvalues γ_1, γ_2 are negative, the perturbation will exponentially vanish in time [see (1.29)] and the equilibrium point will be stable. The equilibrium point is a stable node. The behavior is sketched in Figure 1.16(a), where the equilibrium point is located, for simplicity, at the origin of the coordinate axes. The fact that both eigenvalues are real gives rise to a

nonoscillating approach of neighboring trajectories to the equilibrium point. If the two eigenvalues were positive, the trajectories would move away from the equilibrium point and the arrows in Figure 1.16(a) would point outwards. In this case, the equilibrium point would be an unstable node.

There are a few things to be observed in Figure 1.16(a). The eigenvectors \bar{v}_1 and \bar{v}_2 provide (close to the equilibrium point) the direction of only four of the trajectories that have been represented. In the direction defined by \bar{v}_1 , one trajectory would have (for the case represented in the figure) an initial value in the second quadrant and the other one would have an initial point in the fourth quadrant. Similarly, in the direction defined by \bar{v}_2 , one trajectory would have (for the case represented in the figure) an initial point in first quadrant and the other one would have an initial value in the third quadrant. The rest of the trajectories close to the equilibrium point are the result of linear combinations of the form (1.29).

Observe that the trajectories become nonlinear as the distance to the equilibrium point increases, which is due to the inherent nonlinearity of the system

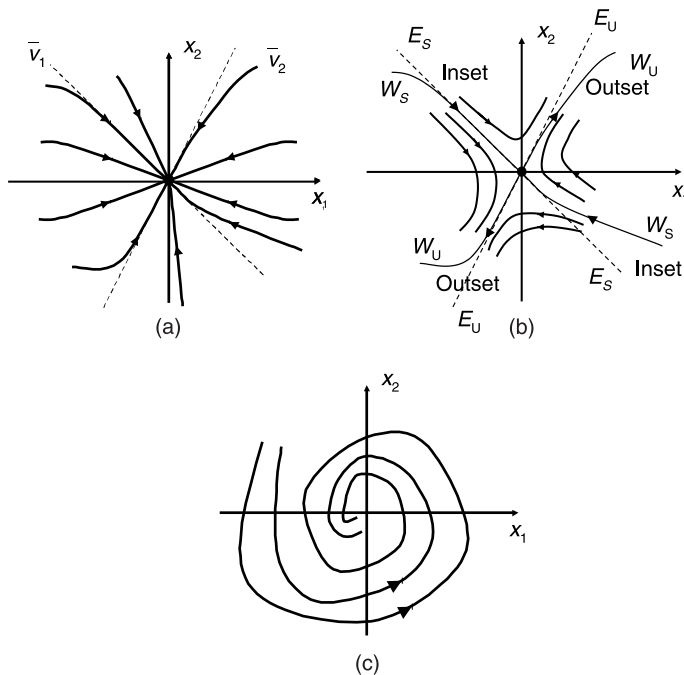


Figure 1.16 Three different types of equilibrium point in a two-dimensional phase space: (a) stable node point, (b) saddle point, and (c) stable focus.

that invalidates the linearization (1.23) for big perturbation amplitude. The nonlinear trajectories are tangent to the eigenvectors \bar{v}_1 and \bar{v}_2 at the equilibrium point, where the linearization is valid. These trajectories will be called here W_1 and W_2 . At the equilibrium point they are tangent to the eigenspaces $E_1 = \{c_1 e^{\gamma_1 t} \bar{v}_1, \forall t \in R\} = \text{Span}\{\bar{v}_1\}$ and $E_2 = \{c_2 e^{\gamma_2 t} \bar{v}_2, \forall t \in R\} = \text{Span}\{\bar{v}_2\}$.

In the case of two negative eigenvalues $\gamma_1, \gamma_2 < 0$, the attraction region of the equilibrium point \bar{x}_{dc} is the whole plane R^2 . Because the nonlinear system (here considered) is a two-dimensional system, the equilibrium point will be attracting for all the neighboring points, so it will be an attractor (thus stable) and physically observable. In the case of two positive eigenvalues $\gamma_1, \gamma_2 > 0$, the point will be a repeller, and thus unstable and unobservable.

The two eigenvectors \bar{v}_1 and \bar{v}_2 define a plane that constitutes the stable (unstable) eigenspace of the equilibrium point. Because the stable eigenspace has the same dimension as the system dimension, the equilibrium point will have the same attracting (or repelling) behavior for all neighboring points. It will either be an attractor (stable node) or a repeller (unstable node).

Saddle Point—Real Eigenvalues with the Opposite Sign

We are now going to move to the more difficult case of two eigenvalues of different sign $\gamma_1 < 0, \gamma_2 > 0$. Then, the equilibrium point is called the *saddle equilibrium point*. The new phase-space situation is depicted in Figure 1.16(b). There are again two main directions close to the equilibrium point given by the two eigenvectors \bar{v}_1, \bar{v}_2 . In the case of a saddle solution, only four trajectories are asymptotic to the equilibrium point (compare with the situation in the node of Figure 1.16(a)). The other trajectories come close to the saddle point, but turn away. These trajectories are obtained as linear combinations of the two independent solutions of the linear differential equation. This fact is essential to understanding the great relevance of saddle-type solutions in the phase space. Actually, the four asymptotic trajectories of Figure 1.16(b) divide the phase space (in this case the plane R^2) into four regions. In each of these regions, solution trajectories have the same qualitative behavior.

Close to the equilibrium point, the vector \bar{v}_1 defines the attracting direction, and the vector \bar{v}_2 defines the repelling direction. The set of points $E_1 = \{c_1 e^{\gamma_1 t} \bar{v}_1, \forall t \in R\}$ is the stable eigenspace, invariant under the linear flow $[J\varphi_t]_{dc}$ because $\forall \bar{\xi} \in E_1, \lim_{t \rightarrow \infty} [J\varphi_t]_{dc} \bar{\xi} \rightarrow \bar{0}$. Thus, we can rename E_1 as the stable eigenspace of the saddle point \bar{x}_{DC} under the linear flow $[J\varphi_t]$ (i.e., $E_S \equiv E_1$). In the same way, $E_2 = \{c_2 e^{\gamma_2 t} \bar{v}_2, \forall t \in R\}$ is the unstable eigenspace of the saddle point \bar{x}_{dc} because $\forall \bar{\xi} \in E_2, \lim_{t \rightarrow -\infty} [J\varphi_t]_{dc} \bar{\xi} \rightarrow \bar{0}$. Then we can rename $E_U \equiv E_2$.

By inspection of Figure 1.16(b), two sets of points can be identified: W_S (tangent to E_S at the equilibrium point) and W_U (tangent to E_U at the equilibrium point). Both sets W_S and W_U are invariant under the nonlinear flow φ_t , in the same way as the sets E_S and E_U are invariant to the linear flow $[J\varphi_t]_{dc}$. The trajectories in W_S approach the equilibrium point and are often called the *inset* of the saddle equilibrium point. The trajectories in W_U move away from the equilibrium point and are often called the *outset* of the equilibrium point. The special sets W_S and W_U can be mathematically defined as

$$W_S(\bar{x}_{dc}) = \{\bar{x} \in U \mid \varphi_t(\bar{x}) \rightarrow \bar{x}_{dc} \text{ for } t \rightarrow \infty \text{ and } \varphi_t(\bar{x}) \in U \forall t \geq 0\}$$

$$W_U(\bar{x}_{dc}) = \{\bar{x} \in U \mid \varphi_t(\bar{x}) \rightarrow \bar{x}_{dc} \text{ for } t \rightarrow -\infty \text{ and } \varphi_t(\bar{x}) \in U \forall t \leq 0\}$$

with $U \in R^n$ being a neighborhood of the equilibrium point.

The set W_S constitutes the stable invariant set (or stable manifold) and the set W_U constitutes the unstable invariant set (or unstable manifold). At the dc point \bar{x}_{dc} , the manifolds are tangent to the eigenspaces. In fact, they can be considered as a nonlinear generalization of the eigenspaces of the system linearization at the dc point \bar{x}_{dc} . The stable and unstable manifolds (W_S and W_U) of the saddle point constitute a special case of invariant sets of the nonlinear flow φ_t that are unbounded, in contrast with the limit sets that have been studied in Section 1.3.3. Note that the manifolds W_S and W_U divide the plane defined by x_1 and x_2 (which in this case constitutes the phase space) into four regions such that trajectories in each of them have the same qualitative behavior.

Focus Point—Complex Conjugate Eigenvalues

For a negative value of D in (1.28), the eigenvalues associated with the linearized system will be complex conjugates. The two eigenvalues can be written $\lambda_1 = \alpha + j\omega$ and $\lambda_2 = \alpha - j\omega$, and the equilibrium point is a focus point. Then, the time evolution of the perturbation will be of the form

$$\bar{\xi}(t) = c_1 e^{(\alpha + j\omega)t} \bar{v}_1 + c_2 e^{(\alpha - j\omega)t} \bar{v}_1^* \quad (1.30)$$

with $c_2 = c_1^*$.

It is clear from (1.30) that the perturbation in addition to having variable amplitude as time evolves (because of the real part αt in the exponents) has an oscillating behavior (because of the imaginary part $j\omega t$). Thus, trajectories in the phase space will have the evolution depicted in Figure 1.16(c), where the

case of a stable focus has been considered. Because we are dealing with of a two-dimensional system, the stable (unstable) space will be the whole plane R^2 because the two eigenvectors \bar{v}_1 and \bar{v}_1^* span the whole plane. The equilibrium point will be an attractor for $\alpha < 0$ or a repellor for $\alpha > 0$.

Inflected Node—Two Real and Equal Eigenvalues

For $D = 0$ in (1.28), the two eigenvalues are real and equal (i.e., $\gamma_1 = \gamma_2$). Then, the trajectories in the phase space combine the geometric characteristics of the node and the focus. The equilibrium point is called the *inflected node*.

The nonhyperbolic situation, $\gamma_1 = 0$ or $\gamma_2 = 0$ (in the case of a node) or $\alpha = 0$ (in the case of a focus), may correspond to a point whose stability cannot be determined from the Jacobian matrix in (1.22), requiring higher-order terms in the Taylor-series expansion. It can also be a point at which a qualitative change of stability takes place. To understand this, it is necessary to think about a possible circuit parameter, a resistance, or the value of a bias generator, such that, as the parameter is modified, a real eigenvalue (in the case of a node) changes sign, and the equilibrium point changes from node to saddle or from saddle to node. The particular point having $\gamma_1 = 0$ or $\gamma_2 = 0$ is the point at which the transition takes place. The same could happen with a focus, the transition taking place at the parameter value for which $\alpha = 0$. The equilibrium point of the conservative system of Example 1.3 has two complex-conjugate eigenvalues with zero real part [see (1.7)]. This kind of point is called a *stability center*. The neighboring trajectories are nesting cycles like the ones depicted in Figure 1.8.

Equilibrium points in higher-dimension spaces can also be classified in a similar way. In a three-dimensional system, for instance, there would be a third eigenvalue, which gives rise to new possibilities, like, for instance, two complex eigenvalues, giving rise to a stable or unstable plane and a real eigenvalue, giving rise to a stable or unstable straight line. Saddles with three real eigenvalues are also possible. On the other hand, the classification into attractor, repellor, and saddle-type equilibrium point that has been carried out here is also valid for the other types of limit sets. However, the other types of solutions (periodic, quasiperiodic, or chaos) are not constant in time, and the stability analysis is not as simple as the one that has been carried out here. To have an idea of the difficulty, think, for instance, that when linearizing a nonlinear system about a periodic solution, the corresponding Jacobian matrix is periodic and not constant. The stability calculation for limit sets other than equilibrium points follows the same small-perturbation principle, enabling the system linearization about the particular limit set. The resulting Jacobian matrix, particularized to the limit set, will be time-varying with the same periodicity (or nonperiodicity) of the limit

set, which greatly increases the complexity of the calculation. General stability-analysis techniques for practical circuits will be proposed in Chapter 3.

The saddle-type solutions have an important role in the phase space of any dynamical system because their stable and unstable manifolds behave as separatrices of trajectories and, together with the limit sets, divide the phase space into different cells with the same qualitative behavior. Due to the Existence Uniqueness theorem, stable (or unstable) manifolds of the same limit set or of different limit sets cannot intersect. However, stable and unstable manifolds of the same limit set or different limit sets can intersect. It will be seen in Chapter 6 that, under some circumstances, the intersection of the stable and unstable manifolds of the same saddle point gives rise to chaos.

To illustrate the above study, the stability of the equilibrium point of the cubic nonlinearity oscillator will be analytically determined in Example 1.7.

Example 1.7: Stability of the equilibrium point in the cubic nonlinearity oscillator

Let the circuit in Example 1.1 (Figure 1.2) be considered. At time origin $t = 0$, the system solution is located at the equilibrium point $(0,0)$ (Figure 1.3). However, as has already been said, this equilibrium point is unstable and under an arbitrarily small perturbation, a transient trajectory will start, leading to the limit cycle. Once the solution reaches the cycle, it remains there because the limit cycle is stable and recovers under small perturbations. That is to say, perturbed trajectories evolve so as to join the limit cycle again.

The behavior of the equilibrium point $(i_L^o, v_C^o) \equiv (0,0)$ (as a repeller, saddle, or attractor) can be mathematically predicted through a stability analysis. To do so, a small perturbation $(\Delta i_L(t), \Delta v_C(t))$ will be considered. The perturbed solution is given by

$$\begin{aligned} i_L(t) &= i_L^o + \Delta i_L(t) \\ v_C(t) &= v_C^o + \Delta v_C(t) \end{aligned} \quad (1.31)$$

Due to the smallness of the perturbation, the nonlinear function f in the system (1.4) can be expanded in a first-order Taylor series about the equilibrium point (i_L^o, v_C^o) . The resulting linearized system is:

$$\begin{aligned} \frac{d\Delta i_L(t)}{dt} &= -\frac{R}{L} \Delta i_L(t) - \frac{1}{L} \Delta v_C(t) \\ \frac{d\Delta v_C(t)}{dt} &= \frac{1}{C} \Delta i_L(t) - \frac{1}{C} \left(a + 3dv_C^{o^2} \right) \Delta v_C(t) \end{aligned} \quad (1.32)$$

Note that the nonlinear differential equation (1.4) has been transformed into the linear equation (1.32). The linearization is only valid in the neighborhood of $(i_L^o, v_C^o) \equiv (0,0)$, but this will be sufficient for the stability analysis. Equation (1.32) can also be expressed in matrix form:

$$\begin{pmatrix} \frac{d\Delta i_L(t)}{dt} \\ \frac{d\Delta v(t)}{dt} \end{pmatrix} = \begin{pmatrix} -\frac{R}{L} & -\frac{1}{L} \\ \frac{1}{C} & -\frac{1}{C}(a + 3dv_C^{o^2}) \end{pmatrix} \begin{pmatrix} \Delta i_L(t) \\ \Delta v(t) \end{pmatrix} \quad (1.33)$$

The matrix on the right side of (1.33) is the Jacobian matrix of the nonlinear system (1.4), which must be evaluated at the constant solution point $(i_L^o, v_C^o) \equiv (0,0)$. The general solution of the linear system (1.33) is given by

$$\begin{pmatrix} \Delta i_L(t) \\ \Delta v(t) \end{pmatrix} = c_1 e^{\lambda_1 t} \bar{v}_1 + c_2 e^{\lambda_2 t} \bar{v}_2 \quad (1.34)$$

where c_1 and c_2 are constants, depending on the initial condition \bar{x}_o ; λ_1, λ_2 are the eigenvalues of the Jacobian matrix; and \bar{v}_1, \bar{v}_2 are the corresponding eigenvectors. These eigenvalues may be real or complex. According to (1.31), for the solution (i_L^o, v_C^o) to be stable, the perturbation $(\Delta i_L(t), \Delta v_C(t))$ must vanish in time. Thus, the eigenvalues λ_1 and λ_2 must have a negative real part [see the exponentials in (1.34)]. The eigenvalues are the roots of the system characteristic equation (1.26) or system poles. This characteristic equation agrees with $Y_L(s) + G_N|_{v_C=0} = 0$, where $Y_L(s)$ is the linear admittance, at the active-element terminals, and $G_N|_{v_C=0}$ is the conductance of the active element, obtained by linearizing its nonlinear characteristic about $v_C = 0$. The characteristic equation [associated with (1.33)] enabling the eigenvalue calculation is

$$s^2 + \left(\frac{R}{L} + \frac{a + 3dv_C^{o^2}}{C} \right) s + \frac{R}{LC}(a + 3dv_C^{o^2}) + \frac{1}{LC} = 0 \quad (1.35)$$

Particularizing to $(i_L^o, v_C^o) \equiv (0,0)$, the eigenvalues are given by

$$\lambda = \frac{1}{2} \left(- \left(\frac{R}{L} + \frac{a}{C} \right) \pm \sqrt{\left(\frac{R}{L} + \frac{a}{C} \right)^2 - 4 \frac{Ra + 1}{LC}} \right) \quad (1.36)$$

Replacing the numerical values appearing in the caption of Figure 1.2 into (1.36), a couple of complex eigenvalues are obtained: $\lambda_{1,2} = 4.49 \cdot 10^5 \pm j 2\pi \cdot 1.535 \cdot 10^6$ rad/sec.

Introducing these values into (1.34), the perturbation will evolve according to:

$$\begin{pmatrix} \Delta i_L(t) \\ \Delta v_C(t) \end{pmatrix} = c_1 e^{(4.49 \cdot 10^5 + j 2\pi \cdot 1.54 \cdot 10^6)t} \bar{v}_1 + c_1^* e^{(4.49 \cdot 10^5 - j 2\pi \cdot 1.54 \cdot 10^6)t} \bar{v}_1^*$$

Because c_1 and the vectors \bar{v}_1, \bar{v}_1^* are constant values, the perturbation amplitude increases exponentially in time. The perturbation has an oscillating behavior due to imaginary part of λ_1 and λ_2 . The equilibrium point is a focus point. When representing this in the phase space, a spiral-like transient is obtained (Figure 1.6). Note that this calculation has a restricted validity because assumption was made of small values for $(\Delta i_L(t), \Delta v_C(t))$. As the perturbation increases, this is no longer true and the system has to be solved through the nonlinear equation (1.4). Note that otherwise the perturbation would grow ad infinitum, which is physically impossible.

In summary, the equilibrium point $(i_L^o, v_C^o) \equiv (0,0)$ is unstable because the eigenvalues have a positive real part, which leads to an exponential increase in time of the perturbation. Because the equilibrium point $(i_L^o, v_C^o) \equiv (0,0)$ is unstable, the solution trajectory moves to the limit cycle under any small perturbation (Figure 1.6). It is, in fact, the common startup of an oscillation, as seen when represented in the phase space.

The equilibrium point $(i_L^o, v_C^o) \equiv (0,0)$ is unstable for the circuit values indicated in the caption of Figure 1.2. If the resistance value is now changed from $R=1$ Ohm to $R=1.5$ Ohm, the situation changes. Using (1.36), the new eigenvalues are

$$\lambda_{1,2} = -6.66 \cdot 10^5 \pm j 2\pi \cdot 1.45 \cdot 10^6 \quad \text{rad/sec}$$

So the perturbation will evolve according to

$$\begin{pmatrix} \Delta i_L(t) \\ \Delta v_C(t) \end{pmatrix} = c_1 e^{(-6.6610^5 + j2\pi 1.4510^6)t} \bar{v}_1 + c_1^* e^{(-6.6610^5 - j2\pi 1.4510^6)t} \bar{v}_2$$

The real part of the complex eigenvalues is now negative, which makes the perturbation decrease exponentially in time. Because there is an imaginary part different from zero, there will also be an oscillating behavior. The perturbation will vanish and the trajectory will come back to the equilibrium point $(i_L^o, v_C^o) \equiv (0,0)$. Note that for any other initial value \bar{x}_o in the neighborhood of the equilibrium point the solution trajectory would evolve to this equilibrium point in a similar fashion. The equilibrium point is robust or able to recover under perturbations, as shown in Figure 1.17. It is thus a physically observable solution.

As has been seen, the stability of the equilibrium point has suffered a qualitative change under the variation of the resistance value R . This change takes place at about the value $R_o = 1.2$ Ohm. For the exact resistance at which $\alpha = 0$ (infinite accuracy is impossible), the equilibrium point will be a nonhyperbolic point. For $R < R_o$ Ohm, the observed solution is a periodic oscillation. For $R > R_o$ Ohm, the observed solution is a dc one.

1.4.3 Coexisting Stable Solutions

When for given values of the system parameters, the basin of attraction of a system solution is the whole phase space, the solution is called *globally asymptotically stable* [9, 22]. It is the only solution that can be physically observed. However, in many cases, two or more different stable solutions can coexist in the phase space for the same values of the system parameters. Then, each stable

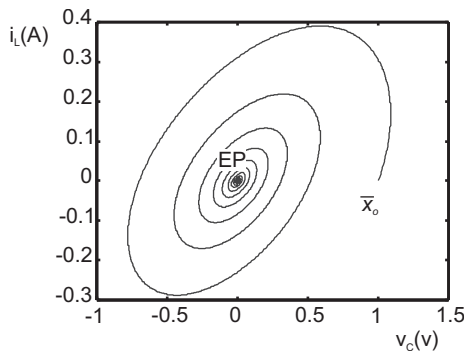


Figure 1.17 Stable equilibrium point for $R = 1.5$ Ohm. The stability situation is different from the one depicted in Figure 1.6.

solution is asymptotically stable but not globally asymptotically stable. The different stable solutions will have different basins of attractions.

In the phase space, stable and unstable solutions alternate. The unstable solution located between two stable solutions acts like a separator of the respective basins of attraction. This is shown in Figure 1.18 illustrating a common situation in electronic circuits. Both the point and the solid-line limit cycle are stable. The dashed-line limit cycle is unstable and acts as a separator between the different basins of attraction. The basin of attraction of the equilibrium point is the interior of the unstable limit cycle. The basin of attraction of the stable limit cycle is the annular region between the two limit cycles and the entire region exterior to this stable cycle. Thus, the point and the two limit cycles divide the space into three different regions, marked a, b, and c. Trajectories in these three regions have the same qualitative behavior.

Because the equilibrium point in Figure 1.18 is a stable solution, it recovers from small perturbations and is continuously regenerating itself, as shown in Figure 1.18. However, if a big perturbation takes place, the trajectory may fall in the basin of attraction of the stable limit cycle. The same is true for perturbations of this limit cycle. Thus, to analyze the stability of a given solution, the perturbation must necessarily be small to avoid falling in the basin of attraction of a different stable solution.

In the situation of Figure 1.18, one could wonder which of the two stable solutions will be actually observed in the experiment. This depends on the region a, b, or c in which the initial point \bar{x}_0 is located. The coexistence of stable solutions is the reason for the hysteresis phenomena, commonly observed in electronic circuits. The hysteresis phenomenon will be studied in detail in Chapter 4.

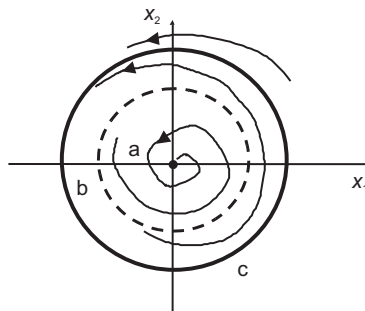


Figure 1.18 Coexisting steady-state solutions. Both the equilibrium point and the solid line limit cycle are stable. The dashed limit cycle is unstable and behaves like a separator between the basins of attraction of the two stable solutions.

1.4.4 Qualitative Variations in the Stability Properties

Example 1.7 showed how the variation in a resistor modified the stability of the equilibrium point. The resistor can be considered as a parameter of the circuit nonlinear equation. The qualitative variation in the stability of a solution when a parameter is continuously modified is known as *bifurcation* [23–28]. This qualitative variation takes place for a particular parameter value and usually has big implications in the observed steady-state solution. Actually, in Example 1.7, the observed solution changed from a limit cycle to an equilibrium point at $R = R_o = 1.2$ Ohm. This constitutes a qualitative change in the steady-state solution, in contrast with quantitative variation, such as continuous variations in the state variables, giving rise to continuous variations in the observed output power or oscillation frequency.

Circuit parameters may be, among others, the value of any of its linear elements, the values of sinusoidal or dc generators, or the temperature. The type of steady-state solution may vary, for instance, from an equilibrium point to a limit cycle or from a limit cycle to a 2-torus. A discontinuous change in the value of the state variables (when the parameter is continuously modified) is also a qualitative variation.

A well-known example of bifurcation is the start-up of a free-running oscillator when a bias voltage V_b is modified. At a critical value V_{bo} , the observed solution changes from a stable dc solution (equilibrium point) to a stable periodic solution (limit cycle). This is shown in Figure 1.19, where only steady-state solutions have been represented. It is in fact the collection of the stable steady-state solutions of the oscillator circuit, represented versus of the bias voltage. For $V_b > V_{bo}$ the variations in the solution are only quantitative, the limit-cycle amplitude increasing with the bias voltage.

A useful tool for analyzing qualitative variations in a circuit solution is the Poincaré map, which is introduced in the following section.

1.5 Poincaré Map

1.5.1 Definition of the Poincaré Map

The Poincaré map allows a representation of the system solution with a reduction of its dimension [7–9]. This proves very useful when the purpose is to observe the qualitative variations in the system solution when a parameter is modified.

The Poincaré map transforms the n -dimensional continuous solution $x(t) = \varphi_t(x_o, t_o)$ into a discrete solution of dimension $n - 1$. This is obtained through the transversal intersection of $\varphi_t(x_o, t_o)$ in the R^n space with an $(n -$

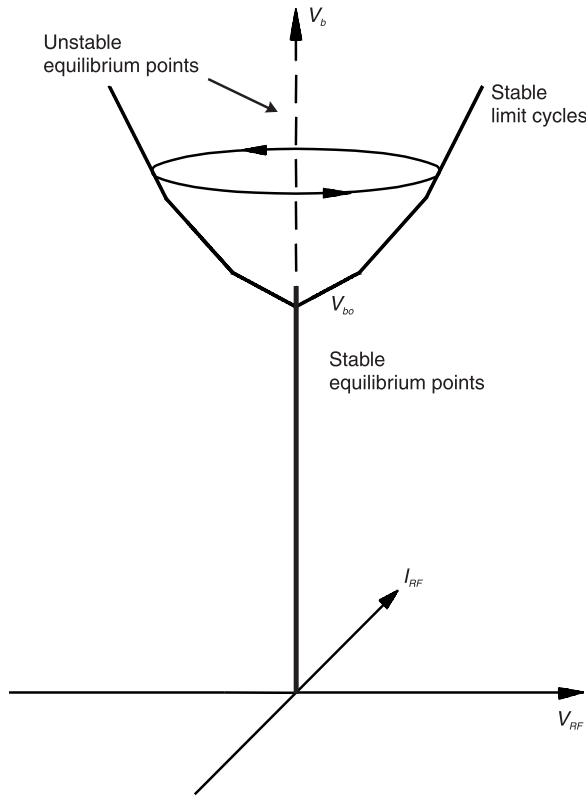


Figure 1.19 Variations in the solution of an oscillator circuit versus the bias voltage V_b . A qualitative variation of the solution takes place for the bifurcation value $V_b = V_{bo}$.

1)-dimensional hyperplane Σ . The flow must be everywhere transverse to the hyperplane. The particular case of a periodic orbit is represented in Figure 1.20. Due to its periodicity, the intersection with the transversal surface Σ gives rise to a single point p . If the orbit were not periodic, the intersection would give rise to many individual points.

The first-return map [9] or Poincaré map $P: \Sigma \rightarrow \Sigma$ is defined as

$$P(\bar{p}) = \varphi_\tau(\bar{p}) = \bar{q} \quad (1.37)$$

with $\bar{p}, \bar{q} \in \Sigma$ and τ being the time required by the solution trajectory to return for the first time to [Figure 1.20(a)]. In the case of periodic regimes, the time τ agrees with the period T . Then, $P(\bar{p}) = \bar{p}$, and \bar{p} is called a *fixed point* of the

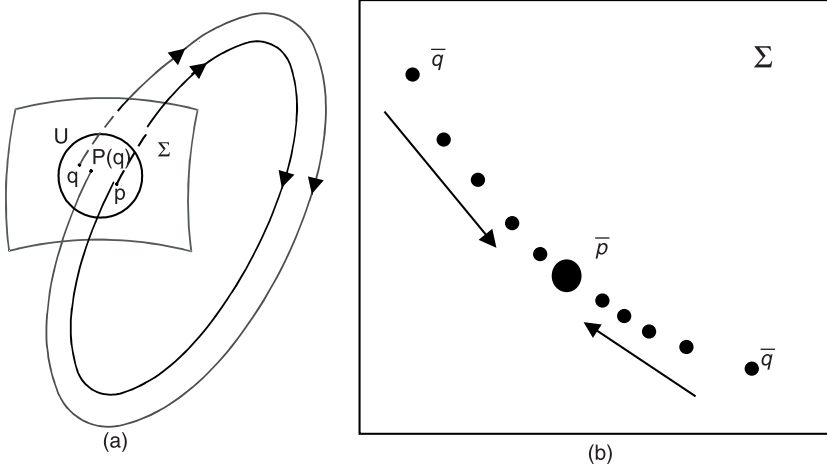


Figure 1.20 Poincaré map: (a) transversal intersection with the surface Σ , and (b) succession of points of the map under a small perturbation of \bar{p} . The point \bar{p} is a stable point.

Poincaré map. The Poincaré defines a discrete flow P in the surface Σ , and the fixed point \bar{p} is an invariant point of the flow. Similarly to what happens with the continuous flow φ_p , the stability of the point \bar{p} can be analyzed by applying a small perturbation and determining the evolution of the neighboring points of the map (obtained in the successive intersections with the surface). These intersection points will approach the point \bar{p} in the case of stability. It can be demonstrated that the stability properties of the point \bar{p} are the same as those of the periodic solution $\bar{x}(t)$ [9, 27]. This is shown in Figure 1.20(b) for the case of a stable point \bar{p} , and thus a stable periodic solution $\bar{x}(t)$. The sequence of map points approaches \bar{p} for any small perturbation. In Figure 1.20(b) two different initial conditions have been considered. As in the case of continuous flows, the Poincaré map can be linearized under small perturbations. This technique is often used for the stability analysis of periodic solutions and will be shown in detail in Chapter 4.

In a nonautonomous system, with a forcing sinusoidal term of period T_g , the Poincaré map can be easily obtained by doing

$$P(\bar{p}) = \varphi_{T_g}(\bar{p}) = \bar{q} \quad (1.38)$$

Remember that a nonautonomous system can always be transformed into an autonomous one by including the variable $\theta = \frac{2\pi t}{T_g} \pmod{2\pi}$ in the state-

variable vector \bar{x} [see (1.3)]. Then the transversal hyperplane Σ may be given by $\theta_o = \frac{2\pi t_o}{T_g}$ with t_o an arbitrary time value, so the solution necessarily returns to

Σ after one period of the forcing term.

Note that in a nonautonomous system with a periodic forcing term of period T_g , the period of the solution $\bar{x}(t)$ does not necessarily agree with T_g . The solution $\bar{x}(t)$ does not even have to be periodic. In some cases, the period may be a multiple of the period of the input generator: kT_g with $k = 1, 2, \dots$, obtaining a period- k solution. For example, if $\bar{x}(t)$ is a period-2 solution (with period $2T_g$), two applications of the map (1.38) are necessary to return to the initial point \bar{p} , that is, $P(\bar{p}) = \bar{p}_1$, $P(\bar{p}_1) = \bar{p}$, with $\bar{p}_1 \neq \bar{p}$ (or $P^2(\bar{p}) = \bar{p}$). The two points \bar{p}_1 and \bar{p} are fixed points of the map. Many successive applications of the map $P^n(\bar{p})$ with $n \rightarrow \infty$ provide the same two points \bar{p}_1 and \bar{p} . If the solution has period NT_g , N different fixed points $\bar{p}_1, \bar{p}_2, \dots, \bar{p}_{N-1}, \bar{p}$ are obtained. It is thus possible to know the multiplicity of the period of a steady-state solution with respect to the input-generator period by sampling the steady state at the time rate T_g and counting the number of different values $\bar{x}(nT_g)$. This will be seen more clearly in Example 1.8.

Example 1.8: Qualitative variations in the Poincaré map of an Impact Avalanche and Transit Time (IMPATT)-based circuit

The former technique has been applied to analyze the qualitative variations in the steady-state solution of a nonlinear circuit when increasing the input-generator amplitude. The circuit consists of an IMPATT diode, loaded by $R_L = 50$ Ohm, and the constant input frequency is $f_g = 50$ GHz [29]. For the circuit simulation, the model in [29, 30] for the IMPATT diode has been used. The IMPATT diodes, capable of producing negative resistance at very high frequencies, are commonly used for power generation at millimeter-wave frequencies. However, instabilities and even chaotic behavior are often encountered in IMPATT-based circuits [31] due to the highly nonlinear processes and time delay involved in their dynamics.

When sampling the steady-state solution of the IMPATT-based circuit according to $\bar{x}(nT_g)$, the diagram of Figure 1.21 is obtained. Up to the generator value $I_g = 0.15A$, one single point is obtained, indicating a solution with the same period as the input generator. In the interval $I_g = 0.15A$ to $I_g = 0.35A$, two points are obtained, indicating a period-2 solution. In other regions, a cloud of irregularly distributed points is obtained, indicating nonperiodic (chaotic) behavior. This example shows the usefulness of the Poincaré map to evidence qualitative variations in the solution of a nonlinear circuit. Note that, under the

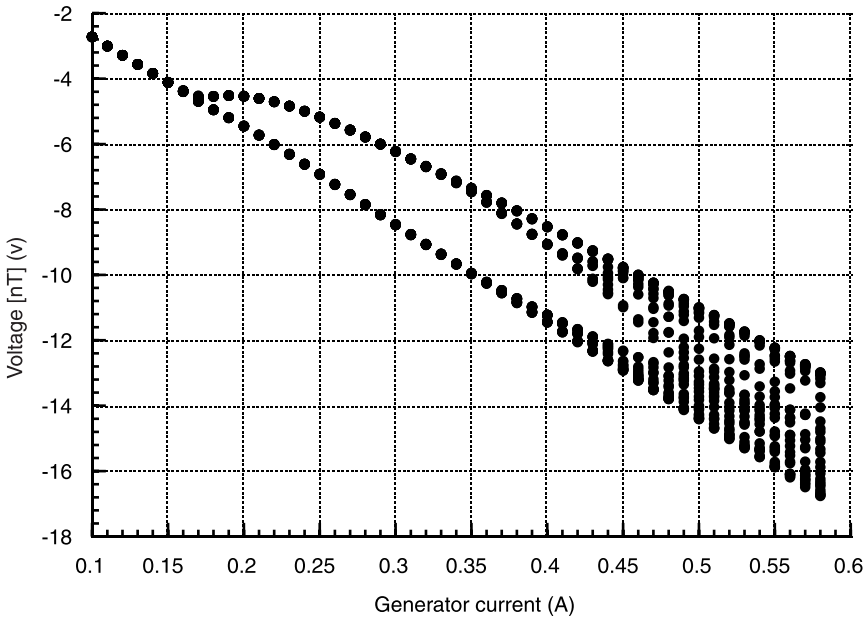


Figure 1.21 The Poincaré map technique is applied to determine the qualitative variations in the solution of an IMPATT-based circuit versus the amplitude of the input generator. (From: [29]. © 1998 IEEE. Reprinted with permission.)

application of the map, the solution becomes discrete and its dimension is smaller in one ($n - 1$).

1.5.2 Poincaré Maps of Limit Sets

The Poincaré maps of the four types of limit sets studied in Section 1.3.3 are going to be presented in the following sections. The Poincaré map of the limit cycle, although already analyzed in Section 1.3.1, is included for completeness.

1.5.2.1 Equilibrium Point

When represented in the phase space, each constant solution of an autonomous system gives rise to a single point. The point is a geometric figure of zero dimensions, and the Poincaré map is not defined.

1.5.2.2 Limit Cycle

As has already been shown, when the periodic steady state (of period T) of an autonomous nonlinear system is represented in the phase space, a closed-orbit,

named limit cycle is obtained. The result of applying the Poincaré map is a single point (Figure 1.20). A period- k limit cycle gives rise to k distinct points in the Poincaré map (Figure 1.21).

1.5.2.3 Quasiperiodic Solutions

Quasiperiodic solutions give rise to tori in the phase space. In the case of two nonrationally related fundamentals, a 2-torus is obtained. This is a two-dimensional figure. The intersection of the 2-torus with a transversal surface Σ , gives rise to a closed curve, of one dimension. Thus, the Poincaré map of a 2-torus is a cycle composed of discrete points (although the cycle is eventually filled). The points are the discrete intersection points of the trajectory with the surface. It is also possible to obtain two cycles, according to the bounded or unbounded definition of the surface Σ (Figure 1.22). An n -torus would give rise to an $(n - 1)$ -dimensional figure.

In the case of a 2-torus with two fundamental frequencies, ω_1, ω_2 , (one of them delivered by an input generator) the Poincaré map can be obtained by sampling the steady-state solution at the period of the input frequency. The resulting points form a cycle in which contiguous points are not consecutive. In each application of the map, the new point (with respect to the former point) rotates an angle $\alpha = r2\pi$, with r being the rotation number. Because r is irrational, under successive applications of the map, the points will eventually fill the cycle. Note that if r were rational, a discrete number of points would be

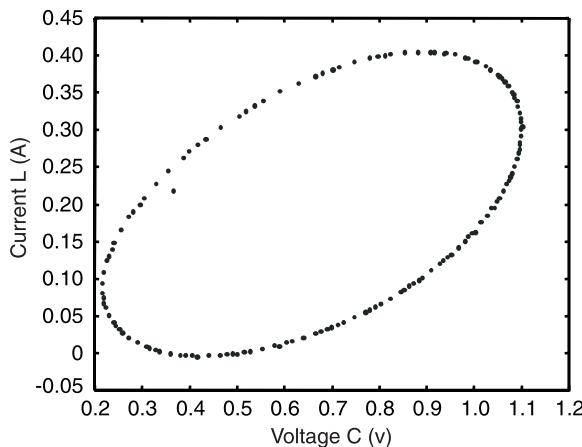


Figure 1.22 Poincaré map of the quasiperiodic solution of Example 1.9 for $E_g = 0.13v$, $f_g = 1.74$ MHz. A cycle is obtained.

obtained. For $r = \frac{m}{n}$, with $m < n$, the number of discrete points will be n (see Example 1.9).

Example 1.9: Poincaré map of the quasiperiodic solution of the cubic nonlinearity oscillator

In Example 1.6, the circuit in Figure 1.2 was solved for the generator values $E_g = 0.13v$ and $f_g = 1.74$ MHz, obtaining a quasiperiodic solution. Sampling at nT_g is now applied to obtain the Poincaré map. The map, as expected, is a cycle composed of discrete points (Figure 1.22) that will eventually be filled.

1.5.3 Chaotic Solutions

The chaotic behavior is in close relationship with a very special performance of the Poincaré map. Actually it has been shown that in chaotic systems, the application of the map over a unit square has two different actions: stretching and folding [7–9]. This is sketched in Figure 1.23(a). The recursive application of the map, backwards and forward, gives rise, as shown in Figure 1.23(b), to a set of isolated points (Cantor set). A very special fact is that two points arbitrarily close in the unit square may end very far from each other after several applications of the map. This is in close relationship with the sensitive dependence on

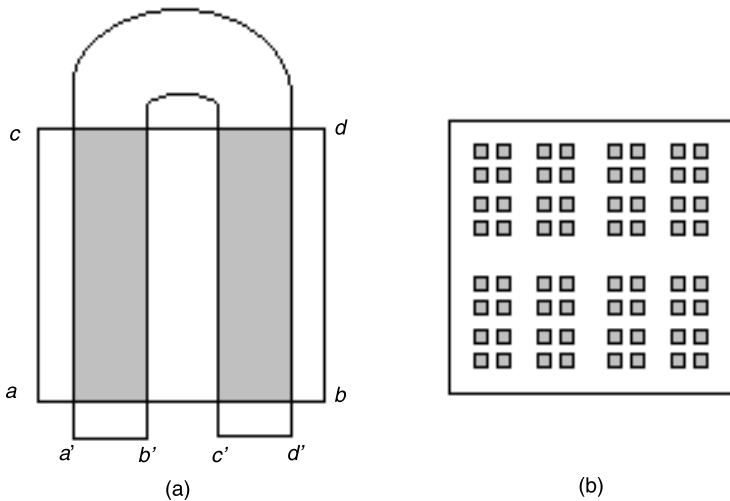


Figure 1.23 (a) Horseshoe map; and (b) Cantor set resulting from repeated applications of the map, backward and forward.

the initial conditions. Another interesting fact is the fractional dimension of the resulting set. Note that the dimension will be higher than that of a line (1) and smaller than that of a complete square (2), so it will be comprised between one and two. This is also true for chaotic solutions when represented in the phase space. They give rise to a limit set with a fractal dimension. A self-similarity property is observed with the same pattern repeating itself under magnification of a section. The property will be seen in the chaotic solution of Example 1.10.

Example 1.10: IMPATT-based circuit with chaotic behavior: Poincaré map

Figure 1.24 shows the schematic of an IMPATT-based self-oscillating mixer to operate in millimetric band [13]. The autonomous frequency ω_o mixes with that of the input generator ω_g to provide the intermediate frequency $\omega_{IF} = |\omega_g - \omega_o|$. Thus, in standard operation, this circuit provides a quasiperiodic solution that, when represented in the phase space, gives rise to a 2-torus [Figure 1.25(a)]. However, under increment of the bias current or reduction of the linear resistance, the solution becomes chaotic. When represented in the phase space, the chaotic limit set of Figure 1.25(b) is obtained.

The Poincaré-map technique has been applied to the chaotic solution of Figure 1.25(b). The application of this map discretizes the solution and reduces its dimension by one. Because the circuit of Figure 1.26 is a nonautonomous system, the Poincaré map can be easily obtained, according to (1.38), by sampling the solution $\bar{x}(t)$ at integer multiples of the input-generator period [i.e., $\bar{P}^n(\bar{p}) = \bar{\varphi}_{nT_g}(\bar{p})$]. When proceeding like this, the map of Figure 1.26 is obtained. The self-similarity property is evidenced in Figure 1.26(b).

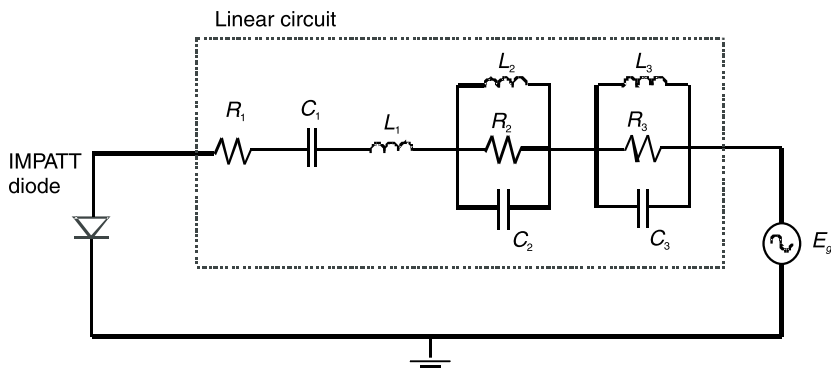


Figure 1.24 Self-oscillating mixer based on the use of an IMPATT diode.

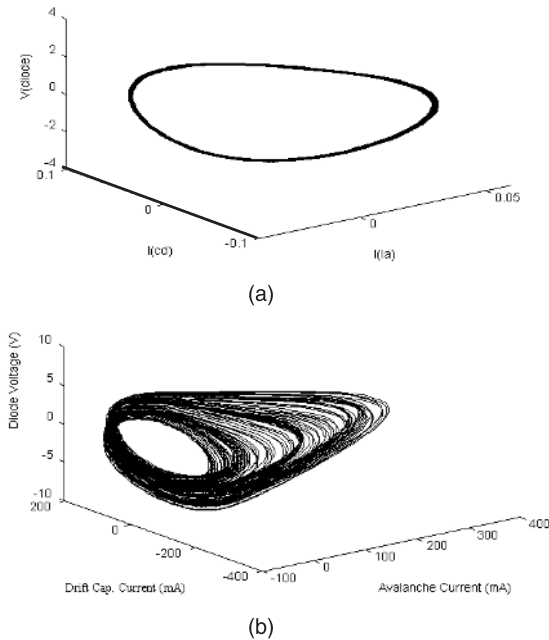
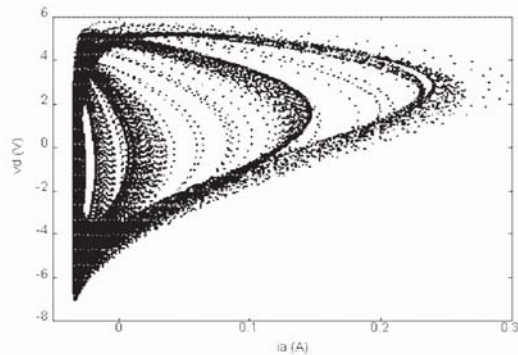


Figure 1.25 Solution of the self-oscillating mixer: (a) standard operation, 2-torus, and (b) chaotic operation.

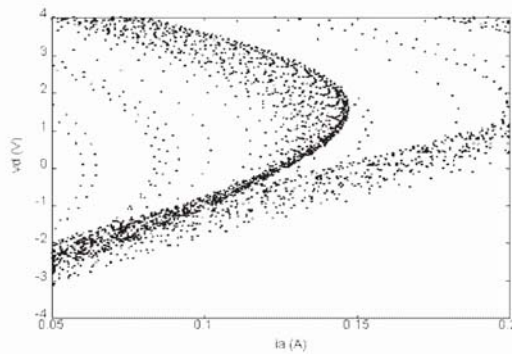
1.6 Entrainment: Phase-Locked Solutions in the Torus

In Example 1.6, a periodic input generator of period T_g was connected to the self-oscillating circuit of Figure 1.2. For the particular values considered in the example, a self-oscillating mixer behavior was obtained (Figure 1.11). The steady-state solution was quasiperiodic, giving rise to a 2-torus when represented in the phase space (Figure 1.12). However, this is not the only possible behavior in an oscillator circuit with an external generator. Other kinds of solution, periodic of different periods kT_g and even chaotic (in some circuits), can also be obtained [32–34].

For fixed circuit-element values, the observation of periodic behavior at ω_g or quasiperiodic behavior at ω_g and ω_o (2-torus) depends on the amplitude E_g and frequency ω_g of the input generator. Actually, the self-oscillation frequency ω_o depends on the generator value $\omega_o \equiv \omega_o(E_g, \omega_g)$ and, under some circumstances, the self-oscillation frequency may become equal to that of the input generator: $\omega_o(E_g, \omega_g) = \omega_g$. This phenomenon is called *entrainment* [8, 9].



(a)



(b)

Figure 1.26 (a) Poincaré map of the chaotic solution of an IMPATT-based self-oscillating mixer; and (b) expanded view, showing a self-similar pattern.

The resulting periodic solution is *phase-locked* to the input-generator signal (or synchronized), meaning that there is a constant phase shift between the two. When this happens, the rotation number (1.15) takes the value $r = 1$ and keeps it for a certain input-frequency interval.

The synchronization phenomenon is only possible in nonlinear systems. In contrast, the self-oscillation in a linear dissipative system vanishes in time. The transient will have two different frequencies involved: the frequency of the forcing generator and the self-generated frequency. However, the later decays after certain time and only the externally introduced oscillation remains in the steady state [8]. In contrast, a nonlinear, nonconservative system can exhibit self-sustained oscillations, which, as will be shown, are able to synchronize to the periodic input signal. This case will be studied in the following.

Let the free-running-oscillation frequency (in the absence of generator) be $\omega_o = \omega_{of}$. When the input generator is connected, for relatively low amplitude E_g , synchronization takes place in a frequency band about ω_{of} given by $(\omega_{g1}, \omega_{g2}) \equiv (\omega_{of} - \Delta\omega, \omega_{of} + \Delta\omega')$. In general, the synchronization bands are symmetric about ω_o for low input-generator amplitude, but become nonsymmetric as the input amplitude increases. They are wider for bigger generator amplitude (bigger influence on the autonomous oscillation). Outside these bands, the circuit operates in the quasiperiodic regime (see Figure 1.27).

The synchronization phenomenon may also take place for generator frequencies close to a harmonic component $k\omega_{of}$ of the free-running oscillation frequency [8, 14]. This is another situation of bigger influence on the autonomous oscillation because the k th harmonic component of the self-oscillation is able to synchronize with the input-generator signal. The synchronization bands usually become narrower as the order k increases. In each of these bands, the rotation number (1.15) takes the constant value $r = \frac{1}{k}$, and keeps it for a certain input frequency interval (Figure 1.27). In between the bands $\frac{1}{k}$ and $\frac{1}{k+1}$, other synchronization bands exist of the form $\frac{m}{n}$, $m \neq 1$ which are usually narrower [8, 14]. The synchronized solutions of the cubic nonlinearity oscillators, with rotation numbers $r = 1$ and $r = \frac{1}{3}$ are analyzed in Example 1.11.

Example 1.11: Synchronized solutions in the forced cubic nonlinearity oscillator

In this example, the same circuit-element values as in Example 1.6 are going to be considered. The cubic nonlinearity oscillator exhibits a free-running

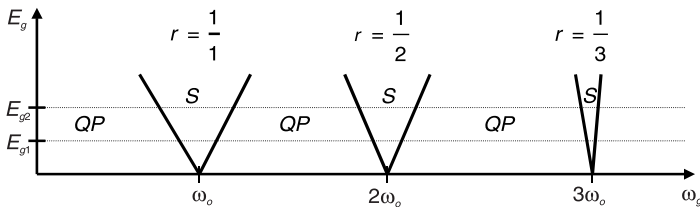


Figure 1.27 Schematic representation of the synchronization bands versus the input-generator values. Larger synchronization bandwidths are obtained for higher input-generator amplitudes. Asynchronous extinction of the autonomous frequency usually takes place in the higher range of input-generator amplitude and has not been represented. Quasiperiodic behavior is obtained outside the synchronization bands.

oscillation in the absence of the input generator. This oscillation takes place at the frequency $f_{of} = 1.6$ MHz. If the periodic voltage generator of Figure 1.2 is now connected, synchronization, according to Figure 1.28, is expected to take place for generator frequencies relatively close to the free-running oscillation frequency $f_{of} = 1.6$ MHz. Here the input-generator amplitude $E_g = 0.1$ v and frequency $f_g = 1.63$ MHz have been considered. The resulting solution is a periodic solution with the same frequency as that of the input generator, as shown in Figure 1.28(a). Both the input-generator voltage (the smaller amplitude waveform) and the voltage across the capacitor v_C have been represented. Note

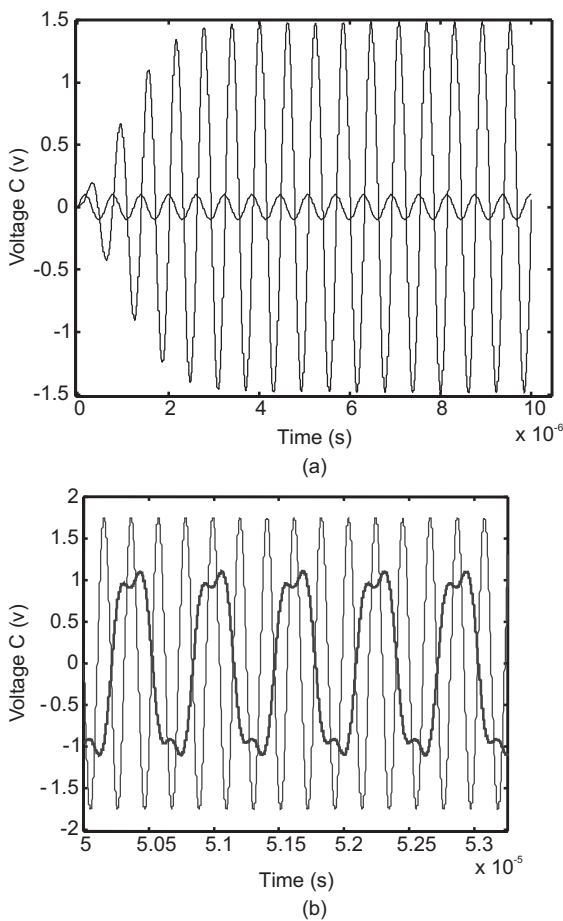


Figure 1.28 Phase-locked solutions of the cubic nonlinearity oscillator: (a) period-1 solution for $E_g = 0.1$ v and $f_g = 1.63$ MHz; and (b) period-3 solution for $E_g = 1.75$ v and $f_g = 4.8$ MHz. The resistance is $R = 1$ Ohm.

the constant phase shift between the two. The rotation number corresponding to this solution is $r = 1$.

In a second analysis, the input-generator frequency is close to the third harmonic component of the free-running oscillation frequency $f_{of} = 1.6$ MHz. The chosen input frequency is $f_g = 4.8$ MHz. The synchronization bands about the third harmonic component are, of course, much narrower than those around the first one (Figure 1.27), so to obtain synchronization, the input-generator amplitude has been increased to $E_g = 1.5v$. The resulting synchronized solution is shown in Figure 1.28(b). The input-generator voltage has also been represented. Note that there is also a constant phase shift between the two waveforms. However, the solution frequency is that of the input generator

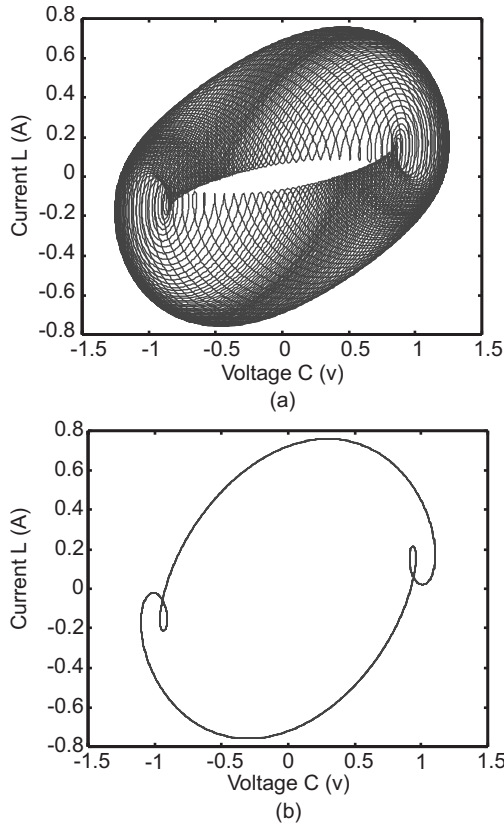


Figure 1.29 Cubic nonlinearity oscillator. Injection at about three-times the free-running oscillation frequency. (a) $f_g = 4.85$ MHz. Quasiperiodic solution. (b) $f_g = 4.8$ MHz. Phase-locked solution. The resistance is $R = 1$ Ohm.

divided by three. The rotation number takes the value $r = \frac{1}{3}$ and the circuit behaves like a frequency divider by three (period-3 solution). In Figure 1.29, the phase-locked solution is compared, in the phase space, with the torus-like solution obtained for the generator frequency $f_g = 4.85$ MHz. Note that, for the rational rotation number $r = \frac{1}{3}$, the steady-state trajectory does not fill the whole torus surface, unlike the case of a quasiperiodic solution. The trajectories in the torus have been attracted by a single periodic orbit. The case of a generator frequency of about twice the free-running oscillation value has not been considered because the free-running oscillator does not generate even harmonic components because of the cubic nonlinearity.

One example of the applications of synchronization in practical circuits is the design of analog frequency dividers. In harmonic-injection dividers by the order k , the input-generator signal synchronizes with the harmonic k of the oscillation frequency ω_o , so that $\omega_g = k\omega_o$. The self-oscillation frequency becomes the divided-by- k frequency. Outside the synchronization bands, the undesired self-oscillating mixer regime is observed.

References

- [1] Plaat, O., *Ordinary Differential Equations*, San Francisco, CA: Holden-Day, Inc., 1974.
- [2] Hartman, P., *Ordinary Differential Equations*, New York: John Wiley & Sons, 1964.
- [3] Starzhinski, V. M., *Applied Methods in the Theory of Nonlinear Oscillations*, Moscow, Russia: Mir Publishers, 1980.
- [4] Butenin, N., Y. Neimark, and N. Fúfaev, *Introduction to Nonlinear Oscillations*, Moscow, Russia: Mir Publishers, 1987.
- [5] Arrowsmith, D. K., and C. M. Place, *Dynamical Systems, Differential Equations, Maps and Chaotic Behavior*, London: Chapman & Hall/CRC, 1992.
- [6] Drazin, P. G., *Nonlinear Systems*, New York: Cambridge University Press, 1993.
- [7] Parker, T. S., and L. O. Chua, *Practical Algorithms for Chaotic Systems*, Berlin, Germany: Springer-Verlag, 1989.
- [8] Thompson, J. M. T., and H. B. Stewart, *Nonlinear Dynamics and Chaos*, New York: John Wiley & Sons, 1986.
- [9] Guckenheimer, J., and P. Holmes, *Nonlinear Oscillations, Dynamical Systems and Bifurcations of Vector Fields*, New York: Springer-Verlag, 1990.

-
- [10] Wiggins, S., *Introduction to Applied Nonlinear Dynamical Systems and Chaos*, Berlin, Germany: Springer-Verlag 1990.
- [11] Kurokawa, K., "Some Basic Characteristics of Broadband Negative Resistance Oscillator Circuits," *Bell Syst. Tech. J.*, Vol. 48, No. 6, 1969, pp. 1937–1955.
- [12] Vakman, D., *Signals, Oscillations, and Waves: A Modern Approach*, Norwood, MA: Artech House, 1998.
- [13] Suárez, A., et al. "Chaos Analysis in a Millimeter-Wave Self-Oscillating Mixer," *IEEE Microwave Guided Wave Lett.*, Vol. 9, No. 10, Oct. 1999.
- [14] Ios, G., and D. D. Joseph, *Elementary Stability and Bifurcation Theory*, 2nd ed., New York: Springer-Verlag, 1990.
- [15] Devaney, R. L., *A First Course in Chaotic Dynamical Systems*, Reading, MA: Addison-Wesley, 1992.
- [16] Cvitanovic, P., *Universality in Chaos*, Philadelphia, PA: Institute of Physics Publishing, 1996.
- [17] Lichtenberg, A. J., and M. A. Leiberman, *Regular and Chaotic Dynamics*, New York: Springer-Verlag, 1991.
- [18] Abarbanel, H. D. I., *Analysis of Observed Chaotic Data*, New York: Springer-Verlag, 1995.
- [19] Lasota, A., and M.C. Mackey, *Chaos, Fractals and Noise*, New York: Springer-Verlag, 1994.
- [20] "Special Issue on Chaotic Systems," *IEEE Trans. Circuits Syst.*, Aug. 1987.
- [21] Kapitanik, T., (ed.), *Chaotic Oscillators Theory and Applications*, Singapore: World Scientific, 1992.
- [22] Hasler, M. J., and P. Verburgh, "On the Uniqueness of the Steady State for Nonlinear Circuits with Time Dependent Sources," *IEEE Trans. Circuits Syst.*, Vol. 31, No. 8, Aug. 1984, pp. 702–713.
- [23] Mees, A. I., and L. O. Chua, "The Hopf Bifurcation Theorem and Its Applications to Nonlinear Oscillations in Circuits and Systems," *IEEE Trans. Circuits Syst.*, Vol. 26, No. 4, April 1979, pp. 235–254.
- [24] Odyniec, M., "On the Application of Hopf Bifurcation to Oscillator Analysis," *Integrated Nonlinear Microwave and Millimetric Wave Circuits, INMMC'90*, Duisburg, Germany, 1990, pp. 51–62.
- [25] Mees, A. I., "A Plain Man's Guide to Bifurcations," *IEEE Trans. Circuits Syst.*, Vol. 30, No. 8, Aug. 1983, pp. 512–517.
- [26] Colonius, F., and L. Grüne, *Dynamics, Bifurcations and Control*, Berlin, Germany: Springer-Verlag, 2002.

-
- [27] Kawakami, H., "Bifurcation of Periodic Responses in Forced Dynamic Nonlinear Circuits: Computation of Bifurcation Values of the System Parameters," *IEEE Trans. Circuits Syst.*, Vol. 31, No. 3, March 1984, pp. 248–260.
- [28] Arnold, V. I., et al., *Bifurcation and Catastrophe Theory*, Berlin, Germany: Springer-Verlag, 1999.
- [29] Suárez, A., A. Mediavilla, and J. Luy, "Period Doubling Route to Chaos in SiGe IMPATT Diodes," *IEEE Microwave Guided Wave Lett.*, Vol. 8, No. 4, April 1998, pp. 170–172.
- [30] Gannet, J., and L. Chua, "A Nonlinear Circuit Model for IMPATT Diodes," *IEEE Trans. Circuits Syst.*, Vol. 25, No. 5, May 1978, pp. 299–307.
- [31] Gonda, J., and W. Schroeder, "IMPATT Diode Design for Parametric Stability," *IEEE Trans. Microwave Theory Tech.*, Vol. 25, No. 5, May 1977, pp. 343–352.
- [32] Odyniec, M., "Nonlinear Synchronized LC Oscillators: Theory and Simulation," *IEEE Trans. Microwave Theory Tech.*, Vol. 41, No. 5, May 1993, pp. 774–780.
- [33] Suárez, A., J. Morales, and R. Quéré, "Synchronization Analysis of Autonomous Microwave Circuits Using New Global Stability Analysis Tools," *IEEE Trans. Microwave Theory Tech.*, Vol. 46, No. 5, May 1998, pp. 494–504.
- [34] Morales, J., A. Suárez, and R. Quéré, "Accurate Determination of Frequency Dividers Operating Bands," *IEEE Microwave Guided Wave Lett.*, Vol. 6, No. 1, Jan. 1996, pp. 46–48.

2

Nonlinear Analysis Techniques

As shown in Chapter 1, the nonlinear circuits may exhibit very complex behavior [1, 2]. Thus, they require powerful analysis techniques. Different methods are possible, like time-domain integration [3–12], harmonic balance (in frequency domain) [13–24], or the more recent mixed time-frequency approaches [25–30]. The particular choice of one or another method depends on the type of circuit, the frequency range of operation, and even the type of regime. The emphasis in this chapter will be on harmonic balance [13–24] because of its efficiency when dealing with microwave circuits and its wide use at this frequency range. A brief summary of time-frequency approaches, like the envelope-transient technique [26] will also be presented.

With the harmonic-balance method only steady-state solutions are analyzed. The simulator directly analyzes the steady-state solution, avoiding the transient, and thus, it does not follow the actual time evolution of the variables, unlike time-domain integration. Because the coexistence of stable and unstable steady-state solutions is possible (see Section 1.4), the harmonic-balance technique may converge to either a stable or an unstable solution. Thus, it is possible to obtain solutions toward which the circuit never actually evolves in time. This can be a difficulty for the simulation of circuits like free-running oscillators for which an equilibrium point always coexists with the limit cycle. Other circuits difficult to simulate are those containing subharmonic frequencies (like frequency dividers) or autonomous frequencies (like self-oscillating mixers).

When considering the variation of a circuit parameter (a linear element or a generator value), the application of *continuation techniques* [16, 17] provides the evolution of the steady-state solution versus the parameter. Solution curves

are obtained in terms of the output power or a representative circuit variable. The continuation techniques are efficiently combined with harmonic balance because of its direct analysis of the steady-state regime. The possible convergence of harmonic balance to unstable solutions enables the tracing of the entire solution curve, including stable and unstable sections. This can be an advantage for the in-depth study of the nonlinear-circuit dynamics.

The so called *time-frequency techniques* [25–30] are an interesting compromise between time and frequency-domain techniques, enabling the efficient simulation of circuits that operate on multiple time scales. An example is a mixer with two high-frequency fundamentals, giving rise to a very small intermediate frequency. In [26–29] two different time variables are used, which allows the expression of the circuit variables in a harmonic series with time-varying phasors. The phasors become the unknowns of a system of differential algebraic equations. The advantage over time-domain integration is its lower computational cost. The envelope transient [26] uses harmonic balance for the high-frequency dynamics and time-domain integration for the low-frequency modulations.

Other authors have already covered the harmonic-balance method [13–24] and aspects like the numerical treatment of quasiperiodic signals [16–19] or the efficient application of the method to large-scale circuits, containing many active devices [20–24] will not be studied here. Instead, this chapter focuses on the application of harmonic balance to autonomous and synchronized regimes, providing efficient techniques to avoid convergence to trivial mathematical solutions. The algorithms are presented in two versions: one for application to in-house software and the other for external application by the user to commercial harmonic-balance software.

This chapter is organized as follows: Section 2.1 reviews some features of the time-domain analysis technique for introductory purposes. Section 2.2 summarizes the harmonic-balance technique as established for nonautonomous circuits like amplifiers or mixers. Section 2.3 presents techniques for the harmonic-balance analysis of autonomous and synchronized regimes. Section 2.4 introduces the transient-envelope technique with an example illustrating its application to oscillator circuits. Section 2.5 presents continuation techniques for the tracing of solution curves versus a parameter. Equivalents of these algorithms for use in closed harmonic-balance (commercial) software are given in Section 2.6.

2.1 Time-Domain Simulation

Since circuits actually operate in time domain, the methods using time-domain descriptions [3–10] for all the circuit elements are the most intuitive and

natural for circuit simulation. In the direct-integration methods, the steady-state solution is obtained after the calculation of the whole transient [3–10]. Due to this fact, the simulation time (and the number of required simulation points) may be very big for short integration step and long duration of the transient. On the other hand, the direct integration methods can, in principle, be used for the simulation of any kind of regime, periodic, quasi-periodic or chaotic, and with periodic or nonperiodic input signals. Since they provide the whole solution curve (including the transient state), if convergence is achieved, the steady-state solution will be stable.

Let us assume that in the time domain, a nonlinear circuit with lumped elements can be represented by a system of nonlinear differential equations, of the form

$$\begin{aligned} \frac{d\bar{x}}{dt} &= f(\bar{x}, t) \\ \text{with } \bar{x}(t_o) &= \bar{x}_o \end{aligned} \quad (2.1)$$

with $\bar{x} \in R^n$ and $f \in R^n$. As is already known, the components of \bar{x} will be node voltages and branch currents. In the resolution, the time variable t is discretized, with a time step Δt , so that $t_k = t_o + k\Delta t$, and the system is integrated through a numerical algorithm [5]. There are many different algorithms, from a simple Euler's method, which only requires one input point (either \bar{x}_{k-1} , for the explicit Euler's method, or \bar{x}_k , for the implicit one) to complex multistep algorithms, like Gear's, which require several input points. A detailed classification of the different integration algorithms is provided in [5]. The efficiency of one or another algorithm depends on the particular problem.

The system (2.1) is iteratively solved in a certain time interval $[t_o, t_o + T_s]$, which provides both transient and steady-state solution. In these *direct-integration* methods, problems may arise if very high and very low frequency terms are contained in the circuit solution. Actually, a rule of thumb for accurate integration is the selection of a time step Δt in the order of $1/(50f_{\max})$, with f_{\max} being the highest frequency with a relevant influence. If the spectrum of the solution contains low frequencies, the integration-time interval T_s must also be long enough to take them into consideration, so a very long simulation time with a very short simulation step Δt might be required, giving rise to an enormous amount of calculation points.

If the circuit contains distributed elements, it is necessary to take into account the delay introduced by each of them [6–9]. Then, the system of differential equations becomes a differential-difference equations system, which, in some cases, takes the explicit form

$$\begin{bmatrix} \frac{d\bar{x}_1(t)}{dt} \\ x_2(t + \tau_i) \end{bmatrix} = \begin{bmatrix} \bar{f}_1(\bar{x}_1(t), \bar{x}_2(t), t) \\ \bar{f}_2(\bar{x}_1(t), \bar{x}_2(t), t) \end{bmatrix} \quad (2.2)$$

In (2.2), the vector \bar{x}_1 contains the variables referring to the discrete elements, while the vector \bar{x}_2 contains the variables referring to the distributed elements and $\bar{x} = (\bar{x}_1, \bar{x}_2)$. Each distributed element i has a delay τ_i , which has been symbolized $\bar{x}_2(t + \tau_i)$. Due to the different delays τ_i that are present in the circuit, the initial conditions must be evaluated over the interval $[t_o - \tau_{\max}, t_o]$, with τ_{\max} being the maximum delay. The integration step $\Delta \cong \frac{1}{50f_{\max}}$ must be

a submultiple of the delay of each transmission line. Example 2.1 shows how the differential-difference equation of a distributed oscillator circuit is obtained.

Example 2.1: Nonlinear differential-difference equations of a cubic nonlinearity oscillator with an ideal transmission line

As an example of system of the form (2.2), the equations of a cubic nonlinearity oscillator containing a transmission line are going to be derived [8]. The circuit is identical to the one in Example 1.1, except for the replacement of the inductor with a short-circuited ideal transmission line.

In Figure 2.1, $a(t, z)$ and $b(t, z)$ are, respectively, the incident voltage waveform (into the transmission line) and the reflected voltage waveform. These waveforms are related with the voltage v_2 and current i_2 through the well-known expressions [8, 9]

$$v_2(t, z) = a(t, z) + b(t, z) \quad (2.3a)$$

$$i_2(t, z) = \frac{a(t, z) - b(t, z)}{Z} \quad (2.3b)$$

where z is the longitudinal coordinate and Z is the characteristic impedance of the transmission line. On the other hand, because the transmission line is short-circuited, the following relationship is also fulfilled:

$$b(t + 2T, z) = -a(t, z) \quad (2.4)$$

where T is the line delay. Now, applying Kirchoff's laws, it is possible to write

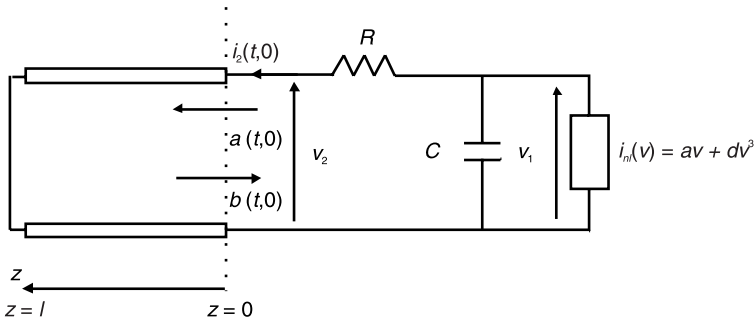


Figure 2.1 Cubic nonlinearity oscillator with an ideal transmission line.

$$C \frac{dv_1}{dt} + i_{nl}(v_1) + \frac{v_1 - v_2}{R} = 0 \tag{2.5a}$$

$$i_2 = \frac{1}{R}(v_1 - v_2) \tag{2.5b}$$

Combining (2.5) with (2.3) and (2.4), the following system of difference-differential equations is obtained, in the variables v_1 and $b(t)$:

$$\begin{aligned} \frac{dv_1}{dt} &= -\frac{inl(v_1)}{C} - \frac{v_1}{C(R+Z)} + \frac{2}{C(R+Z)}b(t) \\ b(t+\tau) &= -\frac{Z}{Z+R}v_1 - \frac{R-Z}{R+Z}b(t) \end{aligned} \tag{2.6}$$

where the new variable $\tau = 2T$ has been introduced and the spatial coordinate $z=0$ has been dropped, for notation simplicity. The system (2.6) is an example of differential-difference equation system of the form (2.2). It is resolved by discretizing the time variable and using numerical integration techniques [5, 6]. The time step Δt must be a submultiple of τ .

For a general circuit, it will not always be possible to obtain an equation system of the form (2.1) or (2.2). Instead, the circuit will be ruled by the following system of implicit equations:

$$\bar{g}\left(\bar{x}_1, \bar{x}_2, \frac{d\bar{x}}{dt}, \bar{x}(t-\tau_i), t\right) = 0 \tag{2.7}$$

with $\bar{g} \in R^n$. In the time discretization, the derivatives and time delays are approximated by a linear combination of the samples $\bar{x}(t_k)$. In programs like SPICE, advantage is taken of this time discretization, to transform each linear reactive element (inductance or capacitance) into a resistive equivalent [10]. Discrete equivalent models are also obtained for ideal transmission lines, depending on the time delay τ_i . In turn, the nonlinear elements are linearized through the Newton-Raphson algorithm, with the linear model, associated with each nonlinearity, varying in each iteration. After the discretization and linearization of the circuit elements, the circuit is solved applying Kirchoff's laws, which provide a modified nodal equation, in terms of the equivalent models, of the form [10]

$$[Y]\bar{V} = \bar{J} \quad (2.8)$$

where \bar{V} is the vector of voltage nodes and \bar{J} the vector of input currents. Equation (2.8) is solved through an iterative procedure. As has already been said, in circuits containing distributed elements, the integration step must be a submultiple of the delay of each transmission line, which can only be satisfied in an approximate manner. On the other hand, the simulation of realistic distributed elements is difficult. The models of these elements require either a lumped approximation of high order or the use of the impulse response [11]. This last representation requires the numerical calculation of convolution integrals and is computationally very expensive.

The direct-integration methods spend most of the calculation time on the evaluation of the transient regime. To avoid this, the shooting methods [12] provide, through an optimization technique, a vector of initial conditions \bar{x}_0 , from which the circuit behaves in steady-state regime. In the case of periodic regimes, this is done by imposing the constraint $\bar{x}(t) = \bar{x}(t + T)$ with T the period of the solution. However, there is no equivalent constraint for the case of quasiperiodic regimes, and thus, this technique is not appropriate for this kind of solution. On the other hand, when the aim is to simulate the steady state, the use of frequency-domain techniques is usually more convenient [11] because the distributed elements are more easily described and analyzed in the frequency domain, especially in the case of dispersive transmission lines.

2.2 Harmonic Balance for Nonautonomous Circuits

As mentioned earlier, the distributed elements can be easily described in the frequency domain. Actually, the convolution integrals that can be used for a

general time-domain description of distributed elements become simple transfer functions in the frequency domain. The lumped linear elements also have very simple current-voltage relationships in the frequency domain. However, for nonlinear elements, the transfer functions are undefined. Instead, these elements must be described by their instantaneous transfer characteristics, for example, $i(t) \equiv i(v(t))$ for currents, $q(t) \equiv q(v(t))$ for charges, and $\phi(t) \equiv \phi(i(t))$ for fluxes.

The harmonic-balance technique [13–15] to be presented in this section is a technique that uses frequency-domain descriptions for the linear elements, while keeping the necessary time-domain description for the nonlinear elements. The direct and inverse Fourier transforms are used to translate the circuit variables from one to another domain. In the piecewise harmonic balance, to be presented here, the state variables are the control variables of the nonlinear devices. The number of variables is typically much smaller than in nodal harmonic balance, using the node voltages. Due to the employment of Fourier series expansions for the circuit variables, harmonic balance only analyzes the solution steady state. This is often an advantage because of the shorter simulation times that are usually required, compared to time-domain integration. However, there may also be some difficulties because different steady-state solutions may coexist for the same parameter values. Harmonic balance may converge to either attractors or unstable solutions (repellers or saddles), so a complementary stability analysis is necessary. This analysis will be the object of Chapter 3.

2.2.1 Harmonic-Balance Equations

To obtain the harmonic-balance equation, the general circuit of Figure 2.2 will be considered. Three different kinds of elements can be distinguished: the state variables x_k with $1 \leq k \leq Q$, the nonlinear elements y_m with $1 \leq m \leq P$ and the independent generators g_l with $1 \leq l \leq S$. The set of state variables is composed of the variables (generally voltages or currents) that control the nonlinear elements. The nonlinearities of the circuit are considered as nonlinear dependent sources [13]. These nonlinear sources may be currents, charges, or fluxes. Such a representation is very common in nonlinear device modeling.

For a matrix formulation of the circuit equations, three vectors will be defined, containing respectively the nonlinearities, the state variables, and the independent generators (including bias and RF generators). For P nonlinearities, Q state variables, and S independent generators, these vectors are given by

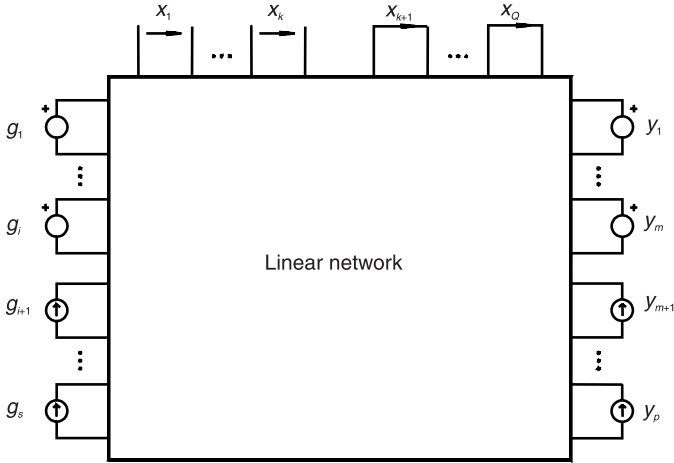


Figure 2.2 Harmonic-balance representation of the nonlinear circuit.

$$\begin{aligned}
 \bar{y}(t) &= (y_1(t), y_2(t), \dots, y_p(t))^t \\
 \bar{x}(t) &= (x_1(t), x_2(t), \dots, x_Q(t))^t \\
 \bar{g}(t) &= (g_1(t), g_2(t), \dots, g_s(t))^t
 \end{aligned} \tag{2.9}$$

with t indicating the transpose operation. Note that the vectors in (2.9) are time-domain vectors. On the other hand, a general expression for the nonlinear relationship between the vectors \bar{y} and \bar{x} will be

$$\bar{y}(t) = \bar{f}_{nl} \left(\bar{x}(t), \frac{d\bar{x}}{dt}, \dots, \frac{d^n \bar{x}}{dt^n}, \bar{x}(t - \tau) \right) \tag{2.10}$$

with τ being a possible time delay [14]. The rest of circuit components will be linear, lumped, or distributed.

In harmonic balance, the fundamental frequency or frequencies of the solution must be initially guessed. In the case of nonautonomous circuits, the independent generators deliver these fundamental frequencies, so it is not a problem. Things are more complicated in the case of autonomous circuits, and this will be the object of Section 2.4. Let a nonautonomous circuit with k fundamental frequencies (provided by the independent generators) be considered. These frequencies will be: $\omega_1, \omega_2, \dots, \omega_k$. Once the frequency basis is established,

the components of the three vectors x , y , and g can be expanded in a Fourier series:

$$\begin{aligned} \bar{x}(t) &= \sum_{m_1=-\infty}^{\infty} \dots \sum_{m_k=-\infty}^{\infty} \bar{X}_{m_1\dots m_k} e^{j(m_1\omega_1+\dots+m_k\omega_k)t} \\ \bar{y}(t) &= \sum_{m_1=-\infty}^{\infty} \dots \sum_{m_k=-\infty}^{\infty} \bar{Y}_{m_1\dots m_k} e^{j(m_1\omega_1+\dots+m_k\omega_k)t} \\ \bar{g}(t) &= \sum_{m_1=-\infty}^{\infty} \dots \sum_{m_k=-\infty}^{\infty} \bar{G}_{m_1\dots m_k} e^{j(m_1\omega_1+\dots+m_k\omega_k)t} \end{aligned} \quad (2.11)$$

In practice, the series must be truncated to a limited number of harmonic components. NH will be the number of positive frequencies, and the total number of analysis frequencies, $2NH + 1$ (including dc). The truncation of the series is carried out after the estimation of the nonlinearity order nl . In some cases, this order can be determined from the power-series expansion of a representative nonlinearity y [19]. Assuming a single-control variable $x(t)$, the expansion is given by

$$y(t) = \sum_{n=0}^{\infty} a_n (x(t))^n \quad (2.12)$$

and, in general, it is possible to identify an integer nl such that

$$\frac{a_n \|x(t)\|^n}{a_{nl} \|x(t)\|^{nl}} < \varepsilon \quad \text{for } n > nl \quad (2.13)$$

The integer nl is the nonlinearity order. In the case of a periodic regime, nl is the highest harmonic component to be taken into account, and $NH = nl$. In the case of quasiperiodic regimes, nl defines the maximum value of the addition $|m_1| + |m_2| + \dots + |m_k|$, all over the complete Fourier series. Thus, only intermodulation products with addition of indexes below nl are taken into account. The total number of positive frequencies NH is a function of nl . In the case of two fundamental frequencies (ω_1 and ω_2), it is easily shown that $NH = nl(nl + 1)$. Of course, the determination of nl through (2.13) is generally difficult in practical cases, so this quantity is usually estimated. In circuits having different amplitudes at each fundamental, it is also possible to assign a different maximum nl_k to each harmonic index m_k .

Once the Fourier basis has been established, the three vectors \bar{x} , \bar{y} , and \bar{g} can be translated to the frequency domain. Three new vectors \bar{X} , \bar{Y} , and \bar{G} , containing respectively the harmonic components of \bar{x} , \bar{y} , and \bar{g} , are defined

$$\begin{aligned}\bar{X} &= \begin{bmatrix} (X_{-NH}^1, \dots, X_{NH}^1) \dots \\ (X_{-NH}^Q, \dots, X_{NH}^Q) \end{bmatrix}^t = [\bar{X}_{-NH}, \dots, \bar{X}_k, \dots, \bar{X}_{NH}]^t \\ \bar{Y} &= \begin{bmatrix} (Y_{-NH}^1, \dots, Y_{NH}^1) \dots \\ (Y_{-NH}^P, \dots, Y_{NH}^P) \end{bmatrix}^t = [\bar{Y}_{-NH}, \dots, \bar{Y}_k, \dots, \bar{Y}_{NH}]^t \\ \bar{G} &= \begin{bmatrix} (G_{-NH}^1, \dots, G_{NH}^1) \dots \\ (G_{-NH}^S, \dots, G_{NH}^S) \end{bmatrix}^t = [\bar{G}_{-NH}, \dots, \bar{G}_k, \dots, \bar{G}_{NH}]^t\end{aligned}\quad (2.14)$$

where the subvectors \bar{X}_k , \bar{Y}_k , and \bar{G}_k , containing respectively the control variables, nonlinear elements, and independent generators at each spectral frequency k , have been introduced. Now the analysis frequencies have been arranged in increasing order, using one single index k . The subindex $k=0$ corresponds to the dc component, the subindex $k=1$, to the smallest frequency, and the subindex $k=NH$ to the highest one. Note that because we are dealing with real variables, the Fourier coefficients contained in the vectors (2.14) fulfill $C_k = C_{-k}^*$, with C standing for any component of either \bar{X} , \bar{Y} , or \bar{G} . Thus, it is equally possible to consider a Fourier expansion only containing positive frequencies. The harmonic-balance variables would be given, in this case, by the real and imaginary parts of the Fourier components. The transformation from one set of variables to the other is straightforward.

The next step is the application of Kirchoff's laws to the circuit in Figure 2.2, providing the linear relationships existing between the Fourier components of \bar{X} , \bar{Y} , and \bar{G} . Equating the total node currents and branch voltages, a matrix relationship is obtained, which defines an error function \bar{H} . The relationship is as follows [15]:

$$\bar{H}(\bar{X}) = [A_x] \bar{X} - [A_y] \bar{Y}(\bar{X}) - [A_g] \bar{G} = 0 \quad (2.15)$$

where $[A_x]$, $[A_y]$ and $[A_g]$ are frequency-dependent linear matrixes, with respective orders $Q \times Q$, $Q \times P$, and $Q \times S$. These linear matrixes have the general form:

$$[A] = \begin{bmatrix} [A_{-NH}] & \dots & [0] & [0] \\ [\dot{0}] & \dots & [\dot{A}_k] & \dots & [\dot{0}] \\ [\dot{0}] & \dots & [\dot{0}] & \dots & [\dot{A}_{NH}] \end{bmatrix} \quad (2.16)$$

with $[A]$ standing for any of the three matrixes $[A_x]$, $[A_y]$, or $[A_g]$.

The total number of equations is $(2NH + 1)Q$ in $(2NH + 1)Q$ unknowns. Equation (2.15) is, in fact, a nonlinear equation because the functions \bar{Y} and the state variables \bar{X} are nonlinearly related through (2.10). For a given \bar{X} , the corresponding $\bar{Y}(\bar{X})$ is indirectly obtained through inverse (F^{-1}) and direct (F) Fourier transforms:

$$\bar{x} = F^{-1}(\bar{X}) \rightarrow \bar{y} \equiv \bar{y}(\bar{x}) \rightarrow \bar{Y} = F(\bar{y}) \quad (2.17)$$

Equation (2.15) is satisfied when a state-variable vector \bar{X} fulfills $\bar{H}(\bar{X}) = 0$. The equation is solved through a numerical method that is briefly described in Section 2.2.2. In the case of periodic signals, the *discrete Fourier transform* (DFT) is used. This requires $2NH + 1$ sample points in the time domain, which are equally spaced within the period. This calculation has great accuracy since the rows of the transformation matrix are orthogonal and the matrix is well conditioned. In the case of quasi-periodic signals, the time points have to be carefully selected to avoid the ill-conditioning of the matrix. The description of the algorithms for the calculation of the direct and inverse Fourier transforms is beyond the scope of this book. In [16, 17, 19], the DFT is generalized to quasiperiodic signals. Detailed algorithms for the efficient calculation of quasiperiodic spectra can be found in [19].

2.2.2 Numerical Resolution of the Harmonic-Balance Equations

The harmonic-balance equation (2.15) is solved through a numerical method that minimizes the norm of the error vector \bar{H} . A threshold value in the norm of this vector $\|\bar{H}\| = \varepsilon$, below which the equation is considered to be satisfied, is initially imposed. This value determines the accuracy of the resolution. An iterative technique is used. This requires an initial value for the state-variable vector \bar{X}^0 . In a nonautonomous circuit, with low input-generator amplitudes, this vector can be estimated from (2.15), simply doing $\bar{Y} = 0$. If $[A_x]$ is invertible,

$$\bar{X}^0 = [Ax]^{-1} [Ag] \bar{G} \quad (2.18)$$

So the initial state-variable vector is determined from the values of the external generators. The general case of high input-generator amplitudes is treated in 2.2.3.

In the resolution process, the following steps are initially followed:

1. Calculate \bar{X}^0 from (2.18).
2. Calculate $\bar{Y}^0 : \bar{x}^0 = F^{-1}(\bar{X}^0) \rightarrow \bar{y}^0 = \bar{y}(\bar{x}^0) \rightarrow \bar{Y}^0 = F(\bar{y}^0)$.
3. Introduce both \bar{X}^0 and \bar{Y}^0 in (2.15).
4. Evaluate the norm $\|\bar{H}^0\|$.
5. Decision: For $\|\bar{H}^0\| \leq \varepsilon$, convergence is achieved. Otherwise, a new value \bar{X}^1 must be introduced in (2.15)

The choice of the next vector \bar{X}^1 [and, in general, of the vector \bar{X}^{j+1} to be introduced in (2.15) after each iteration] is crucial for the success of the convergence process. The calculation of this vector is based on the result \bar{H}^j of the former error evaluation. The Newton-Raphson algorithm [14] is one of the most efficient and most usually employed. Using this technique, the new vector \bar{X}^{j+1} is obtained from a linearization of the nonlinear system about the point \bar{X}^j , resulting from the previous iteration. This is equated as

$$\bar{X}^{j+1} = \bar{X}^j - [JH]_j^{-1} \bar{H}^j(\bar{X}) \quad (2.19)$$

where $[JH]$ is the Jacobian matrix of (2.15). This matrix is obtained through

$$[JH] \equiv \left[\frac{\partial \bar{H}}{\partial \bar{X}} \right] = [Ax][I] - [Ay][U] \quad (2.20)$$

with $[I]$ being the identity matrix and $[U]$ being the Jacobian matrix of the harmonic components of the nonlinearities \bar{Y} with respect to the harmonic components of the state variables \bar{X} . For a nonlinear dependence $\bar{y} \equiv f_{nl}(x)$, $\frac{\partial Y_k^p}{\partial X_i^q}$

agrees with the frequency component $k - i$ of $\frac{\partial y^p}{\partial x^q}(t)$. It is easily shown [14]

that the calculation of this matrix requires $4NH + 1$ components in the Fourier-series expansions of the nonlinear-function derivatives $\frac{\partial y_i}{\partial x_j}$.

After the first iteration (Steps 1 to 5), the rest of the convergence process, starting from $\bar{X}^0, \bar{H}^0 (j=0)$ already evaluated in Step 4, can be summarized as follows:

6. Calculate $\bar{X}^{j+1} : \bar{X}^{j+1} = \bar{X}^j - [JH]_j^{-1} \bar{H}^j(\bar{X})$.
7. Calculate $\bar{Y}^{j+1} : \bar{x}^{j+1} = F^{-1}(\bar{X}^{j+1}) \rightarrow \bar{y}^{j+1} = \bar{y}(\bar{x}^{j+1}) \rightarrow \bar{Y}^{j+1} = F(\bar{y}^{j+1})$.
8. Introduce both \bar{X}^{j+1} and \bar{Y}^{j+1} in (2.15).
9. Evaluate the norm $\|\bar{H}^{j+1}\|$.
10. Decision: For $\|\bar{H}^{j+1}\| \leq \varepsilon$, convergence is achieved. Otherwise, return to Step 6.

The Newton-Raphson algorithm (2.19) may be difficult to implement in the case of very large circuits. The matrix factorization required for the Jacobian inversion is very demanding in terms of computing time and memory storage. They both increase quickly with the number of analysis frequencies and nonlinear devices. To cope with this problem, sparse-matrix solvers [20–24] can be applied. In [20], selected elements of the Jacobian matrix are set to zero (according to a physical criterion), which leads to a sparse Jacobian matrix. The sparse linear system can be solved through preconditioned Krylov subspace methods [24]. Techniques for the harmonic-balance simulation of large linear systems arising from the Newton-Raphson algorithm are given in [24].

The formulation summarized in (2.18) to (2.20) constitutes one possible implementation of the harmonic-balance method. However, there was an initial assumption of low input-generator level in the choice of \bar{X}^0 . What happens when this is not the case? If the initial state-variable vector \bar{X}^0 is far from the actual solution \bar{X}^S , there will be serious convergence problems, in spite of the efficiency of the Newton-Raphson algorithm. This may be overcome by making use of a continuation method.

2.2.3 Continuation Technique for High Amplitude of the RF Generators

In this section, the resolution of the harmonic-balance system in case of high input-generator amplitude is going to be presented. This resolution is based on the use of what is called a *continuation technique*. In such a technique, variations in a parameter η , which may belong to the original system (like a generator) or

be artificially introduced, are considered [17–43]. For the continuation technique to be of any use, the harmonic-balance system must be easily solvable for a given parameter value η_1 . Conversely, the parametrized system must agree with the original system for a different parameter value $\eta = \eta_N$.

To achieve the desired solution (corresponding to $\eta = \eta_N$), the parameter, with the initial value $\eta = \eta_1$, is incremented in steps $\Delta\eta$ and a whole harmonic balance resolution is carried out for each discrete value η_n . In the harmonic-balance calculation for η_{n+1} , the final harmonic balance solution for η_n , X_n , is taken as initial guess $\bar{X}_{n+1}^0 = \bar{X}_n$. This avoids the initial-value problem of the Newton-Raphson algorithm. The process is sketched in the following:

$$\begin{aligned} \eta_1 : \bar{X}_1^o &\xrightarrow{HB} \bar{X}_1 \\ \eta_2 : \bar{X}_2^o &= \bar{X}_1 ; \bar{X}_2^o \xrightarrow{HB} \bar{X}_2 \\ &\vdots \\ \eta_N : \bar{X}_N^o &= \bar{X}_{N-1} ; \bar{X}_N^o \xrightarrow{HB} \bar{X}_N \end{aligned}$$

In the case of high-amplitude generators, the parameter η can be a factor (or level), multiplying the generator values: $\bar{G}(\eta) = \eta \bar{G}$. The parameter will vary between a value close to zero ($\eta_1 \cong 0.001$, for instance) and $\eta_N = 1.0$, with N being the maximum number of steps. This parameter allows gradually increasing the amplitude of the input generators because, at each step, the generator vector is given by $\bar{G}_n = \eta_n \bar{G}$. Thus, the solution of the high-amplitude problem, corresponding to the generator values $\bar{G}_N \equiv \eta_N \bar{G} = 1\bar{G}$, is obtained from the solution of the small-signal problem $\bar{G}_1 = \eta_1 \bar{G}$.

In some cases, the continuation technique is initially applied to the dc generators \bar{G}_{dc} only, while maintaining the RF ones at their small-signal values $\bar{G}_{RF1} = \eta_1 \bar{G}_{RF}$. Then, the continuation technique is applied to the RF generators with the dc generators at their final values. The approach thus consists of two consecutive parallel applications of the continuation technique in the sense that, in each case (dc and RF), all the independent generators are simultaneously increased. In the literature [44, 45], the possibility of a series application of the continuation technique to one generator after another has also been investigated. The most convenient choice depends on the particular problem.

The resolution process is illustrated in Figure 2.3. The variable X_k is simply a representative variable of the system, for instance, the first harmonic component of a control voltage. In some cases, the solution curve, composed by the points η_n, X_{nk} , may exhibit infinite-slope points or *turning points*. The

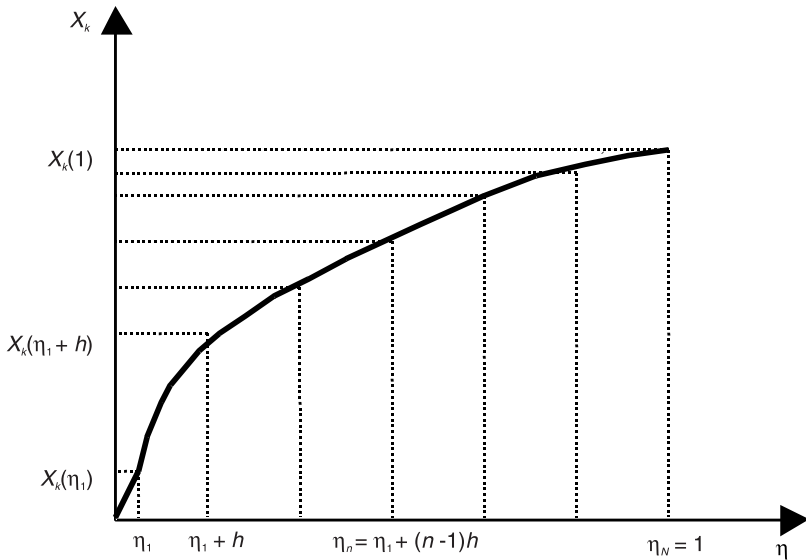


Figure 2.3 Continuation technique for harmonic balance: The solution of the continuation problem, traced in terms of a representative variable X_k , is easily determined for $\eta = \eta_1$. It agrees with the desired solution for $\eta = 1$.

way to circumvent this problem is presented in detail in Section 2.5, showing how continuation techniques [46, 47] can be applied to obtain multivalued solution curves versus a parameter η .

With all the above formulations, the harmonic-balance algorithm is ready for its application to well-behaved nonautonomous regimes. However, the case of autonomous or synchronized regimes has not been tackled yet and will be the object of the next section. As will be shown, the problem with the autonomous or synchronized solutions [31–33] comes from their coexistence with trivial mathematical solutions to which the harmonic-balance equations more easily converge.

2.3 Harmonic Balance for Autonomous and Synchronized Circuits

In an autonomous regime, the number of fundamental frequencies is higher than the number of frequencies delivered by the external generators [36]. When simulating autonomous regimes, the disadvantage of harmonic balance, compared with time domain, comes from the necessity to fix in advance the frequency basis of the Fourier series (as has already been shown). This may be difficult when dealing with circuits with complex dynamics for which the

actual behavior is somehow unexpected. Omitting one fundamental would lead to wrong (mathematical) solutions without physical existence (see Section 1.4). On the other hand, even when the frequency basis is correctly established (with the inclusion of the autonomous fundamentals), the harmonic balance may fail to converge to the desired autonomous solution. This is due to its intrinsically forced nature. The problem comes from the use of (2.18) to obtain the initial point of the convergence algorithm. Equation (2.18) can only give an initial value to fundamental frequencies at which generators are present. It leaves all the autonomous and subharmonic components at zero value and the convergence process is unable to fill them by itself. The resulting solution will be a mathematical solution, usually without physical existence.

The difficulties in the frequency-domain simulation of autonomous and synchronized circuits are illustrated in Example 2.2, where the cubic nonlinearity oscillator of Example 1.1 is approximately analyzed by means of the describing function [31–33].

Example 2.2: Approximate analysis of the cubic nonlinearity oscillator through the use of the describing function

Let the circuit of Example 1.1 be considered here. The analysis of the free-running oscillation of this circuit, through the describing function, was already carried out in Example 1.4. The circuit schematic, under this sinusoidal approach, is shown in Figure 2.4. The oscillating solution (for $E_g = 0$ and $R=1\Omega$) is given by $V_o = 1.09v$ and $\omega_o = 10 \times 10^6 \text{ s}^{-1}$. This solution has been marked “FO” in Figure 2.5, where it coexists with the trivial one $V_o = 0$ (see Example 1.4).

Let the connection of the input generator E_g now be considered. Synchronized solutions will only exist for some values of this generator in terms of its amplitude E_g and frequency ω_g (see Figure 1.27). Here, a synchronized solution will be assumed. This means the existence of only one fundamental in the circuit, equal to the input-generator frequency ω_g and the existence of a constant

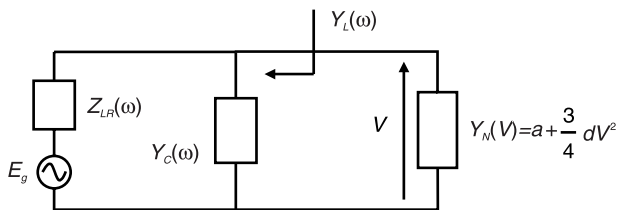


Figure 2.4 Simplified model of the cubic nonlinearity oscillator for its approximate analysis by means of the describing function.

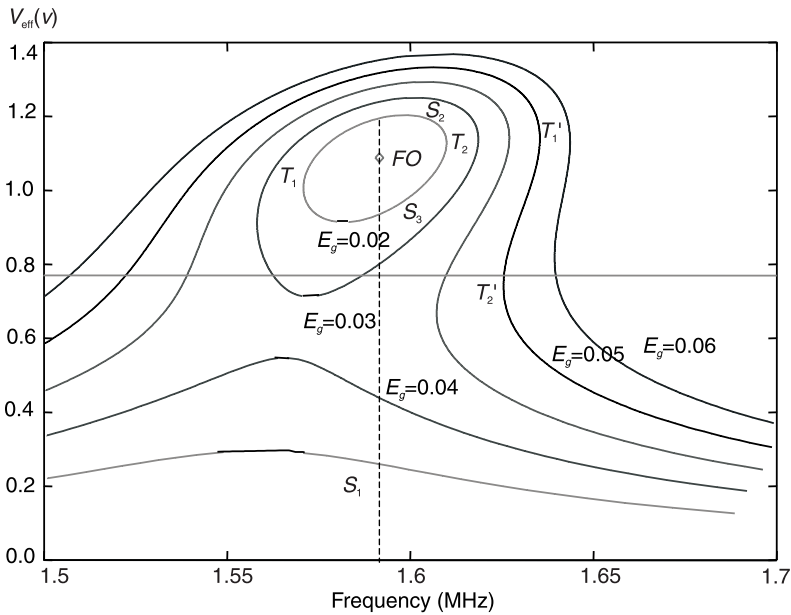


Figure 2.5 Solution curves of the cubic nonlinearity oscillator for several values of the input-generator amplitude E_g . A synchronized solution has been assumed, which is only true above the horizontal line at $V = 0.78v$. The curves have actually been obtained with the harmonic-balance technique of Sections 2.3 and 2.5. The represented variable V_{eff} is an average of all the harmonic components of the independent variable $v(t)$. With less accuracy, they can also be obtained through resolution of (2.21).

phase shift ϕ between the circuit solution $v(t)$ and the input-generator signal $e_g(t)$. With this assumption, the application of Kirchoff's laws provides

$$\begin{aligned}
 E_g e^{-j\phi} &= [Z_{LR}(\omega_g)Y_{NL}(V) + Z_{LR}(\omega_g)Y_C(\omega_g) + 1]V = \\
 &= \left[Z_{LR}(\omega_g) \left(a + \frac{3}{4}dV^2 \right) + Z_{LR}(\omega_g)Y_C(\omega_g) + 1 \right]V
 \end{aligned}
 \tag{2.21}$$

The former complex equation is a cubic equation in V , which can be solved for each generator value E_g , ω_g by splitting into real and imaginary parts, and making the phase variable disappear. The solutions may be real or complex in V , but only real solutions make sense in this problem. A representation versus the input-generator frequency ω_g of these solutions has been carried out in Figure

2.5. (The curves, for better accuracy, have actually been obtained through harmonic balance, following the techniques in Section 2.3 and 2.5.)

As shown in Figure 2.5, for some values of the input generator (E_g, ω_g), there are three possible solutions (in terms of V and ϕ), respectively noted S_1 , S_2 , and S_3 . This is typically the case for low generator amplitudes ($E_g = 0.02v$ and $E_g = 0.03v$ in the figure). Note that for these small generator amplitudes, there are, in fact, two solution curves, versus the input frequency ω_g . One curve is closed (containing both S_2 and S_3) and the other (containing S_1) is open (defined for all frequency values between zero and infinity) and corresponds to S_1 . The amplitude of the latter is much lower than that of the free-running oscillation. This solution (analogous to $V = 0$ in a free-running oscillator) is a solution for which the self-oscillation is not taken into account and no synchronization is actually observed. The difficulty when simulating injected oscillators through harmonic balance comes from the high risk of convergence toward this asynchronous solution.

The two solutions S_2 and S_3 have amplitude in the order of that of the free-running oscillation. However, only the solution S_2 , in the upper section of the closed curve (above the axis defined by the two turning points T_1 and T_2) is stable and will be physically observable. All these stability aspects will be discussed in Chapter 3. Observing the family of solution curves of Figure 2.5, it is clear that the free-running oscillation is, in fact, a degenerate solution of the same family with the closed curve degenerating in a point and the low-amplitude curve lying on the horizontal axis.

For higher input-generator amplitude, the higher and lower amplitude solutions merge. There is only one real solution of (2.21) (except for a small multivalued interval on the higher frequency side). This does not mean, however, that all the solution points in this single solution curve are stable (physically observable). Actually, only points above the horizontal line above $V = 0.78v$ are stable. Again, this stability analysis will be discussed in Chapter 3. Here, we are only dealing with the steady-state solutions and the harmonic-balance techniques to obtain them. However, the possible instability of these solutions must be kept in mind.

2.3.1 Analysis of Free-Running Oscillators

The simplest case of autonomous regime is that of a well-behaved free-running oscillator. Due to the circuit autonomy, the exact fundamental frequency ω_o is an unknown to be added to the set \bar{X} , containing the Fourier components of the Q control variables \bar{x} . This means the existence of $(2NH + 1)Q + 1$ unknowns in (2.15), only containing $(2NH + 1)Q$ equations. However, the

number of unknowns and equations can be made equal by taking into account the autonomous nature of the system. Actually, in Section 1.1 it was shown that the nonlinear differential equations ruling the behavior of autonomous circuits do not explicitly depend on time. The solution does not depend on its time origin and, in the frequency domain, it is independent of the phase origin. Due to this fact, the real or imaginary part of one of the components of the vector \bar{X} may be arbitrarily fixed to any value. A convenient choice is [14]:

$$\text{Im}(X_1^1) = 0 \quad (2.22)$$

The above equation balances the system, now having $(2NH + 1)Q + 1$ equations in $(2NH + 1)Q + 1$ unknowns. In the practical resolution of the system, through the Newton-Raphson algorithm or any other, the usually big difference in magnitude order between the frequency ω_o and the control variables \bar{X} must be taken into account. Normalization of the frequency is necessary: $\nu = \omega_o / \omega_N$, with ω_N a prefixed normalization value.

The problem is now well equated and ready for its solution. However, we come again to the problem of the initial value \bar{X}^0 . Remember that in the free-running oscillator circuit, aside from the periodic oscillation (limit cycle), there is always an equilibrium point (Figure 1.6). This is a dc solution of the circuit. When using harmonic balance, the equilibrium point and the limit cycle constitute two different steady-state solutions to which the system may converge. However, convergence to the dc solution is much easier because the bias generators are forcing this solution, while at the oscillation frequency there are no forcing generators at all (as was pointed out in Section 2.2.3). Due to this fact, unless a close-enough initial point \bar{X}^0 is provided, the system will converge to the dc solution, regardless of the appropriate selection of the frequency basis $k\omega_o$.

Over the years, several strategies have been proposed [34–40] to avoid undesired convergence to the equilibrium point (in cases of coexistence of both solutions). The one that will be presented here is based on the use of auxiliary generators. This technique takes advantage of the forced nature of the harmonic-balance algorithm. In fact, the auxiliary generator plays the role of the nonexistent generator at the autonomous frequency and forces a periodic solution, avoiding the problem of convergence to the dc point. The solution obtained with the aid of this auxiliary generator must be the actual oscillator solution, and must, of course, entirely agree with the one that would be obtained without the auxiliary generator.

Two different types of auxiliary generator are possible: voltage generators, connected in parallel at a circuit node, and current generators, connected in

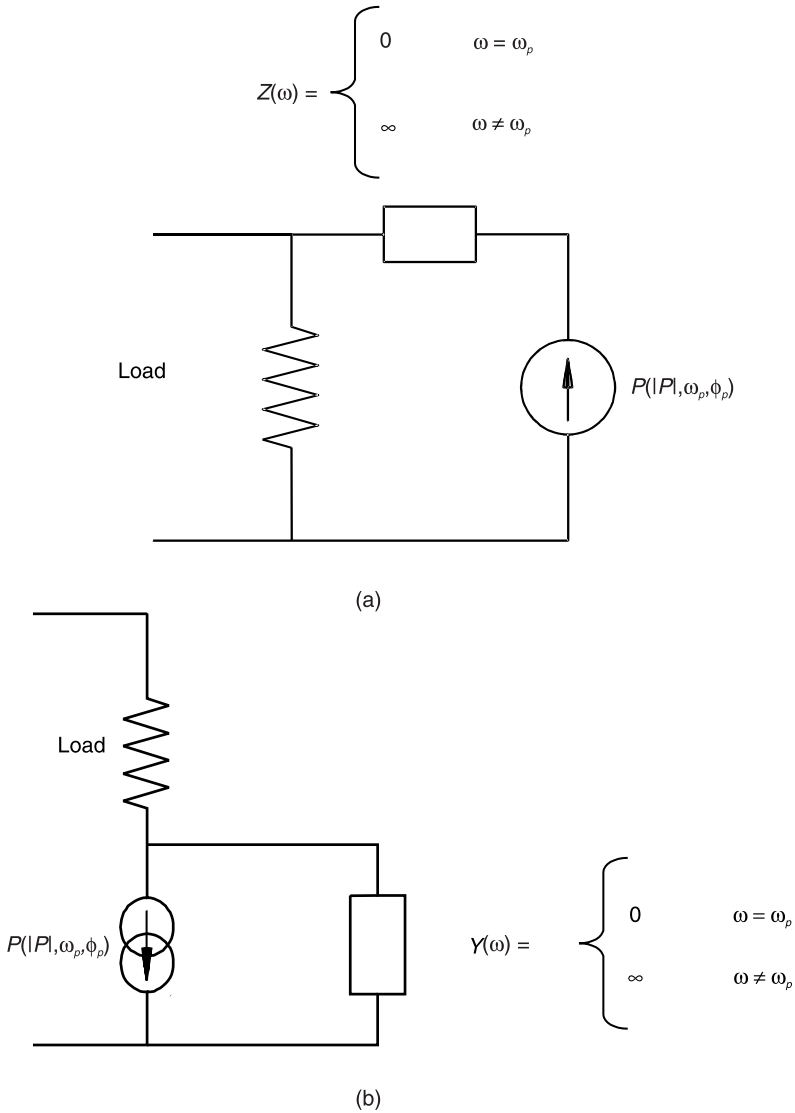


Figure 2.6 Auxiliary generators: (a) voltage generator, and (b) current generator.

series at a circuit branch (Figure 2.6). The generator, as formerly said, operates at the oscillation frequency ω_o to be determined. It must also be taken into account that voltage generators and current generators are, respectively, short circuits and open circuits at frequencies different from the ones that they

deliver. Thus, an ideal filter is necessary in each case to avoid a big perturbation of the circuit due to the short-circuiting/opening of the harmonic components. In the case of a voltage generator, the ideal filter is connected in series with this generator, as shown in Figure 2.6(a). The filter has a zero impedance value at the generator frequency $\omega_p = \omega_o$ and infinite impedance at any other frequency (for which the generator will have no effect). In the case of a current generator [Figure 2.6(b)], the filter is connected in parallel with this generator, and it will exhibit infinite impedance at the frequency ω_p and zero impedance at any other one, letting frequencies different from ω_p pass unperturbed.

Finally, so that the generator may have no influence over the circuit steady-state solution, it must have a zero admittance value at the delivered frequency, in case of a voltage generator, or a zero impedance value, in case of current generator. Thus, in the calculation of the free-running oscillator solution, both the generator amplitude $|P|$ and frequency $\omega_p = \omega_o$ must be determined in order to fulfill these conditions. Note that due to the irrelevance of the phase origin in the free-running oscillator solution, the generator phase may be arbitrarily fixed to zero. Equation (2.22) is no longer employed. In this way, the system has two more unknowns, $|P|$ and frequency ω_p , and two more equations, given by the real and imaginary parts of the auxiliary-generator *immittance* function (admittance or impedance, according to the type of generator). To equate this, the immittance function \bar{H}_p will be defined:

$$\begin{aligned} \bar{H}_p \equiv \begin{bmatrix} \text{Re } Z_p \\ \text{Im } Z_p \end{bmatrix} &= \begin{bmatrix} \text{Re} \left(\frac{V_p}{|P|} \right) \\ \text{Im} \left(\frac{V_p}{|P|} \right) \end{bmatrix} && \text{For a current source } P \\ \bar{H}_p \equiv \begin{bmatrix} \text{Re } Y_p \\ \text{Im } Y_p \end{bmatrix} &= \begin{bmatrix} \text{Re} \left(\frac{I_p}{|P|} \right) \\ \text{Im} \left(\frac{I_p}{|P|} \right) \end{bmatrix} && \text{For a voltage source } P \end{aligned} \tag{2.23}$$

Note that the use of the above immittance relationships avoids the dc solution. To see this more clearly, if, in the case of a voltage generator, a zero value for the current through this generator had been imposed (instead of a zero admittance value), the solution with zero amplitude $P=0$ would still have been possible. This is no other than the dc solution. The same is valid for the current generator, replacing current with voltage and admittance with impedance.

The new equation system is:

$$\bar{H}_p(\bar{X}, |P|, \omega_p) = 0 \quad (2.24a)$$

$$\bar{H}_b(\bar{X}, |P|, \omega_p) = 0 \quad (2.24b)$$

where the lower equation is the harmonic-balance equation \bar{H} we had been dealing with in the study of nonautonomous circuits [see (2.15)]. For the sake of clarity, this harmonic-balance equation has been renamed \bar{H}_b in (2.24). Note that the auxiliary generator P must be included in the vector \bar{G} of \bar{H}_b . Equation (2.24) is a well-balanced system of $(2NH + 1)Q + 2$ unknowns in $(2NH + 1)Q + 2$ equations. The equations can be solved through a full Newton-Raphson or using a two-level Newton-Raphson. In the latter case, the Jacobian matrix $JH_p[|P|, \omega_p]$ is used for (2.24a). The derivatives with respect to $|p|$ and ω_p are calculated through increments, performing a harmonic balance resolution for each $|P| \pm \Delta|P|$ and $\omega_p \pm \Delta\omega_p$. In Example 2.3 the harmonic-balance system is formulated for the case of the cubic nonlinearity oscillator. For illustration, the linear matrixes are analytically obtained.

Example 2.3: Use of an auxiliary generator to obtain the oscillating solution of the cubic nonlinearity oscillator

The cubic nonlinearity oscillator of Figure 1.2 (the same that had already been used in Example 1.1) is analyzed here. Because of the absence of time-varying

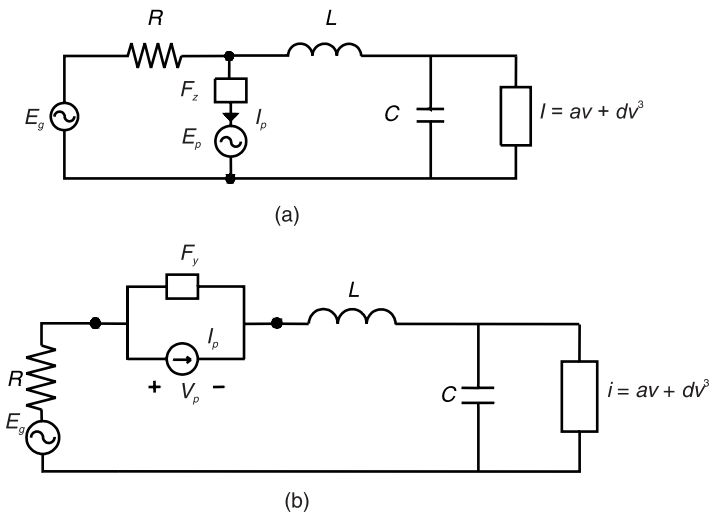


Figure 2.7 Introduction of auxiliary generators into the cubic nonlinearity oscillator: (a) voltage generator, and (b) current generator.

generators, the harmonic-balance analysis converges, by default, to the dc solution $\bar{V} = \bar{0}$ with no oscillation at all. This will be avoided through the introduction of an auxiliary generator. To see this, the circuit of Figure 1.2 is reproduced in Figure 2.7, with the inclusion of a voltage auxiliary generator in Figure 2.7(a) or a current auxiliary generator in Figure 2.7(b). Either of them can be used for the analysis, although, for the sake of brevity, only the case of a voltage auxiliary generator will be considered here.

The nonlinear function is given by $inl(v) = av + dv^3$. Thus, in the harmonic-balance formulation, the nonlinearity is $y \equiv i_{nl}$ and the state variable is $x \equiv v$. The Fourier-series expansion of the control variable v provides

$$v(t) = \sum_{k=-NH}^{NH} V_k e^{j\omega_k t} \tag{2.25}$$

with NH being the number of harmonic components that are taken into account for the analysis. In the case of a free-running oscillation, $\omega_k \equiv k\omega_o$, with ω_o the fundamental frequency. The harmonic-balance equations are given by

$$H_k = [A_v(\omega_k)]V_k - [A_i(\omega_k)]I_k - [A_g(\omega_k)]G_k = 0 \tag{2.26}$$

with $-NH \leq k \leq NH$

In (2.26), the matrixes $[A_v(\omega_k)]$ and $[A_i(\omega_k)]$ are obtained from the application of Kirchoff's laws to the circuit of Figure 1.2. For generality, the generator vector \bar{G} contains two generators: the input generator E_g and the auxiliary generator E_p at their operating frequencies. The former is included here to allow the later application of the formulation to the analysis of the synchronized oscillator at the fundamental frequency. Thus, both E_g and E_p are considered to operate at ω_1 , although, of course, for the free-running oscillation analysis $E_g = 0$.

With the above considerations, the order of linear matrixes is $(2NH + 1) \times (2NH + 1)$ for $[A_v]$ and $(2NH + 1) \times (2NH + 1)$ for $[A_i]$ because there is only one linear element, and $(2NH + 1) \times (2NH + 1)2$ because there are two independent generators. Applying Kirchoff's laws, it is clearly seen that the matrix $[A_v]$ agrees with the identity matrix. The matrix $[A_i]$ is given by

$$\begin{aligned}
 A_i(\omega_1) &= \frac{-j\omega_1 L}{1 - LC\omega_1^2} \text{ for } k=1 \\
 A_i(\omega_k) &= \left[-\frac{R + jL\omega_k}{1 - LC\omega_k^2 + jRC\omega_k} \right] \text{ for } 0 \leq k \leq NH \text{ and } k \neq 1 \quad (2.27) \\
 A_i(\omega_{-k}) &= A_i^*(\omega_k)
 \end{aligned}$$

To obtain the general harmonic-balance equation $\bar{H}_b = 0$ (2.15), the 1×1 submatrixes (2.27) must be introduced in a general $[A_i]$ matrix, containing all the harmonic terms, of the form (2.16). The vector \bar{G} is organized as follows:

$$\bar{G}^T = \begin{bmatrix} G^T(-NH) \\ \vdots \\ G^T(0) \\ \vdots \\ G^T(NH) \end{bmatrix} \text{ with } G^T(k) = \begin{bmatrix} E_g(k) \\ E_p(k) \end{bmatrix} \quad (2.28)$$

Then, the submatrixes $[A_g(\omega_k)]$ are given by

$$\begin{aligned}
 A_g(\omega_1) &= \left[\frac{1}{1 - LC\omega_1^2 + jRC\omega_1}, \frac{1}{1 - LC\omega_1^2} \right]^t \text{ for } k=1 \\
 A_g(\omega_k) &= \left[\frac{1}{1 - LC\omega_k^2 + jRC\omega_k}, 0 \right]^t \text{ for } 0 \leq k \leq NH \text{ and } k \neq 1 \quad (2.29) \\
 A_g(\omega_{-k}) &= A_g^*(\omega_k) \quad \forall k
 \end{aligned}$$

The 2×1 submatrixes (2.29) must be introduced in a general $[A_g]$ matrix, containing all the harmonic terms, of the form (2.16). Note that because of the ideal filter F_g in series with E_p , this auxiliary generator only has influence over the circuit at the fundamental frequency $\omega_p = \omega_1 \equiv \omega_o$. Thus, the expression for $[A_g(\omega_1)]$ is different from $[A_g(\omega_k)]$ with $k \neq 1$.

Equations (2.27) and (2.28) provide the matrixes to introduce in the harmonic-balance equation (2.26). Thus, the equation $\bar{H}_b = 0$ is already formulated. The admittance equation $\bar{H}_p = 0$ is given by

$$\bar{H}_p \equiv \begin{bmatrix} \operatorname{Re} Y_p \\ \operatorname{Im} Y_p \end{bmatrix} = 0 \quad (2.30)$$

$$\text{with } Y_p = \frac{\bar{I}_p(\omega_1)}{E_p(\omega_1)}$$

with \bar{I}_p indicating the phasor of the current through the voltage generator E_p . Note that this current-voltage relationship is calculated at the harmonic component at which the generator E_p operates, in this case, at the fundamental frequency $\omega_p \equiv \omega_1$. The current \bar{I}_p can be obtained from the application of Kirchoff's laws at the frequency . In this case, it is given by

$$I_p(\omega_1) = [B_i(\omega_1)]I_{nl1} + [B_g(\omega_1)]\bar{G}_1 \quad (2.31)$$

with the matrixes

$$[B_i(\omega_1)] = \left[-1 - \frac{LC\omega_1^2}{1 - LC\omega_1^2} \right]$$

$$[B_g(\omega_1)] = \left[\frac{1}{R} \quad -\frac{1}{R} - \frac{1}{j\left(L\omega_1 - \frac{1}{C\omega_1}\right)} \right] \quad (2.32)$$

Equations (2.26) and (2.30) compose the system to be solved through a Newton-Raphson algorithm.

To provide the auxiliary generator E_p with a suitable starting value, it might be useful to employ an initial double sweep in the frequency and amplitude of this generator. For a small-signal amplitude of the auxiliary generator $|E_{ps}|$, the real part of the admittance observed by this generator must be negative in a certain frequency band about the oscillation frequency. A good estimation of this oscillation frequency is the value at which the imaginary part of this small-signal admittance is equal to zero. Thus, the initial frequency sweep is stopped when $\operatorname{Im}\{-Y_p(|E_{ps}|, \omega_p^o)\} = 0$. From this point, the generator amplitude is swept, until a zero value of the real part of the admittance is obtained: $\operatorname{Re}\{-Y_p(|E_{ps}|, \omega_p^o)\} = 0$. Thus, the starting values of the auxiliary generator for the Newton-Raphson algorithm will be $|E^o|, \omega_p^o$. The variations along this process of the circuit input admittance from the auxiliary generator

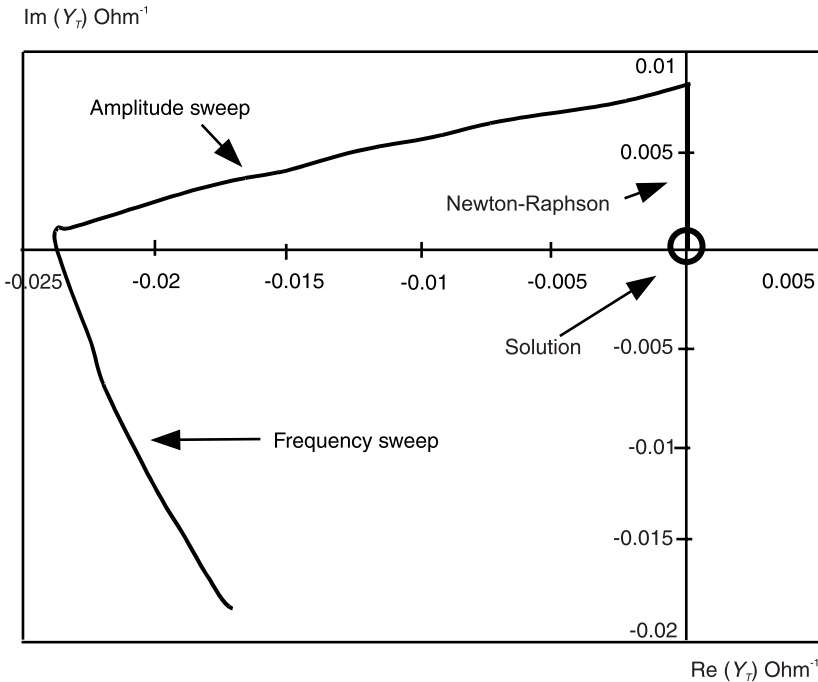


Figure 2.8 Convergence process of a free-running oscillator using an auxiliary generator.

terminals, $Y_T = -Y_p$, are represented in a polar diagram in Figure 2.8. Proceeding in this way, the following spectrum is obtained for the independent voltage $v(t)$:

$$\omega_o = 1.6 \text{ MHz}$$

$$1^\circ \text{ arm} - V_1 = 1.00 \angle 0.0$$

$$3^\circ \text{ arm} - V_3 = 0.11 E-2 \angle 10.0$$

$$5^\circ \text{ arm} - V_5 = 0.07 E-3 \angle 59.3$$

This solution point is the point marked FO in the curves of Figure 2.5. Note that the cubic nonlinearity, in the absence of dc generators, does not generate harmonic components of even order.

2.3.2 Analysis of Synchronized Circuits

Another kind of behavior that may be difficult to simulate through harmonic balance is the synchronized regime [31–33, 41–43]. To study this regime, the connection of an external generator to a free-running oscillator is considered (see Section 1.6). As was pointed out in Chapter 1, for some frequency values of this generator, relatively close to the self-oscillation frequency ω_o or any of its harmonic components $k\omega_o$, synchronization may occur (see Example 2.2). Then only one fundamental is observed in the circuit, unlike the case of self-oscillating mixers (see Section 1.3). Two main cases are possible: subharmonic synchronization for an integer rotation number

$$r = \frac{\omega_o}{\omega_g} = k \quad (2.33)$$

and frequency division [48] for a fractional rotation number

$$r = \frac{\omega_o}{\omega_g} = \frac{1}{k} \quad (2.34)$$

In case of subharmonic synchronization, the oscillation frequency ω_o becomes $\omega_o = k\omega_g$. In case of frequency division, the oscillation frequency ω_o becomes the subharmonic $\frac{\omega_g}{k}$.

For $k = 1$, the circuit behaves as a synchronized oscillator. However, as has already been shown in Example 2.2, for some input-generator values, the synchronized solution at the generator frequency ω_g may coexist with an unstable periodic solution with the same fundamental frequency ω_g (see Figure 2.5). It is a trivial solution to be avoided in the convergence process. For a frequency divider with $r = \frac{1}{k}$, the synchronized solution always coexists with a mathematical solution with no frequency division at all. In this trivial solution forced by the input generators, the subharmonic components are not taken into account. The same kind of problem is encountered in the analysis of subharmonically synchronized oscillators for which $r = k$. Again, in the trivial solution provided by default by the harmonic-balance simulator, the self-oscillation is not taken into account and the frequency component at $k\omega_g$ is just a harmonic component of the input-generator frequency.

As has been seen, in a synchronized regime the oscillation frequency becomes a submultiple (frequency dividers) or a multiple (subharmonically synchronized oscillators) of the input-generator frequency. This oscillation frequency is the frequency at which the auxiliary generator must operate. For brevity, only the case of frequency dividers will be considered here, so the auxiliary generator frequency will be $\omega_p = \frac{\omega_g}{k}$. Note that the extension to subharmonic synchronization is straightforward, replacing the former expression with $\omega_p = k\omega_g$.

When analyzing synchronized regimes, the phase of the auxiliary generator is an essential variable, unlike the case of autonomous regimes. Actually, in a synchronized solution, there is a constant-phase shift between the input generator and the self-oscillation (see Figure 1.28). Thus, the two unknowns concerning the auxiliary generator are now the generator amplitude $|P|$ and the generator phase ϕ_p . The auxiliary-generator frequency, given by $\omega_p = \frac{\omega_g}{k}$, is not unknown. In the case of a frequency divider, the harmonic-balance equations are

$$\omega_p = \frac{\omega_g}{k} \rightarrow \begin{cases} \bar{H}_p(\bar{X}, |P|, \phi_p) = 0 \\ \bar{H}_b(\bar{X}, |P|, \phi_p) = 0 \end{cases} \quad (2.35)$$

It is again a system of $Q(2NH + 1) + 2$ equations in $Q(2NH + 1) + 2$ unknowns. Example 2.4 analyzes the cubic nonlinearity oscillator operating as a synchronized oscillator at the first harmonic component $k=1$.

Example 2.4: Use of an auxiliary generator to analyze the synchronized regime of the cubic nonlinearity oscillator

This example illustrates how an auxiliary generator can help obtain the synchronized solution at $k=1$ of the cubic nonlinearity oscillator of Figure 1.2. As in Example 2.3, the voltage auxiliary generator of Figure 2.7(a) is chosen for the calculation. Unlike the case of Example 2.3, in which the free-running oscillation was analyzed, the amplitude of the input generator E_g must be different from zero. Here the harmonic-balance system is solved for the harmonic-balance variables \bar{X} and the auxiliary generator variables $|E_{ps}|$ and ϕ_p (see 2.38). The same formulation (2.27) and (2.29) for the linear matrices of

the harmonic-balance equation $\overline{H}_b = 0$ is used here. In the same way, the expression for $\overline{H}_p = 0$ is given by (2.31) and (2.32).

In this example, the generator values $E_g = 0.02v$ and $\omega_g = 1.59$ MHz are initially considered. Without the use of the auxiliary generator, the harmonic values of the independent voltage are given by

$$1^\circ \text{ arm—} V_1 = 0.26 \angle 114.1$$

$$3^\circ \text{ arm—} V_3 = 0.16E-3 \angle 62.1$$

$$5^\circ \text{ arm—} V_5 = 0.16E-6 \angle 14.2$$

This low-amplitude solution is called S_1 in Figure 2.5. In this figure, a geometric average of the harmonic components of the independent voltage is used as a representative variable in the vertical axis V_{eff} . Introducing the auxiliary generator, the harmonic values change to

$$1^\circ \text{ arm—} V_1 = 1.19 \angle -70.4$$

$$3^\circ \text{ arm—} V_3 = 0.16E-2 \angle -27.0$$

$$5^\circ \text{ arm—} V_5 = 0.37E-3 \angle 179.3$$

obtaining the solution S_2 of Figure 2.5.

For relatively low input-generator amplitude, the synchronization curves are closed ($E_g = 0.01v$ and $E_g = 0.03v$ in Figure 2.5). For higher input amplitudes, the synchronization curves open up, still exhibiting turning points for intermediate values of the input-generator amplitude. At each turning point, the curve folds, giving rise to multivalued solutions ($E_g = 0.04v$ to $0.06v$ in Figure 2.5). Turning points (and, thus, multivalued solutions) are very common not only in synchronized oscillators, but also in many other nonlinear circuits (e.g., VCOs). The ability to pass through turning points at the time to trace the solution curve is essential to obtaining multivalued solution curves. However, passing through these points is impossible through a simple parameter sweep. It is necessary to employ special continuation techniques, which will be discussed in Section 2.5.

2.3.3 Analysis of Self-Oscillating Mixers

Like the free-running oscillator, the self-oscillating mixer is an example of circuit with an autonomous frequency [36, 48–50]. In a self-oscillating mixer, there are two fundamental frequencies: one is provided by an external generator, ω_g , and the other is a self-oscillation frequency ω_o . The input generator influences the oscillation frequency ω_o , and its value is not the same as in free-

running oscillation [48, 50]. The frequency ω_o is an unknown of the equation system.

When using harmonic balance, special strategies are needed to avoid convergence toward the forced periodic solution (with ω_g as only fundamental). In a similar way to the case of free-running oscillators, an auxiliary generator is introduced at the autonomous frequency $\omega_p = \omega_o$. As in the case of free-running oscillators, there is no phase relationship between the Fourier components at the self-oscillation frequency ω_p and the input generator at ω_g , so the phase of the auxiliary generator, can take any value. For simplicity, it will arbitrarily be fixed at zero. The harmonic-balance system, composed of $\overline{H}_b = 0$ and $\overline{H}_p(\overline{X}, |P|, \omega_p) = 0$, is solved in similar way as the solution presented Section 2.3.1, now using a two-fundamental Fourier-series expansion for the circuit variables, in the frequencies ω_g and ω_o . Example 2.5 shows the application of the technique to the cubic nonlinearity oscillator of Figure 1.2, operating as a self-oscillating mixer.

Example 2.5: Use of an auxiliary generator to analyze the self-oscillating mixer regime of the cubic nonlinearity oscillator with an external generator

The circuit of Figure 1.2 is now going to be analyzed in the two-fundamental regime that is obtained for $E_g = 0.13v$ and $f_g = 1.74$ MHz (see Figures 1.9 and 1.10). Because there are two fundamental frequencies, the variables of the circuit will be expanded in a two-fundamental Fourier series. In the case of the control voltage $v(t)$, the expansion is as follows:

$$v(t) = \sum_{k,l} V_{k,l} e^{j(k\omega_g + l\omega_o)t} \quad (2.36)$$

For a nonlinearity order $nl=7$, the number of positive frequencies will be $NH = nl(nl+1) = 56$. However, there are other possibilities. One could use a different maximum index for each frequency, letting the $|k|$ vary up to the maximum value 3 and $|l|$ up to the maximum value 7, for instance. The choice of even orders would, in this case, be useless because in the absence of dc bias, the cubic nonlinearity does not generate even harmonic components.

In the harmonic-balance simulation, the trivial periodic solution at the input generator frequency ω_g must be avoided. An auxiliary generator E_p will be introduced, as indicated in Figure 2.7(a). The spectral components k,l of the generator vector \overline{G} , referring to the frequencies $k\omega_g + l\omega_o$, are given by:

$$G_{1,0} = \begin{bmatrix} E_g \\ 0 \end{bmatrix}; G_{0,1} = \begin{bmatrix} 0 \\ E_p \end{bmatrix}; G_{k,l} = \begin{bmatrix} 0 \\ 0 \end{bmatrix}; \quad (2.37)$$

for $(k, l) \neq (1,0)$ or $(0,1)$

and the expression of the matrix $[A_g]$, given in (2.29), must change accordingly:

$$A_g(0,1) = \left[0, \frac{1}{1 - LC\omega_o^2} \right] \text{ for } k, l = 0,1 \quad (2.38)$$

$$A_g(k,l) = \left[\frac{1}{1 - LC\omega_{k,l}^2 + jRC\omega_{k,l}}, 0 \right] \text{ for } k, l \neq 0,1$$

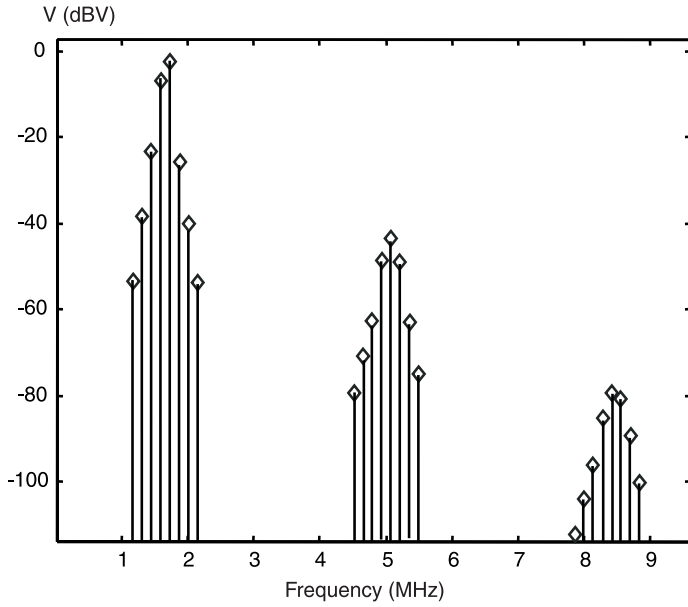
The expressions (2.27) for A_i are still valid, replacing $k = 1$ with $k, l = 0,1$.

The current through the generator is calculated with the same equations (2.31) and (2.32) by making zero the term affecting the input generator. In addition to the $2NH + 1$ Fourier components of the independent voltage \bar{V} , the auxiliary generator amplitude and frequency must be solved through the equations $\bar{H}_b = 0$ and $\bar{H}_p(X, |P|, \omega_p) = 0$.

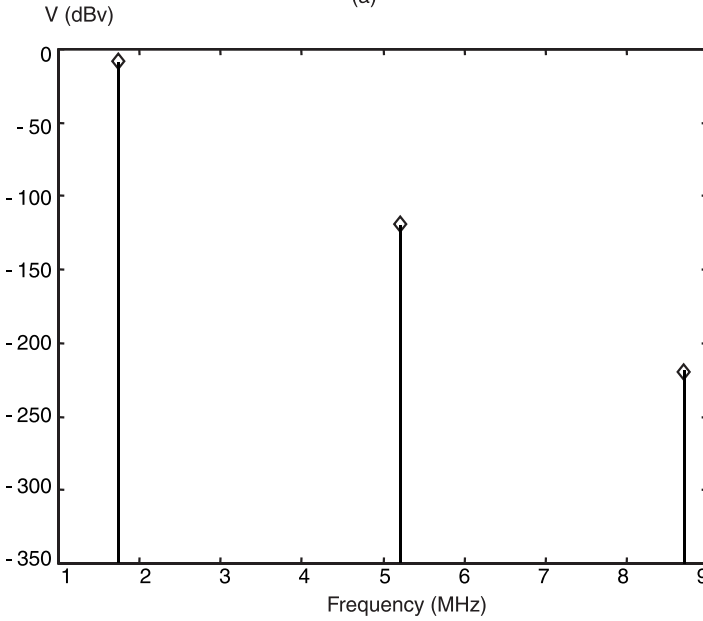
For the input-generator amplitude $E_g = 0.13v$ and frequency $f_g = 1.74$ MHz, the spectrum of Figure 2.9(a) is obtained. There is a small shift in the self-oscillation frequency due to the influence of the external generator. Note that without the use of the auxiliary generator, the harmonic balance converges to a trivial mathematical solution having ω_g as only fundamental [Figure 2.9(b)].

2.4 Envelope Transient

Circuits with modulated signals or with multiple time scales cannot be stimulated through standard harmonic balance [25]. Obviously, the modulated signals cannot be represented in a Fourier series of the form (2.11). On the other hand, the application of harmonic balance to circuits with multiple time scales, like a mixer with two high-frequency fundamentals, f_1 and f_2 , and a very small intermediate frequency $f_{IF} = |f_1 - f_2|$ may be inefficient or even inaccurate because of the closeness of the fundamentals. To overcome these problems, time-frequency techniques have been developed [25–29]. In these techniques, two different time rates, t_1 and t_2 , are used in the sampling of the variables. Assuming periodicity in the faster time t_2 , the circuit variables can be expanded in a harmonic series of the form



(a)



(b)

Figure 2.9 Spectrum of the cubic nonlinearity oscillator for $E_g = 0.13v$ and $f_g = 1.74$ MHz: (a) when using an auxiliary generator at the autonomous frequency ω_0 , and (b) without the auxiliary generator.

$$\bar{x}(t_1, t_2) = \sum_{k=-NH}^{NH} \bar{X}_k(t_1) e^{jk\omega_o t_2} \quad (2.39)$$

where ω_o is the high-frequency carrier and $\bar{X}_k(t_1)$ are the slow varying envelopes. Of course, because the two time scales are fictitious, the circuit variables $\bar{x}(t_1, t_2)$ will only agree with $\bar{x}(t)$ for $t_1 = t_2$. Formulating the circuit through a modified nodal equation [27–29] and using the expression (2.39) for the circuit variables, the original system of nonlinear ordinary differential algebraic equations becomes a system of partial differential equations. This is due to the existence of two time variables, t_1 and t_2 . Two different derivative operators are required with respect to the two time variables, t_1 and t_2 . For fixed t_1 , the derivative with respect to t_2 will simply be given by the multiplication of the harmonic terms by the $jk\omega_o$. This provides an algebraic system of differential equations in the harmonic terms $\bar{X}_k(t_1)$ to be sampled (in the numerical integration) at a lower rate Δt_1 than the original system. This allows an efficient simulation of complex regimes at low computational cost.

In the transient-envelope technique [26], the general harmonic-balance system is reformulated using the representation (2.39) for the circuit variables. It is possible to write

$$\begin{aligned} [A_x(jk\omega_o + j\omega)]\bar{X}(t_1) + [A_y(jk\omega_o + j\omega)]\bar{Y}(t_1) \\ + [A_g(jk\omega_o + j\omega)]\bar{G}(t_1) = 0 \end{aligned} \quad (2.40)$$

where ω is the frequency associated with the time variations in t_1 . Assuming slow variations of the harmonic components, the linear matrixes can be expanded in a Taylor series about $\omega = 0$. For $\omega \ll \omega_o$, a first-order expansion will be sufficient:

$$\begin{aligned} [A_x(jk\omega_o)]\bar{X}(t_1) + \left[\frac{\partial A_x}{\partial jk\omega_o} \right] j\omega \bar{X}(t_1) + [A_y(jk\omega_o)]\bar{Y}(t_1) \\ + \left[\frac{\partial A_y}{\partial jk\omega_o} \right] j\omega \bar{Y}(t_1) + [A_g(jk\omega_o)]\bar{G}(t_1) + \left[\frac{\partial A_g}{\partial jk\omega_o} \right] j\omega \bar{G}(t_1) = 0 \end{aligned} \quad (2.41)$$

The multiplication by $j\omega$ in (2.41) is equivalent to a time derivation in t_1 , so the former expression can be rewritten as follows:

$$\begin{aligned}
& [A_x(jk\omega_o)]\bar{X}(t_1) + \left[\frac{\partial A_x}{\partial jk\omega_o} \right] \frac{d\bar{X}(t_1)}{dt_1} + [A_y(jk\omega_o)]\bar{Y}(t_1) \\
& + \left[\frac{\partial A_y}{\partial jk\omega_o} \right] \frac{d\bar{Y}(t_1)}{dt_1} + [A_g(jk\omega_o)]\bar{G}(t_1) + \left[\frac{\partial A_g}{\partial jk\omega_o} \right] \frac{d\bar{G}(t_1)}{dt_1} = 0
\end{aligned} \tag{2.42}$$

The above equation constitutes a differential algebraic equation in the harmonic coefficients of $\bar{X}(t_1)$ that can be solved through standard integration techniques. A harmonic-balance analysis can also be carried out for each time t_1 of the envelope. Due to the development of the linear matrixes in a first order Taylor series, it will only be valid for slowly varying $\bar{X}(t_1)$, $\bar{Y}(t_1)$, $\bar{G}(t_1)$ (i.e., for narrowband harmonic components). Formulations of the envelope transient without this constraint are possible, using the modified nodal approach [27].

Example 2.6 shows the analysis, through the transient-envelope technique, of the free-running-oscillation regime of the cubic nonlinearity oscillator circuit.

Example 2.6: Envelope-transient analysis of the cubic nonlinearity oscillator

Here the envelope-transient technique is used to simulate the cubic nonlinearity oscillator of Example 1.1 and Examples 2.2 to 2.5. In this example, no input generator E_g is considered, so the circuit operates as a free-running oscillator. No auxiliary generators are used either. However, a perturbation is required to start the transient leading to limit cycle. This perturbation is an impulse generator, only having a value different from zero at the initial simulation time $t_o = 0$.

The analysis requires an initial estimation f'_o of the free-running oscillation frequency. As an example, the value $f'_o = 149$ GHz is taken here. The harmonic expansion of the independent voltage $v(t)$ will have the form

$$v(t_1, t_2) = \sum_{k=-NH}^{NH} V_k(t_1) e^{jk\omega'_o t_2} \tag{2.43}$$

and, in the periodic steady state, the following relationship must be fulfilled:

$$V_k(t_1) = V_k^o e^{jk(\omega_o - \omega'_o)t_1} \tag{2.44}$$

with V_k^o being the constant harmonic components of $v(t)$ and ω_o , the actual oscillation frequency.

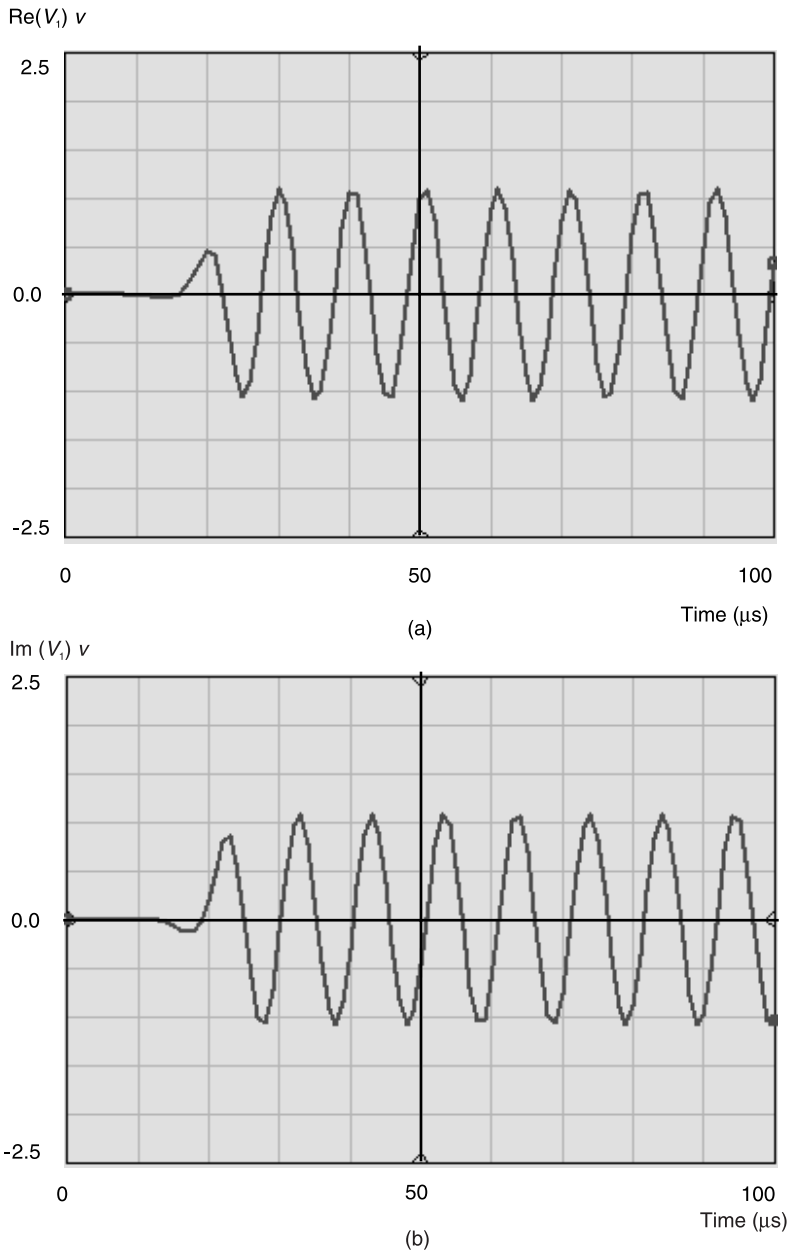


Figure 2.10 Time variations of the real and imaginary parts of the first harmonic $V_1(t)$ of the independent voltage $v(t)$ in the cubic nonlinearity oscillator. In the harmonic expansions, the fundamental frequency $f_0 = 149$ GHz has been used: (a) real part, and (b) imaginary part.

The sampling rate of the harmonic components $V_k(t_1)$ is determined by the frequency error $f_o - f'_o$, resulting, of course, in a much lower value than that required for a standard time-domain integration. The difficulty of the method comes from this a priori selection of the integration step Δt_1 . A wrong choice may lead to convergence problems, especially in the case of autonomous circuits. For this kind of circuits, the transient-envelope method has been combined in some recent works [31] with the use of auxiliary generators. The amplitude and frequency of the generator are functions of the slow time variable t_1 during the oscillation transient.

The result of the simulation is shown in Figure 2.10, where the real and imaginary parts of $V_1(t)$ have been represented. There is well-distinguished transient, after which the harmonic component $V_1(t)$ reaches its steady-state behavior. When this happens, the amplitude of $V_1(t)$ takes the constant value $\text{abs}(V_1(t)) = 1.008v$, in perfect agreement with the previous harmonic-balance results. However, in spite of having reached the steady state, the variables $\text{Re}(V_1(t))$ and $\text{Im} \text{Re}(V_1(t))$ keep varying in time. It is, in fact, as shown in (2.44), a low-frequency oscillation, at the frequency difference between the actual oscillation frequency f_o and the frequency f'_o used for the harmonic expansions. The oscillation is due to the fact that the transient-envelope software employed here does not update the value f'_o . Instead, the frequency f'_o remains at the initial value provided by the user.

2.5 Continuation Technique for Tracing Solution Curves Versus a Circuit Parameter

Due to its convergence to the circuit steady state, avoiding the transient, and the ability of convergence to both stable and unstable solutions, the harmonic balance is very well suited for determining the evolution of the steady-state solution of a given circuit versus any parameter η . Such a parameter may be, for instance, the bias voltage of the varactor diode in a VCO, or the input-generator amplitude or frequency in a synchronized circuit (as in Figure 2.5). For this purpose, a continuation technique must be applied, like that in Section 2.2.3. However, the possibility of multivalued solutions due to turning points must be taken into account.

To obtain the evolution of the circuit independent variables versus the parameter $\bar{X}(\eta)$, the parameter η is incremented in steps $\Delta\eta$. Different solution points \bar{X}_n are obtained for the different parameter values η_n , which gives rise to a curve when a representative circuit variable, such as a harmonic component of a given state variable X_k^j or the output power P_{out} is represented versus the parameter η . This curve will be called the solution curve here. The curves in

Figure 2.5 are examples of solution curves. They have been traced through a continuation technique in two stages: prediction and correction, with parameter switching [46], which will be described in the following.

To obtain the evolution of the circuit solution versus the parameter $\bar{X}(\eta)$, the parameter is initially incremented in steps $\Delta\eta = h$. The first point of the curve (η_1, \bar{X}_1) can be obtained through application of the technique outlined in Section 2.2.3 or through the use of an auxiliary generator (see Section 2.4). In general, once a solution point $(\eta_{n-1}, \bar{X}_{n-1})$ has been determined, the next one (η_n, \bar{X}_n) is estimated through the linearization of the harmonic-balance system about the previous point $(\eta_{n-1}, \bar{X}_{n-1})$. This estimated point will be called $(\eta_{np}, \bar{X}_{np})$ here. The linearization of the harmonic-balance system is obtained by differentiating the error function \bar{H} :

$$\Delta\bar{H} = [JH]_{n-1} (\bar{X}_{np} - \bar{X}_{n-1}) + \left. \frac{\partial\bar{H}}{\partial\eta} \right|_{n-1} (\eta_n - \eta_{n-1}) = 0 \rightarrow \tag{2.45}$$

$$\bar{X}_{np} = \bar{X}_{n-1} - [JH]_{n-1}^{-1} \left. \frac{\partial\bar{H}}{\partial\eta} \right|_{n-1} (\eta_n - \eta_{n-1})$$

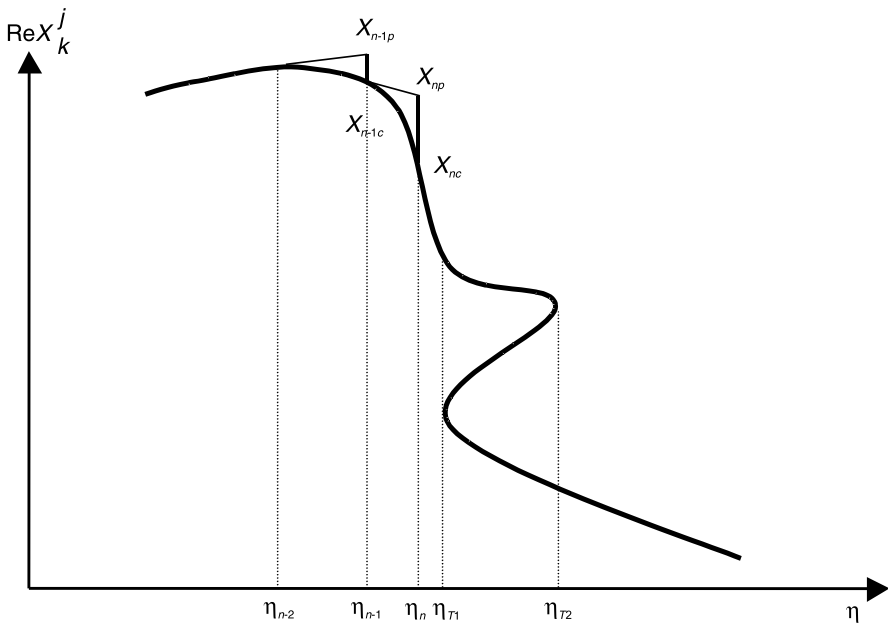


Figure 2.11 Graphical representation of the prediction-correction algorithm.

The Jacobian matrix $[JH]_{n-1}$ and the derivative of \bar{H} with respect to the parameter are evaluated at the preceding solution point $n-1$. The predicted point $(\eta_{np}, \bar{X}_{np})$ is not the actual solution point because the actual system $\bar{H}(\bar{X}, \eta) = 0$, unlike (2.45), is nonlinear. The point obtained from (2.45) is a linear estimation (Figure 2.11) of the solution for η_n . Thus, the calculation (2.45) constitutes the prediction stage of the continuation algorithm.

At the correction stage of the continuation technique, the Newton-Raphson algorithm is applied for the correction of the estimated point n , which is done for constant parameter value $\eta = \eta_{np}$. The input of this algorithm is the estimation $(\eta_{np}, \bar{X}_{np})$, which is used as the starting point: $\bar{X}_n^o \equiv \bar{X}_{np}$. Unlike \bar{X}_{np} , the point resulting from the Newton-Raphson convergence $X_n = X_n^c$ is an actual solution point and the represented variable (X_k^j or P_{out}) belongs to the solution curve (Figure 2.11).

However, problems may arise if the Jacobian matrix $[JH]$ becomes singular at a particular parameter value η_T or approaches a singularity (η approaches η_T). If this happens, the Newton-Raphson will fail to converge. But what is the meaning of this singularity? It means that the slope of the solution curves (in terms of the components of \bar{X}) tends to infinite at η_T (i.e., η_T is a turning point of the curve). This is easily understood from (2.45):

$$\left. \frac{\partial \bar{X}}{\partial \eta} \right|_{n-1} = \frac{\bar{X}_{np} - \bar{X}_{n-1}}{\eta_n - \eta_{n-1}} = -[JH]_{n-1}^{-1} \left. \frac{\partial \bar{H}}{\partial \eta} \right|_{n-1} \rightarrow \infty \quad (2.46)$$

This indicates that the solution curve folds over itself and, as a result, has a multivalued interval, like the interval η_{T1}, η_{T2} in Figure 2.11. Remember that turning points had already been obtained in the solution curves of Figure 2.5. The big implications of turning points on the circuit dynamics will be analyzed in detail in Chapter 4.

The continuation algorithm fails in the neighborhood of turning points because of the small value of the determinant of the Jacobian matrix. To cope with this problem, a parameter-switching algorithm [46] can be employed. In this algorithm, the continuation parameter is, at sections of the curve, different from the actual circuit parameter η . In fact, at each prediction stage $(\eta_{np}, \bar{X}_{np})$, the predicted increments of the different variables (including the parameter η)

$$\left| \operatorname{Re} \Delta X_{0n}^1 \right|, \left| \operatorname{Im} \Delta X_{0n}^1 \right|, \dots, \left| \operatorname{Re} \Delta X_{NHn}^Q \right|, \left| \operatorname{Im} \Delta X_{NHn}^Q \right|, \left| \Delta \eta_n \right|$$

are compared, taking the variable with the biggest increment as a new analysis parameter. If the new parameter is, for instance, $\text{Re } X_k^j$, the increment h is assigned to this variable:

$$\text{Re } \Delta X_{kn}^{j \text{ new}} = \text{sign}(\text{Re } \Delta X_{kn}^j) h \quad (2.47)$$

where $\text{Re } \Delta X_{kn}^{j \text{ new}}$ indicates the new increment of the variable $\text{Re } X_k^j$. Note that the sign of the increment (positive or negative) of $\text{Re } \Delta X_{kn}^j$ is respected in the above assignment. Now $\text{Re } \Delta X_{kn}^{j \text{ new}}$ is not considered unknown. Instead, the parameter increment $\Delta \eta_n$ is an unknown of the problem to be determined in the resolution process. Note that taking the variable with the biggest increment as a parameter prevents any unbounded growth of the circuit variables. Through this technique, points of infinite slope (turning points) become points of zero slope. In this particular example, this is written as follows:

$$\begin{bmatrix} \bar{X}_{np} \\ \eta_{np} \end{bmatrix} = \begin{bmatrix} \bar{X}'_{n-1} \\ \eta_{n-1} \end{bmatrix} - \left[JH' \frac{\partial \bar{H}}{\partial \eta} \right]_{n-1}^{-1} \left. \frac{\partial \bar{H}}{\partial \text{Re } X_k^j} \right|_{n-1} \text{sign}(\text{Re } \Delta X_{kn}^j) h \quad (2.48)$$

where \bar{X}'_{np} is the state-variable vector in which $\text{Re } X_k^j$ is missing and $[JH']$ is the harmonic-balance Jacobian matrix in which the column of derivatives with respect to $\text{Re } X_k^j$ is missing. Note that in (2.48), because of the replacement of $[JH]$ by $\left[JH' \frac{\partial H}{\partial \eta} \right]$, the singularity problem has been eliminated. The predicted point is corrected through Newton-Raphson.

When applying this continuation technique to autonomous or synchronized circuits, the use of the auxiliary generator (as shown in Section 2.3) is only necessary for the first point of the solution curve (η_1, \bar{X}_1) . Because the convergence process for (η_2, \bar{X}_2) uses (η_1, \bar{X}_1) as a starting point, there is no longer a risk of convergence to trivial solutions, so the connection of the auxiliary generator may be eliminated. This will enable a faster simulation due to the reduction in the number of unknowns.

2.6 Analysis of Autonomous and Synchronized Circuits in Closed Harmonic-Balance Programs

The formerly presented analysis techniques for autonomous and synchronized regimes and for the tracing of solution curves versus a circuit parameter are intended for in-house software. This means that the user must have unrestricted access to the harmonic-balance algorithm. However, many microwave designers use closed harmonic-balance software. This enables very accurate descriptions of the circuit (due to the availability of specific libraries, for distributed elements, for instance) and an easy introduction of complex topologies, containing many passive and active devices.

The advantage of the analysis techniques for autonomous and synchronized regimes, presented in Sections 2.3 and 2.5, is that they can be implemented on closed harmonic-balance software. Their application to this kind of software relies on the use of auxiliary generators (in a similar way to that presented Sections 2.3 and 2.4) and requires the availability of optimization tools. Now the auxiliary generators are introduced in an external manner through their inclusion in the circuit schematic. These generators cope with the harmonic-balance difficulties with autonomous and synchronized regimes and enable great analysis flexibility, which, in most cases, goes beyond the original simulation options of the software.

Three main techniques will be presented here. The first consists of the tracing of immittance diagrams to estimate the steady-state solution of autonomous and synchronized circuits. The second consists of the employment of nonlinear optimization tools to correct graphical estimations. The third is a new continuation technique, exclusively based on the use of the auxiliary generator and software optimization tools.

2.6.1 Autonomous Circuits

2.6.1.1 Immittance Diagrams

The auxiliary generators, used in Section 2.3, can also be employed in commercial harmonic-balance software. As an example, let the parallel connection of an auxiliary generator of voltage type at a given circuit node m be considered (Figure 2.12). Suitable locations for the auxiliary generators are the nonlinear device terminals to which feedback branches are connected. The ideal filter F_z is a short circuit at the auxiliary generator frequency ω_{AG} and an open circuit at frequencies different from ω_{AG} . The ratio between the phasor \bar{I}_{AG} of the first-harmonic of the current, entering the circuit node, and the generator voltage

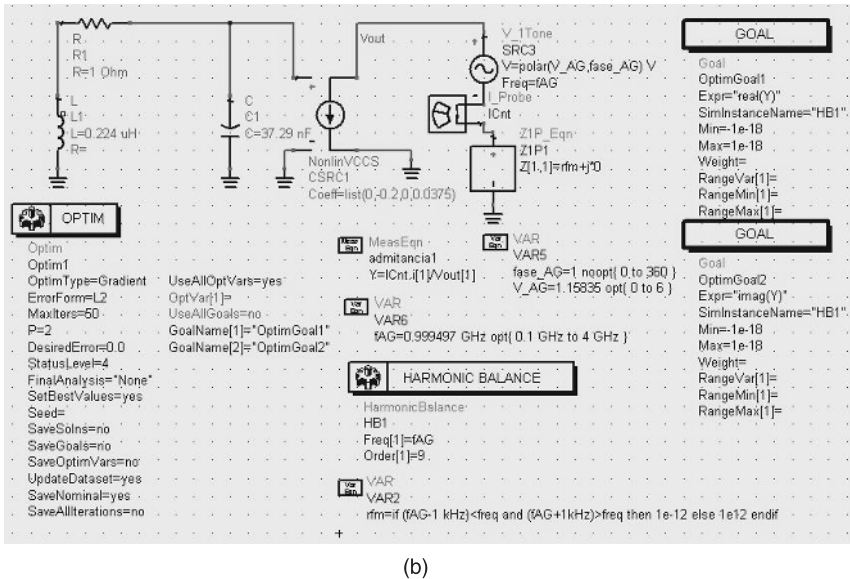
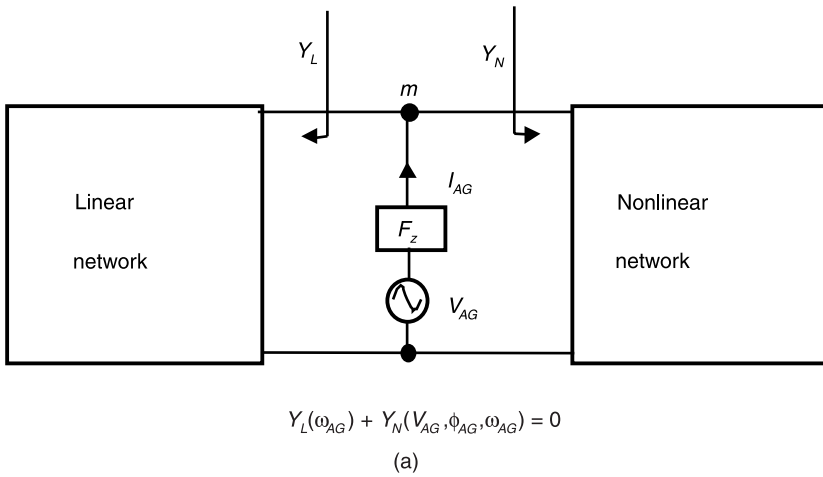


Figure 2.12 Auxiliary generator for tracing the admittance diagrams. (a) Introduction of an auxiliary generator in an oscillator circuit. F_z is an ideal filter. (b) Implementation of the auxiliary generator on the commercial harmonic-balance software HP-ADS.

V_{AG} agrees with the total admittance function $Y_T(V_{AG}, \phi_{AG}, \omega_{AG})$ at the particular node m . From Figure 2.12, this can be equated as follows:

$$Y_T(V_{AG}, \phi_{AG}, \omega_{AG}) = \frac{\bar{I}_{AG}}{V_{AG} e^{j\phi_{AG}}} = Y_L(\omega_{AG}) + Y_N(V_{AG}, \phi_{AG}, \omega_{AG}) \quad (2.49)$$

An impedance-function analysis $Z_T(I_{AG}, \phi_{AG}, \omega_{AG})$, using a current-auxiliary generator connected in series at a circuit branch, would equally be possible. For the analysis of an autonomous oscillation, the phase of the auxiliary generator can be arbitrarily fixed $\phi_{AG} = 0$.

For a small-signal auxiliary generator $V_{AG} = \varepsilon$, (2.49) enables the evaluation of the oscillation startup conditions $\text{Re} Y_T < 0$, $\text{Im} Y_T = 0$. On the other hand, the admittance function $Y_T(V_{AG}, \omega_{AG})$ will be zero when the auxiliary-generator frequency and amplitude respectively agree with the self-oscillation frequency $\omega_{AG} \equiv \omega_o$ and first-harmonic amplitude $V_{AG} \equiv V_o$.

Figure 2.12(b) shows how a voltage auxiliary generator would be introduced in the commercial harmonic-balance software HP-ADS for the analysis of the cubic nonlinearity oscillator of Figure 1.2. The voltage generator is a one-tone harmonic-balance generator with its amplitude, phase, and frequency given by the symbolic variables V_AG , $phase_AG$, and f_AG , respectively. The filter F_z of Figure 2.12(a) is implemented through the ideal impedance $Z[1,1]$, whose value, $Z[1,1] = rfm + j0$, depends on the harmonic frequency $freq$ and is specified by a conditional sentence. Note the calculation of the current-to-

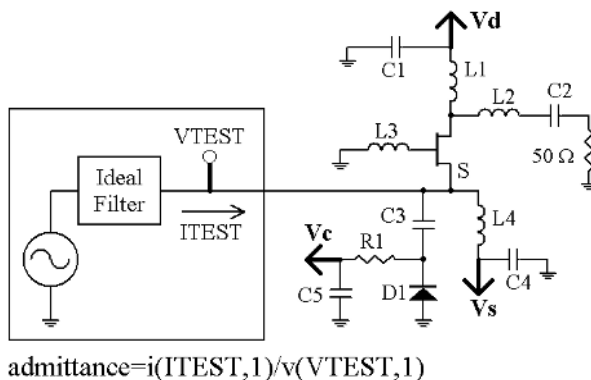


Figure 2.13 Ku-band VCO; use of a voltage auxiliary generator.

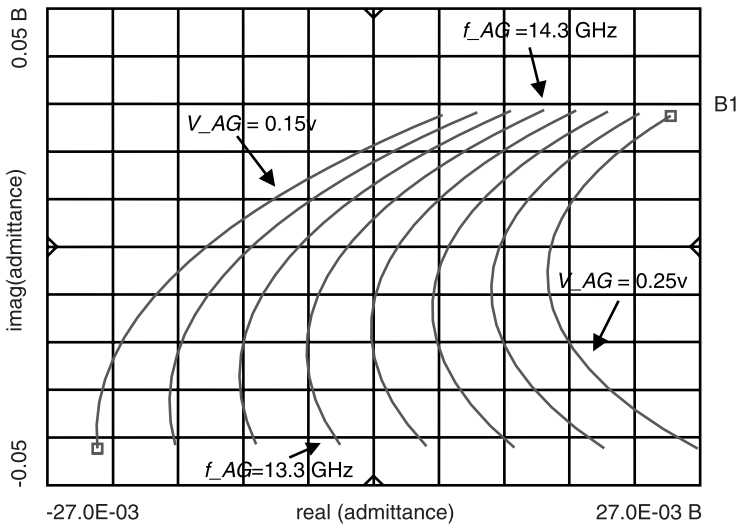


Figure 2.14 Family of curves obtained from the evaluation of the admittance function in the Ku-band VCO. The curves have been obtained using commercial harmonic balance. (From: [51]. © 1998 IEEE. Reprinted with permission.)

voltage relationship Y as the ratio between the first harmonic of the current through the current probe $ICnt$ and the first harmonic of the node voltage V_{out} .

The graphical representation of the admittance function $Y_T(V_{AG}, \omega_{AG})$ on a polar plot for different values of V_{AG} and ω_{AG} can lead to a good estimation of the oscillating solution. These admittance diagrams are traced as a family of constant amplitude curves with variable frequency f_{AG} . When using a polar representation, the intersection with the origin provides the first-harmonic amplitude $V_{AG} \equiv V_o$ and frequency $\omega_{AG} \equiv \omega_o$ of the steady-state oscillation for which the auxiliary generator has no influence due to its zero admittance $Y_T(V_o, \omega_o) = 0$. Taking this into account, a rough initial sweep is carried out, enabling a first approach to the solution, also warning about the possibility of more than one oscillating point. The choice of the sweeping amplitude range is never difficult for microwave circuits, as it will always be comprised between zero and a few volts. Example 2.7 shows an application of the technique to estimate the solution of a Ku-band oscillator.

Example 2.7: VCO in Ku-band

A Ku-band VCO, in monolithic technology [51], has been simulated here (Figure 2.13). The transistor is a HEMT. Series feedback at the source terminal is used, with the varactor diode indicated as D_1 in the figure. Note the

connection of the voltage auxiliary generator in parallel at the source node. Initially the bias voltage $V_{DS} = 1.5v$ and a medium control voltage $V_C = 0$ were considered. A first approach to the oscillating solution was obtained by representing the admittance function Y_T (2.49) in a polar plot. The curves are traced through a rough double sweep in amplitude and frequency of the auxiliary generator. This is shown in Figure 2.14. Each curve has been traced for constant amplitude V_{AG} and variable frequency f_{AG} . There is an obvious intersection with the origin, so an oscillating solution will exist. The accuracy in the estimation of the oscillating solution can be improved through a fine sweep. However, the employment of optimization tools, if available in the harmonic-balance simulator, provides a fast and useful way to increase the accuracy [see the optimization blocks in Figure 2.12(b)].

2.6.1.2 Optimization

In a second stage of the simulation process, the oscillation points estimated through the admittance (or impedance) diagrams are accurately determined by using nonlinear optimization tools. Figure 2.12(b) shows the practical implementation of this optimization in the commercial harmonic-balance software HP-ADS. The goal is the minimization of the admittance magnitude, optimizing the auxiliary generator amplitude V_{AG} and frequency f_{AG} .

$$\text{Goal: } \begin{cases} \text{abs}(\text{Re} Y_T) < Y\text{Error} \\ \text{abs}(\text{Im} Y_T) < Y\text{Error} \end{cases}$$

$$\text{Optimization variables: } V_{AG}, f_{AG}$$

In a standard workstation, this optimization, for eight harmonic components and a threshold admittance magnitude of 10^{-8} , takes about 1 minute. Using the software optimization tools, it is also possible to employ the auxiliary generator for oscillator design. Its frequency is fixed to the desired value $\omega_p \equiv \omega_o$ and its amplitude is fixed according to the desired output power. Two circuit elements (a resistance and an inductance, for instance) are then optimized to minimize Y_T . For the resulting values, the fulfillment of the oscillation start-up conditions must be checked.

Example 2.7: VCO in Ku-band (continued)

The use of optimization tools in the Ku-band VCO provided the final oscillation values $V_{AG} = 0.2003v$ and $f_{AG} = 13.8092$ GHz.

2.6.2 Synchronized Circuits

It has been shown how in injected oscillators, several solutions may coexist for the same input-generator values. The synchronous solutions may coexist with a mathematical solution for which the self-oscillation is not taken into account (see Figure 2.5). The commercial harmonic-balance simulators converge by default to this solution for which no synchronization is actually observed. This undesired convergence can be avoided through the use of auxiliary generators.

The auxiliary generator is introduced in an identical way to the case of an autonomous circuit (see Figure 2.13). (Note that a dual analysis in terms of impedances using a current auxiliary generator is also possible.) In the case of a frequency divider by k , its operation frequency will be that of the input generator, divided by k : $\omega_{AG} = \frac{\omega_g}{k}$. Now, the admittance function Y_{AG} must be evaluated versus the phase of the auxiliary generator, instead of its frequency.

$$Y_T(\phi_{AG}, V_{AG}) = \frac{\bar{I}_{AG}}{V_{AG} e^{j\phi_{AG}}} \tag{2.50}$$

with \bar{I}_{AG} standing for the current phasor. Immittance diagrams are traced on a polar plot in analogous way to what was done in Figure 2.14 for the case of an autonomous circuit. For each amplitude value, as the phase varies from $\phi_{AG} = 0$

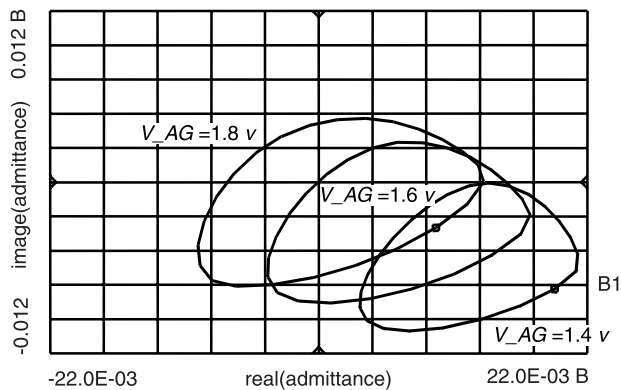


Figure 2.15 Admittance diagrams of the HEMT frequency divider by two with input frequency $f_g = 18.2$ GHz. The curves have been obtained using commercial harmonic balance.

to $\phi_{AG} = 2\pi/k$ (with k being the subharmonic order), a closed curve is obtained because of the periodicity in phase of the admittance function. As in the case of autonomous circuits, the intersection (one or more) with the origin will provide the synchronized solutions. The solutions are estimated from these diagrams and corrected through optimization:

$$\text{Goal: } \begin{cases} \text{abs}(\text{Re } Y_T) < Y\text{Error} \\ \text{abs}(\text{Im } Y_T) < Y\text{Error} \end{cases}$$

Optimization variables: $V_{AG}, \text{phase}_{AG}$

In Example 2.8, the simulation technique will be applied to a frequency divider by two.

Example 2.8: Synchronized solution of a frequency divider by two with input frequency 18.2 GHz

The new simulation technique has been applied to a frequency divider by 2 [52]. The transistor is a HEMT with four $50\text{-}\mu\text{m}$ fingers. The input frequency is $f_g = 18.2$ GHz. The circuit schematic [52] is not relevant for the understanding of the method and has been omitted here. To trace the admittance diagrams $Y_T(V_{AG}, \phi_{AG})$, an auxiliary generator has been connected in parallel between the transistor gate and ground. For $P_g = 0$ dBm and $f_g = 18.2$ GHz, the resulting admittance diagrams obtained through commercial harmonic-balance software are shown in Figure 2.15. Each curve corresponds to an amplitude of the auxiliary generator, with the phase ϕ_{AG} varying between 0 and π . As has already been said, the closed shape of the curves is due to the periodicity of the admittance function Y_T with the phase value.

The intersection with the origin provides the synchronized solution, here obtained for $V_o = 1.59v$ and $\phi = 57.3^\circ$ degrees. These values agree with the amplitude and phase of the first harmonic component of the voltage at the gate terminal (where the auxiliary generator has been connected).

2.6.3 Continuation Method Based on the Use of Auxiliary Generators

Both in VCOs and synchronized circuits, a parametric analysis is generally necessary as a function of the tuning voltage in the former, or as a function of the input-generator amplitude or frequency in the latter. As is already known, the solution curve may be multivalued, and tracing the whole solution curve will be difficult because of the convergence problems associated with turning points at which the Jacobian matrix $[JH]$ becomes singular. This is solved here by means

of a continuation technique, also based on parameter switching [47, 49]. The difference with respect to the continuation technique presented in Section 2.5 is that the one presented here is exclusively based on the use of an auxiliary generator and the optimization tools of the harmonic-balance software. This technique can be applied to both autonomous and synchronized circuits, and it is possible to employ both voltage (admittance analysis) and current auxiliary generators (impedance analysis).

The case of a voltage auxiliary generator will be considered here. For the sake of the compactness of the formulation, the variable ξ is introduced. This variable refers to the auxiliary generator frequency (in the case of an autonomous regime) or phase (in the case of a synchronized regime). For notation simplicity, the subindex *AG* is also dropped, so the generator amplitude is called *V*.

Once a point of the solution curve, given by the set $(\eta_{n-1}, V_{n-1}, \xi_{n-1})$ has been obtained, the following point *n* can be estimated [in a way similar to (2.45)] by differentiating the admittance function about the point *n* – 1:

$$\Delta \bar{Y} = \begin{bmatrix} \frac{\partial Y_T^r}{\partial V} & \frac{\partial Y_T^r}{\partial \xi} \\ \frac{\partial Y_T^i}{\partial V} & \frac{\partial Y_T^i}{\partial \xi} \end{bmatrix}_{n-1} \left(\begin{bmatrix} V_{np} \\ \xi_{np} \end{bmatrix} - \begin{bmatrix} V_{n-1} \\ \xi_{n-1} \end{bmatrix} \right) + \begin{bmatrix} \frac{\partial Y_T^r}{\partial \eta} \\ \frac{\partial Y_T^i}{\partial \eta} \end{bmatrix}_{n-1} (\eta_n - \eta_{n-1}) = 0 \quad (2.51)$$

In the following, the admittance Jacobian matrix will simply be called $[JY]$. The predicted solution is given by

$$\begin{bmatrix} V_{np} \\ \xi_{np} \end{bmatrix} = \begin{bmatrix} V_{n-1} \\ \xi_{n-1} \end{bmatrix} - [JY]_{n-1}^{-1} \left. \frac{\partial \bar{Y}_T}{\partial \eta} \right|_{n-1} (\eta_n - \eta_{n-1}) \quad (2.52)$$

Now the derivative of the real and imaginary parts of *V* and ξ , with respect to the parameter, can be calculated from (2.52), obtaining:

$$\begin{bmatrix} \left. \frac{\partial V}{\partial \eta} \right|_{n-1} \\ \left. \frac{\partial \xi}{\partial \eta} \right|_{n-1} \end{bmatrix} = -[JY]_{n-1}^{-1} \left. \frac{\partial Y_T}{\partial \eta} \right|_{n-1} \quad (2.53)$$

Thus, turning points will have a singular Jacobian matrix $[JY]$. The slope of the two curves, respectively providing the auxiliary generator amplitude V and frequency or phase ξ , versus the parameter η , will be infinite. The two curves $V(\eta)$ and $\xi(\eta)$ will have turning points versus the parameter, and so will all the circuit variables. Actually, both V and ξ belong to the set \bar{X} of state variables of the circuit. Thus, the turning points will fulfill the following condition:

$$\det[JY] = \frac{\partial Y_T^r}{\partial V} \frac{\partial Y_T^i}{\partial \xi} - \frac{\partial Y_T^r}{\partial \xi} \frac{\partial Y_T^i}{\partial V} = 0 \quad (2.54)$$

The solution path of a circuit may exhibit more than one turning point versus a given parameter. As will be shown in Chapter 4, this simple equation allows a

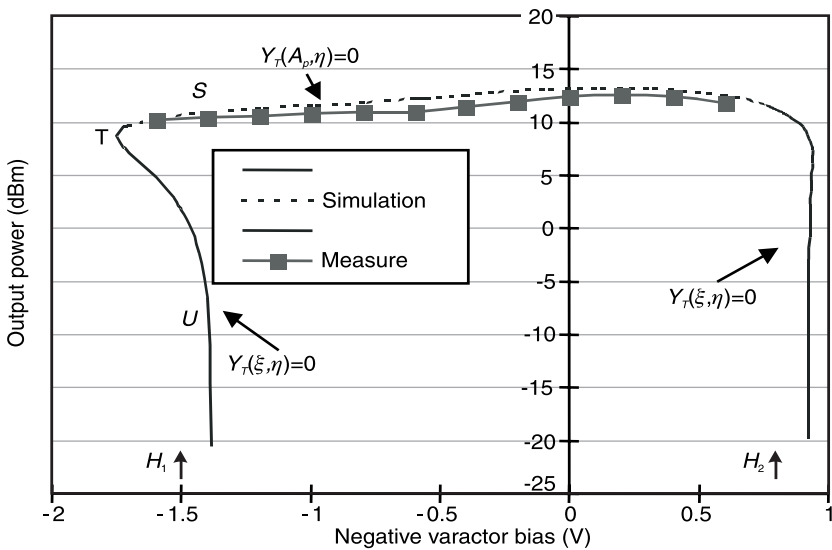
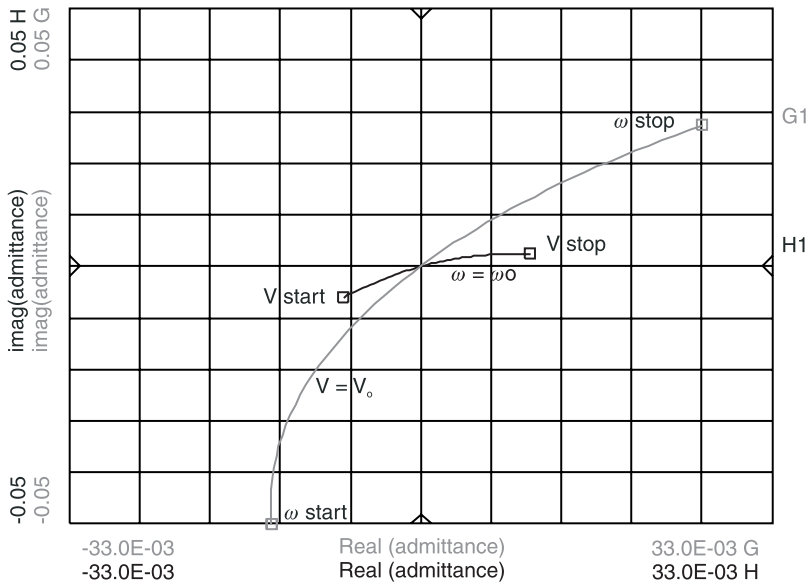
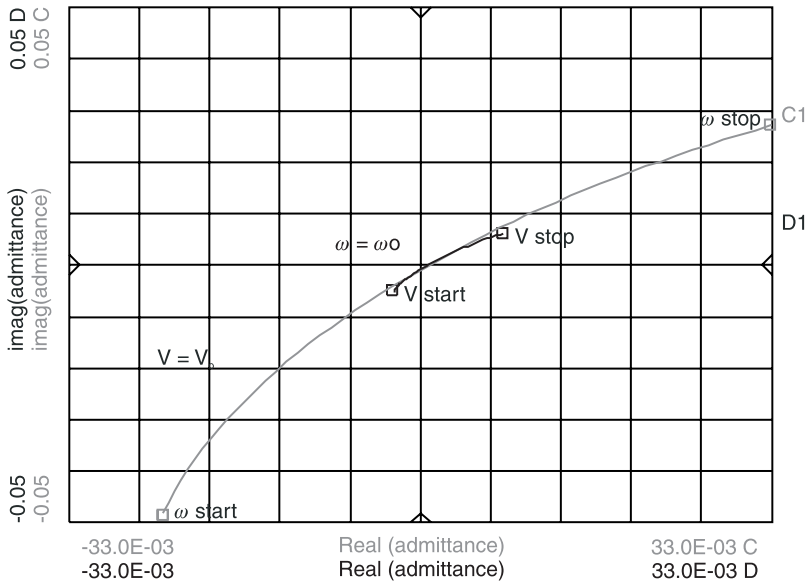


Figure 2.16 Evolution of the output power of the Ku-band VCO versus tuning voltage for the bias voltage $V_{\text{drain}} = 2v$. Measurements have been superimposed. All points in the curve have been obtained using commercial harmonic balance. (From: [51]. © 1998 IEEE. Reprinted with permission.)



(a)



(b)

Figure 2.17 Tangential condition at turning points of the solution curve of Figure 2.16: (a) tuning voltage $V_c = -1.5v$, and (b) tuning voltage $V_c = -1.75v$. The plots have been obtained using commercial harmonic balance. (From: [51]. © 1998 IEEE. Reprinted with permission.)

very efficient numerical determination of the circuit parameter values for which turning points are obtained.

Defining a vector $Y_T = (\text{Re}(Y_T), \text{Im}(Y_T))$, the sign and magnitude of the crossed product (2.54) agree with those of the vectorial product $\frac{\partial Y_T}{\partial V} \wedge \frac{\partial Y_T}{\partial \xi}$.

This provides a graphical technique for the detection of turning points when using any closed-harmonic-balance program. The solution point (V_o, ξ_o) will be a turning point if the tangents to the two curves $Y_T(V_o, \xi)$ and $Y_T(V, \xi_o)$ at the origin of the polar diagram form an angle $\alpha = k\pi$, with k being an integer number. Thus, if the solution point is a turning point, both curves are tangent to each other at the origin of the polar plot. This is shown in Example 2.8.

In view of (2.53), the continuation technique will be based on a parameter switching between the auxiliary generator variables V and ξ and the actual circuit parameter η in way similar to the parameter-switching technique of Section 2.5. Initially, the analysis parameter will be η , with the increment $\Delta\eta = h$, using V and ξ as the optimization variables. After each optimization, the increments $(\Delta V, \Delta\xi, \Delta\eta)$ with proper normalization should be compared, using the variable with the largest increment as the new analysis parameter. The increment h will be assigned to the new parameter, V or ξ . If the closed harmonic-balance software does not allow the automatic comparison of the increments, the switching of optimization variables in sections of difficult convergence will be manually carried out by the designer. In Example 2.9, the continuation

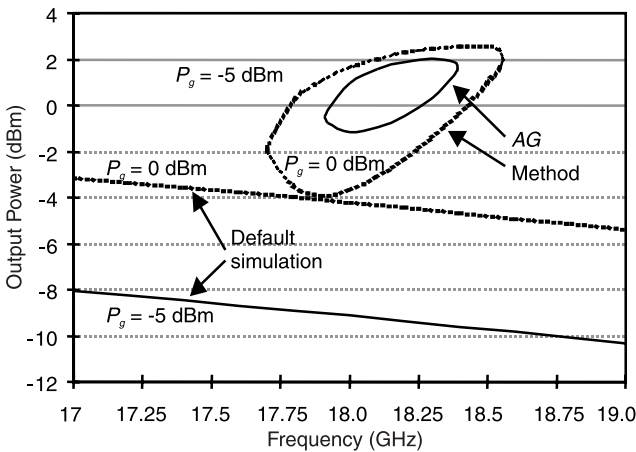


Figure 2.18 Synchronization curves of the frequency divider by two with input frequency $f_g = 18.2$ GHz. All points in the curve have been obtained using commercial harmonic balance.

technique is applied to obtain the variations in the solution of the Ku-band VCO versus the tuning voltage.

Example 2.9 Solution curves of the Ku-band VCO versus the tuning voltage

The continuation technique of Section 2.6.3 has been used to trace the oscillation frequency and output power of the Ku-band VCO (Example 2.4) versus the tuning voltage. The bias voltage of the HEMT is $V_{DS} = 2v$. The results are shown in Figure 2.16. All the points of the solution curve have been obtained through commercial harmonic balance. The points have been exported and the curve has been traced using EXCEL. The solution curve shows a turning point at the lower operation border. Note that the optimization variables that have been used in each curve section are indicated in the figure. The turning point is responsible for a strong hysteresis phenomenon that has been confirmed by the experiment. The shift in the tuning voltage has been found to be due to inaccurate varactor modeling.

The fulfillment of the tangential condition (2.54) at the turning points of the solution curve is verified in Figure 2.17. This figure shows how, as a turning point is approached, the angle α between the tangents at the origin of the two admittance curves $Y_7(V_o, \xi)$ and $Y_7(V, \xi_o)$ gets closer to $k\pi$. Actually, Figure 2.17(a) has been traced for the control voltage $V_c = -1.5v$ and Figure 2.17(b), for the control voltage $V_c = -1.75v$, the latter corresponding to one of the turning points of Figure 2.16. Example 2.10 presents the application of the technique to obtain the solution curves of the frequency divider of Example 2.8 versus the input frequency.

Example 2.10: Solution curves of the frequency divider by two versus the input-generator frequency

In this example, the continuation technique of Section 2.6.3 has been used to obtain the synchronization curves of the frequency divider of Example 2.8. The curves, traced in terms of the output power at the divided frequency, for two different input power levels $P_g = -5$ dBm and $P_g = 0$ dBm, are shown in Figure 2.18. All the points in the curves have been obtained using commercial harmonic balance. The points have been exported and the curves have been traced using EXCEL. The actual synchronized solutions are the closed curves with an output power in the order of that of the free-running oscillation. These closed curves can also be obtained by sweeping the phase of the auxiliary generator between 0 and π and optimizing its frequency and amplitude for each phase value. This is another way to circumvent the tuning points. The lower power curves are mathematical solutions for which the self-oscillation is not taken into account. The left-hand-side and right-hand-side turning points provide,

in each case, the borders of the synchronization band. Only the upper section of each synchronization curve is stable. The stability of synchronized regimes will be studied in detail in Chapter 4.

References

- [1] Thompson, J. M. T., and H. B. Stewart, *Nonlinear Dynamics and Chaos*, New York: John Wiley & Sons, 1986.
- [2] Guckenheimer, J., and P. Holmes, *Nonlinear Oscillations, Dynamical Systems and Bifurcations of Vector Fields*, Berlin Germany: Springer-Verlag, 1990.
- [3] Ho, C. W., A. E. Ruehli, and P. A. Brennan, "The Modified Nodal Approach to Network Analysis," *IEEE Trans. Circuits Syst.*, Vol. 22, No. 6, June 1975, pp. 504–509.
- [4] Pederson, D. O., "A Historical Review of Circuit Simulation," *IEEE Trans. Circuits Syst.*, Vol. 31, No.1, Jan. 1984, pp. 103–111.
- [5] Parker, T. S., and L. O. Chua, *Practical Algorithms for Chaotic Systems*, Berlin, Germany: Springer-Verlag, 1989.
- [6] Sobhy, M. I., and A. K. Jastrzebsky, "Direct Integration Methods of Nonlinear Microwave Circuits," *15th European Microwave Conf. Proc.*, Paris, France, Sept. 1985, pp. 1110–1118.
- [7] Maio, I., and F. G. Canavero, "Differential-Difference Equations for the Transient Simulation of Lossy MTLs," *IEEE Int. Symp. Circuits Syst., ISCAS'95*, Vol. 2, 1995, pp.1402–1415.
- [8] Biey, M., et al., "Qualitative Analysis of the Dynamics of the Time-Delayed Chua's Circuit," *IEEE Trans. Circuits Syst.-I*, Vol. 44, No. 6, June 1997, pp. 486–500.
- [9] Biey, M., et al., "Influence of the Parasitics on the Time Delayed Chua's Circuit," *Electrotechnical Conf. MELECON'96*, Vol. 1, 1996, pp. 443–446.
- [10] Nagel, L. W., "SPICE 2: A Computer Program to Simulate Semiconductor Circuits," Ph.D. Thesis No. ERL-M520, University of Berkeley, Electronic Research Laboratory, May 1975.
- [11] Kundert, K. S., and A. Sangiovanni-Vicentelli, "Finding the Steady-State Response of Analog and Microwave Circuits," *IEEE Custom Integrated Circuits Conf.*, 1998, pp. 6.11–6.17.
- [12] Bonet, J., P. Palá, and J. M. Miló, "A Discrete-Time Approach to the Steady State Analysis of Distributed Nonlinear Autonomous Circuits," *IEEE Intl. Symp. on Circuits and Systems, ISCAS'98*, May 31–June 3, 1998, pp.460–464.
- [13] Camacho-Peñalosa, C., "Numerical Steady-State Analysis of Nonlinear Microwave Circuits with Periodic Excitation," *IEEE Trans. Microwave Theory Tech.*, Vol. 31, No. 9, Sept. 1983, pp. 724–730.

-
- [14] Rizzoli, V., and A. Neri, "State of the Art and Present Trends in Nonlinear Microwave CAD Techniques," *IEEE Trans. Microwave Theory Tech.*, Vol. 36, No. 2, Feb. 1988, pp. 343–356.
- [15] Quéré, R., et al., "Large Signal Design of Broadband Monolithic Microwave Frequency Dividers and Phase-Locked Oscillators," *IEEE Trans. Microwave Theory and Techniques*, Vol. MTT-41, No. 11, Nov. 1993, pp. 1928–1938.
- [16] Ushida, A., and L. O. Chua, "Frequency-Domain Analysis of Nonlinear Circuits Driven by Multi-Tone Signals," *IEEE Trans. Circuits Syst.-I*, Vol. 31, No. 9, Sept. 1984, pp. 766–778.
- [17] Hente, D., and R. H. Jansen, "Frequency-Domain Continuation Method for the Analysis and Stability Investigation of Nonlinear Microwave Circuits," *IEE Proc.*, Vol. 133, Pt. H, No. 5, Oct. 1986, pp. 351–362.
- [18] Kundert, K. S., G. B. Sorkin, and A. Sangiovanni-Vicentelli, "Applying Harmonic Balance to Almost Periodic Signals," *IEEE Trans. Microwave Theory Tech.*, Vol. 36, No. 2, Feb. 1988, pp. 366–378.
- [19] Ngoya, E., et al., "Efficient Algorithms for Spectra Calculations in Nonlinear Microwave Circuit Simulators," *IEEE Trans. Circuits Syst.*, Vol. 37, No. 11, Nov. 1990, pp. 1339–1353.
- [20] Rizzoli, V., et al., "The Exploration of Sparse-Matrix Techniques in Conjunction with the Piecewise Harmonic Balance Method for Nonlinear Microwave Circuit Analysis," *IEEE MTT-S Digest*, 1990, pp. 1295–1298.
- [21] Brachtendorf, H. G., G. Welsch, and R. Laur, "Fast Simulation of the Steady State of Circuits by the Harmonic-Balance Technique," *IEEE Intl. Symp. on Circuits and Systems, ISCAS'95*, Vol. 2, April 30–May 3, 1995, pp. 1388–1391.
- [22] Dag, H., and F. L. Alvarado, "Computation-Free Preconditioners for the Parallel Solution of Power System Problems," *IEEE Trans. Circuits Syst.*, Vol. 12, No. 2, May 1997, pp. 585–591.
- [23] Freund, R. W., "Passive Reduced-Order Modelling Via Krylov-Subspace Methods, *Proc. 2000 IEEE Int. Symp. Computer-Aided Control Syst. Design*, Anchorage, AK, Sept. 2000, pp. 261–266.
- [24] Melville, R., and H. G. Brachtendorf, "An Effective Procedure for Multi-tone Steady-State Analysis of Mixers," *8th IEEE Conf. Elec. Circuits Syst., ICECS*, Maltas, Sicily, Vol. 3, Sept. 2–5, 2001, pp. 1449–1253.
- [25] Mayaram, K., et al., "Computer-Aided Circuit Analysis Tools for RFIC Simulation: Algorithms, Features and Limitations," *IEEE Trans. Circuits Syst.-II*, Vol. 47, No. 4, Apr. 1997, pp. 274–286.
- [26] Ngoya, E., and R. Larcheveque, "Envelope Transient Analysis: A New Method for the Transient and Steady State Analysis of Microwave Communication Circuits and Systems," *Proc. IEEE MTT Symp.*, San Francisco, CA, June 1996, pp. 1029–1032.

-
- [27] Brachtendorf, H. G., G. Welsch, and R. Laur, "A Novel Time-Frequency Algorithm for the Simulation of the Steady State of Circuits Driven by Multi-Tone Signals, *IEEE Int. Symp. Circuits Syst.*, Hong Kong, China, June 1997, pp. 1508–1511.
- [28] Roychowdhury, J., "Efficient Methods for Simulating Highly Nonlinear Multi-Rate Circuits," *Design Automation Conference*, Anaheim, CA, June 9–13, 1997, pp. 269–274.
- [29] Brachtendorf, H. G., G. Welsch, and R. Laur, "A Time-Frequency Algorithm for the Simulation of the Initial Transient Response of Oscillators," *IEEE Intl. Symp. on Circuits and Systems, ISCAS'98*, 1998, pp. 236–239.
- [30] Ngoya, E., J. Rousset, and D. Argollo, "Rigorous RF and Microwave Oscillator Phase Noise Calculation by the Envelope Transient Technique," *IEEE Trans. Microwave Theory Tech.*, June 11–16, 2000, pp. 90–94.
- [31] Kurokawa, K., "Some Basic Characteristics of Broadband Negative Resistance Oscillator Circuits," *Bell Syst. Tech. J.*, Vol. 48, No. 6, 1969, pp. 1937–1955.
- [32] Gustafsson, L., K. I. Lundstrom, and G. H. B. Hansson, "On the Use of the Describing Functions in the Study of Nonlinear Active Microwave Circuits," *IEEE Trans. Microwave Theory Tech.*, Vol. 20, No. 6, June 1972, pp. 402–409.
- [33] Calandra, E., and A. M. Sommariva, "Stability Analysis of Injection Locked Oscillators in Their Fundamental Mode of Operation," *IEEE Trans. Microwave Theory Tech.*, Vol. 29, No.11, Nov. 1981, pp. 1137–1144.
- [34] Xuan, Y., and C. M. Snowden, "A Generalized Approach to the Design of Microwave Oscillators," *IEEE Trans. Microwave Theory Tech.*, Vol. 35, No. 12. Dec. 1987, pp. 1340–1347.
- [35] Elad, D., A. Majdar, and A. Bar-Lev, "A New Approach to the Analysis and Design of Microwave Feed-Back Oscillators," *European Microwave Conf.*, Sept. 4–7, 1989, pp. 386–391.
- [36] Rizzoli, V., and A. Neri, "Harmonic Balance Analysis of Multitone Autonomous Nonlinear Microwave Circuits," *IEEE MTT-S Digest, B-6*, San Diego, CA, June 10–14, 1991, pp. 107–110.
- [37] Rizzoli, V., and A. Neri, "A Fast Newton Algorithm for the Analysis and Design of Microwave Oscillators and VCOs," *IEEE MTT Symp.*, Dallas, TX, May 8–10, 1990, pp. 386–394.
- [38] Rizzoli, V., et al., "Simulation and Design of Nonlinear Microwave Circuits: An Overview of Frequency-Domain Techniques for the Treatment of Oscillators," *Int. Workshop West German IEEE*, Duisburg, Germany, Oct. 1990, pp. 123–136.
- [39] Chang, C. R., et al., "Computer Aided Analysis of Free Running Microwave Oscillators," *IEEE Trans. Microwave Theory Tech.*, Vol. 39, No. 10, Oct. 1991, pp. 1735–1745.
- [40] Suárez, A., et al., "Large Signal Design of Broadband Monolithic Microwave Frequency Dividers," *IEEE MTT Symp.*, Albuquerque, NM, June 1992, pp. 1595–1599.
- [41] Hansson, G. H., and K. I. Lundstrom, "Stability Criteria for Phase-Locked Oscillators," *IEEE Trans. Microwave Theory Tech.*, Vol. 20, No. 10, Oct. 1972, pp. 641–645.

-
- [42] Gustafsson, L., K. I. Lundstrom, and G. H. B. Hansson, "Maximum Phase-Locking Bandwidth Obtainable by Injection Locking," *IEEE Trans. Microwave Theory Tech.*, Vol. 21, 1973, pp. 353–355.
- [43] Knochel R., "Unified Large-Signal Stability and Noise Theory for Synchronised Oscillators," *IEE Proc.* Vol. 128, Pt. H, No. 3, June 1981, pp. 137–145.
- [44] Melville, R. C., et al., "Artificial Parameter Homotopy Methods for the DC Operating Point Problem," *IEEE Trans. Computer Aided Design Integrated Circuits Syst.*, Vol. 12, June 1993, pp. 861–877.
- [45] Green, M. M., and R. C. Melville, "Sufficient Conditions for Finding Multiple Operating Points of DC Circuits Using Continuation Methods," *IEEE Int. Symp. Circuits Syst., ISCAS'95*, 1995, pp. 117–120.
- [46] Chua, L. O., "A Switching Parameters Algorithm for Finding Multiple Solutions of Non-Linear Resistive Circuits," *Int. J. Circuit Theory Applications*, Vol. 4, July 1976, pp. 215–239.
- [47] Suárez, A., J. Morales, and R. Quéré, "Synchronization Analysis of Autonomous Microwave Circuits Using New Global Stability Analysis Tools," *IEEE Trans. Microwave Theory Tech.*, Vol. 46, No. 5, May 1998, pp. 494–504.
- [48] Morales, J., A. Suárez, and R. Quéré, "Accurate Determination of Frequency Dividers Operating Bands," *IEEE Microwave Guided Wave Lett.*, Vol. 6, No. 1, Jan. 1996, pp. 46–48.
- [49] Suárez, A., et al., "Stability Analysis of Analog Frequency Dividers in the Quasiperiodic Regime," *IEEE Microwave Guided Wave Lett.* Vol. 4, No. 5, May 1994, pp. 138–140.
- [50] Morales, J., et al., "Global Stability Analysis of Self-Oscillating Mixers," *Proc. 25th European Microwave Conf.*, Bologna, Italy, Sept. 1995, pp. 1216–1219.
- [51] Palazuelos, E., et al., "Hysteresis Prediction in Autonomous Microwave Circuits Using Commercial Software. Application to a Ku Band MMIC VCO," *IEEE J. Solid-State Circuits*, Vol. 33, No. 8, Aug. 1998, pp. 1239–1243.
- [52] Palazuelos, E., et al., "Bifurcation Analysis of Synchronized Microwave Circuits Using Commercial Software," *GaAs Symposium 1998*, Amsterdam, the Netherlands, Sept. 1998, pp. 1239–1243.

3

Local Stability Analysis¹

In Chapter 2, various methods for obtaining the steady-state behavior of non-linear microwave circuits were presented. Emphasis has been placed on the harmonic-balance techniques, which are well fitted for microwave circuits. The main assumption of this technique is that the steady-state working regime can be projected on a particular functional basis of time-domain functions: $\Psi_i(t)$. Thus, the problem to be solved is to find the coefficients X_i of the projection:

$$x(t) = \sum_i X_i \cdot \Psi_i(t) \quad (3.1)$$

However, as the basis is chosen a priori, nothing ensures that it will be full. Indeed, supposing that the basis is only constituted of a constant function $\Psi_o(t) = 1$, the solution of the balance equation will represent the bias point of the circuit. If the circuit oscillates at the angular frequency ω_0 , it is evident that the chosen basis is incomplete and must be augmented with a set of periodic functions of period $T_0 = \frac{2\pi}{\omega_0}$. Such behavior can be detected by a perturbation

analysis of the solution obtained with the previous choice. Thus, to ensure that the chosen basis is complete, a stability analysis must be performed once the solution has been obtained. This analysis will be based on the response of the

1. This chapter was written by Raymond Quéré.

circuit, working in the linear or nonlinear regime, to a small perturbation of the solution found by the harmonic-balance analysis technique. So, the stability of the circuit will be locally determined and no information will be obtained about large perturbations of the solution.

From a practical point of view, microwave designers frequently face stability problems. Those problems are more and more critical as the technology of transistors improves with the constantly increasing gain of the transistors. Power amplifiers and oscillators are very prone to stability problems. In power amplifiers, these manifest themselves as parasitic oscillations, which arise when the bias is applied or when the input RF power is applied. In the latter case, a frequency division by two phenomenon can take place in the circuit when the amplifier enters in the gain compression zone. Some techniques associated with a careful stability analysis prevent power amplifiers' circuits from oscillating as this chapter will show. In the case of oscillators, linear stability analysis enables the prediction of the starting point of the oscillation as the nonlinear stability analysis is used to determine the possible existence of unstable modes.

The chapter is organized as follows. Section 3.1 develops the concept of local stability both for linear and nonlinear circuits. The relations existing between time-domain techniques and frequency-domain techniques will be described. Basic examples will be given to allow a better understanding of the basis of the method. In Section 3.2 the characteristic system for harmonic-balance equations will be obtained in the general case and the reduction of the equation for stability analysis of the dc regime will be given. Section 3.3 will be devoted to the stability analysis of multidevice circuits in the linear and nonlinear regimes using the open-loop approach first introduced by Bode. It will be shown that this approach can be extended to the nonlinear case and applied using standard *computer-aided design* (CAD) software.

3.1 Stability Concept for Linear and Nonlinear Circuits

The stability concept is generally associated with the theory of ordinary *differential equations* (ODE). Recalling the general equation given in Chapter 2

$$\begin{aligned}\frac{d\bar{x}}{dt} &= f(\bar{x}, t) \\ \bar{x}(0) &= \bar{x}_0\end{aligned}\tag{3.2}$$

The stability of a solution of (3.2) is determined by the asymptotic behavior of a perturbation $\delta\bar{x}(t)$ of this solution $\bar{x}(t)$ as the time goes to infinity.

The solution of the ODE (3.2) will be stable if a perturbation $\delta\bar{x}(t)$ of the solution $\bar{x}(t)$ is such that [1]:

$$\delta\bar{x}(t) \xrightarrow{t \rightarrow \infty} 0 \quad (3.3)$$

We will examine the conditions that are required to satisfy (3.3) in the case of linear and nonlinear circuits.

3.1.1 Stability of Linear Circuits

3.1.1.1 Stability in the Case of Lumped Circuits

Circuits that do not include dispersive elements can be described by the canonical system of equations, which results from the modified nodal analysis [2] of the circuit. This system reads

$$\begin{aligned} \mathbf{C} \cdot \frac{d\bar{x}(t)}{dt} + \mathbf{G} \cdot \bar{x}(t) + \bar{u}(t) &= 0 \\ \bar{x}(0) &= \bar{x}_0 \end{aligned} \quad (3.4)$$

where $\bar{x}(t)$ is the vector of node voltages augmented with voltage source and inductance currents. The $\bar{u}(t)$ is the vector of independent sources. \mathbf{C} and \mathbf{G} , respectively, are the generalized capacitance and conductance matrixes.² In most cases (3.4) does not represent an ODE system as the matrix \mathbf{C} is not invertible. In fact (3.4) represents a *differential algebraic equation* (DAE), the solution of which is not obtained through classical integration methods.

However, solutions of (3.4) can be easily obtained either with a phasor analysis in the case of a sinusoidal steady-state regime or with Laplace analysis for arbitrary inputs. Moreover, the Laplace analysis gives the basis for stability analysis and, thus, will be briefly reviewed here.

We define the solution in the Laplace domain as

$$\bar{X}(s) = \mathbf{L}\{\bar{x}(t)\} = \int_0^{\infty} \bar{x}(t) \cdot e^{-s \cdot t} \cdot dt \quad (3.5)$$

Applying (3.5) to the derivative of $\bar{x}(t)$, we obtain

2. \mathbf{C} and \mathbf{G} are denoted as generalized capacitance and conductance matrixes as they can contain various quantities as capacitors inductors, conductances, resistances, or dimensionless coefficients.

$$\mathbf{L} \left\{ \frac{d\bar{x}(t)}{dt} \right\} = \int_0^{\infty} \frac{d\bar{x}(t)}{dt} \cdot e^{-s \cdot t} \cdot dt = s \cdot \bar{X}(s) - \bar{x}(0) \quad (3.6)$$

Inserting (3.5) and (3.6) into (3.4), we obtain the circuit equation in the Laplace domain:

$$(s \cdot \mathbf{C} + \mathbf{G}) \cdot \bar{X}(s) - \mathbf{C} \cdot \bar{x}(0) + \bar{U}(s) = 0 \quad (3.7)$$

Letting $\mathbf{A} = -\mathbf{G}^{-1} \cdot \mathbf{C}$, (3.7) can be rewritten as

$$(\mathbf{I} - s \cdot \mathbf{A}) \cdot \bar{X}(s) + \mathbf{A} \cdot \bar{x}(0) + \mathbf{G}^{-1} \cdot \bar{U}(s) = 0 \quad (3.8)$$

The general solution of (3.8) is given by

$$\bar{X}(s) = (\mathbf{I} - s \cdot \mathbf{A})^{-1} \mathbf{G}^{-1} \mathbf{C} \cdot \bar{x}(0) - (\mathbf{I} - s \cdot \mathbf{A})^{-1} \mathbf{G}^{-1} \cdot \bar{U}(s) = 0 \quad (3.9)$$

Generally the inverse of the matrix $(\mathbf{I} - s \cdot \mathbf{A})$ is difficult to obtain as it is a symbolic representation of the solution. However, further investigations of the solution and its stability can be performed by calculating the eigenvalues and eigenvectors of matrix \mathbf{A} . Supposing that the eigenvalues of \mathbf{A} are $\lambda_1, \lambda_2, \dots, \lambda_n$ the matrix can be factorized as

$$\mathbf{A} = \mathbf{P} \cdot \mathbf{D} \cdot \mathbf{P}^{-1} \quad (3.10)$$

where $\mathbf{D} = \begin{bmatrix} \lambda_1 & 0 & \dots & 0 \\ 0 & \lambda_2 & & \vdots \\ \vdots & & \ddots & \\ 0 & \dots & 0 & \lambda_n \end{bmatrix}$, and $\mathbf{P} = [\bar{p}_1, \bar{p}_2 \dots \bar{p}_n]$ is the matrix which

consists of the eigenvectors \bar{p}_i of \mathbf{A} . Inserting (3.10) into (3.9) leads to

$$\begin{aligned} \bar{X}(s) &= \mathbf{P} \cdot (\mathbf{I} - s \cdot \mathbf{D})^{-1} \mathbf{P}^{-1} \cdot \mathbf{G}^{-1} \mathbf{C} \cdot \bar{x}(0) - \mathbf{P} \cdot (\mathbf{I} - s \cdot \mathbf{D})^{-1} \mathbf{P}^{-1} \\ &\cdot \mathbf{G}^{-1} \cdot \bar{U}(s) = 0 \end{aligned} \quad (3.11)$$

Now the diagonal matrix can be easily inverted, and we can obtain the *zero-input solution* by letting $\bar{U}(s) = 0$ as

$$\bar{X}(s) = P \cdot \begin{bmatrix} \frac{1}{1 - \lambda_1 \cdot s} & 0 & \dots & 0 \\ 0 & \frac{1}{1 - \lambda_2 \cdot s} & & \vdots \\ \vdots & & \ddots & \\ 0 & \dots & 0 & \frac{1}{1 - \lambda_n \cdot s} \end{bmatrix} \bar{\nu}_0 \quad (3.12)$$

with $\nu_0 = \mathbf{P}^{-1} \cdot \mathbf{G}^{-1} \mathbf{C} \cdot \bar{x}(0)$.

Thus, the k th component of the solution vector to the *zero-input solution* is given in the s domain by

$$\begin{aligned} X_k(s) &= \sum_{j=1}^n \frac{-p_{k,j} \cdot \nu_{0,j}}{\lambda_j} \cdot \frac{1}{s - s_j} = r_{k,\infty} \\ &+ \sum_{j=1}^{n'} \frac{r_{k,j}}{s - s_j} \text{ with } n' \leq n \end{aligned} \quad (3.13)$$

where $s_j = \frac{1}{\lambda_j}$ is the pole of the transfer function, $r_{k,\infty}$ is the residue of the function

at the poles located at infinity (i.e., corresponding to $\lambda_j = 0$), and n' corresponds to the number of nonzero eigenvalues of matrix \mathbf{A} .

Taking the inverse Laplace transform of $X_k(s)$, the time-domain solution $x_k(t)$ is

$$x_k(t) = r_{k,\infty} + \sum_{j=1}^{n'} r_{k,j} \cdot e^{s_j t} \quad (3.14)$$

As the poles s_j can be either real or complex-conjugated, it is evident that the circuit will be stable if all the poles have a negative real part. Thus, the stability criterion for linear lumped circuits can be given as follows:

A linear lumped circuit characterized by (3.4) will be stable if all the eigenvalues of the matrix ($\mathbf{A} = -\mathbf{G}^{-1}\mathbf{C}$), different of zero, have a negative real part.

However, microwave circuits are characterized by the presence of dispersive, distributed elements, such as transmissions lines, couplers, and stubs. For

these circuits, (3.4) does not hold and has to be modified. In this case, the previous analysis must be carried out in the frequency domain through the use of the Nyquist criterion.

3.1.1.2 Stability Analysis in the Frequency Domain: Nyquist Criterion

An equivalent way to determine the stability of linear circuits is to use the Nyquist criterion [3], which provides a convenient means to determine the stability of a circuit that is only known by frequency-domain characteristics. This is the case of microwave circuits for which the system of modified nodal equations reads

$$\mathbf{C} \cdot \frac{d\bar{\mathbf{x}}(t)}{dt} + \mathbf{G} \cdot \bar{\mathbf{x}}(t) + \int_{-\infty}^t \mathbf{y}(t - \tau) \cdot \bar{\mathbf{x}}(\tau) d\tau + \bar{\mathbf{u}}(t) = 0 \quad (3.15)$$

where $\mathbf{y}(t)$ is a matrix made up of the time-domain responses of the linear distributed elements to an impulse. In this case, the stability criterion will be established from the behavior of the s -domain transform of (3.15), which reads

$$[s \cdot \mathbf{C} + \mathbf{G} + \mathbf{Y}(s)] \cdot \bar{\mathbf{X}}(s) - \mathbf{C} \cdot \bar{\mathbf{x}}(0) + \bar{\mathbf{U}}(s) = 0 \quad (3.16)$$

leading to the s -transfer function between the state variables $\bar{\mathbf{X}}(s)$, the input $\bar{\mathbf{U}}(s)$, and the zero-input response of the circuit:

$$\bar{\mathbf{X}}(s) = [s \cdot \mathbf{C} + \mathbf{G} + \mathbf{Y}(s)]^{-1} \cdot \mathbf{C} \cdot \bar{\mathbf{x}}(0) + H(s) \cdot \bar{\mathbf{U}}(s) \quad (3.17)$$

Considering a particular state variable $X_k(s)$, it can be expressed as the ratio of two functions of s . Moreover, for a zero input ($\bar{\mathbf{U}}(s) = 0$), the s transform of this particular node voltage is

$$X_{k,o}(s) = \frac{N_k(s)}{D_k(s) \cdot \Delta(s)} = F_k(s) \quad (3.18)$$

$$\Delta(s) = \det[s \cdot \mathbf{C} + \mathbf{G} + \mathbf{Y}(s)]$$

where $D_k(s)$ is a function that appears in the denominator of some term of $\mathbf{Y}(s)$.

The circuit will be stable if the s -domain function $F_k(s)$ obtained for a zero input have no poles with a positive real part.

As the matrix $Y(s)$ describes a purely passive subcircuit, it does not own positive real-part poles. Thus, the zeros of $D_k(s)$ have a real part negative or equal to zero. This zero value occurs for lossless transmission lines. Then, the poles of $F_k(s)$ with a positive real part will coincide with the zeros of $\Delta(s)$ with a positive real part.

This can be checked by the application of the Nyquist criterion, which results from a Cauchy theorem [4] applied with the closed contour constituted of the imaginary axis $s = j\omega$, minus the eventual singularities on the imaginary axis and a circle of infinite radius enclosing the whole right-hand plane of the s -plane, as shown in Figure 3.1. When the s variable travels clockwise through the contour (C), the point M defined by the mapping $s \rightarrow F_k(s)$ travels through the contour Γ_k . If the contour (C) encloses P poles and Z zeros of $F_k(s)$, then the contour Γ_k makes $Z - P$ clockwise encirclements of the origin. Thus, to check for the stability of the circuit the angular frequency ω is swept from zero to ∞ and the locus of

$$F_k(j\omega) = \frac{N_k(j\omega)}{D_k(j\omega) \cdot \Delta(j\omega)} \quad (3.19)$$

is drawn. As all the coefficients of the polynomial expansion of $F_k(s) = \frac{N_k(s)}{D_k(s) \cdot \Delta(s)}$ are real, the locus obtained for negative angular frequencies is simply the complex-conjugated of $F_k(j\omega)$:

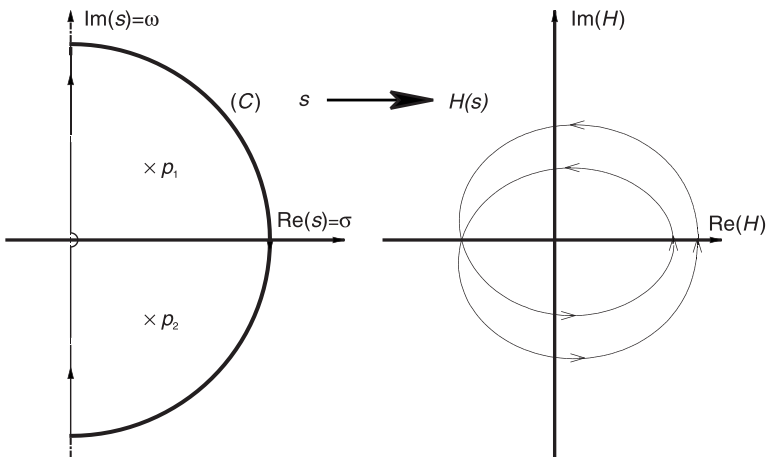


Figure 3.1 Contour of the Nyquist plot.

$$F_k(-j\omega) = F_k^*(j\omega) \quad (3.20)$$

The four cases sketched in Figure 3.2 can be encountered and correspond to a system with no zeros and unstable poles [Figure 3.2(a)], a system with two conjugated unstable poles [Figure 3.2(b)], and a system with two conjugated unstable zeros [Figure 3.2(c)]. Figure 3.2(d) corresponds to a pole zero cancellation. It must be noted that in the latter case there is no encirclement of the origin. Thus, in this case inspection of the Nyquist plot fails to give the correct behavior of the circuit. Only the definition of the eigenvalues of the characteristic system (3.15) can reveal the stability of the circuit.

The transfer function plotted in Figure 3.2 is well behaved [except in Figure 3.2(d)] from the point of view of the interpretation of the Nyquist locus. However, things are generally not so simple, and the choice of the network function to be checked for stability has to be made very carefully. The behavior of the network function must especially be well behaved for $s \rightarrow \infty$ and $s = 0$. Example 3.1 on a simple van der Pol oscillator will illustrate those topics.

Example 3.1: van der Pol oscillator

Let us illustrate these results with a very simple example, which concerns the linear equivalent circuit of a van der Pol oscillator. Two realizations of the circuit are given in Figure 3.3. As it can be seen, those two realizations correspond to a lumped and a distributed circuit respectively. Thus, the modified nodal analysis of the circuit gives the generic system of equations:

$$\begin{aligned} C \frac{dv_1(t)}{dt} + \frac{v_1(t) - v_2(t)}{R} - a \cdot v_1(t) &= 0 \\ \frac{v_1(t) - v_2(t)}{R} - i_2(t) &= 0 \\ v_2(t) - z_2(t) * i_2(t) &= 0 \end{aligned} \quad (3.21)$$

where $z_2(t) * i_2(t)$ is the *convolution product* of the impulse response of the impedance seen at terminal 2 with the current flowing into the dipole. In the case of the lumped version of the circuit, we have

$$z_2(t) * i_2(t) = L \cdot \frac{di_2(t)}{dt} \quad (3.22)$$

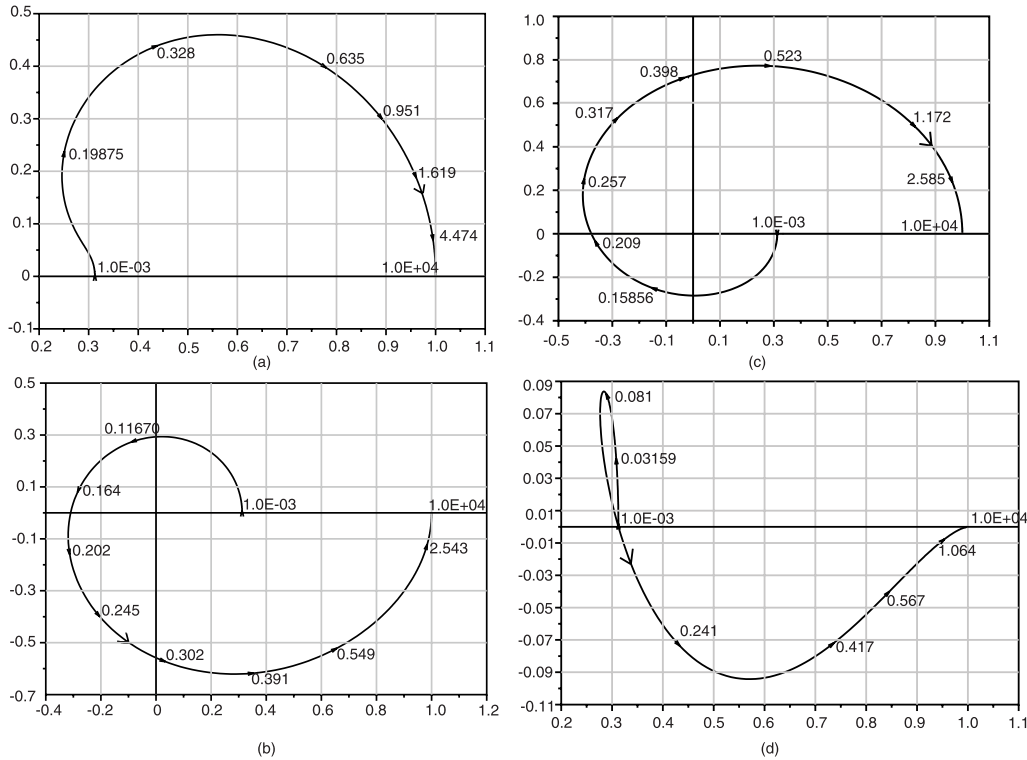


Figure 3.2 Plot of the Nyquist locus of a network function of the type $F_k(s) = \frac{(S - Z_1) \cdot (S - Z_2) \cdot (S - Z_3)}{(S - p_1) \cdot (S - p_2) \cdot (S - p_3)}$: (a) $\text{Re}(z_i) < 0$; $\text{Re}(p_i) < 0$, $i = 1, 2, 3$; (b) $\text{Re}(z_i) > 0$ $i = 1, 2$; $\text{Re}(p_i)$, $i = 1, 2, 3$; (c) $\text{Re}(z_i) < 0$, $i = 1, 2, 3$, $\text{Re}(p_i) > 0$, $i = 1, 2$; and (d) $\text{Re}(z_i) > 0$, $i = 1, 2$, $\text{Re}(p_i) > 0$, $i = 1, 2$.

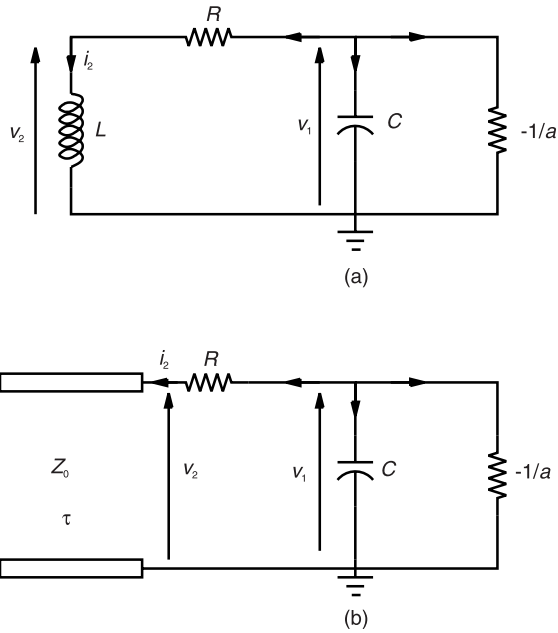


Figure 3.3 Equivalent linear circuit of a van der Pol oscillator corresponding to: (a) a lumped circuit $C = 0.5$ pF; $R = 50\Omega$; $L = 2$ nH; and (b) a distributed circuit: $C = 0.5$ pF; $Z_0 = 50\Omega$; $\tau = 20$ ps.

and the approach presented in Section 3.1.1.1 holds. Thus, the stability can be checked by inspection of the eigenvalues of matrix $\mathbf{A} = -\mathbf{G}^{-1} \cdot \mathbf{C}$ where

$$\mathbf{C} = \begin{bmatrix} C & 0 & 0 \\ 0 & 0 & 0 \\ 0 & 0 & L \end{bmatrix} \quad \text{and} \quad \mathbf{G} = \begin{bmatrix} 1/R - a & -1/R & 0 \\ -1/R & 1/R & 1 \\ 0 & -1 & 0 \end{bmatrix} \quad (3.23)$$

giving

$$\mathbf{A} = \begin{bmatrix} \frac{R \cdot C}{1 - a \cdot R} & 0 & \frac{-L}{1 - a \cdot R} \\ 0 & 0 & -L \\ \frac{C}{1 - a \cdot R} & 0 & \frac{-a \cdot L}{1 - a \cdot R} \end{bmatrix} \quad (3.24)$$

which has three eigenvalues. One of them equals zero and the others read

$$\lambda_1 = \frac{1}{2} \cdot \frac{R \cdot C - a \cdot L \pm \sqrt{(R \cdot C + a \cdot L)^2 - 4 \cdot L \cdot C}}{a \cdot R - 1}$$

$$\lambda_2 = \frac{1}{2} \cdot \frac{R \cdot C - a \cdot L \mp \sqrt{(R \cdot C + a \cdot L)^2 - 4 \cdot L \cdot C}}{a \cdot R - 1}$$

For $(R \cdot C + a \cdot L)^2 - 4 \cdot L \cdot C < 0$ the eigenvalues λ_1, λ_2 are complex-conjugated and the stability condition requires: $\frac{R \cdot C - a \cdot L}{a \cdot R - 1} < 0$. Thus, in the case of linear lumped circuits, the stability can be completely determined by the study of the eigenvalues of the matrix \mathbf{A} .

In the case where the self-inductance is replaced with the short-circuited stub, the previous analysis does not hold, and we must adopt the Nyquist approach. In this case, the Laplace transform of (3.21) gives

$$\begin{bmatrix} C \cdot s + 1/R - a & -1/R & 0 \\ -1/R & 1/R & 1 \\ 0 & 1 & -Z_2(s) \end{bmatrix} \begin{bmatrix} V_1(s) \\ V_2(s) \\ I_2(s) \end{bmatrix} = \begin{bmatrix} C \cdot v_1(0) \\ 0 \\ 0 \end{bmatrix} \quad (3.25)$$

with $Z_2(s) = Z_0 \cdot \tanh(\tau \cdot s)$.

Thus, we have to select a network function to be evaluated for $s = j\omega$ that leads to a simple interpretation of the Nyquist plot. Following (3.19), let us choose the transfer function which relates the voltage $V_1(s)$ to the initial condition. We obtain

$$V_1(s) = \frac{Z_2(s) + R}{1 + (Z_2(s) + R) \cdot (Cs - a)} \cdot Cv_1(0)$$

which can be rewritten as

$$V_1(s) = \frac{Z_p(s)}{1 - a \cdot Z_p(s)} \cdot Cv_1(0) \quad (3.26)$$

where $Z_p(s) = \frac{(Z_2(s) + R) / Cs}{Z_2(s) + R + 1/Cs}$ is the equivalent impedance of the passive circuit embedding the active device with the negative conductance $-a$. As $Z_p(s)$ is purely passive, it does not have poles with positive real part. Thus, the poles of the transfer function are given by the zeros of the function:

$$F(s) = 1 - a \cdot Z_p(s) \quad (3.27)$$

The plot of the Nyquist loci of $F(j\omega)$ for various values of the negative conductance $-a$ are given in Figure 3.4. Those plots lead to a straightforward interpretation of the Nyquist locus.

The previous conclusions will later be generalized to the general circuit approach.

3.1.2 Stability of Nonlinear Circuits

3.1.2.1 General Nonlinear Equation

The fundamental concept of stability has been presented in the previous section. This concept relies on the position of the poles of the transfer functions. When dealing with nonlinear circuits, the previous concept cannot be applied as such. Considering the general modified nodal equation of a nonlinear circuit [2], we obtain (3.28) in the time domain:

$$\frac{d\bar{q}(\bar{x}(t))}{dt} + \bar{f}(\bar{x}(t)) + \int_{-\infty}^t \mathbf{y}(t-\tau) \cdot \bar{x}(\tau) \cdot d\tau + \bar{u}(t) = 0 \quad (3.28)$$

where $\bar{q}(\cdot)$ stands for the linear and nonlinear state variables of the circuit (e.g., charges for capacitors and fluxes for inductors), $\bar{f}(\cdot)$ are the linear and nonlinear resistive currents flowing into the nodes, and $\mathbf{y}(t)$ is the impulse time-domain response of the immittance matrix of the distributed part of the circuit. Finally, $\bar{u}(t)$ represents the vector of the independent sources at each node. For the example of Figure 3.3, considering a nonlinear capacitor C_0 and a nonlinear current source, we obtain (3.29):

$$\begin{aligned} \frac{dq(v_1(t))}{dt} + \frac{v_1(t) - v_2(t)}{R} + f(v_1(t)) &= 0 \\ \frac{-v_1(t) + v_2(t)}{R} + i_2(t) &= 0 \\ v_2(t) - z_2(t) * i_2(t) &= 0 \end{aligned} \quad (3.29)$$

Thus, the stability of the circuit cannot be directly checked by inspection of (3.29). We have to introduce the concept of local and global stability.

3.1.2.2 Concept of Global and Local Stability

To illustrate this point, let us consider a ball free to move on a surface such as the one in Figure 3.5. As it can be easily seen, stable points will correspond to the various minima of the potential energy. However, the energy function can

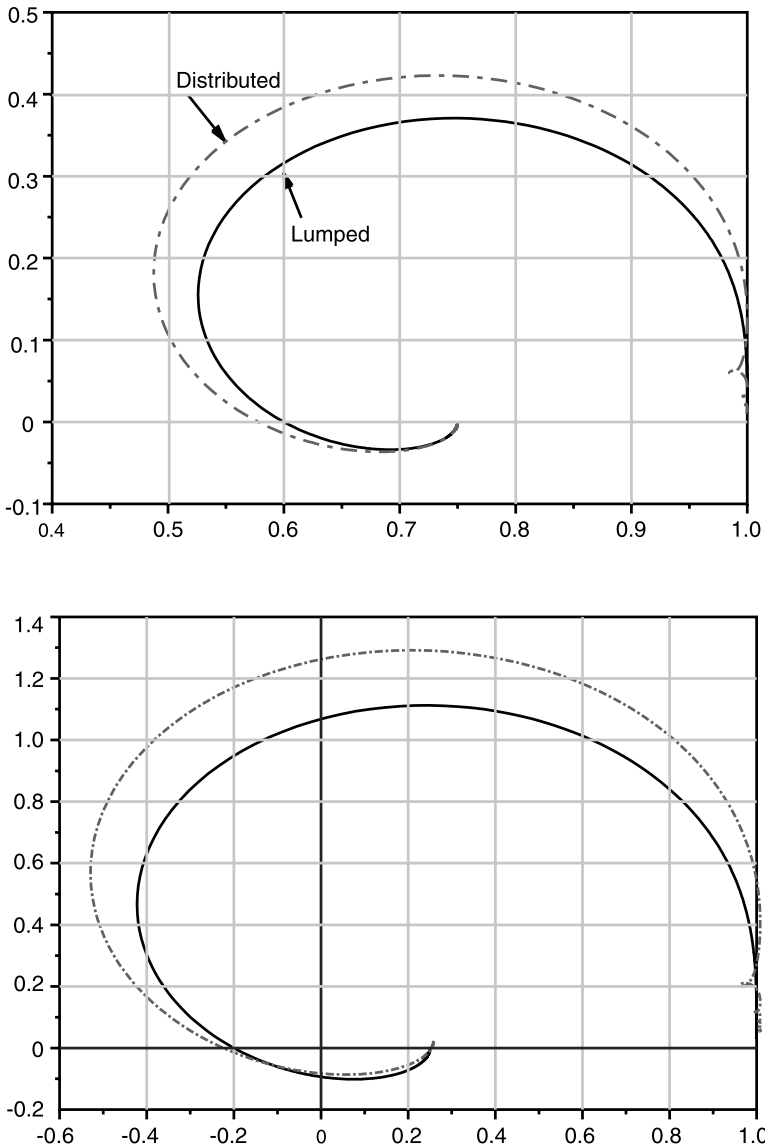


Figure 3.4 Plots of the Nyquist locus of $F(s)$ for various values of a corresponding to (a) a stable configuration $a = 0.01s$, and (b) to an unstable configuration $a = 0.015s$. Dashed lines correspond to the lumped circuit; solid lines correspond to the distributed case.

exhibit several minima, and the stability of the trajectory of the ball around a minimum is only ensured for small perturbations of the equilibrium position.

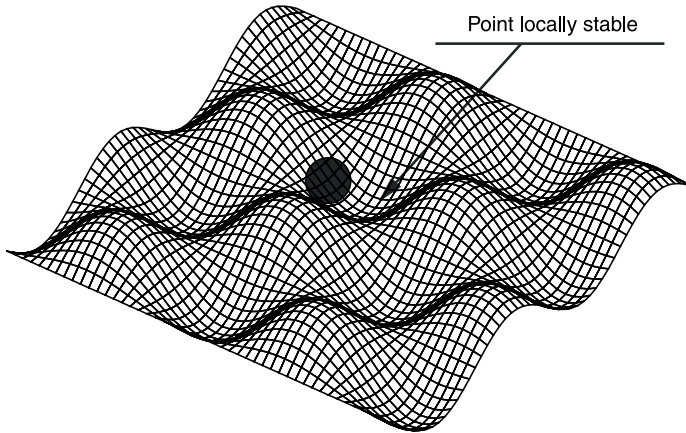


Figure 3.5 A potential energy surface to illustrate the concept of global and local stability.

The set of points that leads to a convergence to a particular minimum is called the *basin of attraction* of this equilibrium point.

Those minima of the energy function are said to be locally stable, unlike the minimum of a spherical energy function, for example, which is globally stable.

3.1.2.3 Condition for Local Stability

Let us assume that we have obtained a solution $\bar{x}_o(t)$ of (3.28). The $\bar{x}_o(t)$ can be either a steady-state dc solution or a time-varying solution. If a small perturbation $\delta\bar{x}(t)$ is superimposed on the steady state, the perturbed solution

$$\bar{x}_o(t) + \delta\bar{x}(t)$$

must satisfy the circuit equation

$$\begin{aligned} \frac{d\bar{q}(\bar{x}_o(t) + \delta\bar{x}(t))}{dt} + \bar{f}(\bar{x}_o(t) + \delta\bar{x}(t)) + \\ \int_{-\infty}^t \mathbf{y}(t-\tau) \cdot (\bar{x}_o(\tau) + \delta\bar{x}(\tau)) \cdot d\tau + \bar{u}(t) = 0 \end{aligned} \quad (3.30)$$

Taking a first-order Taylor development of the nonlinear terms of (3.30) leads to the perturbed equation of the nonlinear system which reads

$$\frac{d}{dt} [\mathbf{C}(\bar{x}(t)) \cdot \delta\bar{x}(t)] + \mathbf{G}(\bar{x}(t)) \cdot \delta\bar{x}(t) + \int_{-\infty}^t \mathbf{y}(t-\tau) \cdot \delta\bar{x}(\tau) \cdot d\tau = 0 \quad (3.31)$$

where $\mathbf{C}(\bar{x}(t)) = \left[\frac{\partial \bar{q}}{\partial \bar{x}} \right]_{\bar{x}=\bar{x}_0(t)}$ and $\mathbf{G}(\bar{x}(t)) = \left[\frac{\partial \bar{f}}{\partial \bar{x}} \right]_{\bar{x}=\bar{x}_0(t)}$, respectively, are

the matrixes of derivatives of reactive and resistive nonlinearities.

Equation (3.31) is the general perturbation system of the nonlinear circuit. The behavior of the solution of this system will determine the local stability of the circuit around the steady-state solution $\bar{x}_o(t)$. To obtain the global stability portrait, the solution must be obtained for all the steady-state regimes of interest when a parameter of the circuit is changed. This will be presented in the next chapter.

Thus, the general condition for local stability around a particular steady-state solution is defined as follows:

A nonlinear circuit is locally stable around the steady-state solution $\bar{x}_o(t)$ if the solution $\delta\bar{x}(t)$ of the perturbed system (3.31) goes to zero as t goes to infinity.

Starting from (3.31), two cases have to be considered. The first case corresponds to an equilibrium point of the circuit, such as $x_o(t) = x_o(o) \forall t$, which corresponds to the bias point of the circuit. It will be useful for the determination of the starting frequency of an oscillator or for the analysis of the potential parasitic oscillations of power amplifiers. The second case will deal with time-varying conditions when the operating point is a function of time. In most cases, this function of time will be periodic and obtained through a harmonic-balance analysis. However, the perturbation equation as stated in (3.31) remains valid for any condition and can be used for the determination of the stability of quasiperiodic regimes bifurcating into chaotic ones.

3.2 Derivation of the Characteristic System in the Harmonic-Balance Formulation

Stability of linear and nonlinear circuits was presented in the previous section. The techniques discussed lead us to give the perturbation equation in the time

domain. In the case of microwave circuits, frequency-domain techniques are most often involved. Thus, it is necessary to derive an equation giving the stability conditions in the frequency domain. Moreover harmonic-balance analysis is based on the projection of Kirchoff's equations on a particular basis of functions in the Fourier space. Nothing ensures that the chosen basis is complete, meaning that there are no other frequencies corresponding to instabilities appearing in the circuit. Thus, a stability analysis must complement any questionable solution obtained through harmonic-balance analysis. This is especially the case for potentially unstable circuits, such as oscillators, frequency dividers, and power amplifiers.

3.2.1 Expression of the Characteristic System

Let us now examine the behavior of the time-domain characteristic equation (3.31) in the case of a periodic steady-state regime. In this case, the derivative

$$\text{matrixes, } \mathbf{C}(\bar{x}(t))\Big|_{\bar{x}=\bar{x}_0(t)} = \left[\frac{\partial \bar{q}}{\partial \bar{x}} \right]_{\bar{x}=\bar{x}_0(t)} \quad \text{and} \quad \mathbf{G}(\bar{x}(t))\Big|_{\bar{x}=\bar{x}_0(t)} = \left[\frac{\partial \bar{f}}{\partial \bar{x}} \right]_{\bar{x}=\bar{x}_0(t)},$$

are periodic with the same period as the steady-state solution $\bar{x}_0(t)$. Thus, the constitutive terms of the matrixes can be expanded in Fourier series giving for the general (m, n) term the following relation:

$$\begin{aligned} c_{mn}(t) &= \sum_{k=-\infty}^{\infty} C_{mn,k} \cdot e^{jk\omega_0 t} \\ g_{mn}(t) &= \sum_{k=-\infty}^{\infty} G_{mn,k} \cdot e^{jk\omega_0 t} \end{aligned} \quad (3.32)$$

Moreover, the perturbation signal³ can be expressed in the frequency domain as

$$\delta x(t) = \sum_{k=-\infty}^{\infty} \Delta X_k \cdot e^{st} \cdot e^{jk\omega_0 t} \quad (3.33)$$

where $s = \sigma + j\omega$ is the complex perturbation frequency.

Inserting (3.32) and (3.33) into the general perturbation equation

3. For the sake of clarity, we derive the characteristic equation for a circuit containing only one node. The results can be easily extended to the general case of multinode circuits.

$$\frac{d}{dt} [C(t) \cdot \delta x(t)] + G(t) \cdot \delta x(t) + \int_{-\infty}^t y(t-\tau) \cdot \delta x(\tau) \cdot d\tau = 0$$

we obtain

$$\begin{aligned} & \frac{d}{dt} \left\{ \sum_m \sum_l C_m \Delta X_l \cdot e^{[j(m+l)\omega_0 + s]t} \right\} \\ & + \left\{ \sum_m \sum_l G_m \Delta X_l \cdot e^{[j(m+l)\omega_0 + s]t} \right\} \\ & + \sum_k \Delta X_k \int_{-\infty}^t y(t-\tau) \cdot e^{j(k\omega_0 - js)\tau} \cdot d\tau = 0 \end{aligned} \quad (3.34)$$

Let us take $k = m + l$, or equivalently, $m = k - l$. In that case, (3.34) is transformed and can be rewritten as

$$\begin{aligned} & \frac{d}{dt} \left\{ \sum_k \sum_l C_{k-l} \Delta X_l \cdot e^{[jk\omega_0 + s]t} \right\} + \\ & \left\{ \sum_k \sum_l G_{k-l} \Delta X_l \cdot e^{[jk\omega_0 + s]t} \right\} + \\ & \sum_k \Delta X_k \int_{-\infty}^t y(t-\tau) \cdot e^{j(k\omega_0 - js)\tau} \cdot d\tau = 0 \end{aligned} \quad (3.35)$$

Equation (3.35) must be satisfied for every t , thus every k th component of the Fourier expansion must equal zero, leading to the transformation of (3.35) into an infinite set of equations that can be put in the following form:

$$\begin{aligned} & (jk\omega_0 + s) \cdot \sum_l C_{k-l} \Delta X_l + \\ & \sum_l G_{k-l} \Delta X_l + Y(jk\omega_0 + s) \cdot \Delta X_k = 0 \\ & -\infty < k < \infty \end{aligned} \quad (3.36)$$

In practical cases the number of harmonics taken into account is limited to N_H . Thus, (3.36) can be expressed in a matrix form that reads

$$(s \cdot \mathbf{C} + [\mathbf{\Omega}] \cdot \mathbf{C} + \mathbf{G} + \mathbf{Y}(s)) \cdot \Delta \bar{\mathbf{X}}(s) = 0 \quad (3.37)$$

where

$$\mathbf{C} = \begin{bmatrix} C_0 & C_{-1} & \dots & C_{-2N_H} \\ C_1 & C_0 & \dots & \vdots \\ \vdots & \vdots & \ddots & \vdots \\ C_{2N_H} & \dots & \dots & C_0 \end{bmatrix} \quad \mathbf{G} = \begin{bmatrix} G_0 & G_{-1} & \dots & G_{-2N_H} \\ G_1 & G_0 & \dots & \vdots \\ \vdots & \vdots & \ddots & \vdots \\ G_{2N_H} & \dots & \dots & G_0 \end{bmatrix}$$

are the matrixes made up of the Fourier coefficients of reactive and conductive elements, respectively, which are defined by

$$C_k = \frac{1}{T_0} \cdot \int_{T_0} c(t) \cdot e^{jk\omega_0 t} \quad \text{and} \quad G_k = \frac{1}{T_0} \cdot \int_{T_0} g(t) \cdot e^{jk\omega_0 t}$$

$[\Omega]$ and $[\mathbf{Y}]$ are diagonal matrixes that read

$$[\Omega] = \begin{bmatrix} -j \cdot N_H \cdot \omega_0 & 0 & \dots & \dots & 0 \\ 0 & \ddots & \dots & \vdots & \vdots \\ \vdots & \vdots & 0 & \vdots & \vdots \\ \vdots & \dots & \dots & \ddots & 0 \\ 0 & \dots & \dots & 0 & j \cdot N_H \cdot \omega_0 \end{bmatrix}$$

$[\mathbf{Y}] =$

$$\begin{bmatrix} Y(j \cdot (-N_H \cdot \omega_0 - js)) & 0 & \dots & \dots & 0 \\ 0 & \ddots & \dots & \vdots & \vdots \\ \vdots & \vdots & Y(-js) & \vdots & \vdots \\ \vdots & \dots & \dots & \ddots & 0 \\ 0 & \dots & \dots & 0 & Y(j \cdot (-N_H \cdot \omega_0 - js)) \end{bmatrix}$$

Equation (3.37) is the general characteristic equation in the frequency domain. We can notice that it corresponds to the general conversion equation for large-signal/small-signal analysis. In that case, the right-hand side of the equation is equal to the perturbation signal like the RF signal in mixer or noise.

While (3.37) has been obtained in the case of a single node, it can easily be extended to the general case where the circuit has N nodes. In this case, each term of the conversion matrixes is expanded in $(N \times N)$ blocks of the form

$$C_k \rightarrow C_k \begin{bmatrix} C_{k,11} & C_{k,12} & \cdots & C_{k,1N} \\ C_{k,21} & C_{k,22} & & \\ \vdots & & \ddots & \\ C_{k,N1} & & & C_{k,NN} \end{bmatrix}$$

and the characteristic system (3.37) becomes a $((2N_H + 1)N \times (2N_H + 1)N)$ matrix system that can be rewritten in a more compact form as

$$\begin{aligned} [\bar{\Gamma}(s)] \cdot [\Delta \bar{X}(s)] &= 0 \\ \bar{\Gamma}(s) &\in C^{(N(2N_H+1)) \times (N(2N_H+1))} \end{aligned} \quad (3.38)$$

Referring to (3.38), the system will be stable if all the zeros of the characteristic equation

$$\det[\bar{\Gamma}(s)] = 0 \quad (3.39)$$

have a negative real part.

However, depending on the nature of the circuit, various techniques for the analysis of the behavior of the characteristic system (3.38) or of the characteristic equation (3.39) can be used. Indeed, we can distinguish circuits that do not involve distributed elements, such as many integrated RF circuits, from those that involve distributed, dispersive elements that do not have a simple representation as a ratio of polynomials in s . Here we find again the observations given in Section 3.1.

Moreover, even for distributed circuits, there exist various approaches that can be used for the determination of the stability of the circuit. Those approaches rely either on a feedback loop formulation or on the negative-resistance concept.

3.2.2 Stability Analysis of Lumped Circuits

3.2.2.1 Expression of the Eigenvalue Problem

When only lumped elements are involved in the circuit equations, a modified nodal analysis leads to a system of Kirchoff's equations where the time domain immittance matrix of the distributed elements cancels, that is, $\bar{y}(t) = 0$.

In that case, (3.38) reduces to

$$(s \cdot C + [\Omega] \cdot C + G) \cdot [\Delta X(s)] = 0 \quad (3.40)$$

Equation (3.40) is a generalized eigenvalue system that can be rewritten in the following form:

$$\begin{aligned} (s \cdot \mathbf{C} + \mathbf{J}) \cdot \Delta \bar{\mathbf{X}}(s) &= 0 \\ \mathbf{J} &= [\mathbf{\Omega}] \cdot \mathbf{C} + \mathbf{G} \end{aligned} \quad (3.41)$$

where \mathbf{J} is the Jacobian matrix of the nonlinear system of equations which is calculated when the harmonic-balance process has converged to the steady-state regime.

When the circuit can be represented as a state equation, the capacitance matrix \mathbf{C} is invertible and we face a classical eigenvalue problem of the type

$$s \cdot \Delta \bar{\mathbf{X}}(s) = -\mathbf{C}^{-1} \cdot \mathbf{J} \cdot \Delta \bar{\mathbf{X}}(s) \quad (3.42)$$

Algorithms are available to obtain those eigenvalues based on Schur [5] decomposition. However, most frequently this representation does not exist, and the capacitance matrix is not invertible. Thus, generalized eigenvalues search algorithms, such as *QZ* [5], must be used. In this case, the eigenvalue system reads

$$s \cdot \mathbf{C} \cdot \Delta \bar{\mathbf{X}}(s) = -\mathbf{J} \cdot \Delta \bar{\mathbf{X}}(s) \quad (3.43)$$

In the case of large circuits with a significant number of harmonics, Bolcato [6] uses an improved Arnoldi method to compute the eigenvalue of the characteristic system.

Two remarks are to be made about the characteristic system:

1. In the ac case around a dc solution $\bar{x}_o(t) = \bar{X}_o$, (3.42) holds with $[\mathbf{\Omega}] = 0$ and reduces to the eigenvalue analysis presented in Section 3.1.1.1. All the conclusions given in this paragraph are still valid
2. In the large-signal periodic steady-state regime, the eigenvalues obtained from (3.43)

$$s_i = \sigma \pm j(\omega_i + k\omega_0)$$

are approximately periodic with a period of ω_0 [7, 8] and are strongly related to the characteristics exponents of the Poincaré map (see Chapter 5) of the solution obtained.

Small and large signal instabilities of a capacitively coupled oscillator will be illustrated in Example 3.2.

Example 3.2: Capacitive oscillator

To illustrate this topic, let us consider a very simple example. Consider the simplified capacitively coupled van der Pol oscillator given in Figure 3.6.

The following equations govern the circuit:

$$\begin{cases} -C_1 \frac{dv_1}{dt} + C_1 \frac{dv_2}{dt} + i_{NL}(v_2) + i_{L_1} = 0 \\ (C_1 + C) \frac{dv_1}{dt} - C_1 \frac{dv_2}{dt} + \frac{v_1}{R} + i_L = 0 \\ L \frac{di_L}{dt} - v_1 = 0 \\ L_1 \frac{di_{L_1}}{dt} + R_1 i_{L_1} - v_2 + V_{dc} = 0 \end{cases} \quad (3.44)$$

For this circuit we have

$$\begin{aligned} [\bar{x}] &= [v_1, v_2, i_L, i_{L_1}]^T; [\bar{u}] = [0, 0, 0, V_{dc}]^T \\ [\bar{q}] &= [C_1(v_2 - v_1), (C_1 + C) \cdot v_1 - C_1 v_2, L \cdot i_L, L_1 \cdot i_{L_1}]^T \end{aligned} \quad (3.45)$$

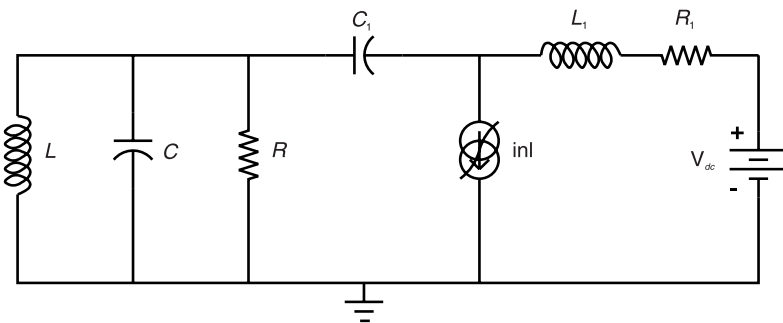


Figure 3.6 Schematic of the capacitively coupled oscillator: $L = 0.8$ nH; $C = 31.7$ pF; $R = 35\Omega$; $C_1 = 50$ pF; $L_1 = 10$ nH; $a = 0.04$ s; $b = 0.0025$ s \cdot v⁻².

$$[\bar{f}] = [f_1, f_2, f_3, f_4]^T \text{ with } \begin{cases} f_1 = i_N(\nu_2) + i_L \\ f_2 = \frac{\nu_1}{R_2} + i_L \\ f_3 = -\nu_1 \\ f_4 = R_1 i_{L1} - \nu_2 \end{cases} \quad (3.46)$$

$$i_{NL}(\nu_2) = -a \cdot \nu_2 + b \cdot \nu_2^3 \quad (3.47)$$

Letting

$$g_m = \frac{\partial i_{NL}(\nu_2)}{\partial \nu_2} = -a + b \cdot \nu_2^2 \quad (3.48)$$

the capacitances and conductance matrixes are given by

$$[\bar{C}] = \begin{bmatrix} -C_1 & C_1 & 0 & 0 \\ C_1 + C & -C_1 & 0 & 0 \\ 0 & 0 & L & 0 \\ 0 & 0 & 0 & L_1 \end{bmatrix} \text{ and } [\bar{G}] = \begin{bmatrix} 0 & g_m & 0 & 1 \\ \frac{1}{R} & 0 & 1 & 0 \\ -1 & 0 & 0 & 0 \\ 0 & -1 & 0 & R_1 \end{bmatrix} \quad (3.49)$$

The steady-state dc solution for the circuit is $[X_0] = [0, V_{20}, 0, I_{NL0}]^T$, where the dc values are the solutions of the following nonlinear equation:

$$\begin{aligned} I_{NL0} - a \cdot V_{20} + b \cdot V_{20}^3 &= 0 \\ R_1 \cdot I_{NL0} + V_{dc} - V_{20} &= 0 \end{aligned} \quad (3.50)$$

Thus, the stability is given by the sign of the real part of the eigenvalues of the characteristic system (3.43) evaluated at the dc. The loci of the four eigenvalues are given in Figure 3.7 when the resistance R_1 is varied from 1Ω to 20Ω . From the plot of Figure 3.7(b) it can be deduced that an oscillation at $f_0 \approx \frac{1}{2\pi\sqrt{LC}} = 1 \text{ GHz}$ is always possible. However, the plot of the low-

frequency poles shown in Figure 3.7(a) shows that for values of the resistance R_1 below a critical value, a low-frequency oscillation can also take place.

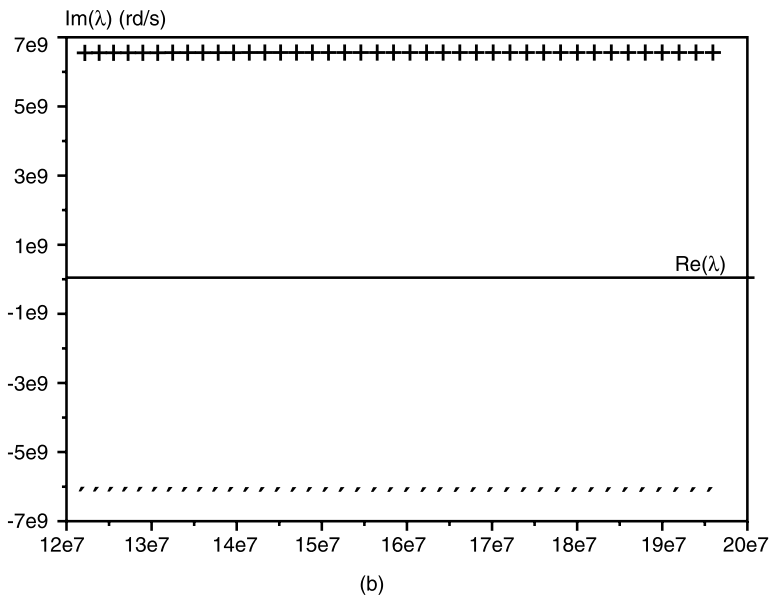
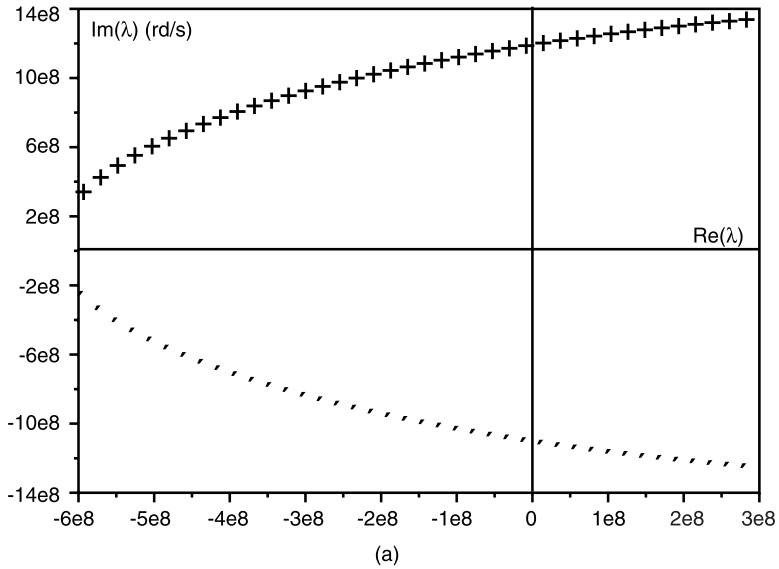


Figure 3.7 Plots of the loci of the four poles of the circuit of Figure 3.6 when the resistance R_1 is varied from 1Ω to 20Ω : (a) low-frequency poles, and (b) high-frequency poles.

Let us now examine the large-signal steady-state regime obtained from a harmonic-balance analysis as explained in Chapter 2. To obtain the solution,

we have assumed an oscillation at a frequency close to the resonant frequency of the tank, that is, $f_0 \approx \frac{1}{2\pi\sqrt{LC}} = 1$ GHz. A solution is readily obtained with

five significant harmonics. The spectrum of the control voltage of the nonlinearity and the time-domain waveforms obtained from harmonic-balance analysis and time-domain analysis are shown in Figure 3.8. From these plots it is evident that the high-frequency solution obtained from the harmonic-balance analysis is not the correct one. Thus, we have to perform a stability check of the solution. This can be done by calculating the generalized eigenvalues of the characteristic system given in (3.43), which is recalled here for convenience:

$$s \cdot \mathbf{C} \cdot \Delta \bar{\mathbf{X}}(s) = -\mathbf{J}_0 \cdot \Delta \bar{\mathbf{X}}(s)$$

where \mathbf{J}_0 is the Jacobian of the nonlinear system, obtained at the convergence of the oscillatory solution, and \mathbf{C} is the $N_H \times N_H$ expansion of the static generalized capacitance matrix $[\bar{\mathbf{C}}]$. Thus, \mathbf{C} is given by

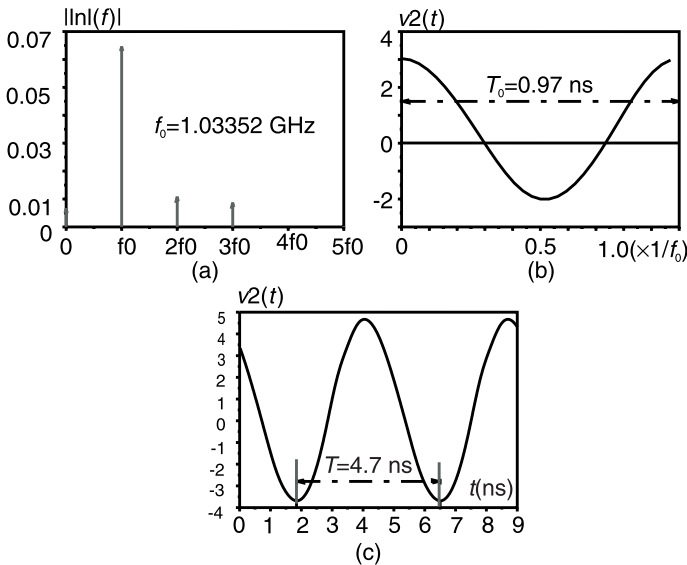


Figure 3.8 Solutions obtained for the capacitively coupled oscillator with $V_{dc} = 0.5$ V and $R_1 = 1\Omega$: (a) spectrum of the control voltage of the nonlinearity obtained from the harmonic-balance analysis, (b) corresponding time-domain waveform, and (c) time-domain wave form obtained from a temporal analysis.

$$C = \begin{bmatrix} [-C_1] & [C_1] & [0] & [0] \\ [C_1 + C] & [-C_1] & [0] & [0] \\ [0] & [0] & [L] & 0 \\ [0] & [0] & [0] & [L_1] \end{bmatrix}$$

where $[C_i] = \underbrace{\begin{bmatrix} C_i & 0 & 0 \\ 0 & \ddots & 0 \\ 0 & 0 & C_i \end{bmatrix}}_{N_H}$ is the $N_H \times N_H$ block expansion of a particular capacitance element. Note that in this example the block expansions are diagonal as all the reactive elements are linear. In the case of a nonlinear reactive element, the block expansion is constituted of the Fourier coefficients of the nonlinear element.

The generalized eigenvalues of the characteristic system are given in Figure 3.9. From this figure it appears that a set of eigenvalues have a positive real part, thus denoting the instability of the solution obtained through the harmonic-balance analysis. Moreover, a careful examination of those eigenvalues brings some interesting remarks. At first, as the solution is self-oscillatory,

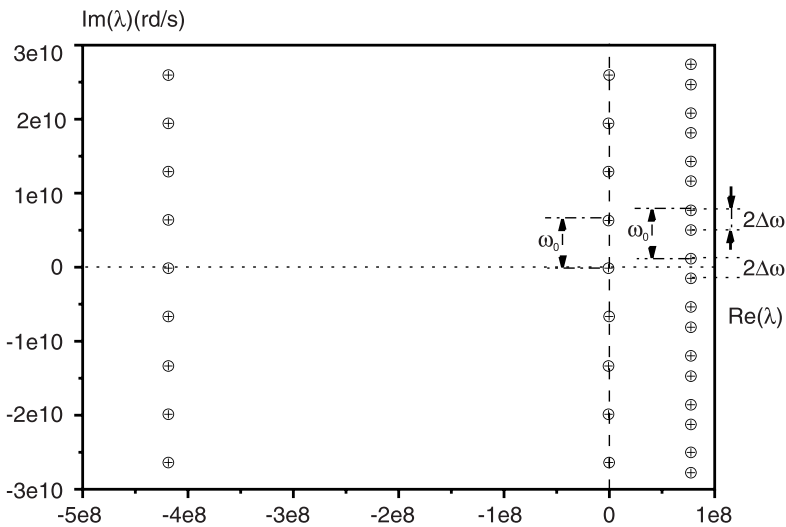


Figure 3.9 Eigenvalues of the characteristic system. Only the eigenvalues' corresponding four harmonics of the steady-state solution are plotted.

the Jacobian matrix of the nonlinear system must be zero. This implies that one eigenvalue must be exactly zero. We can also note in Figure 3.9 the quasiperiodicity of the eigenvalues with a period equal to the fundamental angular frequency given by the tank.

The location of the positive real-part poles requires some comment. As can be seen in Figure 3.9, poles with a positive real part are grouped into a cluster around angular frequencies $k \cdot \omega_0$, and the distance $\Delta\omega$ between two poles is related to the second resonant frequency of the circuit, that is

$$\Delta\omega \cong \frac{1}{\sqrt{L_1 C_1}} = 1.410^9 \quad \text{rd /sec} \quad (3.51)$$

which is precisely the frequency obtained for the solution shown in Figure 3.8(c).

3.2.3 Stability Analysis of Distributed Circuits

3.2.3.1 General Case

The previous approach, based on the calculation of the poles of the conversion matrix, cannot hold for distributed circuits containing transmission lines unless an equivalent rational function is determined to approximate the frequency response of the perturbed circuit. In the general case, the Nyquist approach can cope with this problem either by inspection of a determinant function or by inspection of complex eigenvalues of the characteristic system. Let us recall here the characteristic system derived in (3.37):

$$\bar{\Gamma}(s) \cdot \Delta\bar{X}(s) = (s \cdot \bar{C} + [\Omega] \cdot \bar{C} + \bar{G} + \bar{Y}(s)) \cdot \Delta\bar{X}(s) = 0 \quad (3.52)$$

Thus, the stability of the nonlinear circuit will be determined by the roots of the following equation:

$$\Delta(s) = \det(\bar{\Gamma}(s)) = 0 \quad (3.53)$$

Stability will be ensured if all the roots of (3.52) have a negative real part.

It can be shown [9] that the determinant function can be expanded under the form

$$\det(\bar{\Gamma}(s)) = \det(\bar{\Gamma}(\infty)) \cdot \frac{\prod_j (s - z_j)}{\prod_i (s - p_i)} \quad (3.54)$$

If no cancellation between poles and zeros of the determinant function occurs, and if there are no zeros at infinity, that is, if

$$\det(\Gamma(\infty)) \neq 0 \quad (3.55)$$

then a Nyquist approach can be applied to the determination of the number of zeros with positive real parts, as it can be done in the linear case. Thus, the determination of the stability necessitates an evaluation of the determinant of the general conversion matrix for real frequencies:

$$\Delta(j\omega) = \det(\bar{\Gamma}(j\omega)) = 0 \quad (3.56)$$

However, for microwave circuits, it is not so easy to deal with the general determinant function, which can be of a very high degree. Thus, a modification of the dimension of the characteristic system allows a feedback representation of the characteristic system.

3.2.3.2 The Feedback Formulation

Consider the frequency divider circuit constituted of a *field effect transistor* (FET) embedded in a large multidimensional passive circuit as represented in Figure 3.10. This is representative of the type encountered in microwave circuits.

Reordering the unknowns of the circuit, the vector $\bar{x}(t)$ of the harmonic-balance system can be put in the following form:

$$\bar{x}(t) = [\nu_G(t), \nu_D(t) | \bar{x}_i(t)] \quad (3.57)$$

where $\nu_G(t)$ $\nu_D(t)$ are the controlling voltages of the nonlinearities of the transistor and $\bar{x}_i(t)$ is the vector of inner variables of the linear embedding circuit. Eliminating the inner variables by using the linear Kirchoff's equations involved in the general system (3.28), we obtain the reduced harmonic-balance system described in the Chapter 2 that reads for the particular circuit of Figure 3.10:

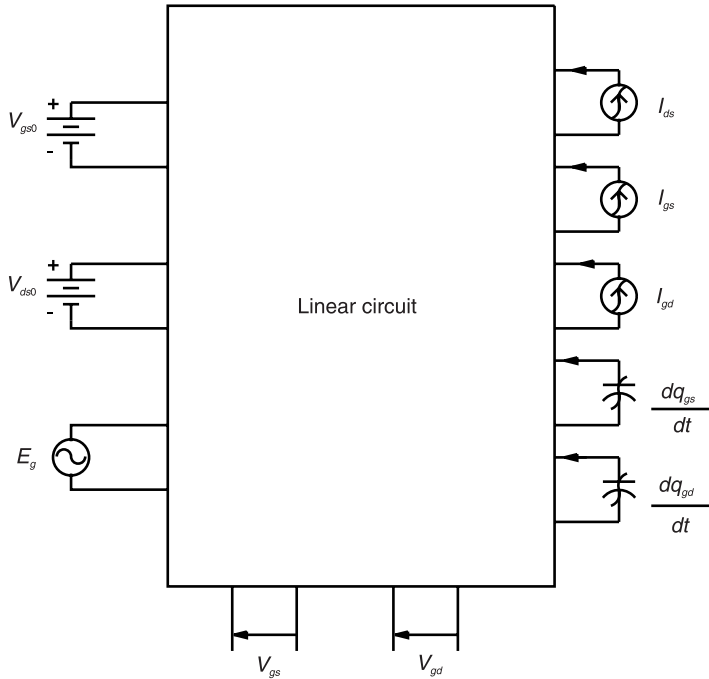


Figure 3.10 Circuit for reduction of the general equation.

$$\begin{bmatrix} v_g(t) \\ v_d(t) \end{bmatrix} + \mathbf{z}(t) * \begin{bmatrix} i_{gs}(t) \\ i_{gd}(t) \\ i_{ds}(t) \\ dq_{gs}(t)/dt \\ dq_{gd}(t)/dt \end{bmatrix} + \mathbf{a}(t) * \bar{\mathbf{e}}(t) = 0 \quad (3.58)$$

where $\left[i_{gs}(t) \ i_{gd}(t) \ i_{ds}(t) \ \frac{dq_{gs}(t)}{dt} \ \frac{dq_{gd}(t)}{dt} \right]^T$ is the vector of nonlinear currents and charges, $\mathbf{z}(t)$ is the impedance matrix linking the control voltages and the nonlinear currents, $\mathbf{a}(t)$ is the transfer matrix between the independent sources and the control voltages and where * stands for the convolution product.

Thus, the characteristic system of the harmonic-balance equation reads

$$[\mathbf{I} + \mathbf{Z}(s) \cdot \mathbf{U}] \cdot \begin{bmatrix} \Delta V_g \\ \Delta V_d \end{bmatrix} = 0 \quad (3.59)$$

where \mathbf{I} is the identity matrix and \mathbf{U} is the matrix of derivatives of the nonlinearities. Then, the stability is determined by the roots of

$$\det[\mathbf{I} + \mathbf{Z}(s) \cdot \mathbf{U}] = 0 \quad (3.60)$$

When more than one transistor is involved in the circuit, the previous equation remains valid by concatenating all the control voltages of the transistors, leading to a multidimensional equation of the type (3.60). Notice that (3.60) is written as a general multidimensional equation. Thus, the theory of stability of feedback systems is valid. Moreover, the matrix of the imbedding impedances is purely passive and, thus, have no poles with positive real parts. The analysis of an analog frequency divider given in Example 3.3 will illustrate the previous conclusions.

Example 3.3: Frequency divider [10]

The circuit given as an example is an analog regenerative frequency divider that is shown in Figure 3.11. This frequency divider is built from a 3 GHz series resonant oscillator. The subharmonic oscillation is synchronized by an input generator delivering the power at 6 GHz. The bifurcation diagram of the frequency divider is shown in Figure 3.12. It has been obtained using techniques of bifurcation analysis given in Chapter 4. The diagram exhibits distinct regions corresponding to the various behaviors of the divider. In region I, where point A is located, corresponding to a low injection power and a frequency out of the synchronization range, the circuit behaves as a mixing oscillator with two incommensurate frequencies corresponding to the input frequency and the oscillation frequency, respectively. In region II, where point B is located, for a high power injected and an input frequency outside the frequency range, the autonomous oscillation is quenched and a single frequency equal to the input frequency can be observed. Finally, the frequency division takes place in region III and is maintained for a frequency range that depends on the input power. Let us now examine the stability of the various regimes and particularly the stability of the regimes corresponding to points A and B of the diagram, respectively.

The steady-state regime at points A and B has been obtained using a single-tone harmonic-balance process with only the input frequency taken into account. Thus, the waveforms obtained are periodic with a period equal to the period of the generator. The stability has been checked using the Nyquist plot

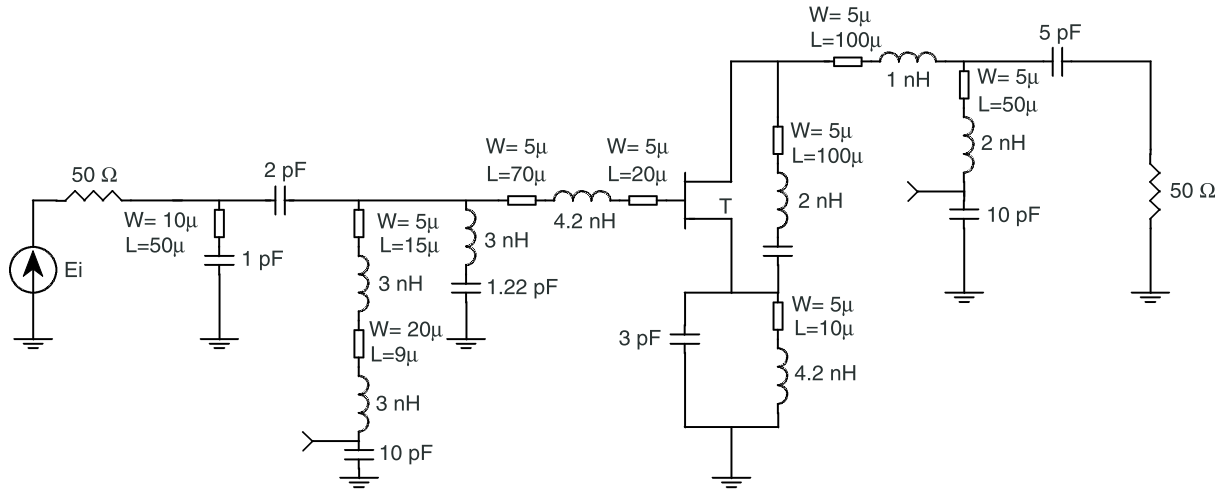


Figure 3.11 Schematic of an MMIC analog frequency divider 6–3 GHz.

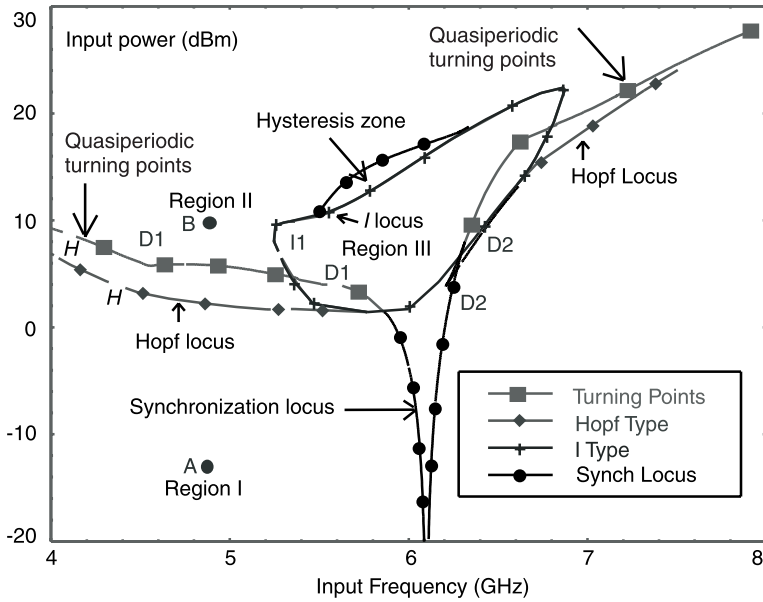


Figure 3.12 Bifurcation diagram of the frequency divider.

of the characteristic determinant $\det[\mathbf{I} + \mathbf{Z}(j\omega) \cdot \mathbf{U}] = 0$. The plots are shown in Figure 3.13.

As can be noticed in this figure, for the regime corresponding to point A, the Nyquist plot encircles the origin clockwise, thus denoting an unstable regime. Moreover, the plot intersects the negative real axis at a frequency $f_r = 2$ GHz. This frequency represents the difference between the input frequency $f_{in} = 5$ GHz and the autonomous frequency $f_a = 3$ GHz. This indicates that in the steady-state nonlinear regime, linear combinations of the input frequency and the resonant frequency $f_r : f = m \cdot f_r + n \cdot f_{in}$ will be found in the signal spectrum as shown in Figure 3.14. In this case, the autonomous frequency corresponds to $n = 1$ and $m = -1$.

Examining the Nyquist plot for the regime corresponding to point B leads to the conclusion that the calculated steady state is stable and that there are no other frequencies than the input frequency and its harmonics: $f = n \cdot f_{in}$.

3.2.4 Characteristic Loci [7]

In the case of pole-zeros cancellation, the previous approach fails to predict the stability of the circuit. Thus, we have to resort to the eigenvalues approach.

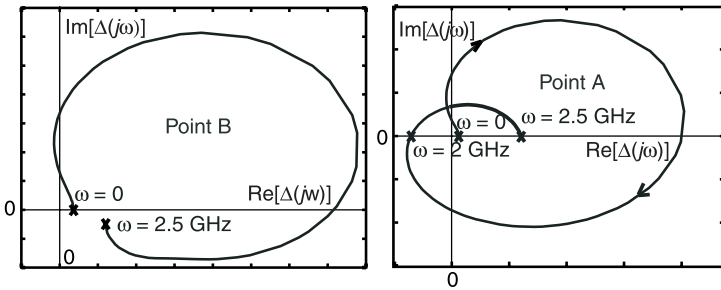


Figure 3.13 Nyquist plots corresponding to periodic steady-state regimes of points A and B.

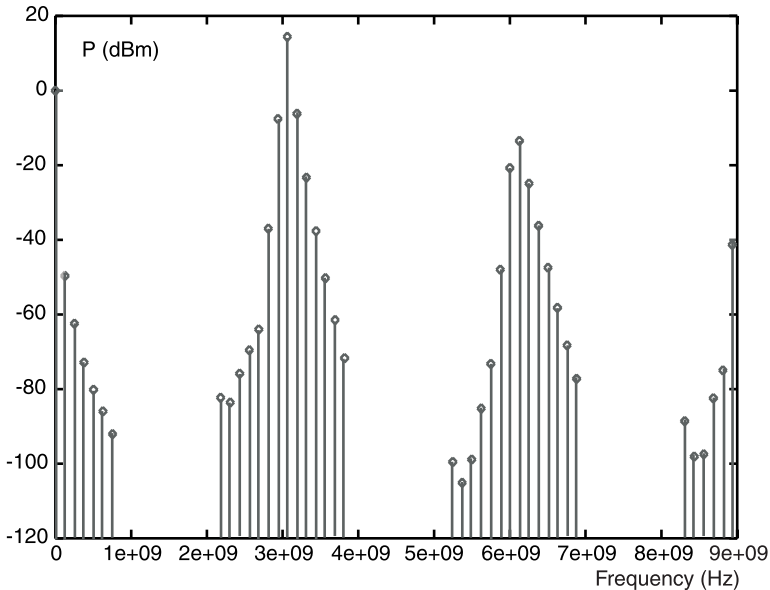


Figure 3.14 Spectrum of the steady-state regime at point A.

Instead of calculating the determinant function, the set of eigenvalues of the characteristic system can be evaluated for all frequencies of interest, and the zeros of those eigenvalues are located through a Nyquist analysis. More precisely, if we consider the characteristic matrix given in (3.59) and suppose that this matrix has a dimension M . Then there exist M eigenvalues $\lambda_m(s) : 1 \leq m \leq M$ that, for a particular value of s , are solutions of the polynomial equation

$$a_m(s) \cdot \lambda^m + a_{m-1}(s) \cdot \lambda^{m-1} + \dots + a_0(s) = 0 \quad (3.61)$$

However, the roots of (3.61) are not rational functions of s and can contain up to m th roots of polynomials in s which are multivalued. For example, consider the following second-order equation:

$$\lambda^2 - 2 \cdot b(s) \cdot \lambda + c = 0 \quad (3.62)$$

the solutions of which are given by

$$\begin{aligned} \lambda_1 &= b(s) \pm \sqrt{\delta(s)} = b(s) \pm \sqrt{b^2(s) - c(s)} \\ \lambda_2 & \end{aligned} \quad (3.63)$$

If the complex function \sqrt{z} has a branching point at $z = 0$, then the complex functions $\lambda_1 ; \lambda_2$ will have also branching points corresponding to $\delta(s) = 0 \Rightarrow \lambda_1 = \lambda_2$. Letting $\delta(s) = r \cdot e^{j\vartheta}$, we have

$$\lambda_1(s) = b(s) + \sqrt{r} \cdot e^{j \frac{\vartheta + 2k\pi}{2}} \quad (3.64)$$

For k odd, the second determination of $\lambda_1(s)$ is nothing else but $\lambda_2(s)$. Thus, the characteristic loci $L_1(s)$ and $L_2(s)$ will be constituted alternately of the eigenvalues $\lambda_1(s)$ and $\lambda_2(s)$ in the following manner:

Suppose that $s_1 < s_2 < s_3 < \dots$ are the pulsations, such that $\delta(s_1) = \delta(s_2) = \delta(s_3) = \dots = 0$ we will have

$$\begin{aligned} 0 < s < s_1 & \quad L_1(s) = \lambda_1(s) \quad L_2(s) = \lambda_2(s) \\ s_1 < s < s_2 & \quad L_1(s) = \lambda_2(s) \quad L_2(s) = \lambda_1(s) \\ s_2 < s < s_3 & \quad L_1(s) = \lambda_1(s) \quad L_2(s) = \lambda_2(s) \end{aligned}$$

An example of characteristic loci for the circuit of Figure 3.15 is given in Figure 3.16. As can be seen, the characteristic loci $L_1(j\omega), L_2(j\omega)$ differ from the loci defined by the eigenvalues: $\lambda_1(j\omega), \lambda_2(j\omega)$.

The previous approach prevents pole-zero cancellation. However, its practical implementation remains difficult because of the sorting that must be performed on a large set of eigenvalues for multidimensional systems. Thus, this method will be used when there are some doubts about as to the decision to make after the determinant approach.

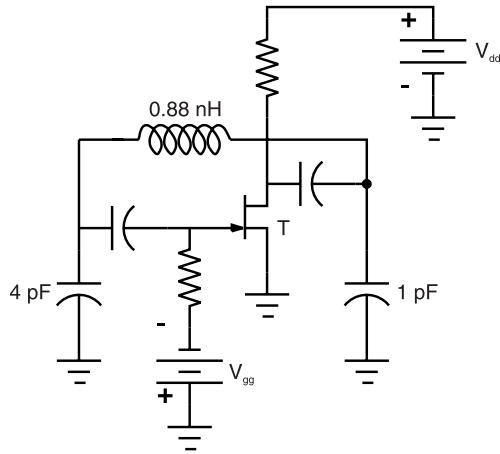


Figure 3.15 FET Colpitts oscillator.

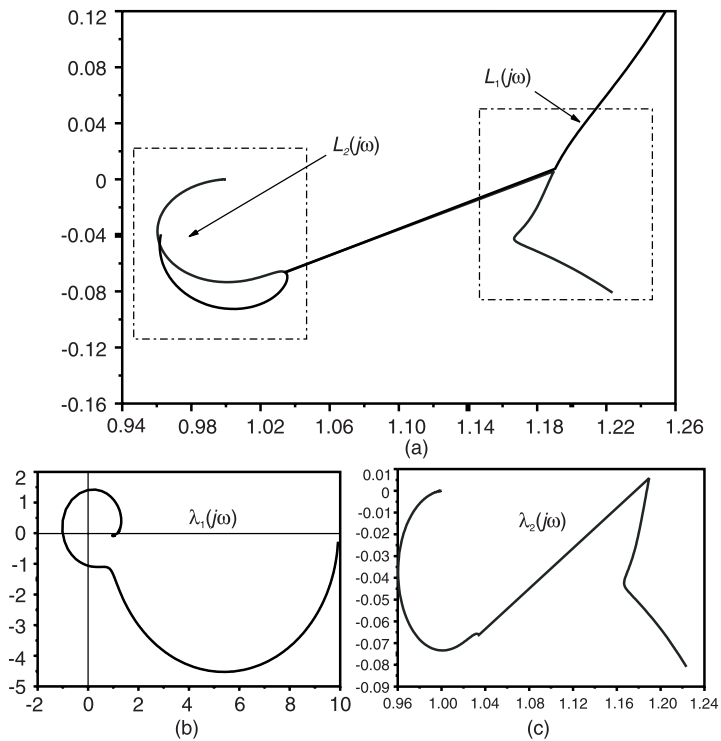


Figure 3.16 Example of characteristic loci for the circuit of Figure 3.15: (a) characteristic locii and (b) and (c) locii of the two eigenvalues.

3.2.5 The Negative Impedance Approach [11]

The last approach presented in this chapter relies on the negative impedance concept. Consider the general linearized system (3.52). If a small perturbation current I_k is injected at a particular node k , the resulting voltage V_k can be expressed as

$$V_k(s) = \begin{bmatrix} 0 & \dots & 1 & \dots & 0 \\ & & \text{\small kth} & & \end{bmatrix} [s \cdot \bar{C} + \bar{G} + \bar{Y}(s)]^{-1} \begin{bmatrix} 0 \\ \vdots \\ I_k \\ \vdots \\ 0 \end{bmatrix} \quad (3.65)$$

As can be seen from (3.65), the node voltage V_k is given by

$$V_k(s) = \frac{\gamma_{kk}(s)}{\det[s \cdot \bar{C} + \bar{G} + \bar{Y}(s)]} \cdot I_k \quad (3.66)$$

where $\gamma_{kk}(s)$ is the (k, k) th term of the transpose of the comatrix of

$$\Gamma(s) = [s \cdot \bar{C} + \bar{G} + \bar{Y}(s)]$$

Thus, the poles of the closed-loop transfer function

$$H_k(s) = \frac{V_k(s)}{I_k} \quad (3.67)$$

are constituted of the zeros of the determinant function, plus the poles of $\gamma_{kk}(s)$. Note that the transfer functions at the various nodes of the circuit share the same poles corresponding to the zeros of the determinant function. Thus, the stability of the circuit can be investigated using the frequency response of the closed-loop transfer function at any node of the circuit. In [11] the problem of pole-zero cancellation is avoided by identifying the poles and zeros of the transfer function using readily available identification methods in general purpose software, such as [12–14]. The injection circuit is shown in Figure 3.17.

The main advantage of this method is the simplicity of the measurement process and the ability to cope with pole-zero cancellation through the identification process. However, one must be careful with the poles and zeros obtained, as unstable poles can be numerically created by the identification method [14].

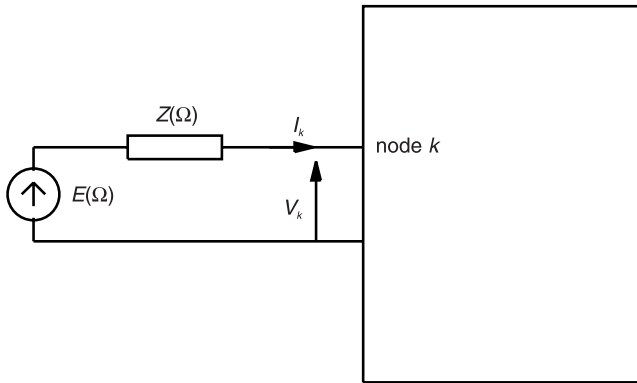


Figure 3.17 Injection circuit for the stability checking of nonlinear circuits in the large-signal regime.

3.3 The Open-Loop Approach

The open-loop approach relies on the works of Bode on electronic circuits [15, 16]. It provides a method that can overcome the limitations inherent to the Rollet Factor calculation for multidevice circuits, as pointed out by Ohtomo [17] and Platzker et al. [18]. They have recently been applied to microwave circuits [18] in the linear case and extended to the nonlinear large-signal regime by Mons et al. [19, 20]. They provide the circuit designer with a rigorous criterion for stability checking that can be easily implemented in common CAD packages.

Let us first recall some of the terminology that will be used in the following. Consider the general feedback system of Figure 3.18.

We have

$$\begin{aligned}
 y &= G \cdot e & d &= y - G \cdot H \cdot y = G \cdot u \\
 r &= H \cdot y & \text{and } r &= G \cdot H \cdot e \\
 e &= u + r & y &= \frac{G}{1 - GH} \cdot u
 \end{aligned}
 \tag{3.68}$$

In (3.68), G is the direct transfer function, H is the return transfer function, $-GH$ is what Bode calls the return ratio and $d = y - G \cdot H \cdot y = (1 - G \cdot H) \cdot y$ is the return difference. Finally $W = \frac{G}{1 - GH}$ is the closed-loop transfer function.

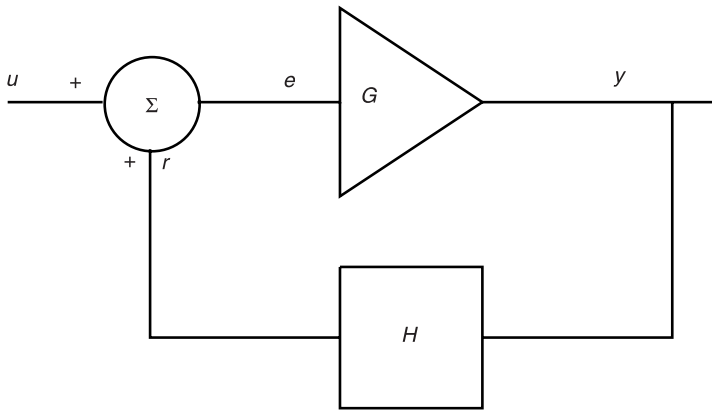


Figure 3.18 General *single-input-single-output* (SISO) feedback system.

3.3.1 The Bode, Platzker Approach for Linear Circuits

3.3.1.1 The One-Transistor Case

The Bode approach relies on the fact that instabilities can take place in an electronic circuit due to the gain of active devices. For a transistor (FET or bipolar), the activity is due to controlled output current sources.

Taking into account the controlling voltage, the circuit for one transistor can be represented as shown in Figure 3.19(a). Four ports may be defined corresponding to the input (port-1), the output (port-2), the control voltage (port-3), and the voltage controlled current source (port-4). The embedding circuit has $N-4$ nodes, and the general equation of the circuit in the frequency domain reads

$$\begin{bmatrix} Y_{11}(s) & Y_{12}(s) & Y_{13}(s) & Y_{14}(s) & \cdot & \cdot & Y_{1,N}(s) \\ Y_{21}(s) & Y_{22}(s) & Y_{23}(s) & Y_{24}(s) & & & \\ Y_{31}(s) & Y_{32}(s) & Y_{33}(s) & Y_{34}(s) & & & \\ Y_{41}(s) & Y_{42}(s) & Y_{43}(s) & Y_{44}(s) & \cdot & \cdot & Y_{4,N}(s) \\ \cdot & & & \cdot & \cdot & & \\ \cdot & & & \cdot & \cdot & & \\ Y_{N1}(s) & & & Y_{N4}(s) & & & Y_{NN}(s) \end{bmatrix} \cdot \begin{bmatrix} V_1 \\ V_2 \\ V_3 \\ V_4 \\ \cdot \\ \cdot \\ V_N \end{bmatrix} = \begin{bmatrix} I_g \\ 0 \\ \cdot \\ \cdot \\ \cdot \\ 0 \end{bmatrix} \quad (3.69)$$

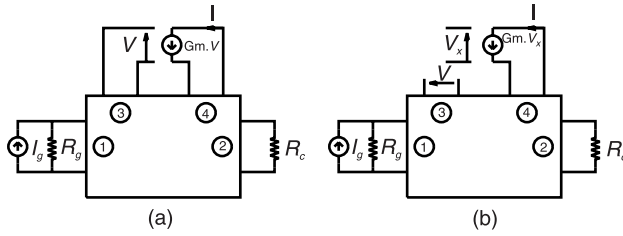


Figure 3.19 General circuit configuration for calculation of the open-loop circuit response: (a) voltage-controlled current source in the closed-loop configuration, and (b) open-loop configuration.

with $Y_{43}(s) = G_m + Y_{43}^0(s)$. Then the loop can be opened as shown in Figure 3.19(b), and (3.69) can be rewritten in the following form:

$$\begin{bmatrix} Y_{11}(s) & Y_{12}(s) & Y_{13}(s) & Y_{14}(s) & \cdots & Y_{1N}(s) \\ Y_{21}(s) & Y_{22}(s) & Y_{23}(s) & Y_{24}(s) & \cdots & Y_{2N}(s) \\ Y_{31}(s) & Y_{32}(s) & Y_{33}(s) & Y_{34}(s) & \cdots & Y_{3N}(s) \\ Y_{41}(s) & Y_{42}(s) & Y_{43}(s) & Y_{44}(s) & \cdots & Y_{4N}(s) \\ \vdots & \vdots & \vdots & \vdots & \ddots & \vdots \\ Y_{N1}(s) & \cdots & Y_{N4}(s) & \cdots & \cdots & Y_{NN}(s) \end{bmatrix} \begin{bmatrix} V_1 \\ V_2 \\ V'_3 \\ V_4 \\ \vdots \\ V_N \end{bmatrix} = \begin{bmatrix} 0 \\ 0 \\ \vdots \\ -G_m \cdot e \\ \vdots \\ 0 \end{bmatrix} \quad (3.70)$$

where I_g has been set to zero as the perturbation does not affect the input generator. Using Cramer's rule, the voltage V'_3 can be obtained as

$$V'_3 = \frac{-G_m \cdot e \cdot \Delta_{43}}{\Delta^0} \quad (3.71)$$

where $\Delta_0 = \Delta|_{G_m=0}$, and Δ_{43} is the cofactor of the (4,3)th term of the admittance matrix. The ratio

$$-\frac{V'_3}{e} = \frac{G_m \cdot \Delta_{43}}{\Delta^0} = RR \quad (3.72)$$

represents the return ratio (RR) and can be easily measured using conventional CAD software.

Then, the return difference function given by

$$F = 1 + RR = 1 + \frac{G_m \cdot \Delta_{43}}{\Delta^0} = \frac{\Delta^0 + G_m \cdot \Delta_{43}}{\Delta^0} = \frac{\Delta}{\Delta^0} = NDF \quad (3.73)$$

is the *normalized determinant function* (NDF) [18]. Thus, a Nyquist analysis or a pole-zero identification process can be applied either to the return ratio or the NDF to determine the stability of the circuit.

Note that the splitting of the admittance matrix into two parts as done in (3.70) allows us to write the characteristic equation (3.70) in the following form:

$$\begin{aligned} [\bar{Y}(s)] &= [\bar{Y}^0(s) + \bar{G}_m] \cdot \Delta \bar{V} = \\ [\bar{Y}^0] \cdot [\bar{I} + \bar{Z}^0 \cdot \bar{G}_m] \cdot \Delta \bar{V} &= 0 \end{aligned} \quad (3.74)$$

where $[\bar{G}_m] = \begin{bmatrix} 0 & 0 & 0 & 0 & \dots \\ 0 & 0 & 0 & 0 & \\ 0 & 0 & 0 & 0 & \\ 0 & 0 & G_m & 0 & \\ \vdots & & & & \ddots \end{bmatrix}$ is the transconductance matrix containing

only one nonzero term. Thus, from (3.74) we obtain

$$\Delta = \det[\bar{Y}(s)] = \det[\bar{Y}^0] \cdot \det[\bar{I} + \bar{Z}^0 \cdot \bar{G}_m] = \Delta^0 \cdot F \quad (3.75)$$

this expression, compared to (3.60), shows the equivalence between the NDF and the characteristic function in the feedback formulation of the harmonic-balance equation.

3.3.1.2 The Multitransistor Case

The previous approach can be extended to circuits containing more than one transistor. In this case, we face a multidimensional stability problem. This configuration is shown in Figure 3.20 where the active controlled P sources have been extracted.

The general transconductance matrix now contains P nonzero terms corresponding to the active current sources:

$$[\bar{\mathbf{G}}_m] = \begin{bmatrix} G_{m1} & 0 & 0 & \dots \\ 0 & G_{m2} & 0 & \\ 0 & 0 & \ddots & 0 & \dots \\ 0 & 0 & 0 & G_{mP} \\ \vdots & \vdots & \vdots & 0 & \ddots \end{bmatrix}$$

The relation stated for one transistor still holds and the NDF is given by

$$NDF = \frac{\Delta}{\Delta^0} = \det[\bar{\mathbf{I}} + \bar{\mathbf{Z}}^0 \cdot \bar{\mathbf{G}}_m] \quad (3.76)$$

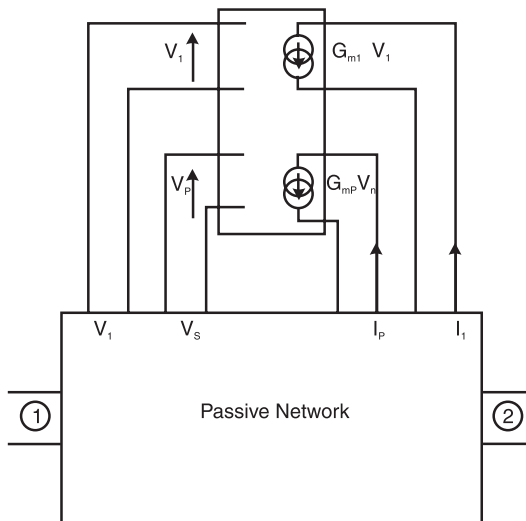


Figure 3.20 Configuration of the multitransistor circuit for the stability analysis.

Evaluation of the NDF is performed using a recursive process (see Appendix 3A). During this process, the P controlled sources are shut down successively, and the return ratios are measured using the open-loop configuration shown in Figure 3.21. Suppose that RR_i corresponding to the i th ($1 \leq i \leq P$) source is to be measured. Then the sources j , ($1 \leq j \leq i - 1$), are shut down, while the sources j ($i + 1 \leq j \leq P$) are in the nominal mode. The return ratio is then given by

$$RR_i = \frac{V_i^i}{e} \quad (3.77)$$

and the NDF is obtained from

$$NDF = \prod_{i=1}^P (1 + RR_i) \quad (3.78)$$

3.3.1.3 Practical Measurement of RR_i

To measure the various return ratios a modification of the equivalent circuit of transistor models is necessary. This modification is shown in Figure 3.22 for an

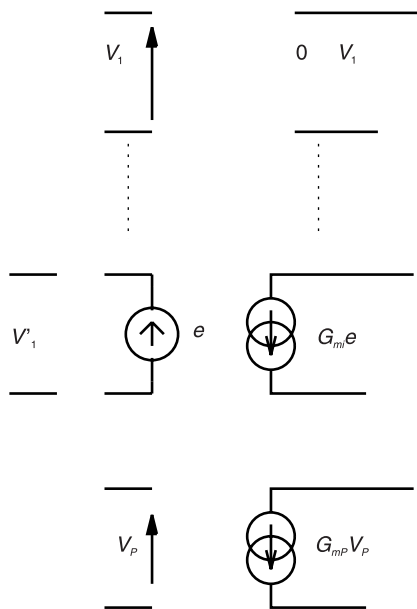


Figure 3.21 Evaluation of the i th return ratio for a multidevice circuit.

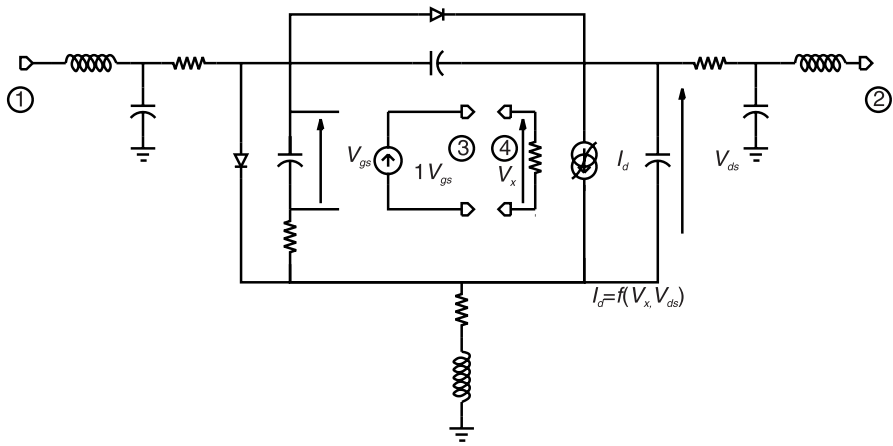


Figure 3.22 Modification of the equivalent circuit of an FET for stability analysis.

FET. The same circuit is also valid for the π_i representation of a bipolar transistor. The main current source of the transistor is now controlled by an external voltage V_x and the equivalent circuit of the transistor has two more access ports corresponding to the measuring port and to the control port. To calculate the NDF, the transistors must work in three regimes: (a) the nominal regime, (b) the open-loop regime, and (c) the shutdown regime. These three modes correspond to the three working configurations shown in Figure 3.23.

3.3.1.4 Remarks

While the NDF provides the circuit designer with a rigorous criterion for checking the stability of a circuit, it does not provide complete information on the electrical path involved in the oscillation birth. To get information about the location of the instability path when a potential oscillation has been

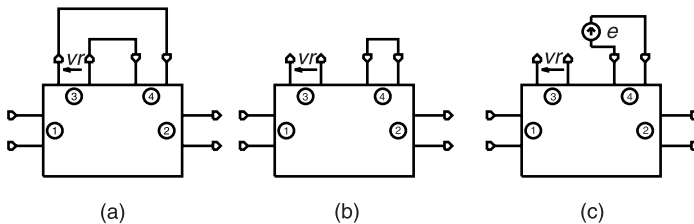


Figure 3.23 Connections required for the three working regimes: (a) nominal, (b) open loop, and (c) shutdown.

detected, we can examine the partial return difference functions [19]. Indeed, consider the two-stage power amplifier composed of transistors numbered one to six as shown in Figure 3.24.

The NDF of this circuit is of the form

$$\begin{aligned} NDF &= (1 + RR_1) \cdot (1 + RR_2) \cdot (1 + RR_3) \cdot (1 + RR_4) \\ &\quad \cdot (1 + RR_5) \cdot (1 + RR_6) \\ &= ND_1 \cdot ND_2 \cdot ND_3 \cdot ND_4 \cdot ND_5 \cdot ND_6 \end{aligned}$$

To get the correct result on the stability behavior of such a circuit, the various loops involved must be investigated. An example of the correct sequence for shutting down the transistors is given in Table 3.1.

In [19] the two configurations ND_2 and ND_5 are shown to be unstable with the same resonant frequency. This was predictable due to the symmetry of the circuit. However, the total NDF exhibits two encirclements of the origin that would lead to the conclusion that two different frequencies of oscillation would exist in the circuit. In fact, those two encirclements are due to the order of the unstable zero of the NDF.

Thus, individual examination of well chosen return difference functions allow us to locate the paths involved in the birth of the oscillation and to think about a possible correction of the circuit. In the previous case mentioned, the

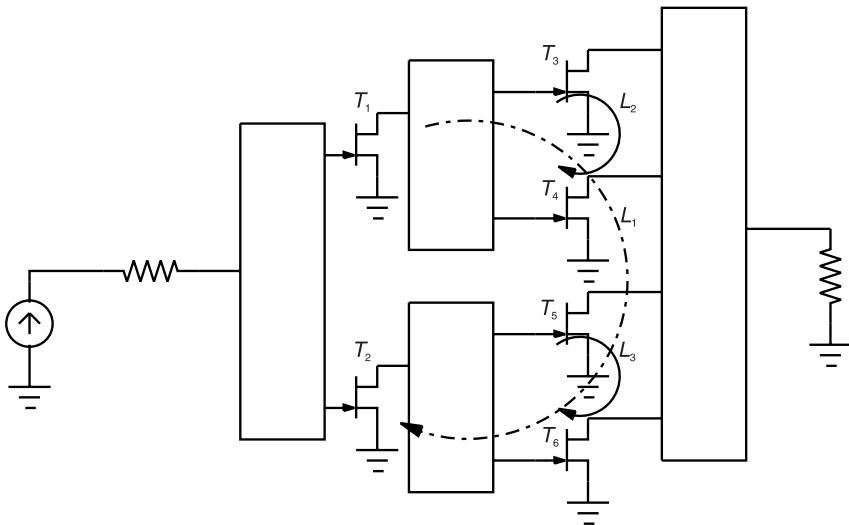


Figure 3.24 Two-stage FET power amplifier.

Table 3.1
Sequential Testing of Various Loops Involved in the Design

Measurement	Nominal	Shutdown	Open	Loop Involved
ND_1	T_2, T_3, T_4, T_5, T_6	—	T_1	L_1
ND_2	T_3, T_4, T_5, T_6	T_1	T_2	L_2
ND_3	T_4, T_5, T_6	T_1, T_2	T_3	—
ND_4	T_5, T_6	T_1, T_2, T_3	T_4	—
ND_5	T_6	T_1, T_2, T_3, T_4	T_5	L_3
ND_6	—	T_1, T_2, T_3, T_4, T_5	T_6	—

solution adopted was to equilibrate loops 1 and 3 with resistances between the gate of transistors T_2, T_3 and T_5, T_6 , respectively.

3.3.2 Extension of the Method for Multibias Circuits

The previous approach is well behaved for linear circuits. However, in the nonlinear design process, one has to know the stability behavior of the circuit as the bias is varied. To do that, a nonlinear model is required, and a slight modification of the open-loop method must be performed. This modification allows us to maintain the original circuit for the dc bias and to open the different loops for the injected ac signal. This can be done using a tracking filter, such as the one represented at Figure 3.25. The filter behaves as a short circuit at the injected frequency and an open circuit at dc. The impedance presented by the filter is shown in Figure 3.25, where the notch frequency is equal to the analysis frequency. Thus, the controlling voltage in the open-loop configuration is expressed as

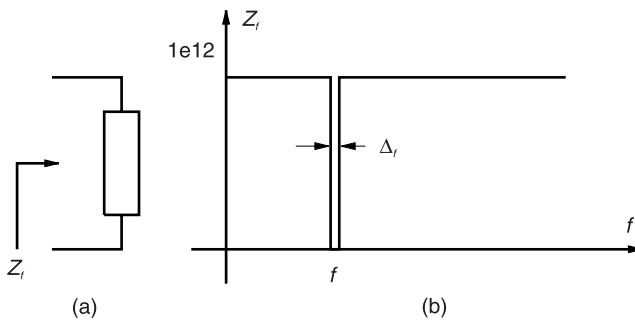


Figure 3.25 Structure of the tracking filter to isolate the dc component from the ac one: (a) structure of the filter and (b) frequency response.

$$v_x(t) = V_{GS,dc} + e(t) \quad (3.79)$$

and the three configurations are given in Figure 3.26. In this case, the small-signal circuit is directly calculated from the nonlinear model of the transistor.

A two-stage hetrojunction bipolar transistor power amplifier was tested using this technique [22]. The layout of the amplifier is given in Figure 3.27. The NDF of the circuit is given for various configurations. At first, when the design was tested on wafer, it showed low-frequency oscillations at a frequency of about 500 MHz. This instability was obtained from the NDF plot shown in Figure 3.28. To observe this instability, an electrical model shown in Figure 3.29 of the test bias card was used. However, when mounted on a chip carrier and with a carefull decoupling of bias, the amplifier was stable for all the bias points of interest as shown by the NDF plot of Figure 3.30. This demonstrates the ability of the method to handle large microwave circuits.

3.3.3 Extension of the Approach to Large-Signal Periodic Steady-State Regimes [19, 20]

As circuits like power amplifiers or oscillators are prone to instabilities in the nonlinear large-signal regime, it is interesting to extend the previous approach to this case. For this purpose, let us recall the general characteristic system stated in (3.52):

$$(\mathcal{L} \cdot [\bar{C}] + [\Omega] \cdot [\bar{C}] + [\bar{G}] + [\bar{Y}(s)]) \cdot [\Delta \bar{X}(s)] = 0$$

Reordering the vector of unknowns $\Delta \bar{X}(s)$ to isolate the P controlling voltages leads to the following system:

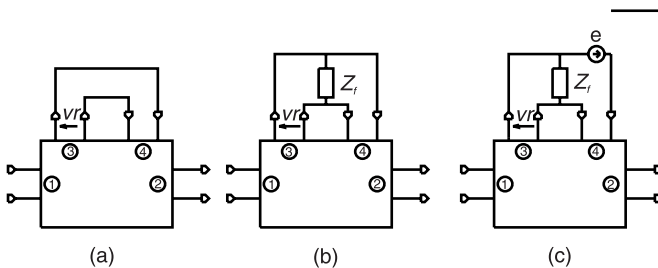


Figure 3.26 The three configurations used with the tracking filter.

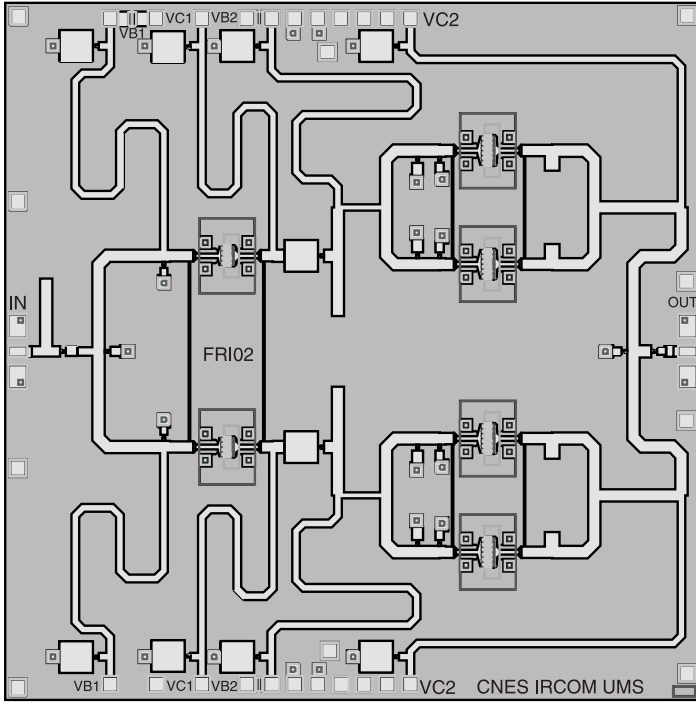
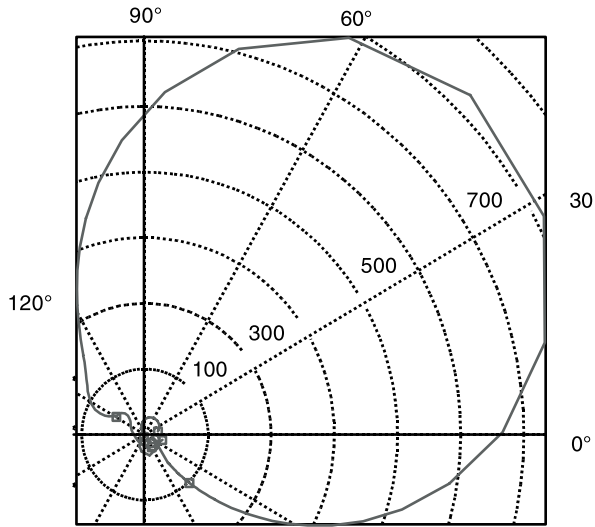


Figure 3.27 Layout of the power heterojunction bipolar transistor amplifier.

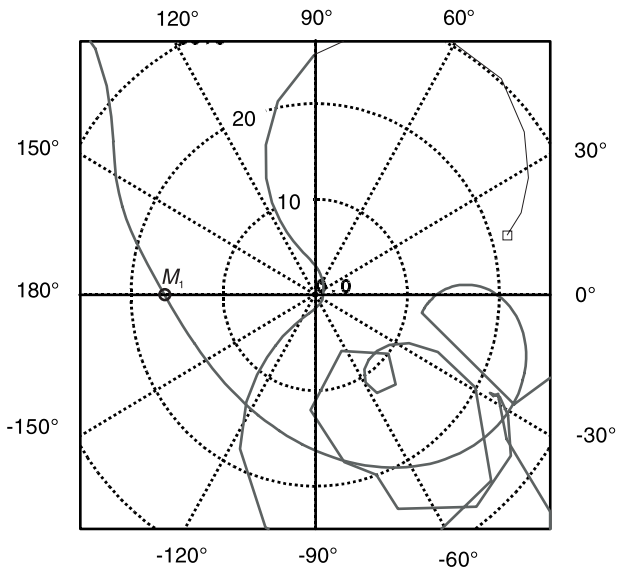
$$\begin{bmatrix} \bar{Y}_{cc}(s) + \bar{G}_m & \bar{Y}_{ci}(s) \\ \bar{Y}_{ic}(s) & \bar{Y}_{ii}(s) \end{bmatrix} \cdot \begin{bmatrix} \Delta \bar{X}_c(s) \\ \Delta \bar{X}_i(s) \end{bmatrix} = 0 \quad (3.80)$$

where

$$\bar{G}_m = \begin{bmatrix} \begin{bmatrix} G_{m1}^{(0)} & \dots & G_{m1}^{(-2N_H)} \\ \vdots & \ddots & \vdots \\ G_{m1}^{(2N_H)} & \dots & G_{m1}^{(0)} \end{bmatrix} & 0 & \dots \\ \vdots & \ddots & \vdots \\ \begin{bmatrix} G_{mP}^{(0)} & \dots & G_{mP}^{(-2N_H)} \\ \vdots & \ddots & \vdots \\ G_{mP}^{(2N_H)} & \dots & G_{mP}^{(0)} \end{bmatrix} \end{bmatrix} \quad (3.81)$$



(a)



Marker M_1 : $f_r=383$ MHz

(b)

Figure 3.28 Nyquist plot of the NDF taking into account the electrical model of the test bias card: (a) global plot and (b) zoom of the plot near the origin.

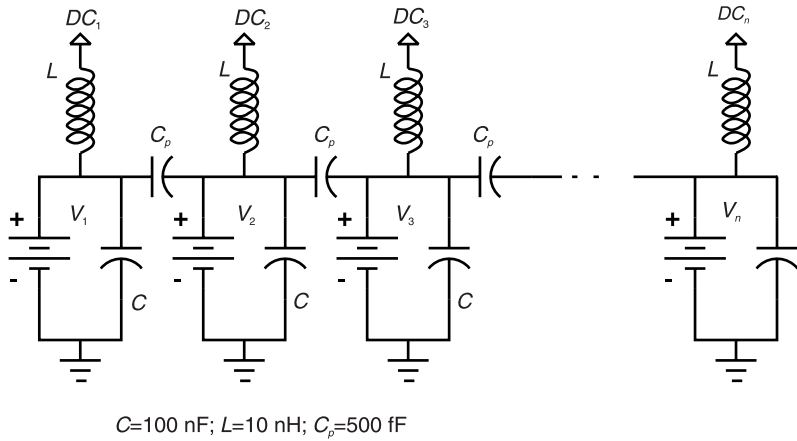


Figure 3.29 Model of the test bias card used for stability analysis of the power amplifier.

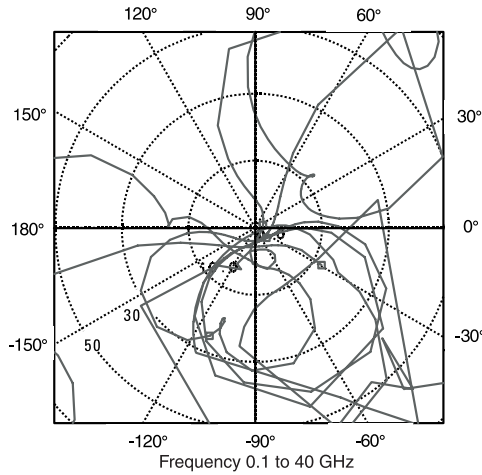


Figure 3.30 Nyquist plot of the NDF for carrier-mounted chip.

is constituted of the conversion matrixes of the controlled sources shown in

Figure 3.20. The $\Delta \bar{X}_c(s) = \left[\begin{matrix} \left[\Delta V_1^{(-N_H)}, \dots, \Delta V_1^{(0)}, \dots, \Delta V_1^{(N_H)} \right], \dots \\ \left[\Delta V_p^{(-N_H)}, \dots, \Delta V_p^{(0)}, \dots, \Delta V_p^{(N_H)} \right] \end{matrix} \right]^T$ is the

vector containing all the sidebands of the controlling voltages $x_c = [\nu_1, \dots, \nu_p]^T$, and $\Delta\bar{X}_i(s)$ is the vector containing the sidebands of the other internal unknowns. Eliminating the internal variables in (3.80), we obtain:

$$\left[[\bar{Y}_{cc}(s) + \bar{G}_m] - [\bar{Y}_{ci}(s) \cdot \bar{Y}_{ii}^{-1}(s) \cdot \bar{Y}_{ic}(s)] \right] \cdot \Delta\bar{X}_c(s) = 0 \quad (3.82)$$

that can be put under the form

$$\begin{aligned} & \left[\bar{Y}_0(s) + \bar{G}_m \right] \cdot \Delta\bar{X}_c(s) = \bar{Y}_0(s) \cdot \left[1 + \bar{Y}_0^{-1}(s) \bar{G}_m \right] \\ & \cdot \Delta\bar{X}_c(s) = 0 \end{aligned} \quad (3.83)$$

with

$$\bar{Y}_0(s) = \bar{Y}_{cc}(s) - \bar{Y}_{ci}(s) \cdot \bar{Y}_{ii}^{-1}(s) \cdot \bar{Y}_{ic}(s) \quad (3.84)$$

Equation (3.83) is of the same nature as (3.74), where the scalar values of the transconductances are replaced by the conversion matrixes corresponding to the controlled sources. Thus, the recursive method used to calculate the NDF in the previous paragraph can be used to obtain the various return ratios. Namely, the system

$$F(\bar{G}_m) = \left[1 + \bar{Y}_0^{-1}(s) \bar{G}_m \right] \quad (3.85)$$

can be expressed (as shown in Appendix 3A) as the product of the various return ratio matrixes \mathbf{RR}_i , $1 \leq i \leq P$, that is,

$$F(\bar{G}_m) = \prod_{i=1}^P [1 + \mathbf{RR}_i] \quad (3.86)$$

Thus, the stability of the large-signal steady-state regime can be checked by evaluating the various \mathbf{RR}_i , $1 \leq i \leq P$ matrixes. To do that, either a two-tone analysis involving the large-signal matrix at fixed frequency f_0 and the small-signal matrix at variable frequency f_p or, better yet, a large-signal/small-signal analysis when it is available, can be performed. In the case of a two-tone analysis, a filter must be used in the feedback loop to open the loop for the small signals and to let the large-signal components work in a closed-loop configuration. Such a filter has the configuration shown in Figure 3.31. It

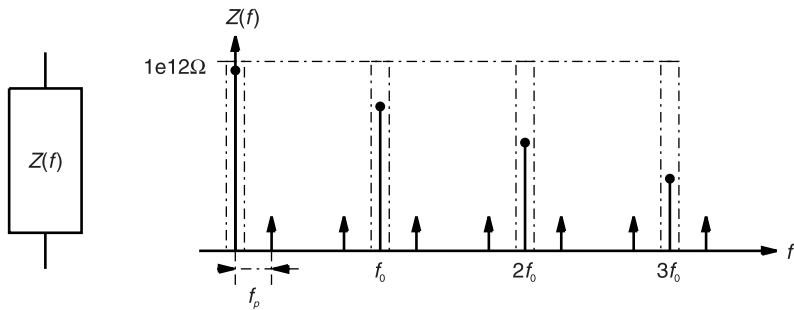


Figure 3.31 Structure of the tracking filter used for measuring the RR matrix RR_i $1 \leq i \leq P$.

presents an open circuit at frequencies $k \cdot f_0$ ($-N_H \leq k \leq N_H$) and a short circuit at all other frequencies.

The connection of the filter is made in the same manner as the connexion shown in Figure 3.26. Thus, we have for a particular source

$$v_x(t) = \sum_{k=-N_H}^{N_H} V_i^{(k)} \cdot e^{jk2\pi f_0 t} + e(t) \quad (3.87)$$

where the second right-hand side term is the small-signal perturbation at frequency $kf_0 + f_p$. Depending of the value chosen for k ($-N_H \leq k \leq N_H$), the sideband voltages are related to the perturbation by

$$\begin{bmatrix} \Delta V_i^{-N_H} \\ \vdots \\ \Delta V_i^0 \\ \vdots \\ \Delta V_i^{N_H} \end{bmatrix} = -[RR_i] \cdot \begin{bmatrix} 0 \\ \vdots \\ E_k \\ \vdots \\ 0 \end{bmatrix} \text{ } k\text{th frequency} \quad (3.88)$$

Thus, the injection of the perturbation signal at the frequency $kf_0 + f_p$ allows us to measure the column of the return ratio matrix relative to that particular frequency. Then, the frequency of the perturbation signal is swept with the following sweep plan:

$$f \in]0, f_0 / 2[\cup]f_0 / 2, f_0[\cup \dots \cup]kf_0 / 2, (k+1)f_0 / 2[\cup \dots$$

Frequencies close to $kf_0/2$ must be avoided. Indeed, the conversion matrix is not defined at those frequencies because signals at frequencies like $f_p = f_0/2$ and $f_0 - f_p = f_0/2$ sum up and are not distinguishable. Then, the various return ratio matrixes can be obtained using the same strategy as the one used in the linear case.

The previous method has been applied to various power amplifiers and oscillators using a standard CAD software. Details about the practical implementation in a standard CAD package can be found in [19]. To illustrate the results obtained using the nonlinear local stability analysis, consider the Ku-band MMIC power amplifier that is shown in Figure 3.32. It works at an input frequency of 12.6 GHz and has to deliver an output power of 1W with a 500-MHz bandwidth. Transistors used were GaInP/GaAs heterojunction bipolar transistor, each transistor having a $240\text{-}\mu\text{m}^2$ emitter area. Experimental data are shown in Figure 3.33. A sharp decrease of the power gain, the power-added efficiency, and the output power can be observed in this figure for an input power beyond 19 dBm. Spectrum measurements for two particular points in this area are shown in Figure 3.34 for input powers of 18.6 dBm and 22.9 dBm. A frequency division by two phenomena is observed in the first case; in

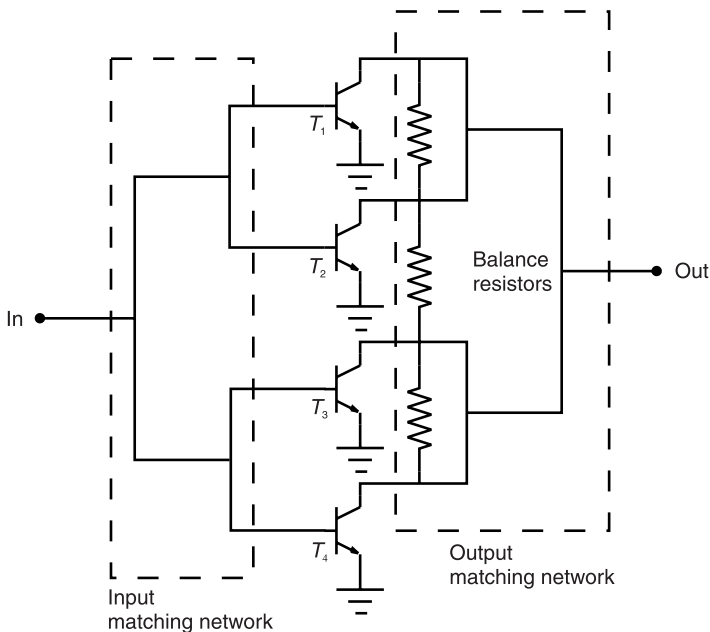


Figure 3.32 Ku-band MMIC power amplifier.

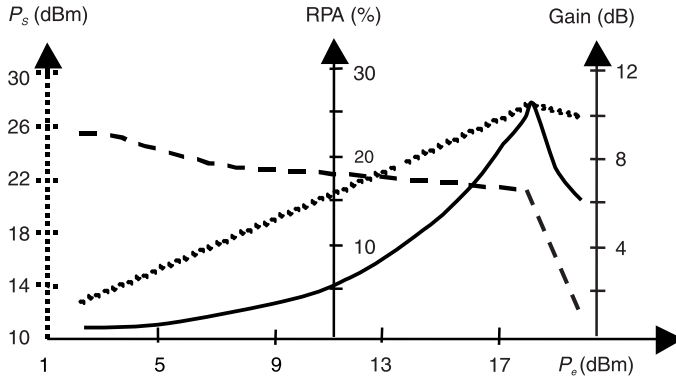


Figure 3.33 Experimental data of the Ku-band MMIC amplifier.

the second case, another spurious signal is superimposed on the frequency divided signal. Stability analysis has been performed for those two input powers. The return difference $RD_1 = \det(1 + \mathbf{RR}_1)$ of the first transistor is plotted in Figure 3.35(a) for an input power of 18.6 dBm. An encirclement of the origin can be observed in the figure where the Nyquist plot crosses the negative real axis at the frequency $f_p = 6.3$ GHz, thus denoting the birth of an oscillation at this frequency corresponding to $f_p = f_0/2$. The same return difference is shown in Figure 3.35(b) for an input power of 20 dBm. In this case, the Nyquist plot makes two encirclements of the origin, denoting the birth of a second instability in the circuit.

The fact that an instability appears by inspection of the first return difference function indicates that an internal feedback in the transistor itself is responsible for this instability. A way to remove those instabilities is to put a parallel resistance capacitance (RC) network in serie with the base of each transistor [23]. The RC network is calculated in such a way that it has a minimum impedance at f_0 (R shunted) and a maximum impedance at $f_0/2$. Moreover it has been noted that balance resistors inserted between the collectors of transistors did not improve the stability of the circuit in the large-signal configuration.

3.3.4 Large-Signal Stability Analysis Using a Simplified Filter

In the previous section it was shown how to measure the individual return ratio matrixes \mathbf{RR}_1 . This method provides the designer with a rigorous tool to detect large-signal instabilities, as shown in Section 3.3.3. However, this technique

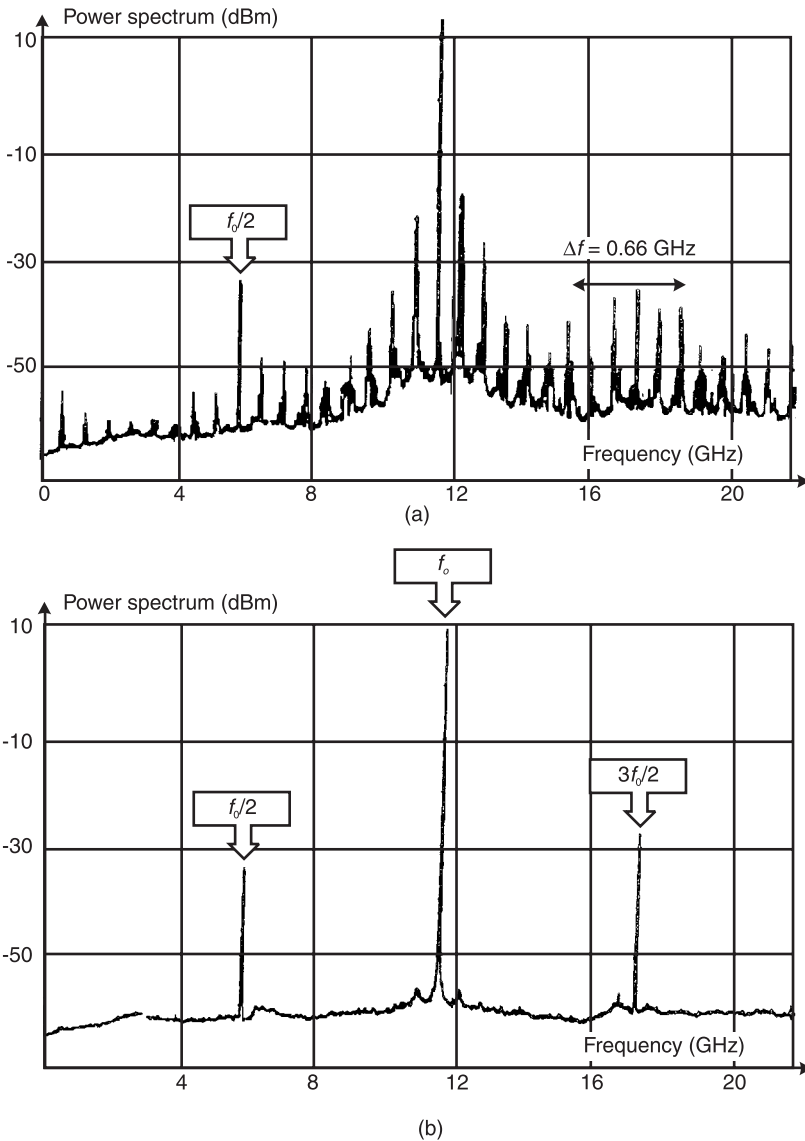


Figure 3.34 Spectrum measurements for two particular points in the unstable regime for input powers of (a) 18.6 dBm and (b) 22.9 dBm.

can be somewhat difficult to implement for designers, as it requires that a large number of analyses be performed. So, a simplified method is proposed and validated in [24]. In this method, the open-loop gain is measured directly, using the filter of Figure 3.25. In this case, the notch frequency is the

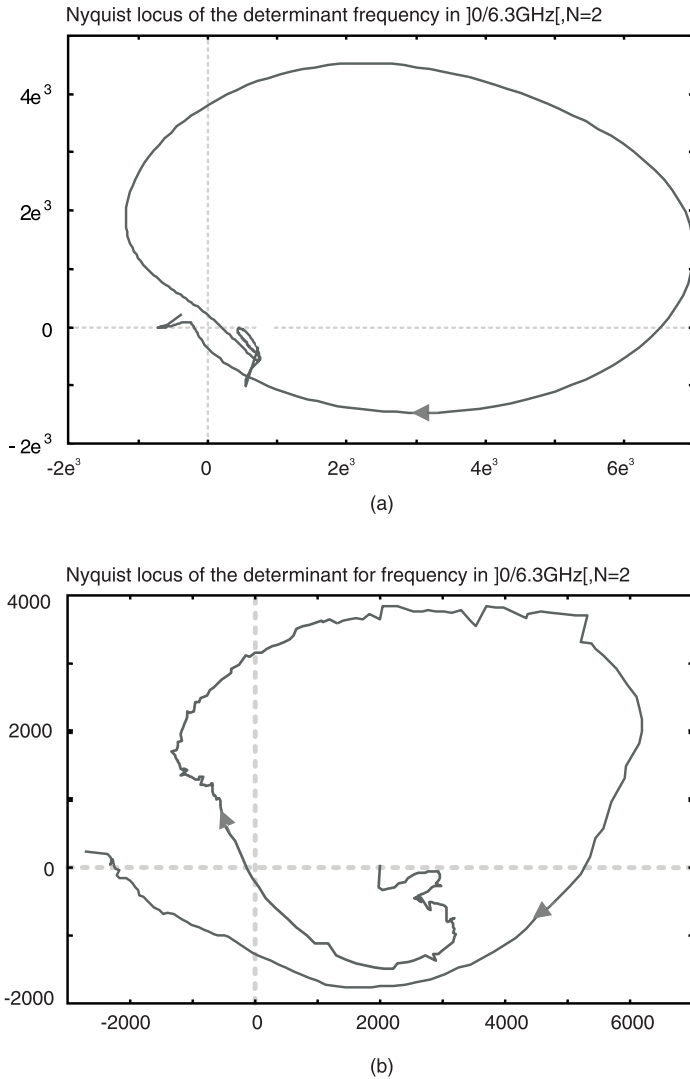


Figure 3.35 The return difference of the first transistor plotted for input powers of (a) 18.6 dBm and (b) 20 dBm.

perturbation frequency, while the filter is transparent for all the harmonics of the large signal and all the intermodulation frequencies $kf_0 \pm F; k \neq 0$. Thus, we have only to measure the return ratio at frequency F , when this frequency varies from 0 to $\frac{f_0}{2}$, which is very easy to do with any CAD software. At this

point, one must be very careful in inspecting the Nyquist locus as it can exhibit complex behavior. One has particularly to examine jumps in the phase of the return ratio to draw the correct conclusions.

References

- [1] Iooss, G., and D. D. Joseph, *Elementary Stability and Bifurcation Theory*, Berlin, Germany: Springer-Verlag, 1990.
- [2] Kundert, K. S., and J. K. White, *Computer Aided Analysis of Electronic Circuits*, Upper Saddle River, NJ: Prentice Hall, 1975.
- [3] Ogata, K., *Modern Control Engineering*, Upper Saddle River, NJ: Prentice Hall, 1990.
- [4] Angot, A., *Compléments de Mathématiques*, Paris, France: Masson & Cie, 1972.
- [5] Golub, G. H., and C. F. Van Loan, *Matrix Computations*, Baltimore, MD: John Hopkins University Press, 1996.
- [6] Bolcato, P., et al., "Efficient Algorithm for Steady-State Stability Analysis of Large Analog/RF Circuits," *Microwave Symp. Digest, IEEE MTT-S Int.*, Vol. 1, 2001, pp. 451–454.
- [7] Mees, A. I., *Dynamics of Feedback Systems*, New York: John Wiley & Sons, 1981.
- [8] Rizzoli, V., and A. Lippardini, "General Stability Analysis of Periodic Steady State Regimes in Nonlinear Microwave Circuits," *IEEE Trans. Microwave Theory Tech.*, Vol. MTT-33, No. 1, Jan. 1985, pp. 30–37.
- [9] Desoer, C. A., and M. Vidyasagar, *Feedback Systems: Input-Output Properties*, New York: Academic Press, 1975.
- [10] Quéré, R., et al., "Large Signal Design of Broadband Monolithic Microwave Frequency Dividers and Phase-Locked Oscillators," *IEEE Trans. Microwave Theory Tech.*, Vol. 41, No. 11, Nov. 1993, pp. 1928–1938.
- [11] Jugo, J., et al., "Closed-Loop Stability Analysis of Microwave Amplifiers," *Elec. Lett.*, Vol. 37, No. 4, Feb. 2001, pp. 226–228.
- [12] MATLAB, at <http://www.mathworks.com/products/matlab>.
- [13] SCILAB, at <http://www.rocq.inria.fr/scilab>.
- [14] OCTAVE, at <http://www.octave.org>.
- [15] Feldmann, P., and R. W. Freund, "Efficient Linear Circuit Analysis by Pade Approximation Via the Lanczos Process," *IEEE Trans. Computer-Aided Design Integrated Circuits Syst.*, Vol. 14, No. 5, May 1995, pp. 639–649.
- [16] Bode, H. W., *Network Analysis and Feedback Amplifier Design*, New York: D. Van Nostrand, 1945.

- [17] Ohtomo, M., "Stability Analysis and Numerical Simulation of Multidevice Amplifiers," *IEEE Trans. Microwave Theory Tech.*, Vol. 41, No. 6, June–July 1993, pp. 983–991.
- [18] Platzker, A., W. Struble, and K. T. Hertzler, "Instabilities Diagnosis and the Role of K in Microwave Circuits," *Microwave Symp. Digest, IEEE MTT-S Int.*, Vol. 3, 1993, pp. 1185–1188.
- [19] Mons, S., "Nouvelles Méthodes d'Analyse de Stabilité Intégrées à la C.A.O. des Circuits Monolithiques Micro-Ondes Non Linéaires," Ph.D. Thesis No. 8-1999, University of Limoges, France, 1999.
- [20] Mons, S., et al., "A Unified Approach for the Linear and Nonlinear Stability Analysis of Microwave Circuits Using Commercially Available Tools," *IEEE Trans. Microwave Theory Tech.*, Vol. 47, No. 12, Dec. 1999, pp. 2403–2409.
- [21] Struble, W., and A. Platzker, "A Rigorous Yet Simple Method for Determining Stability of Linear N-Port Networks [and MMIC Application]," *15th Annual Gallium Arsenide Integrated Circuit (GaAs IC) Symp. 1993, Tech. Digest*, Oct. 1993, pp. 251–254.
- [22] Perez, M. A., "Modèle Électrothermique Distribué de Transistor Bipolaire à Hétérojonction: Application à la Conception Non Linéaire d'Amplificateurs de Puissance Optimisés en Temperature," Ph.D. Thesis No. 61-98, Dec. 1998, University of Limoges, France.
- [23] Teeter, D., A. Platzker, and R. Bourque, "A Compact Network for Eliminating Parametric Oscillations in High Power MMIC Amplifiers," *Microwave Symp. Digest, 1999 IEEE MTT-S Int.*, Anaheim, CA, Vol. 3, 1999, pp. 967–970.
- [24] Mons, S., et al., "Efficient Nonlinear Stability Analysis of Microwave Circuits Using Commercially Available Tools," *European Microwave Conf.*, Milan, Italy, Sept. 2002.

Appendix 3A

For the general circuit of Figure 3.20, we can write the general matrix relations

$$\begin{aligned} \mathbf{V} &= \mathbf{Z} \cdot \mathbf{I} + \mathbf{B} \cdot \mathbf{U} \\ \mathbf{I} &= \mathbf{G}_m \mathbf{V} \\ \mathbf{W} &= \mathbf{C} \cdot \mathbf{I} + \mathbf{D} \cdot \mathbf{U} \end{aligned} \quad (3A.1)$$

where $\mathbf{V} \in \mathfrak{R}^P$ is the vector of voltage controlling the current sources $\mathbf{I} \in \mathfrak{R}^P$, and

$$\mathbf{G}_m = \begin{bmatrix} G_{m1} & & & \\ & \cdot & 0 & \\ & 0 & \cdot & \\ & & & G_{mP} \end{bmatrix} \quad (3A.2)$$

is the transconductance matrix, which is made up of only one nonzero term in each line or column. \mathbf{W} is the vector of output voltages. Eliminating \mathbf{I} in (3A.1) yields

$$\begin{aligned} (\mathbf{I}_p - \mathbf{Z} \cdot \mathbf{G}_m) \mathbf{V} &= \mathbf{B} \cdot \mathbf{U} \\ \mathbf{W} &= \left((\mathbf{I}_p - \mathbf{Z} \cdot \mathbf{G}_m)^{-1} \cdot \mathbf{C} + \mathbf{D} \right) \cdot \mathbf{U} \end{aligned} \quad (3A.3)$$

where \mathbf{I}_p is the unitary matrix of order P . Let us define

$$\mathbf{F}(\mathbf{G}_m) = (\mathbf{I}_p - \mathbf{Z} \cdot \mathbf{G}_m) \quad (3A.4)$$

as the return matrix relative to the active elements characterized by the transconductance \mathbf{G}_m . Evaluation of the determinant of the return matrix will be recursively performed. Indeed, let the transconductance matrix be decomposed as a sum of elementary matrixes containing only one nonzero element.

$$\mathbf{G}_m = \sum_{i=1}^p \mathbf{G}_{mi} \quad \text{with } \mathbf{G}_{mi} = \begin{bmatrix} 0 & & & & & & \\ & \cdot & & & & & \\ & & \cdot & & & & \\ & & & G_{mi} & & & \\ & & & & \cdot & & \\ & 0 & & & & \cdot & \\ & & & & & & \cdot \\ & & & & & & & 0 \end{bmatrix} \quad (3A.5)$$

and

$$\mathbf{K}_i = \sum_{j=i}^p \mathbf{G}_{mj} \quad \mathbf{K}_i = \begin{bmatrix} 0 & & & & & & \\ & \cdot & & & & & \\ & & 0 & & & & \\ & & & \cdot & & & \\ & & & & G_{mi} & & \\ & & & & & \cdot & \\ & 0 & & & & & G_{mi+1} \\ & & & & & & & \cdot \\ & & & & & & & & \cdot \\ & & & & & & & & & G_{mp} \end{bmatrix} \quad (3A.6)$$

Matrix \mathbf{K}_i is obtained by cancelling all the sources up to the $(i-1)$ th included. Then we have

$$\mathbf{G}_m = \mathbf{G}_{m1} + \mathbf{K}_2 \quad (3A.7)$$

and inserting (3A.7) into (3A.3), we obtain

$$\mathbf{V} = \mathbf{Z} \cdot (\mathbf{G}_{m1} + \mathbf{K}_2) \cdot \mathbf{V} + \mathbf{B} \cdot \mathbf{U} \quad (3A.8)$$

(3A.8) can be put under the form

$$\begin{aligned} (\mathbf{I}_p - \mathbf{Z} \cdot \mathbf{K}_2) \cdot \mathbf{V} &= \mathbf{Z} \cdot \mathbf{G}_{m1} \cdot \mathbf{V} + \mathbf{B} \cdot \mathbf{U} \\ \mathbf{V} &= (\mathbf{I}_p - \mathbf{Z} \cdot \mathbf{K}_2)^{-1} \mathbf{Z} \cdot \mathbf{G}_{m1} \cdot \mathbf{V} + (\mathbf{I}_p - \mathbf{Z} \cdot \mathbf{K}_2)^{-1} \cdot \mathbf{B} \cdot \mathbf{U} \end{aligned} \quad (3A.9)$$

and (3A.9) is the return difference equation of a circuit with the following characteristics:

$$\mathbf{F}_{\mathbf{K}_2}(\mathbf{G}_m) = \mathbf{I}_p - (\mathbf{I}_p - \mathbf{Z} \cdot \mathbf{K}_2)^{-1} \mathbf{Z} \cdot \mathbf{G}_{m1} = \mathbf{I}_p - \mathbf{Z}' \cdot \mathbf{G}_{m1} \quad (3A.10)$$

Defining

$$\mathbf{F}(\mathbf{K}_2) = (\mathbf{I}_p - \mathbf{Z} \cdot \mathbf{K}_2) \quad (3A.11)$$

and inserting \mathbf{G}_{m1} into (3A.10), we obtain

$$\begin{aligned} \mathbf{F}_{\mathbf{K}_2}(\mathbf{G}_m) &= \mathbf{I}_p - (\mathbf{I}_p - \mathbf{Z} \cdot \mathbf{K}_2)^{-1} \mathbf{Z} \cdot (\mathbf{G}_m - \mathbf{K}_2) \\ \mathbf{F}_{\mathbf{K}_2}(\mathbf{G}_m) &= \mathbf{I}_p - (\mathbf{I}_p - \mathbf{Z} \cdot \mathbf{K}_2)^{-1} (\mathbf{I}_p - \mathbf{Z} \cdot \mathbf{K}_2 - \mathbf{Z} \cdot (\mathbf{G}_m - \mathbf{K}_2)) \end{aligned} \quad (3A.12)$$

which, when simplified, gives the following important relation:

$$\mathbf{F}_{\mathbf{K}_2}(\mathbf{G}_m) = \mathbf{F}(\mathbf{K}_2)^{-1} \cdot \mathbf{F}(\mathbf{G}_m) \quad (3A.13)$$

The same reasoning can be made for any current source i . With

$$\mathbf{K}_i = \mathbf{G}_{mi} + \mathbf{K}_{i+1} \quad (3A.14)$$

we obtain the recursive equation

$$\mathbf{F}(\mathbf{K}_i) = \mathbf{F}(\mathbf{K}_{i+1}) \cdot \mathbf{F}_{\mathbf{K}_{i+1}}(\mathbf{K}_i) \quad (3A.15)$$

from which we can deduce the return difference equation as

$$F(\mathbf{G}_m) = F(\mathbf{K}_1) = F(\mathbf{K}_{p+1}) \cdot \prod_{i=1}^p F_{\mathbf{K}_{i+1}}(\mathbf{K}_i) \quad (3A.16)$$

Moreover, we have

$$\mathbf{K}_{p+1} = 0 \Rightarrow F(\mathbf{K}_{p+1}) = 1 \quad (3A.17)$$

which finally gives

$$\begin{aligned} F(\mathbf{G}_m) &= \prod_{i=1}^p F_{\mathbf{K}_{i+1}}(\mathbf{K}_i) \\ F_{\mathbf{K}_{i+1}}(\mathbf{K}_i) &= \mathbf{I}_s = \mathbf{Z}' \cdot \mathbf{G}_{mi} \\ \mathbf{Z}' &= (\mathbf{I}_p - \mathbf{Z} \cdot \mathbf{K}_{i+1})^{-1} \mathbf{Z} \end{aligned} \quad (3A.18)$$

Now we have to evaluate the return difference matrix associated with element i th. To do that, the controlled current sources are forced to the configuration given in Figure 3.21. All the $(i-1)$ th first sources are cancelled. Source i th is controlled by an independent external voltage e and the sources ranging from $i+1$ to P are set to their nominal value. The input generator is also set to zero. Thus, we have

$$\begin{aligned} \mathbf{I} &= \mathbf{K}_{i+1} \cdot \mathbf{V} + \mathbf{G}_{mi} \cdot \mathbf{e} \\ \mathbf{e} &= [\dots \quad 0 \quad e^i \quad \dots] \end{aligned} \quad (3A.19)$$

which gives

$$\mathbf{V} = \mathbf{Z} \cdot \mathbf{K}_{i+1} \cdot \mathbf{V} + \mathbf{Z} \cdot \mathbf{G}_{mi} \cdot \mathbf{e} \quad (3A.20)$$

Equation (3A.20) lets us write the return ratio matrix $n^{\circ}i \mathbf{RR}_i$ as

$$\begin{aligned} \mathbf{V} &= (\mathbf{I}_p - \mathbf{Z} \cdot \mathbf{K}_{i+1})^{-1} \mathbf{Z} \cdot \mathbf{G}_{mi} \cdot \mathbf{e} \\ \mathbf{RR}_i &= -(\mathbf{I}_p - \mathbf{Z} \cdot \mathbf{K}_{i+1})^{-1} \mathbf{Z} \cdot \mathbf{G}_{mi} \end{aligned} \quad (3A.21)$$

and the return difference function is

$$F_{\mathbf{K}_{i+1}} = \mathbf{I}_p + \mathbf{RR}_i \quad (3A.22)$$

Taking into account the particular form of the transconductance matrix \mathbf{G}_{mi} , we obtain

$$\mathbf{Z}' = (\mathbf{I}_p - \mathbf{Z} \cdot \mathbf{K}_{i+1})^{-1} \mathbf{Z} = (z'_{ki})_{\substack{1 \leq k \leq P \\ 1 \leq i \leq P}}$$

and

$$\mathbf{Z}' \cdot \mathbf{G}_{mi} = \begin{bmatrix} 0 & \dots & 0 & z'_{1i} G_{mi} & 0 & \dots \\ \vdots & & \vdots & \vdots & \vdots & \\ 0 & \dots & 0 & z'_{ii} G_{mi} & 0 & \dots \\ \vdots & & \vdots & \vdots & \vdots & \\ 0 & \dots & 0 & z'_{pi} G_{mi} & 0 & \dots \end{bmatrix} \quad (3A.23)$$

which allows us to simplify the expression of the determinant. Indeed

$$\det(\mathbf{I}_p - \mathbf{Z}' \cdot \mathbf{G}_{mi}) = \det \begin{bmatrix} 1 & \dots & 0 & -z'_{1i} G_{mi} & 0 & \dots \\ \vdots & & \vdots & \vdots & \vdots & \\ 0 & \dots & 0 & 1 - z'_{ii} G_{mi} & 0 & \dots \\ \vdots & & \vdots & \vdots & \vdots & \\ 0 & \dots & 0 & -z'_{pi} G_{mi} & 0 & \dots \end{bmatrix} = 1 - z'_{ii} G_{mi} \quad (3A.24)$$

Thus, the determinant of the return difference can be obtained from the scalar ratio

$$RR_i = -\frac{V_i}{e} = -z'_{ii} G_{mi} \quad (3A.25)$$

and the NDF is then obtained by measuring successively the various RR_i . Finally we get

$$\det(\mathbf{F}(\mathbf{G}_m)) = \prod_{i=1}^p (1 + RR_i) \quad (3A.26)$$

4

Bifurcation Analysis of Nonlinear Circuits

This chapter studies the stability properties of nonlinear circuits in a global way; that is to say, it takes into account the possible variation of one or more parameters in the circuit. Examples of parameters are the generator values (input RF generators or bias generators), the values of linear elements (capacitance, resistance), and the temperature.

When continuously modifying a circuit parameter η , quantitative variations of the solution are generally observed with a continuous increment or decrease of the solution amplitude, power, or even fundamental frequency (in the case of free-running oscillations). However, a qualitative variation of the steady-state solution may also be obtained, taking place for a critical parameter value η_0 . This is a *bifurcation* parameter value [1–8]. The qualitative variation of the steady-state solution may be a change in the solution type (from a limit cycle to a limit torus, for instance) or a discontinuous variation in its characteristics, such as amplitude, power, or fundamental frequency (in the case of a self-oscillation).

An example of bifurcation is the onset of the free-running oscillation from a given value of the dc generators. At this value, a formerly stable DC solution becomes unstable, and the physically observed solution changes its type from an equilibrium point to a limit cycle [9–11]. Thus, there is a close link between the qualitative change in the stability of a given solution (or bifurcation) and the qualitative variation of the physically observed behavior. There are other possible transformations and, thus, different types of bifurcations.

Bifurcations explain many phenomena commonly observed in the experiment, some of them intended by the designer, like the onset of a free-running oscillation, and others unexpected or unwanted, like the spurious oscillation of a power amplifier.

Bifurcations may take place from a dc regime (or equilibrium point), from a periodic regime (or cycle), from a quasiperiodic regime (or torus), and even from chaos [4, 5, 7]. They can be classified into *local* and *global* bifurcations [2–4]. The local bifurcations are those involving variations, when a parameter is modified, in the local stability properties of a single solution. The global bifurcations, roughly speaking, involve the collision in the phase space, as a parameter is modified, of an attractor with a solution of saddle type (see Sections 1.3 and 1.4).

The chapter is organized as follows. In the first section, an in-depth analysis of local bifurcations from dc and the periodic regimes is presented. In the second section, the Poincaré map is used for a detailed analysis and classification of bifurcations from periodic regime. The third section is devoted to the two main types of global bifurcation: *saddle connection* and the *local/global saddle-node bifurcation*. In the fourth section, general criteria for bifurcation analysis using harmonic balance are presented, considering the cases of dc, periodic, and quasiperiodic regimes. Finally, in the fifth section, some new harmonic-balance tools for bifurcation detection are presented. The tools are based on the introduction into the circuit of an auxiliary generator (in similar way to that presented in Section 1.6), which, as will be shown, enables a simple formulation of bifurcation conditions with algorithms that can easily be integrated to existing harmonic-balance software.

4.1 Local Bifurcations

Before starting our analysis of local bifurcations, a couple of definitions must be introduced. The first one regards the number of parameters that are taken into account for the bifurcation analysis. Bifurcations obtained versus one control parameter η are called *bifurcations of codimension one* [2]. Note that it would also be possible to consider the variation of two different parameters in the system or, in general, the variation of a whole vector of parameters $\bar{\eta}$. Bifurcations requiring the fine tuning of two parameters are called *bifurcations of codimension two* [2].

Another important definition is that of the *structural stability* [2, 4]. A system is said to be structurally stable if for any small perturbation of the original differential equation $\dot{\bar{x}} = f(\bar{x})$, there is no qualitative variation of the solutions in the phase space. The flow is said to be *topologically equivalent* to the

original one [2]. Thus, sufficiently close vector fields f' (different from f) have an equivalent phase portrait. Mathematical models of observable phenomena are always structurally stable due to the unavoidable presence of perturbations in real life. However, if a parameter is considered in the system, the phase portrait will be structurally unstable at the bifurcation points because the qualitative variation in the stability of one of the system solutions necessarily gives rise to a qualitative variation of the phase portrait.

The local bifurcations only depend on the stability properties of a given steady-state solution (not on other elements of the phase portrait). These stability properties vary with the system parameter. Thus, the bifurcation analysis will be carried out in terms of the magnitudes that characterize the stability of the solution. These magnitudes depend on the type of steady-state solution. They will be the eigenvalues of the linearization in the case of a dc solution (see Section 1.4 and Example 1.7), the Floquet multipliers in the case of periodic solutions [3, 12, 13], and the Lyapunov exponents in the case of quasiperiodic or chaotic solutions [13]. Only dc and periodic solutions will be considered in this first section.

4.1.1 Local Bifurcations from the DC Regime

Let a nonlinear autonomous system of n dimension and having a parameter η be considered:

$$\dot{\bar{x}} = f(\bar{x}, \eta) \quad (4.1)$$

with $x \in R^n$, $\eta \in R$, $f: R^n \times R \rightarrow R^n$. The dc solutions of (4.1) \bar{x}_{dc} fulfill $0 = f(\bar{x}_{dc}, \eta)$. According to the theorem of the implicit function [3] it is possible to solve the latter system for the dc solutions, as a function of the parameter η : $\bar{x}_{dc} \equiv \bar{x}_{dc}(\eta)$. This provides what is often termed the *solution path*. The dc solutions depend on η and so does the stability of these solutions. To analyze this stability, a small perturbation $\xi(t) \in R^n$ is introduced into the system. As is already known, the smallness of the perturbation enables the following linearization:

$$\dot{\bar{\xi}} = [Jf(\bar{x}_{dc}, \eta)]\bar{\xi} \quad (4.2)$$

with $[Jf]$ being the Jacobian matrix of (4.1). The general solution of (4.2) is given by

$$\bar{\xi}(t) = c_1 e^{\lambda_1 t} \bar{\xi}_1 + c_2 e^{\lambda_2 t} \bar{\xi}_2 + \dots + c_n e^{\lambda_n t} \bar{\xi}_n \quad (4.3)$$

where λ_i and the vectors $\bar{\xi}_i$ ($i = 1$ to n), respectively, are the eigenvalues and eigenvectors of $[Jf]$ and c_i ($i = 1$ to n) are constants depending on the initial conditions $\bar{\xi}(0) = \bar{\xi}_o$. Actually, for different initial conditions $\bar{\xi}(0) = \bar{\xi}'_o$, a different set of constants c'_i ($i = 1$ to n) would be necessary to fulfill (4.3). The eigenvalues may be real $\lambda_i \equiv \gamma_i$ ($i = 1$ to m) or complex-conjugate $\lambda_{i,i+1} \equiv \alpha_i \pm j\omega$ ($i = m + 1$ to $n - 1$). In general, the dc point \bar{x}_{dc} is a hyperbolic equilibrium point (see Section 1.4.2); that is, the real parts of all the eigenvalues $\text{Re}[\lambda_i]$ ($i = 1$ to n) are different from zero $\text{Re}[\lambda_i] \neq 0$ [4].

Clearly, for the solution $\bar{x}_{dc}(\eta)$ to be stable, all the eigenvalues must fulfill $\text{Re}[\lambda_i] < 0$ ($i = 1$ to n); that is, the perturbation $\bar{\xi}(t)$ must exponentially vanish in time. Thus, all the eigenvalues must be located in the left-hand side of the complex plane. If η is modified in a continuous way, the eigenvalues will also (generally) vary: $\lambda_i(\eta)$. They will describe a path in the complex plane. Then, one or more of the eigenvalues of the linearized system may move from the left-hand side of the complex plane to the right-hand side, as shown in Figure 4.1. The transversal crossing of the imaginary axis $j\omega$ by a real eigenvalue or a pair of complex-conjugate eigenvalues gives rise to a bifurcation. The particular parameter value at which the bifurcation occurs [η'_o in Figure 4.1(a) and η_o in Figure 4.1(b)] is the bifurcation parameter value.

A bifurcation necessarily leads to a qualitative variation of the steady-state solution. This is easily understood from the inspection of (4.3). The movement of a real eigenvalue (or a couple of complex-conjugate eigenvalues) to the right-hand side of the complex plane, for $\eta > \eta'_o$ (or $\eta > \eta_o$), gives rise to one exponent (or two complex-conjugate exponents) with positive real part in (4.2). This leads to an exponential growth in time of the amplitude of the perturbation. This growth soon invalidates the linearization (4.2) about the dc solution $\bar{x}(t) = \bar{x}_{dc}$. Actually, beyond the bifurcation, the system moves away from this solution exponentially in time. As time increases, the solution provided by the linearization (4.2) $\bar{x}(t) = \bar{x}_{dc} + \bar{\xi}(t)$ disagrees more and more with the actual circuit solution. To obtain the new steady state, a new nonlinear analysis of the circuit must be carried out.

In a codimension-one system, there are only two typical bifurcations from dc regime [2, 6]. If a real eigenvalue crosses the imaginary axis, a turning point or fold-type bifurcation is obtained [see Figure 4.1(a)]. If a couple of complex-conjugate eigenvalues crosses the imaginary axis, a Hopf-type bifurcation is obtained [9, 10], with the onset of a free-running oscillation [see Figure 4.1(b)]. When using two parameters, other bifurcations are possible (codimension-two bifurcations) because of the simultaneous crossing of the imaginary axis by eigenvalues of the same or a different nature. Other

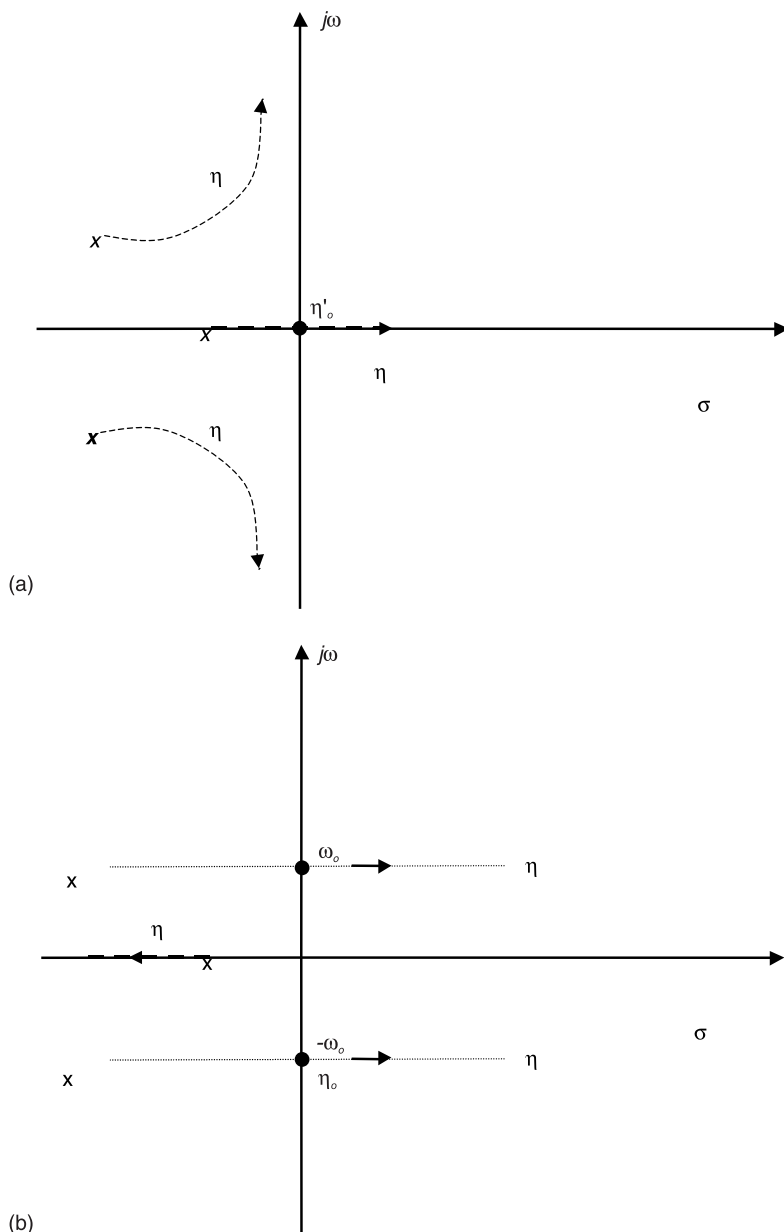


Figure 4.1 Bifurcations from a dc regime. (a) Fold or turning-point bifurcation. A real eigenvalue crosses the imaginary axis to the right of the complex plane for the bifurcation parameter value $\eta = \eta'_o$. (b) Hopf bifurcation. A couple of eigenvalues cross the imaginary axis to the right of the complex plane for the bifurcation parameter value $\eta = \eta'_o$.

codimension-one bifurcations from dc regime require symmetry or additional constraints and are not structurally stable [2] in the sense that a slightly different system (with a slightly different vector field and the same parameter) would not exhibit the same bifurcation versus the parameter. For this reason, only turning-point (or fold-type) and Hopf-type bifurcations will be studied here.

4.1.1.1 Turning-Point Bifurcation: Critical Eigenvalue $\lambda_{io} = \gamma_{io} \in R$

At a turning-point bifurcation, a real eigenvalue of the constant Jacobian matrix (associated with the linearization about a given equilibrium point) crosses transversally the imaginary axis through the origin. When the crossing takes place, the determinant of the Jacobian matrix is equal to zero. The implications of this bifurcation over the evolution of the dc solution versus the parameter $\bar{x}_{dc}(\eta)$ can be better understood if a circuit variable, such as one of the state variables, is represented versus the parameter. At the turning-point bifurcation, the solution curve folds over itself, exhibiting infinite slope at the critical parameter value $\eta = \eta_o$. This is why turning-point bifurcations are also known as fold bifurcations. To understand this, note that the real eigenvalue crossing the imaginary axis at the bifurcation point gives rise, for $\eta = \eta_o$, to a singular Jacobian matrix because one of its eigenvalues is $\lambda_{io} = \gamma_{io} = 0$. The reason a singular Jacobian matrix gives rise to an infinite slope of the solution curve $\bar{X}_{dc}(\eta)$ was shown in Section 2.5 and will not be repeated here.

The folded curve gives rise to a multivalued solution, as shown in Figure 4.2. However, the points in the upper and lower sections of the curve have different stability properties. Above and below the turning point, there is either one more or one less unstable eigenvalue; the number of eigenvalues in the right half of the complex plane is different in one (provided no other bifurcations take place along the solution path). If one of the two sections (upper or lower with respect to the turning point) is stable (zero eigenvalues with positive real part), the other will necessarily be unstable due to the crossing of the imaginary axis by one real eigenvalue at the turning point.

If the upper section of the dc solution path $\bar{X}_{dc}(\eta)$ consists of solutions of node (saddle) type, the lower section will consist of solutions of saddle (node) type. Versus the parameter η , as the bifurcation value η_o is approached, the node and the saddle approach each other and collide at the bifurcation point. This gives rise to a saddle-node bifurcation [2]. Figure 4.3 shows the phase portrait before and after the bifurcation. For $\eta < \eta_o$ [Figure 4.3(a)] there are two equilibrium points of node and saddle type. Only the node will be physically observed. For $\eta = \eta_o$, the node and the saddle collide. This critical situation is depicted in Figure 4.3(b). The collision gives rise to a local annihilation of the two equilibrium points, every solution going to infinity for $\eta > \eta_o$. This is

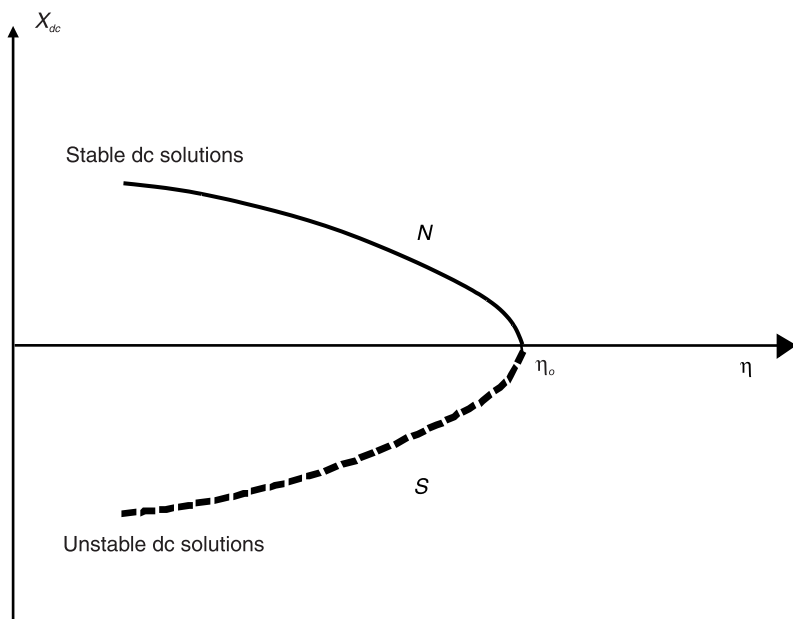


Figure 4.2 Fold-type bifurcation of a dc regime.

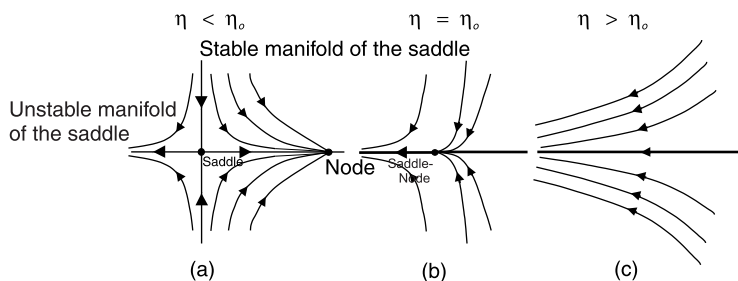


Figure 4.3 Saddle-node bifurcation. Evolution of solutions in the phase space versus the parameter. (a) Saddle and node; (b) collision of saddle and node; and (c) annihilation of solutions.

shown in Figure 4.3(c). To clarify the above ideas, the evolution of the dc solutions of a damped oscillator will be analyzed in Example 4.1.

Example 4.1: Saddle-node bifurcation in a damped oscillator

A damped oscillator is modeled with the following equation:

$$\ddot{x} + a\dot{x} + bx^2 - \eta = 0 \quad (4.4)$$

where a and b are positive constants, and the parameter fulfills $\eta \geq 0$. The above equation can be transformed, through the introduction of a new variable y , into a system of two differential equations of first order:

$$\begin{aligned} \dot{x} &= y \\ \dot{y} &= -ay - bx^2 + \eta \end{aligned} \quad (4.5)$$

The system has two dc solutions that are given by

$$x_{dc} = \pm \sqrt{\frac{\eta}{b}} \quad ; \quad y_{dc} = 0 \quad (4.6)$$

The stability of these solutions is analyzed by linearizing (4.5). The corresponding linear system, in terms of the perturbation, is given by

$$\begin{pmatrix} \dot{\xi}_x \\ \dot{\xi}_y \end{pmatrix} = \begin{pmatrix} 0 & 1 \\ -2bx_{dc} & -a \end{pmatrix} \begin{pmatrix} \xi_x \\ \xi_y \end{pmatrix} \quad (4.7)$$

where x_{dc} will be particularized later on. The two eigenvalues of the above Jacobian matrix are given by

$$\lambda_{dc1,2} = \frac{-a \pm \sqrt{a^2 - 8bx_{dc}}}{2} \quad (4.8)$$

The two dc solutions $x_{dc1} = \sqrt{\frac{\eta}{b}}$ and $x_{dc2} = -\sqrt{\frac{\eta}{b}}$ can now be replaced into (4.8) to obtain the two eigenvalues of each solution:

$$\begin{aligned} \lambda_{dc1} &= \frac{-a \pm \sqrt{a^2 - 8b\sqrt{\frac{\eta}{b}}}}{2} \quad \text{for the solution } x_{dc1} = \sqrt{\frac{\eta}{b}} \\ \lambda_{dc2} &= \frac{-a \pm \sqrt{a^2 + 8b\sqrt{\frac{\eta}{b}}}}{2} \quad \text{for the solution } x_{dc2} = -\sqrt{\frac{\eta}{b}} \end{aligned} \quad (4.9)$$

For $a^2 - 8b\sqrt{\frac{\eta}{b}} > 0$, the two solutions (4.6) will have a pair of distinct real eigenvalues. The equilibrium point \bar{x}_{dc1} will have two different negative eigenvalues and will be a stable node. The equilibrium point \bar{x}_{dc2} will have a positive and a negative eigenvalue and will be a saddle. It is clear from (4.9) that, as the positive parameter decreases to zero, the two solution points approach each other, colliding for $\eta = 0$. At the collision, the single solution point has eigenvalues $\lambda_{dc} = 0$ and $\lambda_{dc} = -2a$. The determinant takes a zero value and the slope of the solution curve $X_{dc}(\eta)$ tends to infinity. This is a turning-point bifurcation of the saddle-node type.

4.1.1.2 Hopf Bifurcation: Critical Eigenvalues $\lambda_{i_0, i+1_0} = \sigma_i \pm j\omega_i \in \mathcal{C}$

For two complex-conjugate eigenvalues crossing the imaginary axis at $\pm j\omega$, a Hopf-type bifurcation of the dc solution is obtained (Figure 4.4). In a direct Hopf bifurcation, the pair of complex-conjugate eigenvalues crosses the imaginary axis $j\omega$, versus the parameter, towards the right-hand side of the complex

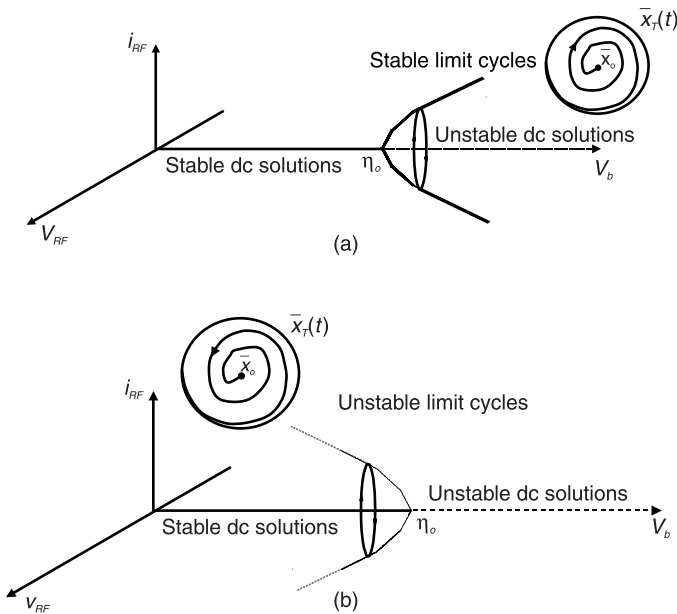


Figure 4.4 Hopf bifurcation. (a) Supercritical: for $\eta = \eta_0$, the equilibrium point is an unstable focus, and the limit cycles are stable. (b) Subcritical: The limit cycles already exist for $\eta < \eta_0$. The equilibrium point is a focus attractor, while the limit cycle is unstable.

plane. In an inverse Hopf bifurcation, the pair of complex-conjugate eigenvalues crosses the imaginary axis $j\omega$, versus the parameter, towards the left-hand side of the complex plane.

The Hopf bifurcation is associated with the change of sign in the damping of an oscillator. Thus, a stable focus changes to an unstable focus in the increasing or decreasing parameter sense. An example of this has already been encountered in Example 1.7 (see Figure 1.19). Considering the situation of Figure 4.1(b), for $\eta > \eta_o$, the two complex-conjugate eigenvalues $\lambda_{i_o, i+1_o}(\eta) = \sigma(\eta) \pm j\omega(\eta)$ give rise to an oscillating transient at the frequency $\omega(\eta)$, leading to a stable limit cycle [see Figure 4.4(a)]. Thus, for $\eta > \eta_o$, the dc solution $\bar{x} \equiv \bar{x}_{dc}(\eta)$ will no longer be physically observable. Instead, a period- T solution $\bar{x} \equiv \bar{x}_o(t, \eta)$ will be obtained with $T = \frac{2\pi}{\omega}$. The frequency ω of this limit cycle will be close to the one provided by the unstable couple of complex eigenvalues $\omega \equiv \omega(\eta)$.

As a final comment, at the Hopf bifurcation ($\eta - \eta_o$), there is a critical situation for which the couple of complex-conjugate eigenvalues take the purely imaginary value $\lambda_{i, i+1}(\eta_o) = \pm j\omega_o$. For $\eta = \eta_o$, the condition $\text{Re}[\lambda_i] \neq 0 (i = 1 \text{ to } n)$ is not fulfilled, and the equilibrium point is not hyperbolic. Under any infinitesimal variation of the parameter, the system will behave either as a stable focus or as an unstable one. Thus, the system is structurally unstable at this point.

To clarify the ideas, Example 4.2 analyzes in detail the Hopf bifurcation of the cubic nonlinearity oscillator encountered in Example 1.7.

Example 4.2: Hopf bifurcation in the cubic nonlinearity oscillator

Example 1.7 analyzed the stability of the equilibrium point $\bar{x}_{dc} = (i_L, v_C) = (0, 0)$ by linearizing (1.4) about that point and finding the eigenvalues of the associated Jacobian matrix. These eigenvalues have the following expression:

$$\lambda_{1,2} = \frac{1}{2} \left(-\left(\frac{R}{L} + \frac{a}{C}\right) \pm \sqrt{\left(\frac{R}{L} + \frac{a}{C}\right)^2 - 4 \frac{Ra + 1}{LC}} \right) \quad (4.10)$$

Here the resistance R will be considered as the system parameter $\eta \equiv R$. For R values fulfilling $\left(\frac{R}{L} + \frac{a}{C}\right)^2 - 4 \frac{Ra + 1}{LC} < 0$, the eigenvalues (4.10) are

complex-conjugate. On the other hand, it is clear that for $\frac{R}{L} + \frac{a}{C} > 0$, the system damping is positive and the equilibrium point $\bar{x}_{dc} = (i_L, v_C) = (0, 0)$ behaves as a stable focus. Thus, this point will be physically observed (see Figure 1.19). This condition is fulfilled for $R > R_o$ with $R_o = -\frac{aL}{C} = 1.2$ Ohm. At

$R = R_o$, the damping is zero and the equilibrium point is structurally unstable. For $R < R_o$, the equilibrium point behaves like an unstable focus, giving rise to an oscillating transient of increasing amplitude (see Figure 1.6).

Two different types of Hopf bifurcations are possible [9]. The case depicted in Figure 4.4(a) corresponds to a supercritical Hopf bifurcation. The stable dc solution becomes unstable at the bifurcation point, giving rise to stable limit cycles that surround the unstable dc solution. A different situation is depicted in Figure 4.4(b). In this case, unstable limit cycles are generated at the Hopf bifurcation and coexist with the stable dc solution for parameter values that are smaller than the bifurcation parameter value η_o . This kind of bifurcation is called *subcritical Hopf bifurcation*. When the dc solution becomes unstable, there is no stable solution in its neighborhood.

When it is time to carry out a graphical representation of a Hopf bifurcation, it can be very helpful to use frequency-domain magnitudes, such as the first harmonic component of a representative circuit variable or the output power. This provides a diagram of the type shown in Figure 4.5. It is a very simple example of bifurcation diagram. The two possibilities of supercritical [Figure 4.5(a)] and subcritical [Figure 4.5(b)] Hopf bifurcation have been considered, showing the different stability situations obtained in each case. Actually, there is a relationship between the stability of the new solution path, constituted of periodic solutions, and that of the bifurcating path, constituted of dc solutions. The two types of bifurcation, versus the parameter η , can be formulated as

$$\begin{aligned}
 dc_s &\rightarrow dc_u + P_s && \text{Supercritical, direct Hopf} \\
 dc_u + P_s &\rightarrow dc_s && \text{Supercritical, inverse Hopf} \\
 dc_s + P_u &\rightarrow dc_u && \text{Subcritical, direct Hopf} \\
 dc_u &\rightarrow dc_s + P_u && \text{Subcritical, inverse Hopf}
 \end{aligned}
 \tag{4.11}$$

where dc stands for dc solution, P for periodic solution, s for stable, and u for unstable.

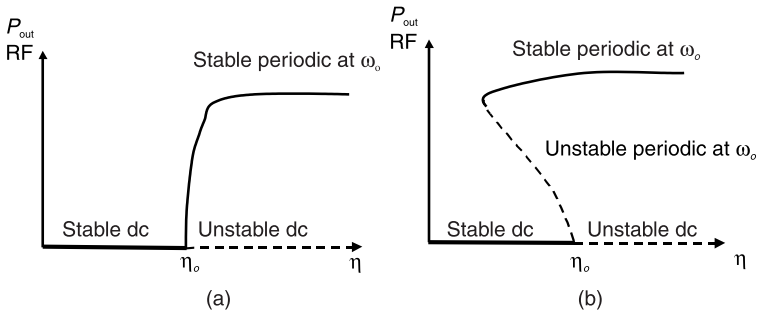


Figure 4.5 Bifurcation diagram for a Hopf bifurcation from a dc regime: (a) supercritical bifurcation, and (b) subcritical bifurcation.

Finally, note that the subcritical Hopf bifurcations are usually associated with a turning point in the newly generated periodic path [see Figure 4.5(b)]. If this happens, limit cycles will generally exist before and after the bifurcation. This turning point is, of course, a bifurcation from periodic regime and will be treated in detail in the next section.

4.1.2 Local Bifurcations from the Periodic Regime

The basis of the analysis of local bifurcations from the periodic regime is similar to that of bifurcations from dc regime. A parameter of interest η is considered in the system, determining the possible qualitative variations of the stability of the periodic solution as this parameter evolves. For the stability analysis, a small perturbation is applied to the periodic solution, which enables the system linearization about this solution, in an analogous way to the linearization about an equilibrium point. The main difference between the analysis in the case of a dc solution or in the case of a periodic solution comes from the magnitudes that characterize the solution stability. In the case of a dc solution, these magnitudes are, as is already known, the eigenvalues of the constant Jacobian matrix of the linearized system. In the case of a periodic solution, they are the Floquet multipliers of the periodic Jacobian matrix [3, 12, 13]. Due to their crucial role in the bifurcation analysis of periodic regimes, the stability analysis through Floquet multipliers will be presented in detail in the following section.

4.1.2.1 Floquet Multipliers

A general nonlinear circuit of n dimension, either autonomous or nonautonomous, is considered. In the case of a nonautonomous circuit, there is a periodic forcing term of period T in the system equations. These equations are given by

$$\dot{\bar{x}} = f(\bar{x}) \quad \begin{cases} x_n = \frac{\theta T}{2\pi} & \text{nonautonomous} \\ x_n & \text{autonomous} \end{cases} \quad (4.12)$$

where the periodically forced nonautonomous system has been converted to an autonomous one.

Let (4.12) have a periodic solution $\bar{x}_o(t)$ of period T . With the aim of analyzing the stability of this solution, a general perturbation $\bar{\xi}(t)$ will be considered. The smallness of the perturbation enables the linearization of (4.12) about the steady-state solution $\bar{x}_o(t)$, obtaining the following linear system:

$$\dot{\bar{\xi}}(t) = [J(\bar{x}_o(t))] \bar{\xi}(t) \quad (4.13)$$

Before continuing, note the difference between (4.2) and (4.13). This difference is in the nature of their respective Jacobian matrixes. In (4.2), the nonlinear system is linearized about a dc solution, so the Jacobian matrix is constant. In (4.13), the nonlinear system is linearized about a periodic solution of period T , so the Jacobian matrix is periodic with the same period T . Thus, (4.13) is a linear system of periodic coefficients, and its general solution is given by

$$\bar{\xi}(t) = c_1 e^{\lambda_1 t} \bar{v}_1(t) + c_2 e^{\lambda_2 t} \bar{v}_2(t) + \dots + c_n e^{\lambda_n t} \bar{v}_n(t) \quad (4.14)$$

where $\bar{v}_1(t)$ to $\bar{v}_n(t)$ are periodic vectors, λ_1 to λ_n are real or complex-conjugate exponents, and c_1 to c_n are constants, which depend on the initial conditions. Actually, for a different initial point $\bar{\xi}(0) = \bar{\xi}'_o$, a different set of constants $c'_1 \dots c'_n$ would be necessary to fulfill (4.14).

As in the case of dc solutions, to determine the stability of the periodic solution $\bar{x}_o(t)$, it will be necessary to find out what happens with the perturbation $\bar{\xi}(t)$ as time evolves. Generally speaking, for the periodic solution to be stable, the perturbation must exponentially vanish in time. However, in the case of periodic solutions of autonomous circuits (see Section 1.1), the perturbations in the direction of the limit cycle do not vanish in time, even when the solution is stable [14]. Instead, they lead the solution to a different point of the cycle. This comes from the fact that, as is already known, because of the time-independence of the vector field, the periodic solution of an autonomous system is invariant in the direction of the limit cycle (see Section 1.3 and Figure 1.5).

In a system of order n , there will be n independent solutions $\bar{\xi}_i(t)$ with $i = 1$ to n . This set of n independent solutions is not unique. To obtain a basis of solutions, a set of linearly independent vectors $\bar{\xi}_{oi}$ with $i = 1$ to n must be

chosen. Then, each of the independent solutions of (4.13), $\bar{\xi}_i(t)$, is obtained by integrating (4.13) from a different vector of initial conditions $\bar{\xi}_{io}$. Once a set of n independent solutions has been determined, it is possible to write the fundamental matrix [6–8] of solutions of (4.13). This is a matrix whose columns are constituted by the independent solutions of (4.13):

$$\psi(t) = [\bar{\xi}_1(t) \bar{\xi}_2(t) \dots \bar{\xi}_n(t)] \quad (4.15)$$

A convenient choice for the n independent vectors of initial conditions $\bar{\xi}_{io}$ is the one given by the columns of the identity matrix, that is,

$$[\bar{\xi}_{oo}] = [\bar{\xi}_{o1} \dots \bar{\xi}_{oi} \dots \bar{\xi}_{on}] = \begin{bmatrix} 1 & 0 & \dots & 0 \\ 0 & 1 & \dots & 0 \\ \vdots & 0 & \ddots & 0 \\ 0 & \dots & \dots & 1 \end{bmatrix} \quad (4.16)$$

A set of independent solutions is obtained from the integration of (4.13) from each of these initial conditions. Replacing these solutions into (4.15), the so-called canonical fundamental matrix $[\psi_m(t)]$ is obtained. This matrix satisfies

$$[\psi_m(0)] = [I] \quad (4.17)$$

with $[I]$ being the identity matrix.

What is interesting about the canonical fundamental matrix is that any other matrix of fundamental solutions $[\psi(t)]$ can easily be expressed in terms of $[\psi_m(t)]$. If the matrix fulfills $[\psi(0)] = [C]$ with $[C]$, an arbitrary $n \times n$ matrix, with columns composed of independent vectors, it is possible to write

$$[\psi(t)] = [\psi_m(t)][C] \quad (4.18)$$

where (4.17) has been taken into account.

In particular, we are going to apply (4.18) to the matrix $[\psi_m(t+T)]$. This matrix is also a fundamental matrix of solutions of (4.13) because of the periodicity of the Jacobian matrix:

$$\begin{aligned} [\dot{\psi}_m(t+T)] &= [Jf(\bar{x}_o(t+T))][\psi_m(t+T)] = \\ &[Jf(\bar{x}_o(t))][\psi_m(t+T)] \end{aligned} \quad (4.19)$$

Thus, $[\psi_m(t+T)]$ must be able to be expressed in the form (4.18):

$$[\psi_m(t+T)] = [\psi_m(t)][C_{oo}] \quad (4.20)$$

where $[C_{oo}]$ is a matrix of constants. Note that $[\psi_m(t+T)] \neq [\psi_m(t)]$ because the solutions of (4.13) are not periodic, as can be gathered from the exponential dependence of (4.14). The matrix of constants $[C_{oo}]$ can easily be determined from (4.20), by making $t=0$. Then

$$[\psi_m(T)] = [I][C_{oo}] = [C_{oo}] \quad (4.21)$$

where the fact that $[\psi_m(t)]$ is a canonical fundamental matrix has been taken into account. Thus, $[\psi_m(T)] = [C_{oo}]$, and the following relationship is fulfilled:

$$[\psi_m(t+T)] = [\psi_m(t)][\psi_m(T)] \quad (4.22)$$

and, in general,

$$[\psi_m(t+kT)] = [\psi_m(t)][\psi_m(T)]^k \quad (4.23)$$

with k integer.

The relationship (4.23) is very useful to find out what happens with the perturbation as time tends to infinity. To see this, the initial value of the perturbation $\bar{\xi}(0) = \bar{\xi}_o$ is expressed in terms of the identity basis by just making $\bar{\xi}(0) = [I]\bar{\xi}_o$. Then, the evolution in time of the perturbation $\bar{\xi}(t)$ can be written

$$\bar{\xi}(t) = [\psi_m(t)]\bar{\xi}_o \quad (4.24)$$

Thus, taking (4.23) into account, the limit of (4.24) as time tends to infinity is given by

$$\lim_{t \rightarrow \infty} \bar{\xi}(t) = \lim_{k \rightarrow \infty} [\psi_m(\tau)][\psi_m(T)]^k \bar{\xi}_o \text{ with } \tau \in [0, T) \quad (4.25)$$

where the limit $t \rightarrow \infty$ has been expressed as $\lim_{k \rightarrow \infty} \tau + kT$ with $\tau \in [0, T)$ and k integer. Because $[\psi_m(\tau)]$ is necessarily bounded in the limited interval $[0, T)$, due to its continuity, the fate of the perturbation (extinction or growth) will exclusively depend on the matrix $[\psi_m(T)]$. The canonical fundamental matrix, evaluated at $t = T$ is called *monodromy matrix* [6–8].

The eigenvalues of the monodromy matrix m_i ($i = 1$ to n) are the *Floquet multipliers*. The multipliers are calculated from

$$[\psi_m(T)]\bar{v}_{mi} = m_i(T)\bar{v}_{mi} \quad i = 1 \dots n \quad (4.26)$$

where \bar{v}_{mi} are the matrix eigenvectors. The multipliers are constant quantities that can be real or complex-conjugate. Now, taking (4.26) and (4.23) into account, it will be possible to write

$$\begin{aligned} [\psi_m(kT)]\bar{v}_{mi} &= m_i(kT)\bar{v}_{mi} = [\psi_m(T)]^k \bar{v}_{mi} = \\ m_i^k(T)\bar{v}_{mi} & \quad i = 1 \dots n \end{aligned} \quad (4.27)$$

In (4.24), the initial perturbation $\bar{\xi}_{o_2}$ had been expressed in terms of the identity basis to apply (4.18). However, $\bar{\xi}_{o_2}$ can also be expressed in the basis provided by the Floquet eigenvectors: $\bar{\xi}_{o_2} = [\bar{v}_{m1} \dots \bar{v}_{mi} \dots \bar{v}_{mn}] \bar{\xi}_{om}$. Then, the solution of (4.13) is given by

$$\bar{\xi}(t + kT) = [\psi_m(t)] \left\{ \begin{array}{l} m_1^k \bar{v}_{m1} \bar{\xi}_{om1} + \dots + \\ m_i^k \bar{v}_{mi} \bar{\xi}_{omi} + \dots + \\ m_n^k \bar{v}_{mn} \bar{\xi}_{omn} \end{array} \right\} \text{ with } t \in [0, T) \quad (4.28)$$

Because $[\psi_m(t)]$ is necessarily bounded in the interval $[0, T)$, the growth or decay of the perturbation as time tends to infinity will only depend on the multipliers. For $|m_i| > 1$ in a given direction \bar{v}_{mi} , the perturbation grows unboundedly in that direction (in this linearized calculation). If $|m_i| < 1$, the perturbation vanishes in time. In periodic solutions of autonomous systems, the perturbations in the direction of the limit cycle necessarily remain in this cycle because of its invariance under the flow. Thus, assuming that the particular vector \bar{v}_{mn} is tangent to the periodic orbit, the corresponding multiplier will be $m_n = 1$. It is clear that in order for the periodic orbit to be stable, the rest of the Floquet multipliers associated with vectors \bar{v}_{mi} transversal to the cycle must fulfill

$$|m_i| < 1 \quad i = 1 \dots n - 1 \quad (4.29)$$

It must also be noted that because $m_i(kT) = m_i^k(T)$, the Floquet multipliers must have an exponential expression:

$$m_i = e^{\lambda_i T} \quad i = 1 \dots n \quad (4.30)$$

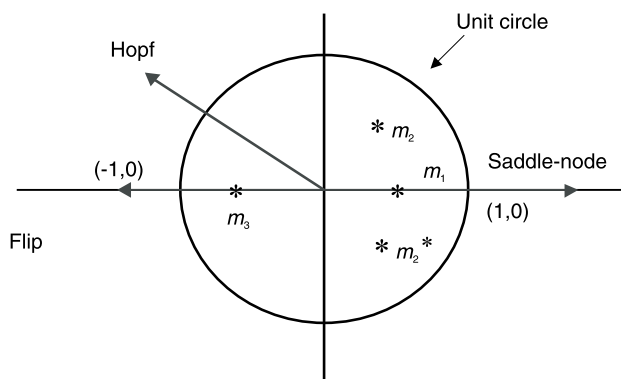


Figure 4.6 Floquet multipliers: representation of the three main types of local bifurcation from a periodic regime.

It is easily shown that the exponents λ_i agree with [12] the exponents in the general solution (4.14) and the periodic vectors are $\bar{v}_i(t) = e^{-\lambda_i t} [\psi_m(t)] \bar{v}_{mi}$. Note that there is not a unique (one-to-one) relationship between the Floquet exponents and multipliers. Actually, it is possible to write

$$m_i = e^{\lambda_i T} = e^{\left(\lambda_i + jn \frac{2\pi}{T}\right)T} \equiv e^{(\lambda_i + jn\omega_o)T} \quad (4.31)$$

with T the period of the periodic solution and ω_o the associated angular frequency.

For the stability of the periodic solution of an autonomous system, its Floquet exponents $i = l \dots n - 1$ must be located on the left-hand side of the complex plane. When this is the case, the perturbation exponentially vanishes in time. In terms of the Floquet multipliers, for stability the Floquet multipliers $i = l \dots n - 1$ must all be located inside the unit circle (Figure 4.6). The practical calculation of Floquet multipliers in electronic circuits can be carried out through the algorithms in [13].

4.1.2.2 The Three Main Local Bifurcations from the Periodic Regime

For the bifurcation analysis of periodic regimes, a parameter η will be introduced in the nonlinear system (4.12):

$$\dot{\bar{x}} = f(\bar{x}, \eta) \quad \begin{cases} x_n = \frac{\theta T}{2\pi} & \text{nonautonomous} \\ x_n & \text{autonomous} \end{cases} \quad (4.32)$$

The system is assumed to have a periodic solution $\bar{x}_o(t, \eta)$ for a certain parameter interval. The frequency of this solution is $\omega_o = \frac{2\pi}{T_o}$. This frequency will

depend on the parameter $\omega_o \equiv \omega_o(\eta)$ in the case of an autonomous circuit or will be delivered by an input RF generator in the case of a nonautonomous (forced) one. For the solution to be stable, all its associated Floquet multipliers m_i (with $i = 1$ to $n - 1$ in the case of an autonomous system) must be located inside the unit circle. The fulfillment of this condition will generally depend on the parameter value. Actually, as η varies, one or more Floquet multipliers may cross the border of the unit circle and escape from it. The solution $\bar{x}_o(t, \eta)$ becomes unstable and a bifurcation takes place in the system for the particular parameter value $\eta = \eta_o$ at which the border of the circle is crossed.

There are three main local bifurcations that can be obtained from a periodic regime, depending on the point or points of the unit circle that are crossed by the real multiplier or the pair of complex-conjugate multipliers.

1. *Multiplier Crossing the Unit Circle Through (1,0): Direct-Type Bifurcation.* A real Floquet multiplier crosses the border of the unit circle through the point (1,0) as the parameter η is varied. This gives rise to a qualitative change in the stability of the solution without a qualitative variation of the fundamental frequency along the solution curve and without the generation of a new fundamental or subharmonic frequency. To see this, note that a multiplier $m_k = 1$ means

$$m_k = 1 = e^{j2\pi} = e^{j\left(0+n\frac{2\pi}{T}\right)T} \equiv e^{jn\omega_o T} \quad (4.33)$$

with ω_o being the frequency of the periodic solution. Note that in (4.33), the nonunique relationship between Floquet multipliers and exponents has been taken into account. From (4.14) and (4.33) and assuming that the remaining Floquet multipliers are still inside the unit circle, the perturbation beyond the bifurcation point η_o will initially grow as

$$\bar{\xi}(t, \eta) = c_{k\eta} e^{\sigma_{k\eta} t} \bar{v}_{k\eta}(t) \quad (4.34)$$

where contributions from other terms in (4.14) have been neglected. Note that because the vector $\bar{v}_{k\eta}(t)$ is periodic at the frequency ω_o , the qualitative change of stability takes place without the generation or

disappearance of fundamental frequencies. Because the solution curve becomes unstable at the D-type bifurcation, the system cannot continue evolving along this curve, so a jump phenomenon will generally take place. This and other possible implications of this bifurcation in the system behavior will be analyzed in detail in Section 4.2.

2. *Multiplier Crossing the Unit Circle at (-1,0): Flip- or Indirect-Type Bifurcation.* When a multiplier crosses the unit circle at (-1,0), there is a division by two of the fundamental frequency ω_o of the periodic regime. This gives rise to a subharmonic oscillation, commonly encountered in the experiment. Actually, a multiplier $m_k = -1$ means

$$-1 = e^{j\pi} = e^{j\left(\frac{\pi}{T} + n\frac{2\pi}{T}\right)T} \equiv e^{j\left(\frac{\omega_o}{2}\right)T} \tag{4.35}$$

Taking (4.35) and (4.14) into account, and assuming that the remaining Floquet multipliers are still inside the unit circle, the perturbation beyond the bifurcation point η_o will initially grow as

$$\xi(t, \eta) = c_{k\eta}^+ e^{\left(\sigma_{k\eta} + j\frac{\omega_o}{2}\right)t} \bar{v}_{k\eta}^+(t) + c_{k\eta}^- e^{\left(\sigma_{k\eta} - j\frac{\omega_o}{2}\right)t} \bar{v}_{k\eta}^-(t) \tag{4.36}$$

where contributions from other terms in (4.15) have been neglected, and the vectors $\bar{v}_{k\eta}^+(t)$ and $\bar{v}_{k\eta}^-(t)$ are complex-conjugate. These vectors are periodic at the frequency ω_o , so from the inspection of (4.36), the flip bifurcation gives rise to the onset or disappearance of a subharmonic at $\frac{\omega_o}{2}$. In the former case, the real Floquet multiplier escapes from the circle through the point -1 (direct flip bifurcation). In the latter case, the real Floquet multiplier enters the circle through the point -1 (inverse flip bifurcation).

3. *Pair of Complex-Conjugate Multipliers Crossing the Unit Circle at $e^{\pm j\theta}$: Secondary Hopf Bifurcation or Naimark Bifurcation.* When a pair of complex-conjugate multipliers escapes from the unit circle through $e^{\pm j\theta}$, a new fundamental frequency nonrationally related with ω_o arises in the system. Actually, a multiplier $m_k = e^{j\theta}$ means

$$1e^{j\theta} = e^{j\alpha 2\pi} = e^{j\left(\alpha\frac{2\pi}{T} + n\frac{2\pi}{T}\right)T} \equiv e^{j\alpha\omega_o T} \tag{4.37}$$

with $\alpha \neq \frac{m}{n}$

The new frequency, nonrationally related to ω_o , can be renamed $\omega_a = \alpha\omega_o$. Then, from (4.14) and (4.37), and assuming that the remaining Floquet multipliers are still inside the unit circle, the perturbation, beyond the bifurcation point η_o , will initially grow as

$$\bar{\xi}(t, \eta) = c_{k\eta}^+ e^{(\sigma_{k\eta} + j\omega_a)t} \bar{v}_{k\eta}^+(t) + c_{k\eta}^- e^{(\sigma_{k\eta} - j\omega_a)t} \bar{v}_{k\eta}^-(t) \quad (4.38)$$

where contributions from other terms in (4.15) have been neglected and the vectors $\bar{v}_{k\eta}^+(t)$ and $\bar{v}_{k\eta}^-(t)$ are periodic with fundamental frequency ω_o and complex-conjugate. The inspection of (4.38) shows the presence of two nonrationally related fundamentals, ω_o and ω_a , giving rise to a quasiperiodic regime.

A more detailed study of the bifurcations from the periodic regime can be carried out in terms of the Poincaré map. This analysis provides information about the stability variations at the bifurcation points of the existing (bifurcating) solutions and about the stability of the newly generated solutions. It will be the object of the following section.

4.2 Bifurcations of the Poincaré Map

The stability analysis to be carried out in this section is applied to the periodic solutions of a forced nonlinear system, although the results can equally be used in the case of periodic solutions of an autonomous system. The bifurcation analysis is based on the stability properties of the Poincaré map [15, 16]. Let the periodic solution $\bar{x}(t) \in R^n$ of a nonlinear forced circuit be given by the expression

$$\bar{x}(t) = \varphi(t, \bar{x}_o) \quad (4.39)$$

where \bar{x}_o is the initial value. The above expression, in terms of the flow φ , provides the value of \bar{x} after a time interval t , when the initial point is \bar{x}_o .

As is already known (see Section 1.5), the Poincaré map of a solution is given by the intersection of this solution with a transversal surface, which enables a dimension reduction of the solution. The Poincaré map of a nonautonomous circuit with a periodic forcing generator of period T can be obtained by sampling its solution at integer multiples of T . Actually, sampling

a solution at the time values $t_o + nT$ is equivalent to considering the intersections of the solution with the transversal surface $\theta_o = \frac{2\pi}{T}t_o$. In the case of the solution (4.39), the first iteration of the Poincaré map is obtained from (see Section 1.5):

$$P(\bar{x}_o) = \varphi(T, \bar{x}_o) \tag{4.40}$$

If \bar{x}_o is a point belonging to the T -periodic steady-state solution, then

$$P(\bar{x}_o) = \bar{x}_o \tag{4.41}$$

and in general, $P^p(x_o) = x_o \forall p \geq 1$, where the super-index indicates the iteration number or the number of successive applications of the map. In the case of a kT -periodic solution, k distinct fixed points $\bar{x}_o, \bar{x}_{o2}, \bar{x}_{ok-1}$ would be obtained through the application of the map.

For the sake of simplicity, a period- T solution with a single fixed point \bar{x}_o is considered here. For the stability analysis of the periodic solution, a small perturbation $\bar{\xi}(t)$ has to be considered. The implications of the perturbation over the Poincaré map are such that, as was has already been shown in Section 1.5.1, in the case of stability (instability), the points resulting from the successive applications of the map converge (diverge), to (from) the fixed point \bar{x}_o (see Figure 1.22). Thus, the stability of the periodic solution $\bar{x}(t) = \varphi(t, \bar{x}_o)$, in terms of the continuous flow φ , agrees with the stability of the fixed point \bar{x}_o , in terms of the (discrete) Poincaré map P .

For the stability analysis of the fixed point \bar{x}_o , a small perturbation $\Delta\bar{x}_o$ will be considered. To obtain the evolution of this perturbation under the discrete map P , and due its smallness, it will be possible to linearize the map P about \bar{x}_o . This linearization is conceptually equivalent to the linearization of the vector field f that has been carried out in the former sections. The linearized map is given by

$$\Delta\bar{x}_1 = [JP(\bar{x}_o)]\Delta\bar{x}_o \tag{4.42}$$

where $[JP]$ is the jacobian matrix of the Poincaré map, and $\bar{x}_1 = \bar{x}_o + \Delta\bar{x}_1$ provides the first iteration of the map. The next point of the map (under this linearization) is calculated from

$$\Delta\bar{x}_2 = [JP(\bar{x}_o)]\Delta\bar{x}_1 = [JP(\bar{x}_o)]^2 \Delta\bar{x}_o \tag{4.43}$$

and, in general,

$$\Delta \bar{x}_k = [JP(\bar{x}_o)]^k \Delta \bar{x}_o \quad (4.44)$$

For the above relationships, it is clear that for stability, all the eigenvalues of the linearized matrix $[JP(\bar{x}_o)]$ must have a modulus less than one. This stability condition reminds us of the condition imposed on the Floquet multipliers. In fact, the eigenvalues of $[JP(\bar{x}_o)]$ agree with the Floquet multipliers of the linearized system (4.13), except for the fact that because the Poincaré map is calculated as the intersection of the solution with a transversal surface, it has one less dimension than the original system.

In the case of the periodic solutions of autonomous systems, the transversal intersection eliminates the direction for which the periodic steady-state solution is invariant. It can easily be shown that the eigenvalues of the linearized Poincaré map agree with the $n - 1$ Floquet multipliers (eigenvalues of the monodromy matrix) different from unity. Actually, it has already been shown that the Floquet multiplier $m_n = 1$ was associated with perturbations in the direction (invariant to the flux) of the periodic orbit.

A fixed point \bar{x}_o of the map is called *hyperbolic* if none of the $n - 1$ eigenvalues of $[JP(\bar{x}_o)]$ has a modulus equal to unity. Nonhyperbolic fixed points are either bifurcation points or degenerate points whose stability cannot be predicted through the linearization (4.42), needing higher order terms in the Taylor-series expansion of the Poincaré map $P(\bar{x}_o)$. The stable subspace E^s of $[JP(\bar{x}_o)]$ is spanned by the eigenvectors associated with multipliers with modulus less than one. In the same way, the unstable subspace E^u of $[JP(\bar{x}_o)]$ is spanned by the eigenvectors associated with multipliers with modulus greater than one. For hyperbolic fixed points, the central subspace spanned by the eigenvectors associated with multipliers with modulus equal to one is, of course, empty, so $R^{n-1} = E^s \oplus E^u$.

For an in-depth analysis of the bifurcations from periodic regimes, a useful classification of hyperbolic fixed points \bar{x}_o has been introduced in [15, 16]. This classification is based on the characteristics of the projection of the matrix $[JP(\bar{x}_o)]$ over its unstable subspace E^u . The resulting matrix is called here $[L^u]$. Two different magnitudes are evaluated: the dimension of E^u and the sign of the determinant of $[L^u]$. The hyperbolic fixed point \bar{x}_o is called *direct* for a positive sign of the determinant of $[L^u]$ and *indirect* for a negative sign of this determinant. The fixed point \bar{x}_o is of *positive* type for an even dimension of E^u and of *negative* type for an odd dimension of E^u . This is summarized in the following:

$$\begin{aligned} \dim E^u & \begin{cases} \text{Even} \rightarrow P \text{ type} \\ \text{Odd} \rightarrow N \text{ type} \end{cases} \\ \det[L^u] & \begin{cases} \text{Positive} \rightarrow D \text{ type} \\ \text{Negative} \rightarrow I \text{ type} \end{cases} \end{aligned} \quad (4.45)$$

Thus, according to the parity of $\dim E^u$ and the sign of the determinant $\det[L^u]$, the possible types of fixed point can be denoted PD , PI , ND , and NI [see (4.45)]. In the particular case of a stable fixed point \bar{x}_o , the number of unstable multipliers is zero, and the point is considered to be of PD -type.

If the Floquet multipliers associated with a hyperbolic fixed point \bar{x}_o are known, the type of the point can immediately be identified. These Floquet multipliers can be real or complex, so for a given fixed point \bar{x}_o , the set of unstable multipliers will be composed of a real multipliers greater than 1, b real multipliers less than -1 , and c complex multipliers with module greater than one. The total number ($n_T = a + b + c$) of unstable multipliers provides the dimension of E^u . The sign of the determinant is determined by b (number of real multipliers less than -1). For odd b , the sign of the determinant is negative. For even b the determinant sign is positive. On the other hand, the parity of $\dim E^u$ only depends on $a + b$. Note that because the complex multipliers appear in complex-conjugate pairs, they do not have an influence either on the parity of the dimension of E^u or in the sign of $\det[L^u]$. Based on a and b , an index can be associated with the fixed point \bar{x}_o , with respect to the k th iteration of the map P^k [see (4.42)].

$$\text{ind}(\bar{x}_o, k) = (-1)^{a+b(k-1)} \quad (4.46)$$

The index value depends on the type of point because so do the integers a and b . This is shown in Table 4.1.

To study the possible bifurcations of a fixed point \bar{x}_o of the Poincaré map, a closed ball B of $n - 1$ dimensions can be considered about this point [16]. The ball is mathematically expressed as

$$B = \{ \bar{x} \in R^{n-1} \mid |\bar{x} - \bar{x}_o| \leq r \} \quad (4.47)$$

It is assumed that when the map is applied as a whole to all the points in the ball B , only the fixed point \bar{x}_o is initially obtained (for given values of the circuit parameters). However, variations in a circuit parameter η may lead to the generation of new fixed points of the map inside the ball, which would be the

Table 4.1
Classification of Fixed Points of the Poincaré Map

Type	$\det[L^u]$	$\dim E^u$	b	a	Index $\text{ind}(\bar{x}_o, k) = (-1)^{a+b(k-1)}$
<i>PD</i>	Positive	Even	Even	Even	+ 1
<i>PI</i>	Negative	Even	Odd	Odd	$(-1)^k$
<i>ND</i>	Positive	Odd	Even	Odd	-1
<i>NI</i>	Negative	Odd	Odd	Even	$(-1)^{k+1}$

result of a bifurcation taking place in the system. The map dependence on the parameter is explicitly stated P_η .

As an example of what may happen in the ball when considering the variation of a parameter η , a direct flip bifurcation would give rise to two fixed points of the map, $P^1(\bar{x}_o) = \bar{x}_{o1}$, $P^2(\bar{x}_o) = \bar{x}_o$, because of the new $2T$ periodicity of the solution. In the case of a direct Hopf bifurcation, a whole closed curve, invariant under the map, would be obtained. This agrees with the fact that when considering a periodic regime of fundamental frequency ω_o , the onset a new fundamental frequency ω_a (through the direct Hopf bifurcation) gives rise to a torus in the phase space. The corresponding Poincaré map, obtained through the intersection of the torus with the transversal surface $\theta = \theta_o = \frac{2\pi}{T}t_o$, is a closed curve.

An important property of the Poincaré map is that, provided that the surface of the ball B defined in (4.47) does not cross any fixed points and no fixed points are originated on the ball surface, the summation of the indexes of all the fixed points contained in the ball remains constant under the continuous deformation of the ball surface S . This total index helps predict and analyze the different bifurcations. The index of the ball is just the summation of the indexes of all the fixed points that are contained in this ball [16]:

$$\text{ind}(S, k, \eta) = \sum_{\bar{x}_o \in B} \text{ind}(\bar{x}_o, k, \eta) \quad (4.48)$$

where the number k indicates that the index is calculated with respect to P^k .

The usefulness of ball index (4.48) for the study of bifurcations will be shown in the following. In the analysis, a stable periodic solution of period T will initially be considered, giving rise to a single fixed point of the Poincaré

map \bar{x}_o . Because the point is stable, it will be of *PD*-type. From Table 4.1, the associated index is $\text{ind}(\bar{x}_o, k) = 1$. Initially, the ball B only contains the fixed point \bar{x}_o . Then its associated index will be $\text{ind}(S, k, \eta) = 1$. When a parameter η is modified, the three possible types of bifurcation are analyzed as follows.

4.2.1 Flip-Type Bifurcations

As is already known, flip bifurcations take place when (for a certain parameter value η_o) a Floquet multiplier crosses the unity circle through the point $(-1, 0)$. In the example we are treating here, the multiplier leaves the unit circle because of the initial stability of \bar{x}_o . Thus, the number of unstable multipliers increases in one after the bifurcation. There is one unstable eigenvalue more after the bifurcation. This modifies the parity of E^u , so the fixed point \bar{x}_o (initially of *P* type) will become *N*-type (odd dimension of E^u). On the other hand, the new negative multiplier will change the sign of $\det[L^n]$, which becomes negative (or *I*-type). Thus, at the bifurcation parameter value η_o , the fixed point \bar{x}_o changes its type from *PD* to *NI*.

According to Table 4.1, the new index of \bar{x}_o , after the flip bifurcation, will be $\text{ind}(\bar{x}_o, k) = (-1)^{k+1}$. It will be 1 for k odd and -1 for k even. Thus, its value depends on the number of repeated applications of the Poincaré map P^k . For P^1 , $\text{ind}(\bar{x}_o, 1) = 1$ before and after the bifurcation. However, for P^2 , we have $\text{ind}(\bar{x}_o, 2) = 1$ before the bifurcation and $\text{ind}(\bar{x}_o, 2) = -1$ after the bifurcation. This is in contradiction with the fact that the index of the ball must remain invariant before and after the bifurcation. Thus, some additional fixed points must have been created inside the ball to compensate for the disagreement. The transformation under which the index of the ball keeps constant is the following [16]:

$$PD_o \leftrightarrow NI_1 + 2PD_o^2 \tag{4.49}$$

where the subindex indicates the dimension of the unstable subspace E^u and the superindex indicates the periodicity of the fixed points (1 is omitted). The double arrow indicates that the bifurcation may take place in the direct sense (arrow pointing rightwards), giving rise to a direct flip bifurcation, or in the inverse sense (arrow pointing leftwards), giving rise to an inverse flip bifurcation.

As shown in (4.49), two new fixed points must have been created inside the ball after the bifurcation. These points are fixed points of P^2 . In terms of the flow, the bifurcation gives rise to two period-2 solutions that are 180° out of phase. As shown in (4.49), in order for the index of the ball to keep constant

before and after the bifurcation, the newly generated points must be of PD -type. Taking Table 4.1 into account, this can be written as follows:

$$\text{ind}(PD,2) = \text{ind}(NI,2) + 2\text{ind}(PD^2,2) = -1 + 2 \cdot 1 = 1 \quad (4.50)$$

As shown in (4.49), if a stable period- T solution suffers a flip bifurcation, it will become unstable after the bifurcation. However, the newly generated period-2 solution will be stable. Note that this stability information was missing in the analyses of Section 4.1. An example of flip bifurcation will be shown in Example 4.3.

Example 4.3: Flip-type bifurcation in an IMPATT-based circuit

The diagram of Figure 4.7 is an expanded view of Figure 1.20. This figure shows the qualitative variations in the solution of an IMPATT-based circuit versus the input-generator amplitude I_g through application of the Poincaré map [17]. For each generator value, the circuit is solved versus the parameter through time-domain integration, using the nonlinear model for the IMPATT diode in [17, 18]. Then, once the solution has reached the steady state, samples of the diode voltage are taken at integer multiples nT of the input-generator period. Note that because of the use of time-domain integration, only stable steady-state solutions can be obtained. For low values of the input-generator amplitude, the sampling at nT provides one single fixed point (see Figure 4.7). This indicates a stable periodic solution of period T . Thus, the fixed point will be of PD -type. For $I_{g_0} = 0.17$ A, there is a qualitative variation in the diagram, obtaining for $I_g > I_{g_0}$ two fixed points of the map. A stable period-2 solution has been created at the bifurcation point, and according to (4.49), the two associated fixed points must be of PD^2 -type. The original period- T solution

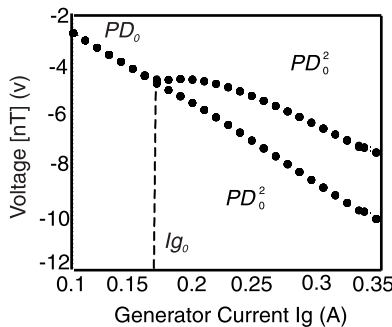


Figure 4.7 Flip bifurcation in the Poincaré map of an IMPATT-based circuit.

continues to exist after the bifurcation. However, this solution is unstable and cannot be obtained through standard time-domain integration. For this reason, the corresponding single fixed point has not been represented in Figure 4.7. This fixed point is of NI -type. As will be shown, the harmonic-balance technique, because of its ability to converge to unstable solutions, is very useful to obtain the entire bifurcation diagram versus the parameter, including stable and unstable sections of the solution curves.

In similar way to what happens with Hopf bifurcations from the dc regime, the flip bifurcations from the periodic regime can be classified into *supercritical* and *subcritical*. At a supercritical bifurcation, stable period-2 cycles are generated from a period-1 solution that becomes unstable at the bifurcation point. The stable period-2 cycle coexists, after the bifurcation, with the unstable period-1 cycle. This has been represented in Figure 4.8(a), where the unstable solutions that cannot be obtained through standard time-domain integration have also been considered. These unstable solutions are traced in solid line. As already indicated, the supercritical bifurcation may be of direct or inverse type, according to the sense of the arrow in (4.49). In the case of Figure 4.8(a), a direct bifurcation (arrow pointing rightwards) will be obtained in the increasing-parameter sense, while an inverse bifurcation (arrow pointing leftwards) is obtained in the decreasing parameter sense.

In a subcritical flip bifurcation, an unstable period-2 solution coexists with the stable period-1 solution before the bifurcation parameter value η_0 is reached. At the bifurcation point, this period-1 solution becomes unstable and there are no stable solutions in its neighborhood. A general case of subcritical bifurcation is shown in Figure 4.8(b), where the complete bifurcation diagram (including unstable solutions) has been represented. The ball to be considered in the bifurcation analysis is explicitly shown in the figure. The explicit indication of this ball is now essential because two different bifurcations are, in fact, present in Figure 4.8(b). The second bifurcation that will not be analyzed for

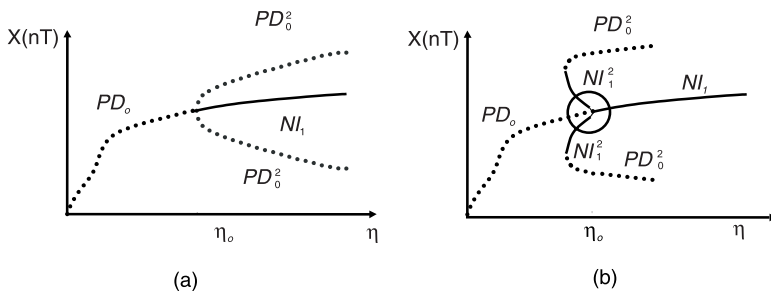


Figure 4.8 Flip bifurcation in the Poincaré map: (a) supercritical, and (b) subcritical.

the moment is a turning point, occurring in the period-2 solution. Centering our study on what happens in the ball around the flip bifurcation, the subcritical flip bifurcation can be formulated:

$$PD_o + 2NI_1^2 \leftrightarrow NI_1 \quad (4.51)$$

Again, for the arrow pointing rightwards, a direct and subcritical flip bifurcation would be obtained. For the arrow pointing leftwards, the bifurcation would be inverse and subcritical. In (4.51), a stable period-1 solution and two unstable period-2 solutions merge to give rise to an unstable period-1 solution. Note the local character of this formulation, requiring the definition of a small ball around the bifurcation point.

Finally, it must also be pointed out that flip-type bifurcations may also take place from period-1 solutions that are unstable. In this case, the bifurcating fixed point \bar{x}_o will have a type different from PD . Taking into account the conservation of the index of the ball before and after the bifurcation, similar relationships to (4.49) and (4.50) can easily be obtained [16].

4.2.2 Direct-Type Bifurcations

At a direct-type (D -type) bifurcation, a Floquet multiplier crosses the unity circle through the point $(1,0)$. Then, the number a of multipliers greater than 1 increases or decreases in one, while the number b of multipliers less than -1 remains constant. At this kind of bifurcation the parity of $\dim E^u$ changes, but not the sign of $\det[L^u]$. As in the former case, before the bifurcation, a stable periodic solution of period T will be assumed. Thus, at the D -type bifurcation, one multiplier leaves the unit circle through the point $(1,0)$. Before the bifurcation, the fixed point \bar{x}_o of the Poincaré map P is of PD -type (because it has zero unstable multipliers). After the D -type bifurcation, the number of unstable multipliers will be one, so the parity of $\dim E^u$ will be odd. On the other hand, the sign of $\det[L^u]$ will be positive because of the positive value of the unstable multiplier. Thus, the new type of the fixed point \bar{x}_o is ND .

To analyze the bifurcation, a ball is considered around the fixed point \bar{x}_o . Before the bifurcation, the ball only contains this fixed point (of PD -type), and the index of the ball is (see Table 4.1) $\text{ind}(\bar{x}_o, k) = 1$. After the bifurcation, the index of the ND fixed point is $\text{ind}(\bar{x}_o, k) = -1$ (see Table 4.1). The index of the ball must remain invariant before and after the bifurcation, so to preserve the ball index, two new fixed points must be created in this ball. The actual transformation is as follows [16]:

$$PD_o \leftrightarrow ND_1 + 2PD_o \tag{4.52}$$

The above transformation corresponds to a supercritical D -type bifurcation. A direct D -type bifurcation is obtained for a transformation with the arrow in (4.52) pointing rightwards. An inverse D -type bifurcation is obtained for a transformation with the arrow in (4.52) pointing leftwards.

The supercritical D -type bifurcation (4.52) also has its subcritical counterpart, with the following equation:

$$PD_o + 2ND_1 \leftrightarrow ND_1 \tag{4.53}$$

Note that compared to the case of flip bifurcations, the new solutions generated at the D -type bifurcation have the same periodicity as the original stable solution, as has already been shown in the analysis of (4.34). The D -type bifurcation (4.52) has been sketched in Figure 4.9(a). This kind of D -type bifurcation is called the *pitchfork* type. A stable symmetric limit cycle of period T gives rise to two asymmetric limit cycles of the same period T . To illustrate this, Figure 4.9(b) shows the phase portrait of a nonlinear system that has suffered a bifurcation of D -type and is, in fact, operating in the right-hand side of (4.52). It is the phase portrait after the bifurcation. As can be seen, the original symmetric cycle, which is now unstable, coexists with two stable asymmetric cycles with respect to the origin. In experiment, the observed solution may correspond to either one or another of the two cycles, depending on the initial conditions. The phase portrait of Figure 4.9(b) has been obtained through harmonic balance because,

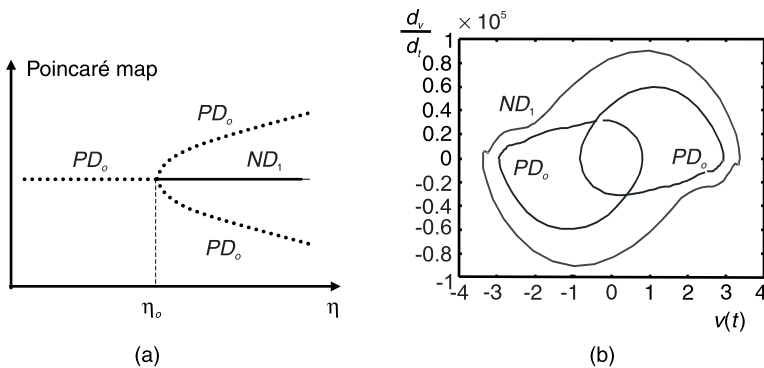


Figure 4.9 Direct-type bifurcation: (a) bifurcation diagram through the Poincaré map, and (b) phase portrait after the bifurcation. It has been obtained through harmonic balance.

as has been said, convergence to unstable solutions is impossible through standard time-domain techniques.

Direct-type bifurcations like the one depicted in Figure 4.9 are not very common because they require symmetry conditions that are not easy to find in practical circuits. The turning-point bifurcation is a particular case of D -type bifurcation that, in contrast with (4.52) and (4.53), is usually obtained in nonlinear circuits. The meaning and implications of a turning point in a periodic solution path are totally equivalent to those of a turning point (or fold bifurcation) in a dc solution path (see Section 4.1.1).

As has already been said, turning points are a special case of D -type bifurcations from the periodic regime. In contrast to the situation of Figure 4.9, there is no solution before the D -type bifurcation takes place, as sketched in Figure 4.10. For $\eta < \eta_o$, there are no fixed points of the Poincaré map and this is indicated as ϕ . For $\eta > \eta_o$ there are two fixed points. In the absence of fixed points, the index of the ball B is zero, and this value must be preserved after the bifurcation. Thus, assuming one stable solution after the bifurcation, the only possible situations is

$$\phi \leftrightarrow PD_o + ND_1 \quad (4.54)$$

Note that the summation of the indexes of the two newly generated fixed points is zero, agreeing with the index that has been associated with ϕ . The two solutions on the right-hand side of (4.54) differ in one unstable Floquet multiplier, in correspondence with the qualitative change of stability that is obtained when a real multiplier crosses the border of the unity circle through the point (1,0) (see Section 4.1.2). This is what happens in Figure 4.10. Assuming that the initial solution belongs the stable section (with a fixed point of the Poincaré

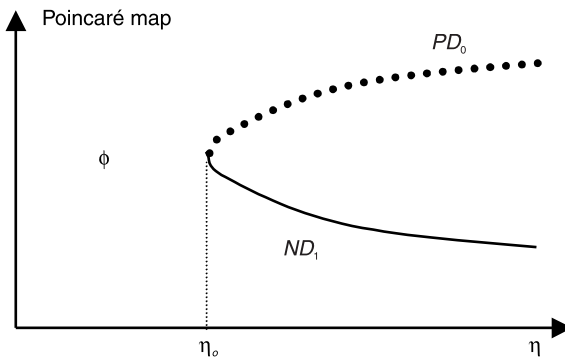


Figure 4.10 Turning point at η_o . Creation of fixed points at $\eta = \eta_o$.

map of PD_o -type), as the parameter η is decreased, a real multiplier $m_i < 1$ approaches the border of the unit circle. For $\eta = \eta_o$, it crosses the border through the point (1,0). When this happens, the solution curve folds over itself, which can also be seen as a creation (or annihilation) of fixed points.

D -type bifurcations may also take place from period-1 solutions that are unstable. If this is the case, the type of bifurcating fixed point will be different from PD . Taking into account the conservation of the index of the ball before and after the bifurcation, similar relationships to (4.52), (4.53), and (4.54) can easily be obtained [16].

As a final comment, subcritical Hopf and flip bifurcations are generally associated with turning points in the bifurcated paths. This can be seen, for instance, in the subcritical flip bifurcation of Figure 4.8(b), for which each of the period-2 branches exhibits a turning point. As an example, a microwave frequency doubler, having a subcritical flip bifurcation will be analyzed in Example 4.4.

Example 4.4: Subcritical flip bifurcation in a varactor-based frequency doubler

The circuit in Figure 4.11 is a microwave frequency doubler, based on the use of a long-lifetime PN -junction varactor diode [19]. Due to the great value of the carrier lifetime, the diffusion capacitance is high and, together with the junction capacitance, gives rise to a very nonlinear behavior versus the instantaneous diode voltage. This nonlinearity is very convenient for harmonic generation. The frequency doubler in Figure 4.11 is composed of an input bandpass filter, selecting the input-generator frequency (5 GHz) and an output filter, selecting the doubled frequency (10 GHz).

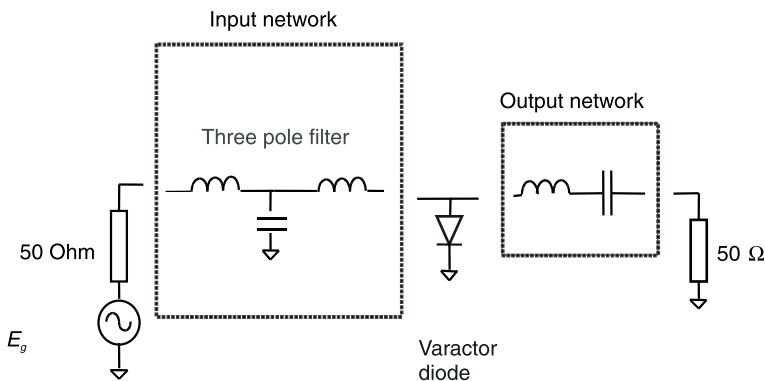


Figure 4.11 Microwave frequency doubler.

The behavior of the doubler circuit will be analyzed through the Poincaré map. Because it is a nonautonomous circuit, the map can be obtained by sampling the steady-state solution at integer multiples of the input-generator period nT_g . As shown in Figure 4.12, for low input amplitude, a single point is obtained, indicating that the period of the solution is the same as the input-generator period $T = T_g$. This is, of course, the kind of behavior expected in the frequency doubler, for which the output signal is just the second harmonic of the input-generator frequency. However, for $E_g = 2.15v$, a flip bifurcation is obtained, giving rise to a period-2 solution and, thus, to two points in the Poincaré map. This bifurcation is a subcritical one [see Figure 4.8(b)]. The subcritical bifurcations, associated with turning points in the bifurcated paths, give rise to broken lines in the Poincaré map, as can be clearly observed in Figure 4.12. Note that the flip bifurcation is itself continuous. The discontinuity (or jump) observed in the map is due to the instability of a section of the period-2 branch [see Figure 4.8(b)]. On the other hand, the period-2 solution exists for before and after the bifurcation actually takes place. Comparing Figure 4.12 with the sketch of Figure 4.8, it is clear that there is a section missing in the period-2 branch of Figure 4.12. This section can be obtained by varying the parameter in the reverse sense [i.e., starting from a generator amplitude in the interval (2.15, 2.7) and decreasing its value]. This is explained by the fact that, in the presence of multiple stable solutions, the observed solution depends on the initial value of the state variables. By decreasing the input-generator amplitude from a value for which a period-2 solution is observed, the solution

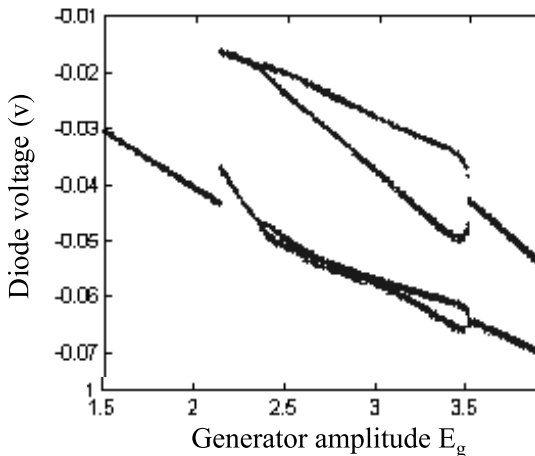


Figure 4.12 Bifurcation diagram of a varactor-based frequency doubler.

for $E_g < 2.15v$ will be conditioned by an initial value close to the period-2 solution. A hysteresis cycle is obtained.

Continuing with the analysis of the bifurcation diagram, for $E_g = 2.7v$, a new flip bifurcation is observed, giving rise to a period-4 regime. This bifurcation is a supercritical one, with no jump versus the parameter. For $E_g = 3.4v$, an inverse supercritical bifurcation is obtained, leading to a period-2 solution.

4.2.3 Hopf-Type Bifurcations

Hopf-type bifurcations are obtained when, for a parameter value $\eta = \eta_o$, a pair of complex-conjugate eigenvalues crosses the border of the unit circle through a point different from $(1,0)$ and $(-1,0)$. As was shown in (4.37), this gives rise to the onset of a new fundamental frequency in the system, ω_o , nonrationally related to ω_o (i.e., $\omega_a = \alpha\omega_o$, with $\alpha \neq \frac{m}{n}$). Thus, after the Hopf bifurcation, the solution will have two nonrationally related fundamentals and will be quasiperiodic. It is the first time that this case is encountered because, both in flip-type and D -type bifurcations, the solution is periodic before and after the bifurcation takes place.

Because the variation in the number of unstable Floquet multipliers is ± 2 , both the parity of $\dim E^u$ and the sign of $\det[L^n]$ remain unchanged. Thus, at the Hopf-type bifurcation, the type of the period-1 fixed point \bar{x}_o does not change after the bifurcation (although its number of unstable Floquet multipliers varies in ± 2).

To study the Hopf-type bifurcation, a stable the period-1 solution will be assumed with associated fixed point of the Poincaré map \bar{x}_o of PD_o -type. After the Hopf-type bifurcation, the stability of the fixed point changes to PD_2 . This unstable fixed point coexists with a stable closed curve generated at the Hopf bifurcation [16]. Remember that the Poincaré map of a quasiperiodic solution is a closed curve (Section 1.5.2), invariant under the map. This can be formulated as

$$PD_o \leftrightarrow PD_2 + C, \quad (4.55)$$

where C_s is a stable closed curve [16]. Note that the classification in Table 4.1 only applies to fixed points, so, in the case of closed curves, the notation will be reduced to C with the subindex s (for stable) or u (for unstable). Equation (4.55) corresponds to a supercritical Hopf-type bifurcation. The subcritical counterpart is given by

$$PD_o + C_u \leftrightarrow PD_2 \quad (4.56)$$

Example 4.5 shows the Hopf-type bifurcation of a cubic nonlinearity oscillator, operating in synchronized regime.

Example 4.5: Hopf bifurcation in the cubic nonlinearity oscillator

The circuit considered here is identical to the one in Figure 1.3. However, the linear element values are modified to $R = 3 \text{ Ohm}$, $L = 296 \text{ nH}$, $C = 17.6 \text{ nF}$ with the nonlinear current source $i(v) = -0.2v + 0.02v^3$. This circuit has a free-running oscillation at the frequency $f_{of} = 1.5 \text{ MHz}$. Now a periodic current generator I_g in parallel with the resistor R will be considered with amplitude $I_g = 50 \text{ mA}$. The period T_g of this generator is taken as the analysis parameter. The resulting Poincaré map, obtained by modifying the period from $T_g = 0.62 \mu\text{s}$ (or $f_g = 1.61 \text{ MHz}$) to $T_g = 0.54 \mu\text{s}$ (or 1.85 MHz), is shown in Figure 4.13. Two different regions can clearly be distinguished. For $T_g > 0.58 \mu\text{s}$, the Poincaré map consists of a single fixed point, so the solution is periodic with the same period as the input generator. However, from $T_g = 0.58 \mu\text{s}$ (or $f_g = 1.72 \text{ MHz}$), the map gives rise to a closed curve, as can be appreciated in the three-dimensional representation of Figure 4.13.

A supercritical Hopf bifurcation takes place for this period value. For $T_g < 0.58 \mu\text{s}$, the transversal section of the map is an invariant closed curve, constituted of discrete points. Successive applications of the map would eventually fill this curve. The evolution of the invariant closed curve can be appreciated in the diagram. The circuit, for $T_g < 0.58 \mu\text{s}$, operates in a quasiperiodic regime with two fundamental frequencies.

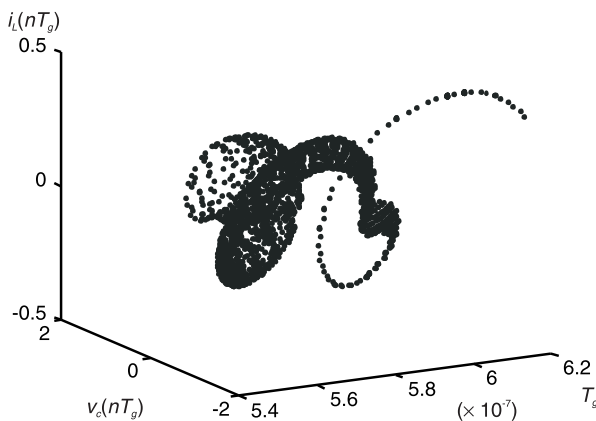


Figure 4.13 Hopf bifurcation in the Poincaré map of a cubic nonlinearity oscillator.

An essential characteristic of both flip and Hopf bifurcation is the continuity. This can be appreciated in the representation of Figure 4.13. The amplitude of the newly generated closed curve increases from zero value. The same would be obtained in the case of a subcritical bifurcation, although the periodic solution starting from zero amplitude value would not be observable because of its instability. In Figure 4.13, the formerly stable fixed point of the map continues to exist after the bifurcation (although it is an unstable point) and the invariant closed curve is located around this point in identical way to what happens in Hopf bifurcations of dc regimes (see Figure 4.4).

4.3 Global Bifurcations

Global bifurcations are associated with qualitative changes in the configuration of the invariant manifolds of a saddle-type solution [2]. The stable (unstable) manifold of a saddle solution is the set of points that under the application of the nonlinear flow φ leads to the saddle solution as $t \rightarrow \infty$ (as $t \rightarrow -\infty$) (see Section 1.4.2). The invariant manifolds act like separatrices of trajectories, as shown in Figure 1.18. As has already been indicated in Chapter 1, stable (unstable) manifolds of different equilibrium points (or fixed points, in the case of the Poincaré map) cannot intersect because of the uniqueness of the solution of the nonlinear system. However, the stable and unstable manifolds of the same or different equilibrium points (or fixed points in the case of the Poincaré map) can intersect.

The changes in the configuration of the manifolds may give rise to a qualitative variation in the basin of attraction of a given solution. Other possibilities with more important implications are the creation of a new attractor or the destruction of an existing one. As will be shown, something peculiar to global bifurcations is the discontinuity with which attractors are created or extinguished.

Here, two types of global bifurcations will be treated: the saddle connection and the saddle-node local/global bifurcation. The two can be observed in flows, in the phase space, or in terms of the Poincaré map, with analogous behavior patterns (versus the parameter). As will be shown, both types of global bifurcation give rise to the discontinuous appearance or disappearance of invariant cycles.

4.3.1 Saddle Connection

Let a saddle equilibrium point of an autonomous system be considered. As is already known, saddle equilibrium points are unstable and, thus, physically

unobservable. When a parameter is modified, the possible intersection of the stable and unstable manifolds of the equilibrium point [2] gives rise to what is known as a saddle connection (see Figure 4.14). A common pattern for the formation of saddle connections is shown in Figure 4.15. The inset of the saddle separates points of trajectories going to the limit cycle from points of trajectories diverging to infinity. As the parameter varies, the saddle point and the limit cycle approach. The collision gives rise to an intersection of the stable and unstable manifolds of the saddle, providing a doubly asymptotic trajectory (Figure 4.15). This trajectory is called *homoclinic orbit* [2, 4, 13, 20]. As the cycle approaches the orbit, its period increases and becomes infinity when the cycle becomes the homoclinic orbit.

The homoclinic orbit only exists for a particular and single value of the parameter. For a transversal intersection of the manifolds the homoclinic orbit gives rise to chaos. In a transversal intersection, the vectors tangent to the manifold at each point of the intersection can generate through linear combination all possible directions in the phase space [8]. An example of this will be shown in Chapter 6, which deals with chaotic solutions. For a nontransversal intersection of the manifolds, the limit cycle is destroyed. Thus, taking the whole process into account, the saddle connection gives rise to the discontinuous extinction of the limit cycle. For a variation of the parameter in the reverse sense, the limit cycle would be discontinuously generated.

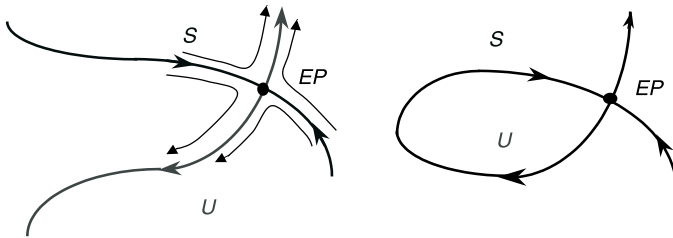


Figure 4.14 Saddle connection.

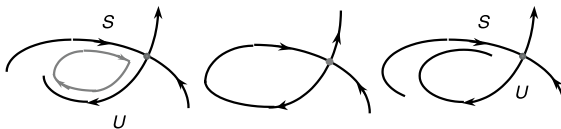


Figure 4.15 Collision of a limit cycle with a saddle equilibrium point with the discontinuous extinction of the cycle.

The process depicted in Figure 4.15 can also be obtained in terms of the Poincaré map with the collision of an invariant cycle of the map (corresponding to a quasiperiodic solution of the nonlinear system) and a fixed point of saddle type (corresponding to a saddle-type periodic solution). This would give rise to the sudden extinction of the autonomous fundamental frequency. In the phase space, a torus (quasiperiodic solution) becomes a periodic cycle. For a reverse variation of the parameter, a cycle becomes a torus.

4.3.2 Saddle-Node Local/Global Bifurcation

A turning-point bifurcation separating a stable section and an unstable section of a solution curve may be viewed as a collision between a node-type solution and a saddle-type solution. This is specifically called *saddle-node bifurcation* [2]. This collision may take place in terms of equilibrium points of the phase space (see Section 4.1.1) or in terms of fixed points of the Poincaré map. The collision gives rise to the destruction of the equilibrium points (fixed points) in the phase space (Poincaré map) and, continuing the modification of the parameter in the same sense, the system may go to a different solution, away from the initial node-type equilibrium point (fixed point). This solution typically exists before the collision, the jump being part of an hysteresis phenomenon. This would be the case of the local saddle-node bifurcation that has already been studied.

In other cases, an invariant manifold connects the saddle and the node, making a loop (although only the node is observable). At the saddle-node, the manifold becomes a limit cycle and the solution becomes oscillatory (see Figure 4.16). The manifold closed at the saddle-node bifurcation of a dc regime gives rise to the discontinuous generation of a limit cycle. The jump in size of the attractor comes from the new configuration of the manifolds, giving rise to the cycle. This discontinuity in the size of the attractor distinguishes this bifurcation from the Hopf bifurcation, at which the limit cycle is generated from zero amplitude (see Figure 4.5). It is often classified as local/global bifurcation because of its association with a turning point of the solution path (which constitutes a local bifurcation) [2, 21–24].

A saddle-node bifurcation with the formation of an invariant cycle may also take place at a fixed point of the Poincaré map. This gives rise to the discontinuous generation of an invariant closed curve under the map (i.e., to the generation of a quasiperiodic solution in the phase space). In [2], this particular case of saddle-node bifurcation is termed *saddle-node bifurcation with mode locking*. In injected oscillators, this bifurcation often delimits the borders of the synchronization band versus a given parameter. In fact, there are two different

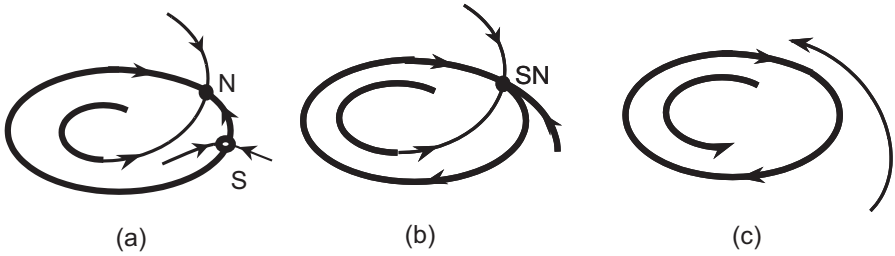
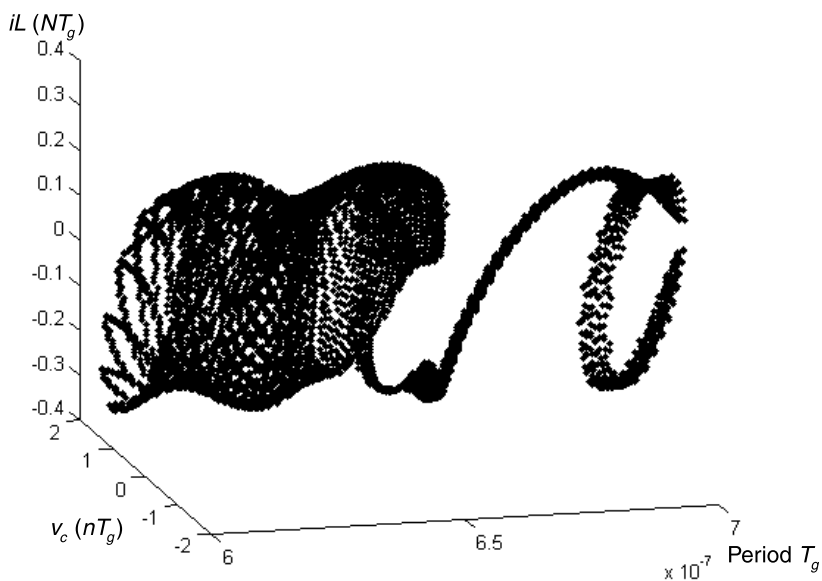


Figure 4.16 Saddle-node giving rise to the discontinuous onset of a limit cycle: (a) A saddle and a node equilibrium point separately exist in the phase space (or a saddle and a node fixed point separately exist in the Poincaré map). (b) Saddle and node merge in a saddle-node bifurcation. (c) A limit cycle is discontinuously created in the phase space (or in the Poincaré map) from the intersecting manifolds in the saddle-node point.

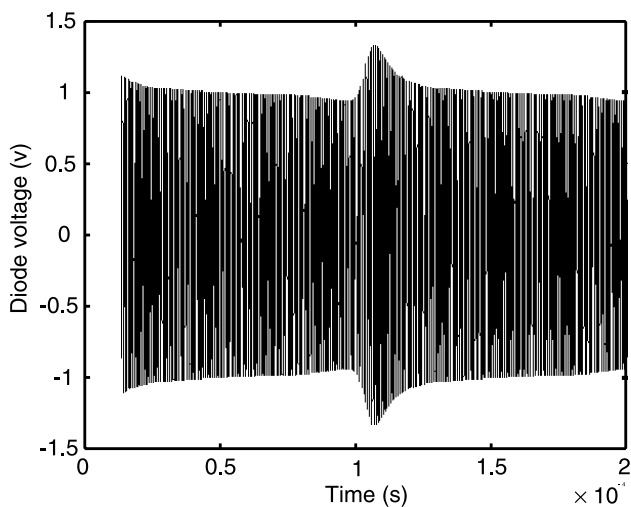
ways in which an injected oscillator operating in a synchronized regime can, as a parameter is modified, lose this synchronized condition. For relatively high amplitude of the input generator, the loss of synchronization is generally due to a Hopf bifurcation (see Example 4.5 for $I_g = 50$ mA). For low input-generator amplitude, the loss of synchronization is generally due to local/global saddle-node bifurcations. To see this more clearly, Example 4.6 analyzes the same circuit for the input current $I_g = 7$ mA .

Example 4.6: Loss of synchronization in the cubic nonlinearity oscillator

The application of the Poincaré map to analyzing the variations in the solution of the cubic nonlinearity oscillator of Example 4.5 for $I_g = 7$ mA provides the diagram in Figure 4.17(a). Two saddle-node bifurcations delimit the synchronization band. These bifurcations respectively occur for $T_g = 0.65 \mu\text{s}$ ($f_g = 1.534$ MHz) and $T_g = 0.69 \mu\text{s}$ ($f_g = 1.45$ MHz). Note the discontinuity with which the limit cycle is created at these two bifurcations. In contrast to what happens at Hopf-type bifurcations, the formerly stable fixed point no longer exists after the saddle-node bifurcation. At the bifurcation, it is contained in the newly created cycle in good correspondance with Figure 4.16(b). This often gives rise, just after the loss of synchronization, to an intermittence phenomenon [8]. After the bifurcation, there is a much higher density of map points about the former fixed point of the map. Due to this fact, the waveform of Figure 4.17(b), obtained for $f_g = 1.449$ MHz, has the appearance of a periodic waveform for long time intervals. Its actual quasiperiodic nature (a cycle in the Poincaré map) gives rise to the bursts that appear in the figure. Another



(a)



(b)

Figure 4.17 Poincaré map of the cubic nonlinearity oscillator for $I_g = 7$ mA: (a) two saddle-node bifurcations (respectively occurring for $T_g = 0.65 \mu\text{s}$ and $T_g = 0.69 \mu\text{s}$) give rise to the discontinuous creation of two limit cycles in the map; and (b) intermittence immediately after the loss of synchronization.

example of intermittence, this time associated with chaotic behavior, is shown in Section 6.5.

4.4 Analysis of Bifurcations from the Harmonic-Balance Characteristic System

As shown in Chapter 2, continuation techniques can efficiently be combined with harmonic balance to trace the circuit solution paths (e.g., in terms of output power) versus a circuit parameter. The continuation techniques enable passing through turning points [19–21], and because harmonic balance can converge to either stable or unstable solutions, the whole solution path, including unstable sections, can be obtained. The use of continuation techniques [25–27] enables obtaining all the coexisting solutions with the same frequency basis (e.g., with one or two fundamentals or with one subharmonic frequency). This provides, as will be seen, a very complete picture of the circuit behavior versus the parameter. Note that some stable solutions may be very difficult to obtain through standard time-domain simulation. This happens in the case of the coexistence of two stable solutions with a big disproportion in their basins of attraction. If the basin of attraction of one is very small compared to that of the other, most sets of initial conditions will lead to the other one.

In this section, the main local bifurcations from dc and the periodic regimes will be restudied in the frequency domain, obtaining bifurcation equations that can be numerically solved in this domain [27–29]. The implementation of these equations in harmonic-balance software can be demanding. In Section 4.5, other techniques that are more easily combined with existing harmonic-balance software will be presented.

4.4.1 Bifurcations from the DC Regime

For a harmonic-balance analysis of bifurcations from a dc regime, the parameter η must be introduced into the harmonic-balance equations:

$$\bar{H}(\bar{X}_{dc}, \eta) = 0 \quad \rightarrow \quad \bar{X}_{dc} \equiv \bar{X}_{dc}(\eta) \quad (4.57)$$

where \bar{X}_{dc} is a vector composed of the state variables (having only dc terms) of the harmonic-balance formulation. Remember that in piecewise harmonic balance the number of state variables is usually much smaller than in the differential equation system. The harmonic-balance variables are generally the control

variables of the nonlinear elements. For m control variables, (4.57) will be a system of m variables in m equations with one parameter η .

As shown in Chapter 2, the stability of \bar{X}_{dc} is analyzed by considering a small amplitude perturbation of complex frequency $e^{(\sigma + j\omega)t}$. This gives rise to the following linearized system:

$$[JH(\sigma + j\omega, \bar{X}_{dc}, \eta)]\Delta\bar{X} = 0 \quad (4.58)$$

where $[JH]$ is the characteristic matrix of the harmonic-balance linearization about the dc solution \bar{X}_{dc} . This matrix is given by

$$[JH] = \left\{ [Ax(\sigma + j\omega)] - [Ay(\sigma + j\omega)] \left[\frac{\partial \bar{Y}}{\partial \bar{X}_{dc}} \right] \right\} \quad (4.59)$$

As is already known, for stability all the poles of the linearized system (4.58) must be located on the left-hand side of the complex plane. These poles are given by the roots of the determinant of $[JH]$:

$$\det[JH(\sigma + j\omega, \bar{X}_{dc}, \eta)] = 0 \quad (4.60)$$

Taking into account the dependence of (4.58) and (4.60) on the parameter η (and the theorem of the implicit function [3]), the location of the poles will generally depend on the value of this parameter. Thus, modifying η , a qualitative variation in the circuit stability conditions (or bifurcation) may take place. Actually, a bifurcation is obtained if for a given parameter value η , the following conditions are fulfilled [27–29]:

$$\det[JH(j\omega, \bar{X}_{dc}, \eta_o)] = 0 \quad (4.61a)$$

$$\left. \frac{d\sigma}{d\eta} \right|_{\eta=\eta_o} \neq 0 \quad (4.61b)$$

This means that for the parameter value $\eta = \eta_o$, a real pole σ or a pair of complex-conjugate poles $\sigma \pm j\omega$ of (4.58) crosses the imaginary axis of the complex plane. For $\omega = 0$, a turning-point bifurcation like the one sketched in

Figure 4.2 will be obtained. The case $\omega \neq 0$ corresponds to a primary Hopf bifurcation like the one shown in Figure 4.4.

To determine the bifurcation points of a dc solution versus a parameter η , the following system should be solved:

$$\bar{H}(\bar{X}_{dc}, \eta_o) = 0 \quad (4.62a)$$

$$\det[JH(j\omega, \bar{X}_{dc}, \eta_o)] = 0 \quad (4.62b)$$

The above system is a well-conditioned system, as will be shown in the following example. In the case of a turning-point bifurcation, the determinant is real, and the system contains $m + 1$ equations in $m + 1$ unknowns. In the case of a Hopf-type bifurcation, the determinant is complex and (4.62b) consists, in fact, of two equations corresponding to the real and imaginary parts of this determinant. Equation (4.62) will contain $m + 2$ equations in $m + 2$ unknowns.

To show how a Hopf bifurcation looks when analyzed through harmonic balance, the VCO in Ku-band [28] of Example 2.9 is considered again in Example 4.7.

Example 4.7: Primary Hopf bifurcation in a VCO in Ku-band

Figure 2.16 showed the analysis of the Ku-band VCO of Figure 2.13 versus the bias voltage of the varactor diode V_D . The vertical axis of this representation is the oscillation output power P_{out} at the first harmonic component. Thus, the dc solutions lie on the horizontal axis $P_{out} = 0$. Two Hopf bifurcations are observed at the respective values of varactor bias voltage $V_{H1} = -1.4v$ and $V_{H2} = 0.9v$. The first bifurcation is a direct Hopf bifurcation, while the latter one is an inverse one, giving rise to the extinction of the free-running oscillation.

The direct bifurcation V_{H1} is a subcritical one because, as is clearly seen, the oscillating solution exists before the diode voltage reaches the bifurcation value $V_{H1} = -1.4v$ and coexists with the stable dc solution. The oscillating path exhibits a turning point T . This is, of course, a bifurcation from the periodic oscillation regime that cannot be detected from (4.61). The periodic section T_{H1} is composed of unstable periodic solutions that cannot be obtained through standard time-domain integration. The subcritical bifurcation V_{H1} gives rise to an hysteresis phenomenon in the oscillator. Actually, when increasing the bias varactor diode, in the absence of oscillation, the oscillation starts at $V_D \equiv V_{H1}$. However, when decreasing the varactor bias from an oscillation state, this oscillation only vanishes at $V_D \equiv V_T$. At the bias voltage $V_D \equiv V_{H2}$, there is another subcritical Hopf bifurcation, with an almost negligible hysteresis range.

Note the continuity of the Hopf bifurcation, with the oscillation power gradually increasing from zero ($P_{\text{out}} = -\infty$ dBm) versus the bias voltage. In spite of this continuity, the growth from zero of the oscillation power versus the parameter is seldom observed in practice. In the case of subcritical bifurcations, this is, of course, because of the involved hysteresis phenomenon. In the case of supercritical bifurcations, the slope of the solution curve (versus the bifurcation) is usually very high near the Hopf bifurcation, which makes the experimental observation of the bifurcation continuity difficult.

4.4.2 Bifurcations from the Periodic Regime

The bifurcation calculation through harmonic balance from a periodic regime will now be considered. The fundamental frequency of this regime will be ω_o . Then, the solution is given by a vector \bar{X}_o , containing the harmonic terms $k\omega_o$ (with k integer) of the state variables of harmonic balance [i.e., having $m(2NH + 1)$ components]. This vector varies with the circuit parameter $\bar{X}_o \equiv \bar{X}_o(\eta)$. When using harmonic balance, a solution path can be partially obtained by tracing, for instance, the amplitude of a harmonic component of any of the independent variables versus the parameter η . In other cases, the output power at the fundamental frequency or the average value of all the harmonic components is represented versus the parameter.

As is already known, to analyze the stability of the steady-state solution, a small amplitude perturbation of complex frequency $e^{(\sigma + j\omega)t}$ is introduced in the system [27, 29]. For a periodic solution \bar{X}_o , this perturbation gives rise to sidebands at the frequencies $\sigma + j(k\omega_o + \omega)$ with $-NH \leq k \leq NH$. The smallness of the perturbation enables the linearization of the harmonic-balance equation, obtaining the following characteristic system:

$$[JH(\sigma + j(k\omega_o + \omega)\bar{X}_o, \eta)]\Delta\bar{X} = 0 \quad (4.63)$$

where the sidebands $k\omega_o + \omega - j\sigma$ are explicitly written to make a difference with (4.58). The characteristic matrix $[JH]$ is written as follows:

$$[JH] = \left\{ \begin{array}{l} [Ax(\sigma + j(k\omega_o + \omega))] - \\ [Ay(\sigma + j(k\omega_o + \omega))] \left[\frac{\partial \bar{Y}}{\partial \bar{X}_o} \right] \end{array} \right\} \quad (4.64)$$

Note that the linear matrixes $[A_x]$ and $[A_g]$ contain boxes [see (2.16)] that are evaluated at the perturbed frequencies $\sigma + j(k\omega_o + \omega)$. For stability, all the poles of the linearized system must be located on the left-hand side of the complex plane. These poles are given by the roots of the characteristic equation, obtained by equating to zero the determinant of the matrix (4.64):

$$\det[JH(\sigma + j(k\omega_o + \omega), \bar{X}_o, \eta)] = 0 \quad (4.65)$$

A bifurcation will take place in the system if, for a given parameter value η_o , the following condition is satisfied [27, 29]:

$$\det[JH(j(k\omega_o + \omega), \bar{X}_o, \eta_o)] = 0 \quad (4.66a)$$

$$\left. \frac{d\sigma}{d\eta} \right|_{\eta=\eta_o} \neq 0 \quad (4.66b)$$

This means that for the parameter value $\eta = \eta_o$, a real pole σ (or a pair of complex-conjugate poles $\sigma \pm j\omega$) of (4.64) crosses the imaginary axis of the complex plane, through the origin (or through $\pm j\omega$). To determine the bifurcation points, the following system must be solved:

$$\bar{H}(\bar{X}_o, \eta_o) = 0 \quad (4.67a)$$

$$\det[JH(j(k\omega_o + \omega), \bar{X}_o, \eta_o)] = 0 \quad (4.67b)$$

The three different types of local bifurcations from periodic regime are obtained for different values of the frequency ω . These are analyzed in the following sections.

4.4.2.1 Turning Point of the Solution Curve: $\omega = 0$

For $\omega = 0$, the determinant in (4.67) agrees with the determinant associated with the harmonic-balance equation $\bar{H}(\bar{X}) = 0$. It corresponds to $\det[JH] = 0$. This implies the existence for the particular parameter value η_o of a turning point in the solution path $\bar{X}_o(\eta)$. The relationship between the zero determinant value and the infinite slope of the solution curve has already been explained in Sections 2.5 and 2.6.3 and will not be repeated here. On the other hand, the fact that (4.67) is satisfied for $\omega = 0$ implies a change of stability without

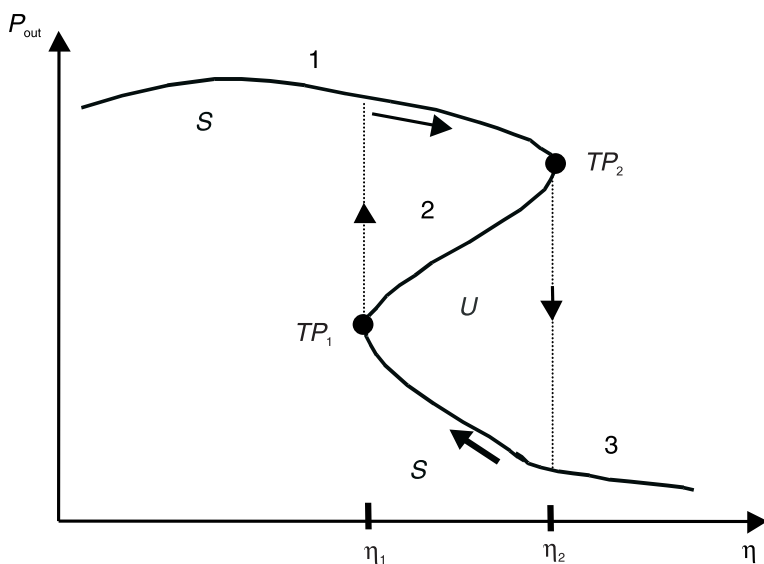


Figure 4.18 Turning points of the solution path: hysteresis phenomenon.

qualitative variation of the fundamental frequency or frequency basis, which agrees with the results of Sections 4.2 and 4.3.

Turning points are thus associated with hysteresis phenomena. The hysteresis may take place between two different periodic regimes or between regimes of different type. An example of the latter has been found in Figure 2.13 with transitions between a dc regime and a periodic regime.

An example of a periodic path with two turning-point bifurcations is sketched in Figure 4.18. The circuit output power has been traced versus a parameter η , obtaining the path of Figure 4.18. As can be seen, there are three different sections, named 1, 2, and 3. Sections 1 and 3 are stable, while section 2 is unstable. For $\eta < \eta_1$, the only possible solution is stable and belongs to section 1. Now, if η is increased along the interval (η_1, η_2) , there are three coexisting solutions, respectively belonging to the sections 1, 2 and 3. However, the physically observed solution will be the one in section 1. This is due to the fact that the circuit was initially operating in section 1 (for $\eta < \eta_1$), which conditions the circuit evolution to the attractor in this section (because the initial values are close to the solutions in section 1).

At $\eta = \eta_2$, the turning point TP_2 is reached. This point is the final point of section 1 because this section does not exist beyond η_2 . Thus, the solution

necessarily jumps to section 3. For $\eta > \eta_1$, there is only one solution, and this solution belongs to section 3. Now, if the parameter is decreased from section 3, it will pass through η_2 without a jump to section 1 because in section 3, no bifurcation takes place for this parameter value. The parameter has to be decreased to η_1 to obtain the upward jump, leading the solution back to section 1. Actually, because of the turning point TP_1 , section 3 does not exist for $\eta < \eta_1$. On the other hand, section 2, in agreement with (4.54), is unstable and is never physically observed.

The two sections merging at a turning point have stability situations differing in one unstable real pole. This means that a stable path reaching a turning point necessarily becomes unstable after this turning point. However, if the path is initially unstable, it might either become stable or continue to be unstable (with one additional unstable pole).

4.4.2.2 Flip Bifurcation: $\omega = \frac{\omega_o}{2}$

If (4.67) is fulfilled for $\omega = \frac{\omega_o}{2}$, a flip bifurcation is obtained in the system. The bifurcation equation is given by

$$\bar{H}(\bar{X}_o, \eta_o) = 0 \quad (4.68a)$$

$$\det \left[JH \left(j \left(k\omega_o + \frac{\omega_o}{2} \right), \bar{X}_o, \eta_o \right) \right] = 0 \quad (4.68b)$$

The flip bifurcation, as is already known, gives rise to the division by two of the fundamental frequency ω_o . Due to the rational relationship between ω_o and the perturbation frequency $\frac{\omega_o}{2}$, the determinant in (4.68) takes a real value. Thus, it is possible to solve (4.68) for the flip-bifurcation points, in terms of η and \bar{X}_o . It is a well-balanced system of $m(2NH + 1) + 1$ equations in $m(2NH + 1) + 1$ unknowns that can be solved for η and \bar{X}_o .

When tracing the solution path (versus the parameter η) in terms, for instance, of the output power at each harmonic component of the solution, the onset of the new frequencies $k\omega_o + \frac{\omega_o}{2}$ modifies the power of the formerly existing frequency components at $k\omega_o$. This gives rise to the birth of solution branches in the existing solution paths at $k\omega_o$. At the same time, new paths arise

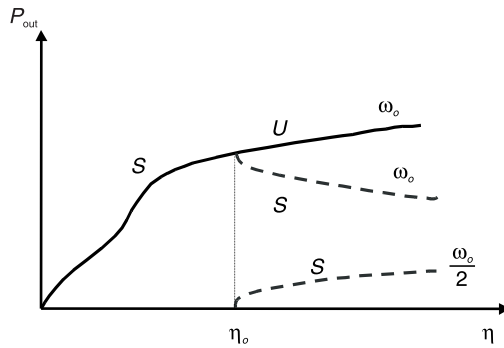


Figure 4.19 Flip bifurcation of supercritical type.

at the new frequency components $k\omega_o + \frac{\omega_o}{2}$. This is sketched in Figure 4.19, where a representation of the output power at the frequency components at ω_o and $\frac{\omega_o}{2}$ has been carried out versus the parameter η . Note that due to the continuity of local bifurcations, the harmonic paths at $k\omega_o + \frac{\omega_o}{2}$ start from a zero amplitude value. For obvious reasons, the flip bifurcation is classified as bifurcation of branching type.

4.4.2.3 Hopf Bifurcation: $\omega = \alpha\omega_o, \alpha \neq \frac{m}{n}$

When the bifurcation condition (4.66) is fulfilled for a frequency ω nonharmonically related with ω_o , a Hopf bifurcation occurs in the circuit. In the direct sense, the Hopf bifurcation gives rise to the onset of a new fundamental frequency ω , whose value can be determined from the bifurcation system:

$$\bar{H}(\bar{X}_o, \eta_o) = 0 \tag{4.69a}$$

$$\det[JH(j(k\omega_o + \omega), \bar{X}_o, \eta_o)] = 0 \tag{4.69b}$$

Due to the nonharmonic relationship between ω and ω_o , the determinant (4.69b) will be complex. Thus, (4.69) is composed of $m(2NH + 1) + 2$ equations in $m(2NH + 1)$ unknown. This enables the determination of the

bifurcation points, which, in addition to η and \bar{X}_o , involves, in this case, the determination of ω .

The Hopf bifurcation is a bifurcation of branching type, as will be seen in the following example, presenting a very complete bifurcation analysis in the frequency domain. The circuit is an analog frequency divider. Analog dividers basically operate like an oscillator with one of its harmonics phase locked to the input signal. The index of the synchronized harmonic provides the division order. These circuits usually exhibit very complex dynamics. Actually, they only operate as frequency dividers for limited ranges of the input-generator power and frequency. Outside these ranges, they can behave like a self-oscillating mixer, with the input-generator frequency f_{in} and the self-oscillation frequency f_i as fundamentals, or like a bad amplifier, providing an output signal at the input-generator frequency f_{in} , with no frequency division. Example 4.8 presents a detailed analysis of bifurcations verse input power in a frequency divider by two.

Example 4.8: Bifurcations in an analog frequency divider by two

The schematic of Figure 4.20 corresponds to a MMIC frequency divider by two [29, 30] with input frequency $f_{in} = 6$ GHz. In the absence of input-generator signal, this circuit behaves like a free-running oscillator at the frequency $f_o = 3$ GHz. Because it is a frequency divider by two, the second harmonic of this oscillation is expected to synchronize to the input signal about $2f_o$. The main parts of the circuit can easily be distinguished in Figure 4.20. These parts are the input filter centered about $2f_o$, the output filter centered about f_o , and the

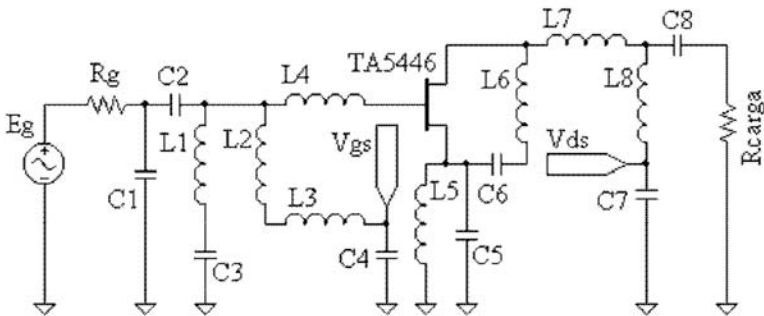


Figure 4.20 MMIC frequency divider by two with 6-GHz input frequency.

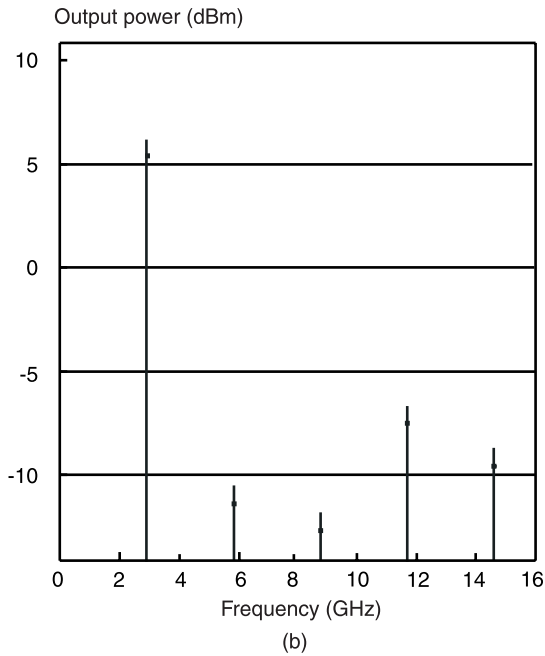
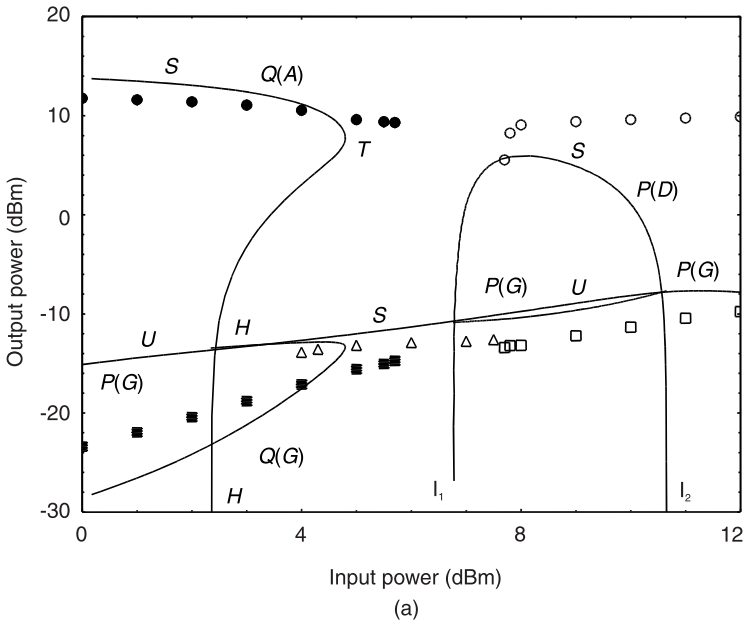


Figure 4.21 Simulations of the MMIC frequency divider by two: (a) bifurcation diagram versus the input power; (b) output power spectrum for $P_{in} = 9.5$ dBm, $f_{in} = 5.9$ GHz.

series feedback network (at f_o) at the transistor source. In addition, a series L-C circuit between drain and source provides isolation at $2f_o$.

The frequency divider of Figure 4.20 has been analyzed for constant input-generator frequency $f_{in} = 5.3$ GHz versus variations in the input-generator power P_{in} . Thus, the input power is the analysis parameter. When increasing the input power from $P_{in} = 0$ dBm to $P_{in} = 12$ dBm, the bifurcation diagram of Figure 4.21(a) is obtained. For low input power, the self-oscillation exists, but is not synchronized. Thus, there are two fundamental frequencies in the circuit (the input-generator frequency f_{in} and the self-oscillation frequency f_a) and the circuit operates in the quasiperiodic regime. The distinction between f_a and f_o when referring to the autonomous fundamental comes from the fact that, as has already been indicated in Chapter 1, the value of the self-oscillation frequency varies under the influence of an external generator. Note that the (relatively) low input-power value at a frequency that is not in the immediate neighborhood of $2f_o$ is not enough to lead the system to synchronization and does not extinguish the existing oscillation.

In Figure 4.21(a), two different paths are associated with this quasiperiodic solution [30]. One of them provides the output power at the autonomous fundamental f_a and is marked $Q(A)$ (Q meaning quasiperiodic). The second path provides the output power at the input-generator frequency f_{in} and is marked $Q(G)$. Note that the quasiperiodic paths exhibit a turning point T , corresponding, in fact, to the same bifurcation because the harmonic values at the two fundamental frequencies (f_a and f_{in}) are part of the same solution. This is a turning-point bifurcation in the quasiperiodic regime, which has not been treated yet. However, its meaning (infinite slope of the solution curve) and implications over the circuit behavior (jumps and hysteresis) are similar to those in the dc and the periodic regimes.

For the input power value $P_{in} = 4.5$ dBm, the quasiperiodic path corresponding to the autonomous fundamental vanishes with the output power tending to $-\infty$ dBm. This situation corresponds to the extinction of the self-oscillation because of an inverse Hopf bifurcation (marked H in the figure). Note that it is an inverse Hopf bifurcation of subcritical type, associated with the turning point T of the quasiperiodic solution. Between the two bifurcations T and H there is an hysteresis range. Starting from a quasiperiodic solution and increasing the input power, the behavior changes to periodic at the turning point T of the quasiperiodic branches. However, if the input power is now decreased from the periodic regime, the circuit will continue to operate in this periodic regime until reaching the Hopf bifurcation point H .

From T , in the increasing sense of the input power, the self-oscillation does not exist, and the circuit behaves as a bad amplifier at the input-

generator frequency f_{in} . However, for the input power $P_{in} = 4.65$ dBm, the circuit suffers a direct flip bifurcation (marked I_1 in the figure) of the supercritical type, leading to a period-2 regime or a regime with a frequency division by two. Now the solution is periodic with a subharmonic at the input-generator frequency divided by two $\frac{f_{in}}{2}$. In the bifurcation diagram, this gives rise to the onset of a new solution path, providing the output power at $\frac{f_{in}}{2}$. This path starts from zero value or $P_{out} = -\infty$ dBm. Due to the generation of this subharmonic, the output power at the input frequency f_{in} reduces its value, giving rise to the birth of a branch in the existing solution path at this frequency. Before the bifurcation, this periodic path (corresponding to a solution of fundamental frequency f_{in}) was stable. In agreement with (4.49), it becomes unstable at the flip bifurcation. The newly generated frequency-divided solution is stable. Figure 4.21(b) shows an output-power spectrum in the frequency-division band, obtained for the input power $P_{in} = 9.5$ dBm. As the input power continues to be increased, an inverse flip bifurcation of the supercritical type is encountered for the input power $P_{in} = 11$ dBm. This inverse bifurcation leads to the end of the frequency-division regime. From this value, the circuit operates again at the input-generator frequency f_{in} with no division and no self-oscillation.

As gathered from the bifurcation diagram of Figure 4.21(a), although the frequency-divider circuits are, of course, intended to operate as frequency dividers, this kind of behavior is only obtained for limited ranges of the input-generator power and frequency. Finally, note that both stable and unstable solution paths have been represented in Figure 4.21(a). These complete diagrams often enable a better understanding of bifurcations, compared to bifurcation diagrams obtained through the Poincaré map. The diagram of Figure 4.21(a) includes periodic and quasiperiodic solution paths and bifurcations in both kinds of regime. The bifurcations in the quasiperiodic regime will be analyzed in detail in the next section.

4.5 Harmonic-Balance Analysis of Bifurcations with the Aid of an Auxiliary Generator

In this section, alternative tools for bifurcation analysis through harmonic balance, different from those in Section 4.4, are presented. They are very well suited for incorporation into existing harmonic-balance software because they

do not require the resolution of the bifurcation system (4.67). This can be advantageous for bifurcation detection from the dc or periodic regime. On the other hand, the techniques in this section are also easily extended to the analysis of bifurcations quasiperiodic regimes. In contrast to bifurcations from the dc or periodic regimes, there is no closed-form classification of bifurcations from the quasiperiodic regime. In the time domain, the stability of the quasiperiodic regime is determined by the Lyapunov exponents [13].

The use of auxiliary generators for the steady-state analysis of autonomous and synchronized regimes through harmonic balance has already been presented in Chapter 2. When an auxiliary generator at the autonomous or synchronized frequency is introduced into the circuit, the analysis may be performed as in a forced regime, taking advantage of the efficiency of harmonic balance in forced operation. For the resulting solution to be valid, the auxiliary generator must satisfy a nonperturbation condition of the steady state, this condition being given by

$$H_p = \frac{I_p}{V_p} = 0 \quad \text{for a voltage auxiliary generator} \quad (4.70)$$

$$H_p = \frac{V_p}{I_p} = 0 \quad \text{for a current auxiliary generator}$$

where V_p and I_p are, respectively, the auxiliary generator voltage and current. Splitting H_p into real and imaginary parts, it is possible to have a vector expression $\bar{H}_p \equiv (\bar{H}_{pr}, \bar{H}_{pi})$. The total harmonic-balance system is

$$\bar{H}_b(\bar{X}, p_1, p_2) = 0 \quad (4.71a)$$

$$\bar{H}_p(\bar{X}, p_1, p_2) = 0 \quad (4.71b)$$

where \bar{H}_b represents the harmonic-balance system and p_1 and p_2 are the two variables characterizing the auxiliary generator. These variables are the generator amplitude and frequency in the case of autonomous regimes, and the generator amplitude and phase in the case of synchronized regimes (see Section 2.6). Equation (4.71) can be solved considering a partial dependence of both \bar{H}_b and \bar{H}_p on \bar{X} and the auxiliary-generator variables. However, the vector \bar{X} corresponding to every \bar{p} value with $\bar{p} = (p_1, p_2)$ can be obtained through

(4.71a). Then, an absolute dependence of \overline{H}_p on the auxiliary-generator vector \overline{p} may be considered:

$$\overline{H}_p(\overline{X}(p_1, p_2), p_1, p_2) \equiv \overline{H}_p(p_1, p_2) = 0 \quad (4.72)$$

The solving strategy is thus based on a two-tiered process where the pure harmonic-balance equation constitutes the inner loop. In this way, a system of only two unknowns in two equations is obtained. Although more demanding in terms of computer time, this method has the advantage of being easily applicable to existing software because it can be implemented separately from the harmonic-balance resolution.

As was shown in Chapter 2, the absolute dependence (4.72) enables the tracing of multivalued curves through a continuation technique based on a parameter switch between the actual analysis parameter η and the two variables characterizing the auxiliary generator p_1 and p_2 . In this section, we will go beyond the tracing of multivalued solution paths to actually detecting bifurcations through the employment of this generator.

The method is based on the properties of the auxiliary-generator amplitude or associated determinant at the bifurcation points [31]. Two main different types of bifurcations will be considered: the *turning-point* bifurcations (in the dc, periodic, or quasiperiodic regime) and the *branching* bifurcations, like the Hopf- and flip-type bifurcations, which give rise to the onset or extinction of solution branches. In the latter case, the approach is based on the detection of these incipient solutions. Thus, the detection is carried out in the regime in which the circuit operates after the bifurcation. As an example, to detect a Hopf bifurcation from the dc regime, the analysis is carried out in the periodic regime. We will look for parameter values for which oscillations of very small amplitude are observed. Because branching bifurcations are continuous, the incipient oscillation will be sufficiently close to the bifurcation point.

Three different regimes will be considered: autonomous periodic, periodic with external excitation, and autonomous quasiperiodic. Remember that in the case of branching bifurcations, the regime of the analysis is the regime in which the circuit operates after the bifurcation.

4.5.1 Autonomous Periodic

4.5.1.1 Primary Hopf Bifurcation: Start of a Free-Running Oscillation

When introducing an auxiliary generator into the circuit, the primary Hopf bifurcation points are given by the solutions of the absolute system (4.72) for a zero value of the auxiliary-generator amplitude, as this is the limit condition for the existence of an autonomous solution. Actually, in an autonomous solution path, a value of the auxiliary-generator amplitude may be assigned to each steady oscillation, while as soon as this autonomous solution is extinguished, the nonperturbation condition (4.70) cannot be satisfied for any amplitude or frequency of the auxiliary generator. Due to the continuity of (4.72), the amplitude will tend to a zero value as the inverse Hopf bifurcation point is approached.

The practical resolution for primary Hopf bifurcation points may be carried out by imposing very small amplitude to the auxiliary generator A_p . Values can be in the order of $A_p = 10^{-5}$ for a voltage generator. The equation system to be solved will be

$$\begin{aligned} H_{pr}(\omega_p, \bar{\eta}) &= 0 \\ H_{pi}(\omega_p, \bar{\eta}) &= 0 \\ A_p &= \varepsilon \end{aligned} \quad (4.73)$$

where the frequency ω_p of the auxiliary generator is, of course, equal to the unknown autonomous frequency ω_a . The vector $\bar{\eta}$ may be composed of one or two parameters. In the case of two elements (η_1, η_2) , a bifurcation locus will be obtained on the plane (η_1, η_2) . Possible parameters are bias voltages or tuning elements. The application of a Nyquist stability analysis (see Chapter 2) provides a good initial estimate of ω_a for a given parameter value, and (4.73) is easily solved through the Newton-Raphson method. Bifurcation loci can be multivalued, so the tracing of the Hopf-bifurcation locus must be complemented with a continuation technique.

4.5.1.2 Turning Points

As is already known, when tracing an oscillator solution path as a function of a tuning parameter, turning points, giving rise to jump or hysteresis phenomena, are often encountered. According to (2.54), these points will satisfy

$$\det[JH_p] = \frac{\partial H_{pr}}{\partial A_p} \frac{\partial H_{pi}}{\partial \omega_a} - \frac{\partial H_{pi}}{\partial A_p} \frac{\partial H_{pr}}{\partial \omega_a} = 0 \quad (4.74)$$

Due to the absolute dependence of the vector \bar{H}_p on the auxiliary-generator variables, the above determinant agrees with the Kurokawa stability function [11] for free-running oscillators. Here the multiharmonic nature of the circuit solution is taken into account for the calculation of the derivatives (through harmonic balance). The turning points can be thus calculated by applying

$$\begin{aligned} H_{pr}(A_p, \omega_p, \bar{\eta}) &= 0 \\ H_{pi}(A_p, \omega_p, \bar{\eta}) &= 0 \\ \det[JH_p(A_p, \omega_p, \bar{\eta})] &= 0 \end{aligned} \quad (4.75)$$

where $\omega_p = \omega_a$. Either a single bifurcation point or a locus may be obtained, according to the dimension of $\bar{\eta}$.

4.5.2 Periodic Regime with External Excitation

From a periodic regime of fundamental ω_{in} , provided by the external generator, different sorts of bifurcations are possible.

4.5.2.1 Flip-Type Bifurcation: Frequency Division by Two

At a flip-type bifurcation of a periodic regime at the frequency ω_{in} , a frequency-divided solution at $\frac{\omega_{in}}{2}$ appears or disappears. By means of an auxiliary generator, such solutions are obtained by fixing the auxiliary generator frequency ω_p to $\frac{\omega_{in}}{2}$ and setting its amplitude to a very small value. Then, the auxiliary-generator system is solved for the bifurcation parameter value (values). Note that due to the continuity of the function \bar{H}_p at the flip-type bifurcation, the equation $\bar{H}_p = 0$ would be fulfilled for a zero value of the auxiliary generator amplitude. The practical resolution is carried out from the following system:

$$\begin{aligned}
 H_{pr}(\phi_p, \bar{\eta}) &= 0 \\
 H_{pi}(\phi_p, \bar{\eta}) &= 0 \\
 A_p &= \varepsilon \\
 \omega_p &= \frac{\omega_{in}}{2}
 \end{aligned} \tag{4.76}$$

For two elements in the vector $\bar{\eta}$, the *I*-type bifurcation locus is obtained.

4.5.2.2 Secondary Hopf Bifurcation: Onset or Extinction of an Autonomous Frequency

At a Hopf bifurcation in the periodic regime (secondary Hopf bifurcation), a quasiperiodic solution appears or disappears. This quasiperiodic solution has two nonrationally related fundamentals, which are given by the input-generator frequency ω_{in} and the autonomous frequency ω_a . By means of an auxiliary generator, the Hopf bifurcation points may be obtained by setting the auxiliary-generator amplitude to a very small value ε and solving for the parameter value and the autonomous frequency ω_a :

$$\begin{aligned}
 H_{pr}(\omega_p, \bar{\eta}) &= 0 \\
 H_{pi}(\omega_p, \bar{\eta}) &= 0 \\
 A_p &= \varepsilon
 \end{aligned} \tag{4.77}$$

where the auxiliary generator frequency ω_p is equal to ω_a . Due to the negligible amplitude of the autonomous fundamental, the number of spectral components for the resolution of (4.77), in a quasiperiodic regime, may be greatly reduced.

4.5.2.3 Turning Points

At turning points, the path stability changes without any variation in the system fundamentals. Using the auxiliary-generator method, the phase and amplitude of this generator will be the variables to be solved in the periodic regime. Turning points may be calculated by applying:

$$\begin{aligned}
 H_{pr} (A_p, \phi_p, \bar{\eta}) &= 0 \\
 H_{pi} (A_p, \phi_p, \bar{\eta}) &= 0 \\
 \det [H_p (A_p, \phi_p, \bar{\eta})] &= 0
 \end{aligned}
 \tag{4.78}$$

Either a single bifurcation point or locus may be obtained, according to the dimension of η . Turning points are associated with jump and hysteresis phenomena. However, as shown in Section 4.3.2, they may also determine the end of phase-locked behavior. When tracing the loci of an injected oscillator in the plane defined by the *input power* and the *input frequency*, the free-running oscillation point will always belong to one of the possible turning point loci, as it is a degenerated point obtained for zero input power. The synchronization phenomenon will be treated in greater detail in the next paragraph

4.5.3 Autonomous Quasiperiodic Regime

An initial autonomous quasiperiodic regime will now be considered. The two fundamentals will be ω_{in} and a self-oscillation frequency ω_a . Possible bifurcations from this regime will be the turning points and the appearance or disappearance of a second autonomous fundamental. In addition to that, the vanishing of autonomous quasiperiodic paths may be due to two different phenomena: synchronization of the two fundamental frequencies and extinction of the autonomous frequency ω_a by an inverse Hopf bifurcation. Each of these phenomena will be treated in the following sections

4.5.3.1 Synchronization

Starting from an autonomous quasiperiodic regime, as the parameter is modified, the autonomous frequency varies too. Synchronization takes place when the two fundamentals ω_{in} and ω_a become commensurable for a certain parameter range. The analysis of the rotation number r is particularly useful to detect the approaching of a synchronization parameter value. This number is given by

$$r(\bar{\eta}) = \frac{\omega_a(\bar{\eta})}{\omega_{in}}
 \tag{4.79}$$

At the synchronization points, r becomes rational, remaining constant for a certain parameter set.

The transformation suffered by the quasiperiodic paths at the synchronization points depends on the value that the return ratio r reaches at these points:

1. $r = 1$. The autonomous component vanishes and the external one becomes the fundamental of the new periodic regime. This is the case of an injected oscillator. At the synchronization points, the amplitude A_p of the auxiliary generator tends to a zero value. A slight discontinuity is usually observed due to the discontinuous nature of the global/local bifurcation.
2. $r = \frac{m}{n} \neq 1$ (with m and n integers). The value of the auxiliary generator (in terms of amplitude and frequency) approaches that of the frequency component $m \frac{\omega_{in}}{n}$ of the new periodic regime. For $r = \frac{1}{n}$, the autonomous component from the quasiperiodic regime becomes the system fundamental.

The rational ratio between the fundamental frequencies at the synchronization points leads to a degeneration of the quasiperiodic harmonic-balance system, making it very difficult to detect these points from a quasiperiodic point of view. In periodic regime, the synchronization of fundamentals is given by a turning point of the solution path. The synchronization points is thus obtained from the same condition (4.78).

4.5.3.2 Tertiary Hopf Bifurcation: Onset or Extinction of a Second Autonomous Fundamental

The appearance of a second autonomous fundamental may be detected through harmonic balance by introducing a second auxiliary generator into the circuit. The system to be solved will then be

$$\begin{aligned} \bar{H}_{\rho 1}(A_p^1, \omega_p^1, \omega_p^2, \bar{\mu}) &= 0 \\ \bar{H}_{\rho 2}(A_p^1, \omega_p^1, \omega_p^2, \bar{\mu}) &= 0 \\ A_p^2 &= \varepsilon \end{aligned} \quad (4.80)$$

where A_p^2 and ω_p^2 , respectively, are the amplitude and frequency of the second auxiliary generator.

Compared with the traditional approach for the bifurcation-point determination (based on the root calculation of the characteristic determinant), the

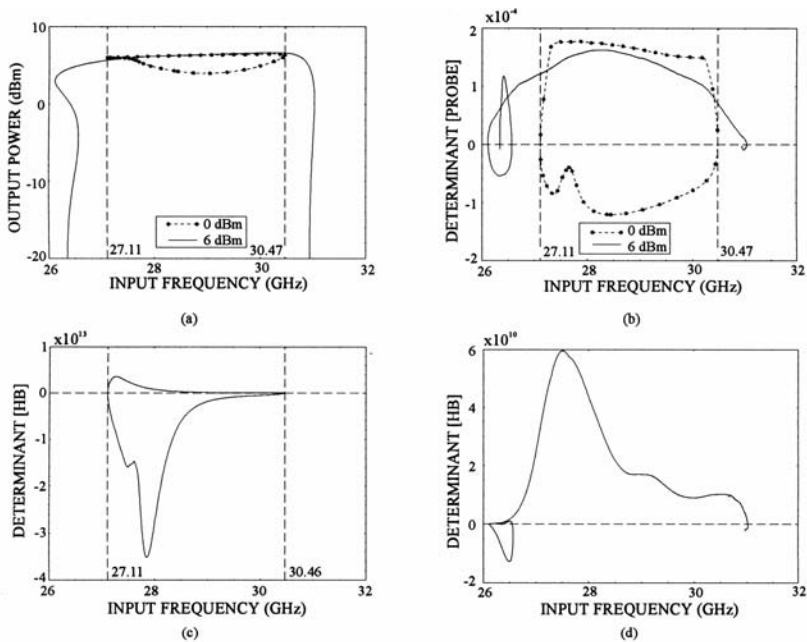


Figure 4.22 Harmonic-balance detection of turning points: (a) two solution curves exhibiting turning points versus the input frequency (circuit parameter); (b) variations of the determinant of the absolute system $\bar{H}_p = 0$ for the two curves; (c) variations of the determinant of the characteristic determinant of harmonic balance for $P_{in} = 0$ dBm; and (d) variations of the determinant of the characteristic determinant of harmonic balance for $P_{in} = 6$ dBm. (From: [31]. © 1998 IEEE. Reprinted with permission.)

new method, based on the use of the auxiliary generator consumes more computer time, but is less demanding from the programming point of view. In addition to that, the new method is more accurate when applied to obtain the bifurcation loci. This is due to the big variations of several orders of magnitude that can be obtained in the determinant of the harmonic-balance system \bar{H}_b when two parameters vary. Thus, in a numerical resolution of the traditional harmonic-balance system, it might be difficult to choose a proper threshold value for the zeroes of the characteristic determinant in the numerical resolution.

To clarify this point, the simulation of two periodic paths showing turning points has been carried out in Figure 4.22. At the turning points [Figure 4.22(a)], the characteristic determinant of the harmonic-balance equations, as well as the determinant of \bar{H}_p , should take a zero value. The variations of the harmonic-balance determinant along two paths, respectively corresponding to

input power $P_{in} = 0$ dBm and $P_{in} = 6$ dBm, are shown in Figure 4.22(c, d). As can be seen, the bifurcation prediction is accurate. However, the resolution of (4.67) with $\omega = 0$ for the two parameters, *input power* and *input frequency*, to obtain the turning point locus would be very difficult because of the big change in the determinant magnitude, as the input power is modified (from order 10^{13} to 10^{10} in this example). The same big variations have been found for other two-parameter analysis. As can be seen in Figure 4.22(b), the variation range of the determinant of \overline{H}_p is similar in both cases. The accuracy problems of the harmonic-balance determinant are even more serious in the quasiperiodic regime because of the high dimension of the characteristic matrix. In the auxiliary-generator method, the system to be analyzed is always a 2×2 system, whatever the number of frequency components taken into account, which greatly reduces the resolution difficulties. For the branching point bifurcations, the threshold value to be imposed always corresponds to a voltage or current variable, which makes the threshold assignment much simpler than for the determinant of a high-order matrix. A system of only two unknowns in two equations is obtained. Although more demanding in terms of computer time, this method has the advantage of being easily applicable to existing software

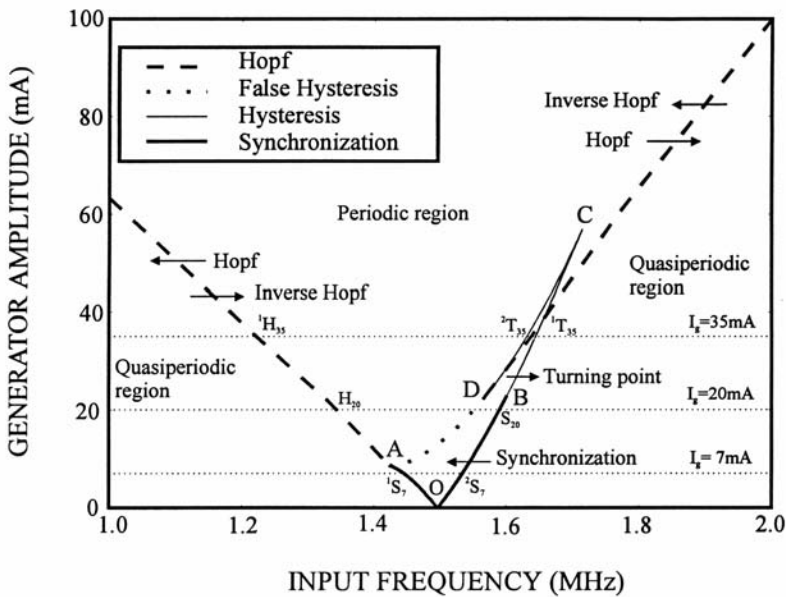
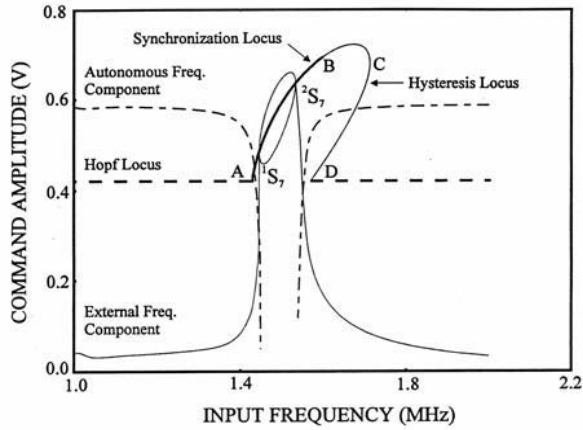
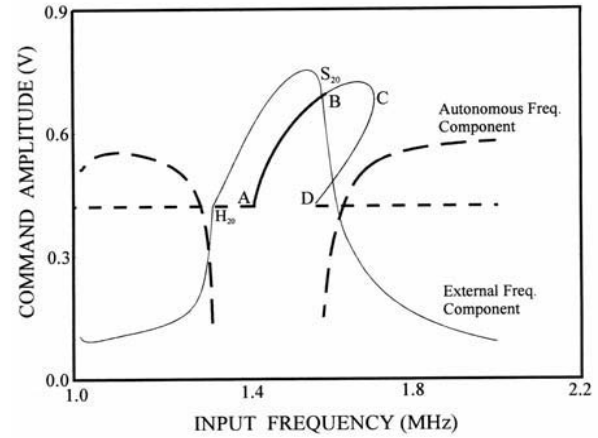


Figure 4.23 Bifurcation loci for the cubic nonlinearity oscillator. (From: [31]. © 1998 IEEE. Reprinted with permission.)



(a)



(b)

Figure 4.24 Bifurcation diagrams as a function of input frequency of the cubic nonlinearity oscillator: (a) for input-generator amplitude $I_g = 7$ mA, and (b) for $I_g = 35$ mA. (From: [31]. © 1998 IEEE. Reprinted with permission.)

because it can be implemented separately from the harmonic-balance resolution.

The two-level formulation of the bifurcation conditions (4.73) to (4.80) (with the harmonic-balance equation $\bar{H}_p = 0$ as the inner level) is directly applicable to in-house software with closed harmonic-balance routines (i.e., considering the harmonic-balance resolution $\bar{H}_b = 0$ as a black box). The extension to commercial harmonic balance is possible although more demanding. The Hopf-bifurcation conditions (4.73), (4.77), and (4.80) and the flip-bifurcation condition (4.76) can be directly applied to obtain the bifurcation points, using the software optimization tools, in similar way to Sections 2.6.1 and 2.6.2. At the time to trace a flip or Hopf bifurcation locus, the possible turning points of the locus itself must be circumvented through a parameter switching manually performed by the user. Examples of this will be shown in Chapter 5. With regard to turning-point bifurcations, the singularity condition of the admittance/impedance function Jacobian matrix (4.75) or (4.78) can be verified by the user, according to Section 2.6.3 and Figure 2.17.

Several studies of bifurcations of injected oscillators in the periodic regime can be found in [29–35]. The bifurcation analysis based on the absolute system $\bar{H}_p = 0$ efficiently applies to this kind of circuit. It enables obtaining bifurcations from the periodic and quasiperiodic regime. In Example 4.9, the

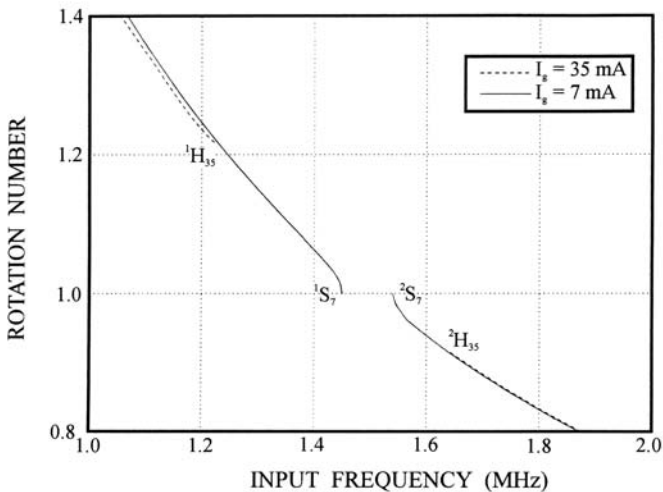


Figure 4.25 Rotation number versus input frequency for input generator amplitudes $I_g = 7$ mA and $I_g = 35$ mA. (From: [31]. © 1998 IEEE. Reprinted with permission.)

bifurcations of the cubic nonlinearity oscillator versus the input-generator amplitude and frequency are analyzed in detail.

Example 4.9: Harmonic-balance analysis of the bifurcations in the cubic nonlinearity oscillator

The analysis method proposed in this section has been applied to the same cubic nonlinearity oscillator of Examples 4.5 and 4.6. As is already known, this circuit may exhibit two main modes of operation: phase-locked oscillator and self-oscillating mixer. The generator values for each operation mode can be determined by tracing the bifurcation loci [33, 34] on the parameter plane, given by the input-generator amplitude and frequency (Figure 4.23). As has already been indicated, the free-running oscillation always belongs to one of the possible turning point loci in the periodic regime. In Figure 4.23, this point is given by O and the corresponding locus by $AOCD$. This turning point locus may contain both synchronization and jump points. Its two common points with the Hopf bifurcation locus at which the latter originates are solutions of (4.78) for a zero value of the auxiliary-generator amplitude and, in the present example, are given by A and D . These points will provide a good estimate for the border between synchronization and jump behavior. Actually for $I_g < I_A$ and $I_g < I_D$, the turning point curve must correspond to synchronization, as the Hopf locus is never traversed.

In Figure 4.24, two bifurcation diagrams as a function of input frequency for two different input-current amplitudes have been traced, including both periodic and quasiperiodic paths. Because in the quasiperiodic regime there are two fundamental frequencies, a solution path is traced for each of them. The synchronization, hysteresis, and Hopf loci have been superimposed. Periodic paths will be unstable inside the turning point locus and below the Hopf locus. For $I_g = 7$ mA [Figure 4.24(a)], the periodic path intersects at both ends (1S_7 and 2S_7) of the synchronization locus. Then, the start of the quasiperiodic regime will be due, on both sides, to a loss of synchronization. For $I_g = 35$ mA [Figure 4.24(b)], the appearance on the left side of the quasiperiodic response is due to a Hopf bifurcation (${}^1H_{35}$). The right part cuts the hysteresis locus twice (${}^1T_{35}$ and ${}^2T_{35}$), which will give rise to an hysteresis phenomenon. Then, the Hopf locus is traversed (${}^2H_{35}$) with appearance of the quasiperiodic paths.

The evolution of the rotation number r as a function of input frequency for $I_g = 7$ mA and $I_g = 35$ mA is shown in Figure 4.25. For $I_g = 7$ mA, the rotation number reaches the unity value at the starting points of periodic operation, which is characteristic of the synchronization phenomenon. For $I_g = 35$ mA, the transformation into the periodic regime is due, at each end, to an

inverse Hopf bifurcation. The value of the number r is nonrational at these points and far from unity.

References

- [1] Mees, A. I., "A Plain Man's Guide to Bifurcations," *IEEE Trans. Circuits Syst.*, Vol. 30, No. 8, Aug. 1983, pp. 512–517.
- [2] Thompson, J. M. T., and H. B. Stewart, *Nonlinear Dynamics and Chaos*, New York: John Wiley & Sons, 1986.
- [3] Ioos, G., and D. D. Joseph, *Elementary Stability and Bifurcation Theory*, 2nd ed., Berlin, Germany: Springer-Verlag, 1990.
- [4] Guckenheimer, J., and P. Holmes, *Nonlinear Oscillations, Dynamical Systems and Bifurcations of Vector Fields*, Berlin, Germany: Springer-Verlag, 1990.
- [5] Wiggins, S., *Introduction to Applied Nonlinear Dynamical Systems and Chaos*, Berlin, Germany: Springer-Verlag, 1990.
- [6] Arnold, V. I., et al., *Bifurcation Theory and Catastrophe Theory*, Berlin, Germany: Springer-Verlag, 1999.
- [7] Lichtenberg, A. J., and M. A. Lieberman, *Regular and Chaotic Dynamics*, New York: Springer-Verlag, 1991.
- [8] Colonius, F., and L. Grüne, *Dynamics, Bifurcations and Control*, Berlin, Germany: Springer-Verlag, 2002.
- [9] Mees, A. I., and L. O. Chua, "The Hopf Bifurcation Theorem and Its Applications to Nonlinear Oscillations in Circuits and Systems," *IEEE Trans. Circuits Syst.*, Vol. 26, No. 4, April 1979, pp. 235–254.
- [10] Odyniec, M., "On the Application of Hopf Bifurcation to Oscillator Analysis," *Integrated Nonlinear Microwave and Millimetric Wave Circuits, INMMC'90*, Duisburg, Germany, Oct. 1990, pp. 51–62.
- [11] Kurokawa, K., "Some Basic Characteristics of Broadband Negative Resistance Oscillator Circuits," *Bell Syst. Tech. J.*, 1969.
- [12] Plaat, O., *Ordinary Differential Equations*, San Francisco, CA: Holden-Day, Inc., 1974.
- [13] Parker, T. S., and L. O. Chua, *Practical Numerical Algorithms for Chaotic Systems*, New York: Springer-Verlag, 1989.
- [14] Starzhinski, V. M., *Applied Methods in the Theory of Nonlinear Oscillations*, Moscow, Russia: Mir Publishers, 1980.
- [15] Butenin, N., Y. Neimark, and N. Fúfaev, *Introduction to Nonlinear Oscillations*, Moscow, Russia: Mir Publishers, 1987.

-
- [16] Kawakami, H., "Bifurcation of Periodic Responses in Forced Dynamic Nonlinear Circuits: Computation of Bifurcation Values of the System Parameters," *IEEE Trans. Circuits Syst.*, Vol. 31, No. 3, March 1984, pp. 248–260.
- [17] Suárez, A., A. Mediavilla, and J. Luy, "Period Doubling Route to Chaos in SiGe IMPATT Diodes," *IEEE Microwave Guided Wave Lett.*, Vol. 8, No. 4, April 1998, pp. 170–172.
- [18] J., Gannett, and L. Chua, "A Nonlinear Circuit Model for IMPATT Diodes," *IEEE Trans. Circuits Syst.*, Vol. 25, No. 5, May 1978, pp. 299–307.
- [19] Suárez, A., and J. M. Collantes, "Harmonic Balance Analysis of Two Bifurcation Routes to Chaos," *IEEE Int. Microwave Symp., MTT-S*, Anaheim, CA, June 1999, pp. 767–770.
- [20] Venkatasubramanian, V., H. Schättler, and J. Zaborski, "Homoclinic Orbits and the Persistence of the Saddle Connection Bifurcation in the Large Power System," *IEEE Int. Symp. Circuits Syst., ISCAS'93*, May 1993, pp. 2648–2651.
- [21] Stensby, J., "Saddle Node Bifurcation in a PLL," *IEEE Proc. Southeastcon'93*, Charlotte, NC, April 5, 1993, p. 4.
- [22] Stensby, J., "False Lock to Phase Lock Bifurcation in a PLL," *IEEE 25th Southeastern Symp. Syst. Theory*, March 1993, pp. 146–150.
- [23] Lynch, J. J., and R. A. York, "Stability of Mode-Locked States of Coupled Oscillator Arrays," *IEEE Trans. Circuits Syst.*, Vol. 48, No. 8, Aug. 1995, pp. 413–418.
- [24] Kousaka, T., et al., "Bifurcation Analysis in Hybrid Nonlinear Systems," *IEEE Int. Symp. Circuits Syst., ISCAS 2001*, Sydney, Australia, May 6–9, 2001, pp. 281, 284.
- [25] Ushida, A., and L. O. Chua, "Frequency Domain Analysis of Nonlinear Circuits Driven by Multi-Tone Signals," *IEEE Trans. Circuits Syst.-I*, Vol. 31, No. 9, Sept. 1984, pp. 766–778.
- [26] Hente, D., and R. H. Jansen, "Frequency-Domain Continuation Method for the Analysis and Stability Investigation of Nonlinear Microwave Circuits," *IEE Proc.*, Vol. 133, Pt. H, No. 5, Oct. 1986, pp. 351–362.
- [27] Rizzoli, V., and A. Neri, "State of the Art and Present Trends in Nonlinear Microwave CAD Techniques," *IEEE Trans. Microwave Theory Tech.*, Vol. 36, No. 2, Feb. 1988, pp. 343–356.
- [28] Palazuelos, E., et al., "Hysteresis Prediction in Autonomous Microwave Circuits Using Commercial Software. Application to a Ku Band MMIC VCO," *IEEE J. Solid-State Circuits*, Vol. 33, No. 8, Aug. 1998, pp. 1239–1243.
- [29] Quéré, R., et al., "Large Signal Design of Broadband Monolithic Microwave Frequency Dividers and Phase-Locked Oscillators," *IEEE Trans. Microwave Theory Tech.*, Vol. 41, No. 11, Nov. 1993, pp. 1928–1938.
- [30] Morales, J., A. Suárez, and R. Quéré, "Accurate Determination of Frequency Dividers Operating Bands," *IEEE Microwave Guided Wave Lett.*, Vol. 6, No. 1, Jan. 1996, pp. 46–48.

- [31] Suárez, A., J. Morales, and R. Quéré, "Synchronization Analysis of Autonomous Microwave Circuits Using New Global Stability Analysis Tools," *IEEE Trans. Microwave Theory Tech.*, Vol. 46, No. 5, May 1998, pp. 494–504.
- [32] Gustafsson, L., G. G. H. Hansson, and K. I. Lundstrom, "On the Use of the Describing Functions in the Study of Nonlinear Active Microwave Circuits," *IEEE Trans. Microwave Theory Tech.*, Vol. 20, No. 6, June 1972, pp. 402–409.
- [33] Calandra, E., and A. M. Sommariva, "Stability Analysis of Injection Locked Oscillators in Their Fundamental Mode of Operation," *IEEE Trans. Microwave Theory Tech.*, Vol. 29, No. 11, Nov. 1981, pp. 1137–1144.
- [34] Hansson, G. H., and K. I. Lundstrom, "Stability Criteria for Phase-Locked Oscillators," *IEEE Trans. Microwave Theory Tech.*, Vol. 20, No. 10, Oct. 1972, pp. 641–645.
- [35] Gustafsson, L., K. I. Lundstrom, and G. H. B. Hansson, "Maximum Phase-Locking Bandwidth Obtainable by Injection Locking," *IEEE Trans. Microwave Theory Tech.*, Vol. 21, 1973, pp. 353–355.

5

Global Stability of Microwave Circuits

In the previous chapter, the most common types of bifurcations were presented and illustrated with examples. This chapter will be devoted to the exhaustive analysis of nonlinear microwave circuits, usually exhibiting bifurcations [1–3], such as oscillators, analog frequency dividers, self-oscillating mixers, and frequency multipliers. Examples of each kind of circuit will be shown, obtaining their stability portraits, versus the most common parameters, through bifurcation diagrams and bifurcation loci. Basic operation principles and design concepts are also provided. As an example of systems containing several individual circuits, bifurcations in phase-locked loops will be studied. The main objective of this chapter is to provide the reader with a better knowledge of the typical behavior of common nonlinear circuits and phase-locked loops in terms of their most usual parameters.

In the case of circuits, the bifurcation analysis will be based on the harmonic-balance technique. As has been shown in Chapter 4, the inclusion of an auxiliary generator into the circuit enables simple bifurcation conditions very well suited for numerical resolution through an error minimization algorithm of the Newton-Raphson type or through optimization. The latter possibility enables the employment of commercial harmonic balance for bifurcation detection. In the case of phase-locked loops, the analysis tool will be time-domain integration [4], employing the Poincaré map for obtaining bifurcation diagrams, as was shown in Chapter 4. Because this chapter is mainly practical, the circuit examples will be embedded within the general text.

5.1 Global Behavior of Free-Running Oscillators

In Chapter 4, examples of analysis of a free-running oscillator under variations of a single parameter were presented (see Example 4.7). The parameter was the bias voltage of a varactor diode [5]. However, it is possible to include in the analysis a second parameter. This additional parameter may be the value of a circuit element, such as the value of an inductor or a resistance, or a transistor bias voltage. To see this, an example, based on the monolithic circuit of Figure 4.22, will be presented in the following.

The circuit of Figure 4.20 had been designed as an analog frequency divider by two, but, as is already known (see Section 1.6 and Example 4.8), dividers based on harmonic synchronization operate as free-running oscillators in the absence of an input RF signal. For zero input voltage, the circuit behaves as a free-running oscillator for some bias points, given by the gate bias-voltage source V_{GO} and the drain bias-voltage source V_{DO} . When keeping V_{DO} constant and varying V_{GO} , the corresponding evolution of the free-running oscillator solution is obtained through application of the continuation techniques of presented in Chapter 2 (see Sections 2.5 and 2.6.3). The solution, in terms of oscillation frequency and output power at the first harmonic component, is shown in Figure 5.1. The drain voltage is $V_{DO} = 3v$. As can be seen, the V_{GO} range for self-oscillation is delimited by two primary Hopf bifurcations. As the bias voltage V_{GO} is increased, a direct bifurcation of supercritical type, leading to the onset of the self-oscillation, is obtained at $V_{GO} = -1.4v$. The self-oscillation is extinguished at an inverse Hopf bifurcation of supercritical type, obtained at $V_{GO} = 1.4v$. Because the two Hopf bifurcations are of supercritical type, the oscillation onset/extinction take place without hysteresis at both ends of the V_{GO} interval.

Considering two parameters at a time, it is possible to determine the set of bias-voltage values (V_{GO}, V_{DO}) for which the circuit exhibits a self-oscillation or limit cycle. For this calculation, the Hopf-bifurcation locus (of primary type) must be traced. The two bias voltages constitute the two components of the parameter vector $\bar{\eta} = (V_{GO}, V_{DO})$ in (4.73). This equation becomes

$$\begin{aligned} H_{pr}(\omega_p, V_{GO}, V_{DO}) &= 0 \\ H_{pi}(\omega_p, V_{GO}, V_{DO}) &= 0 \\ A_p &= \varepsilon \end{aligned} \quad (5.1)$$

where the frequency of the auxiliary generator ω_p is equal to the free-running oscillation frequency ω_o . Equation (5.1) establishes the zero value of the

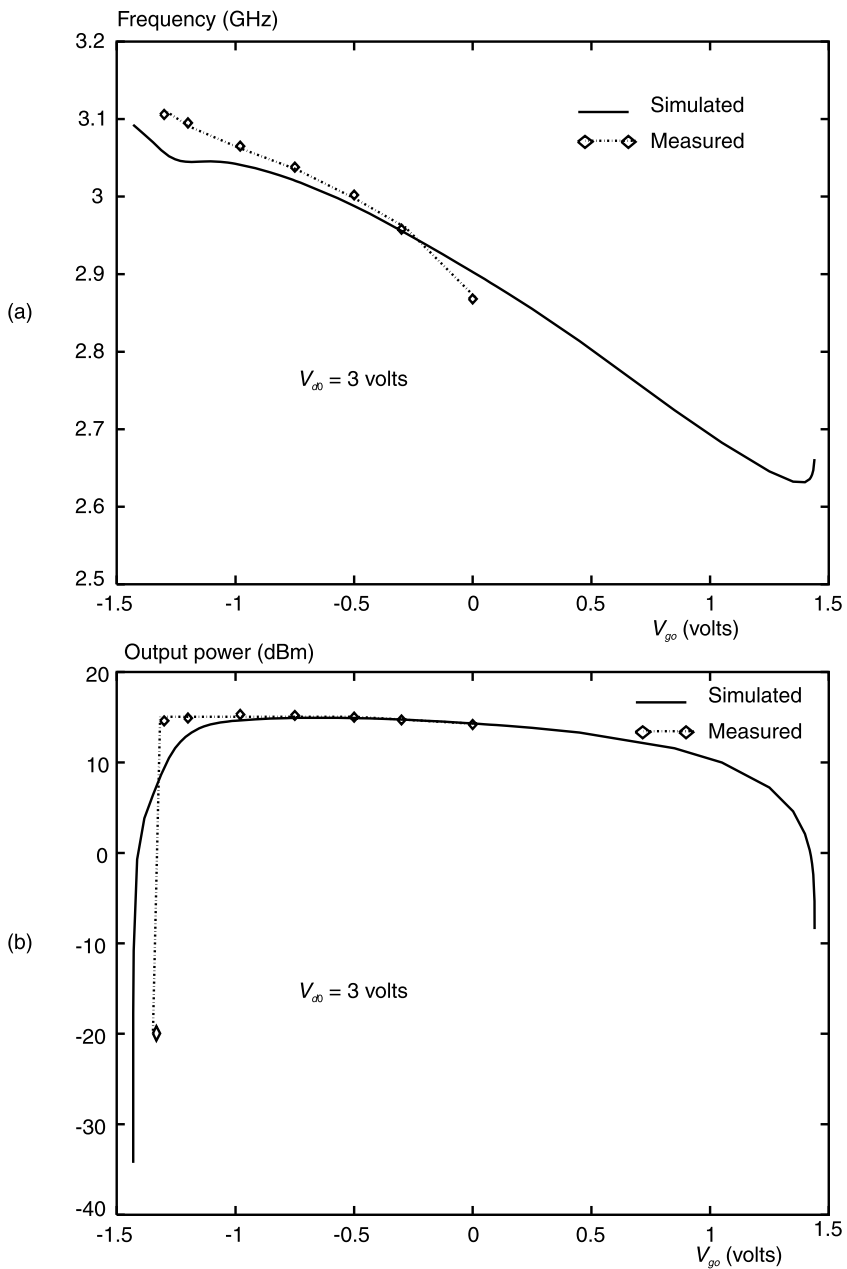


Figure 5.1 Evolution of the free-running oscillation of the monolithic circuit of Figure 4.22 versus the gate bias voltage V_{G0} for constant drain bias voltage $V_{DD} = 3$ v. (a) free-running frequency, and (b) output power at the first harmonic component. (From: [6]. © 1993 IEEE. Reprinted with permission.)

impedance/admittance function \bar{H}_p of the auxiliary generator (nonperturbation condition). The small value of the oscillation amplitude $A_p = \varepsilon$ is in correspondence with the incipient self-oscillation amplitude in the immediate neighborhood of the Hopf bifurcation point (after this bifurcation has actually taken place). Note that (5.1) is solved in combination with harmonic balance, which is employed in the calculation of \bar{H}_p . To trace the bifurcation locus in the (V_{GO}, V_{DO}) plane, the drain voltage V_{DO} is the initial parameter, which is varied in small steps, prefixed by the user. For each step, ω_p and V_{GO} are calculated. This enables obtaining the curve V_{GO} versus V_{DO} . However, owing to the likely existence of turning points in the locus, application of continuation techniques with parameter switching between (V_{GO}, V_{DO}) and ω_p will be necessary. When proceeding this way, the locus of Figure 5.2 is obtained. For points inside the locus, the circuit (in the absence of an input RF signal) behaves as a free-running oscillator. For bias points outside the locus, the dc solution is stable and no oscillation is observed.

When analyzing a free-running oscillator in terms of two parameters, like (V_{GO}, V_{DO}) in the above example, the main loci to be traced are the primary-Hopf bifurcation locus and the turning-point locus in the periodic regime. The later would provide the set of parameter values for which turning points are observed in the oscillation paths [see (4.75)]. Examples of turning points in the solution curves of a free-running oscillator have been seen in Figure 2.16 (for the oscillator circuit of Figure 2.13).

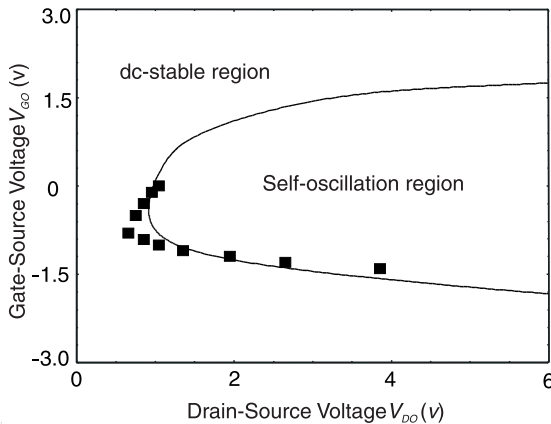


Figure 5.2 Locus of primary Hopf bifurcation of the monolithic circuit of Figure 4.22. The locus delimits the bias conditions in terms of the voltages V_{GO} and V_{DO} for free-running oscillation (inside the locus) from those corresponding to a dc stable regime (no oscillation). Experimental points have been superimposed.

5.2 Global Behavior of Synchronized Oscillators

In injected oscillators, an external RF generator is connected to a free-running oscillator circuit [7]. In synchronized operation (obtained only for some input-generator values), the self-oscillation frequency becomes rationally related to that of the input generator. There is also a constant phase relationship between the self-oscillation and the input-generator signal. Synchronized oscillators can be employed as high-gain amplifiers. However, synchronization is most useful when the input generator provides a frequency close to a harmonic or a subharmonic of the free-running oscillation. In the former case, a harmonic injection divider would be obtained [8]. The latter case (subharmonic synchronization) enables the phase-noise reduction of the higher-frequency oscillator circuit [9].

Here the global behavior of an injected oscillator at the first-harmonic component will be analyzed. Many characteristics of this global behavior are also encountered in the case of harmonic or subharmonic injection, so the analysis remains useful. The two most meaningful parameters for the analysis of synchronized circuits are the power P_{in} and the frequency ω_{in} of the external generator. The study will be illustrated by means of its application to the monolithic circuit of Figure 4.20 [6]. As already indicated, the frequency of the input generator will be close to that of the free-running oscillation. According to the power and frequency values of the input generator, either synchronized or quasiperiodic behavior can be obtained. In Figure 5.3, the synchronized solutions have been represented versus the input frequency in terms of the output power at the first harmonic component. Three different values of input power have been considered. As can be seen, for low input power, the solution curves are closed. In fact, coexisting with each closed curve (for each input-power value), there is a second solution curve with low output power that has not been represented here. As has already been seen in Example 4.9, this low-amplitude solution is an unstable solution and this is why it has not been included in Figure 5.3. Other examples of low input-power solutions in injected oscillators (given by a closed curve and low output-power curve) can be seen in Figure 2.5, corresponding to a van der Pol oscillator.

As the input power increases for a given input-power value, the closed curve and the unstable low-amplitude curve merge, which gives rise to a single solution curve. From this value, there is usually an (intermediate) input-power range for which the curves exhibit turning points. As the input power continues to increase, the turning points disappear. As has already been seen in Example 4.9, the periodic curves of the synchronized oscillator are not entirely stable. This can be verified through application of the Nyquist stability

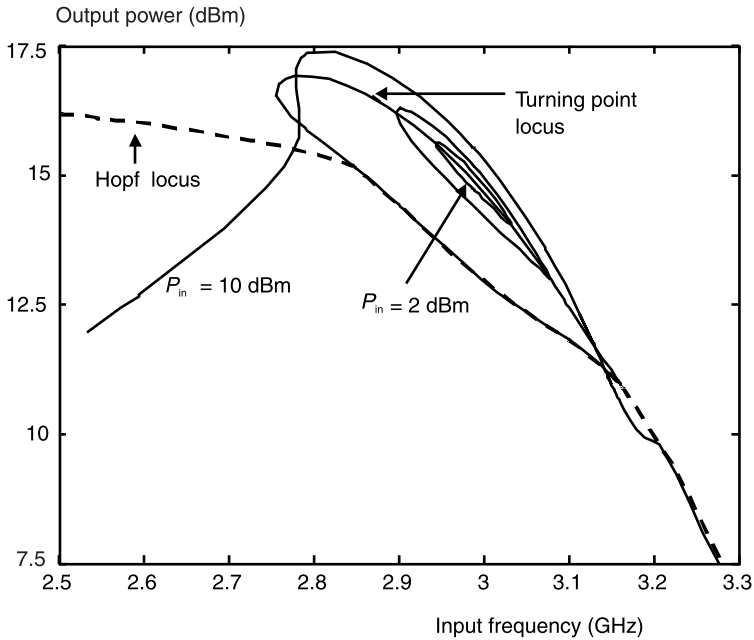


Figure 5.3 Behavior of the circuit of Figure 4.22 as a synchronized oscillator. Synchronization curves have been traced for three different input-power values: $P_{in} = 2$ dBm for the smallest closed curve, $P_{in} = 4$ dBm for the bigger closed curve, and $P_{in} = 10$ dBm for the open curve. The (unstable) low-amplitude curve associated with each closed curve has been omitted. The turning-point/synchronization locus and the secondary Hopf-bifurcation locus have also been represented. Inside the turning-point locus and below the Hopf locus, the synchronization curves are unstable and the corresponding curve sections are physically unobservable. (From: [6]. © 1993 IEEE. Reprinted with permission.)

criterion (see Chapter 3). The stable and unstable sections are separated by bifurcation points, so in Figure 5.3, together with the individual synchronization curves, the turning-point/synchronization locus and the secondary Hopf bifurcation locus have been represented.

The turning-point/synchronization locus is composed of all the points at which the solution curves exhibit infinite slope. As has already been said in Section 4.3, the collision of a node-type periodic solution and a saddle-type periodic solution at an infinite-slope point of the solution curve may give rise to a loss of synchronization. At this global bifurcation, an invariant cycle is formed in the Poincaré map (or a torus in the phase space), giving rise to a quasiperiodic solution (see Section 4.3.2 and Example 4.6). This is generally the case of the turning points in the closed curves obtained for relatively small input

power. In the open solution curves obtained for higher input power, the turning points usually give rise to jumps and hysteresis.

It is not possible to distinguish synchronization and jump points from the simple inspection of the periodic solution curves. The application of the Nyquist stability analysis is not helpful either because the loss of synchronization is a bifurcation of the global type. As has already been said, in the case of closed curves, containing a single turning point at each end (versus the parameter), the two turning points (one at each side) will generally be synchronization points. Problems arise when the closed curve exhibits several turning points, which makes the distinction between synchronization and jump points almost impossible when only periodic simulations are performed. On the other hand, synchronization points can also be encountered in open solution curves, especially for input-power values slightly higher than the one for which the closed curve and the low-amplitude curve merge. As will be shown later, the representation of the turning-point/synchronization locus and the Hopf-bifurcation locus in the plane defined by the input power and frequency can be helpful for distinguishing between synchronization and jump points.

The Hopf-bifurcation locus provides the border between synchronized and quasiperiodic regime for higher input power. Actually, although the open synchronization curves continue to exist below the Hopf locus (see Figure 5.3), sections of the curves below this locus are unstable because of the onset at the Hopf bifurcation points (intersections with the Hopf locus) of an autonomous frequency. This gives rise to a quasiperiodic solution that has not been represented here (see Figure 4.24 for an example). The autonomous frequency is actually the self-oscillation frequency, reappearing in the circuit when the input frequency is relatively far from the self-oscillation frequency and the input power is relatively low, which means small influence of the input generator over the self-oscillation.

To trace the synchronization curves of Figure 5.3, the input frequency ω_{in} has been considered as the analysis parameter, using the continuation techniques of Section 2.5 to pass through the turning points. An auxiliary generator, operating at the input-generator frequency $\omega_p = \omega_{in}$, is employed for the analysis. The turning-point/synchronization locus has been obtained from (4.78). This equation is repeated here, for clarity, using the specific parameters of a synchronized circuit [i.e., $\bar{\eta} = (\omega_{in}, P_{in})$]:

$$\begin{aligned} H_{pr} (A_p, \phi_p, \omega_{in}, P_{in}) &= 0 \\ H_{pi} (A_p, \phi_p, \omega_{in}, P_{in}) &= 0 \\ \det [JH_p (A_p, \phi_p, \omega_{in}, P_{in})] &= 0 \end{aligned} \quad (5.2)$$

where the Jacobian matrix is given by

$$[JH_p] = \begin{bmatrix} \frac{\partial H_{pr}}{\partial A_p} & \frac{\partial H_{pr}}{\partial \phi_p} \\ \frac{\partial H_{pi}}{\partial A_p} & \frac{\partial H_{pi}}{\partial \phi_p} \end{bmatrix} \quad (5.3)$$

As has already been said in Section 4.5, (5.2) must be solved in combination with harmonic balance. The third equation is the condition for turning point, that is, for singularity of the Jacobian matrix of the auxiliary generator impedance/admittance function. Because the determinant is real, (5.2) contains four unknowns in three equations. This provides a solution curve when varying, for instance, ω_{in} at a prefixed step, and solving for the three other variables. However, because of the presence of turning points in the locus itself, (5.2) must be solved in combination with the parameter-switching continuation technique. The parameter will switch between the four variables $A_p, \phi_p, \omega_{in}, P_{in}$. The turning-point/synchronization locus passes through all the points with infinite slope of all the solution curves. As is already known, some of the points will correspond to synchronization and some will be jump points. The application of the Nyquist stability analysis has shown that the sections of the periodic solution curves inside the locus are unstable.

For tracing the secondary Hopf bifurcation locus, (4.77) must be applied. This is repeated here for the sake of clarity:

$$\begin{aligned} H_{pr}(\omega_p, \omega_{in}, P_{in}) &= 0 \\ H_{pi}(\omega_p, \omega_{in}, P_{in}) &= 0 \\ A_p &= \varepsilon \end{aligned} \quad (5.4)$$

where the auxiliary generator frequency is that of the newly generated self-oscillation. As in the case of primary Hopf bifurcations, the amplitude of the incipient oscillation is set to very small value, corresponding to the circuit situation immediately after the bifurcation. Again, the solution of (5.4) is a curve due to the existence of four unknowns $A_p, \omega_p, \omega_{in}, P_{in}$ for three equations.

The representation of both the turning-point/synchronization locus and secondary Hopf-bifurcation locus in the plane defined by $\omega_{in} - P_{in}$ is extremely useful because it provides the kind of circuit operation (synchronized or not) for given generator values [see Figure 5.4(b)]. In the plane defined by $\omega_{in} - P_{in}$,

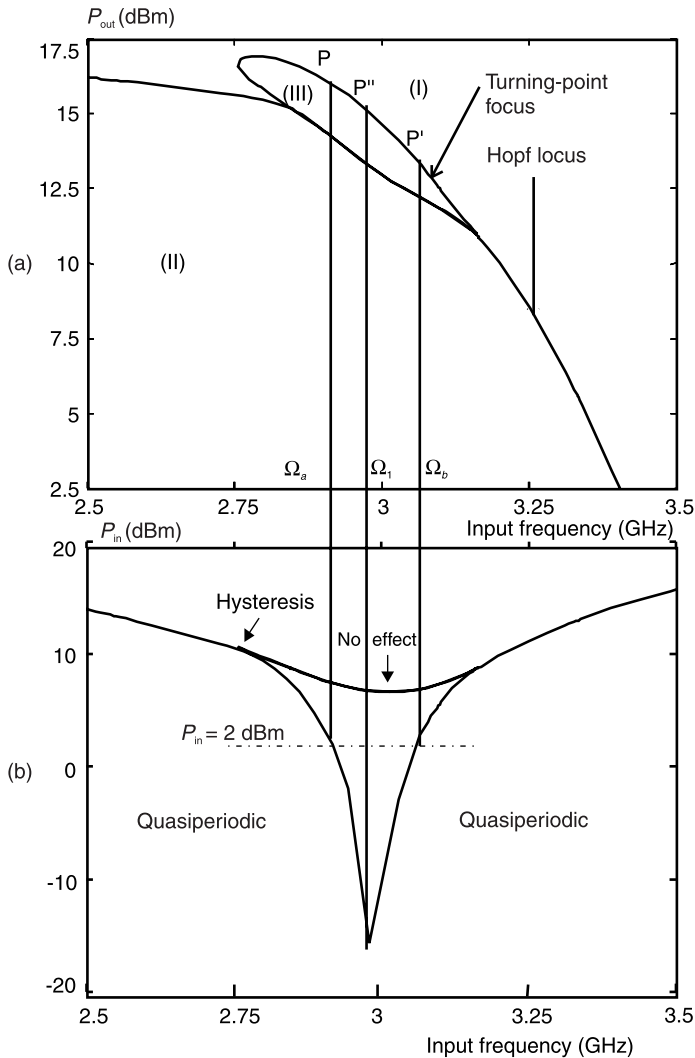


Figure 5.4 Bifurcation loci in a synchronized oscillator. Turning-point/synchronization locus and secondary Hopf bifurcation locus: (a) representation on the plane $\omega_{in}-P_{out}$, and (b) representation on the plane $\omega_{in}-P_{in}$. (From: [6]. © 1993 IEEE. Reprinted with permission.)

the synchronization locus (composed of saddle-node solutions at which synchronization takes place) takes a V shape, with the free-running oscillation point at the lower vertex. This V-shaped locus is often called the *Arnold tongue* in the nonlinear-dynamics literature [1–3] (see Section 1.6). Synchronized

solutions are obtained for input-generator power and input-generator frequency inside this locus [see Figure 5.4(b)]. The turning-point locus joins the Hopf-bifurcation locus on both sides (see Figure 5.4) at two points (one on the left side of the tongue and the other on the right side), belonging at the same time to the two loci. These two points are codimension-two bifurcations. A real multiplier crosses the border of the unit circle at the point (1,0), and a couple of complex-conjugate multipliers cross the border at $1e^{\pm j\theta}$ for the same $P_{in} - \omega_{in}$ values.

For constant and relatively low input power, such that the synchronization limits are given by two points of the V-shaped curve [e.g., $P_{in} = 2$ dBm in Figure 5.4(b)], the synchronization curve will be closed (see Figure 5.4). For higher input power, the periodic solution curves are open and the Hopf-bifurcation locus establishes the limit between synchronized and nonsynchronized solutions, as can be appreciated in Figure 5.4(b). Synchronized solutions exist inside the synchronization locus and above the Hopf-bifurcation locus. Thus, the upper part of the turning-point locus [see Figure 5.4(b)] has no physical effect because the circuit continues to behave in synchronized regime when the input power is increased above this line. Aside from the V-shaped synchronization locus, the turning-point locus includes a small prolongation above the Hopf-bifurcation locus. This corresponds to turning points and hysteresis of the opened curves, as can be seen in Figure 5.3.

In Figure 5.4(a), the bifurcation loci have been represented in the less meaningful plane $\omega_{in} - P_{out}$. For this representation, a calculation of output power has been carried out at each point of the Hopf and turning-point bifurcation loci (i.e., for the input-frequency, input-power for which each bifurcation point is obtained).

5.3 Global Behavior of Frequency Dividers by Two

5.3.1 Design Concepts and Applications of Frequency Dividers

Frequency dividers are essential devices in frequency synthesizers, phase-locked loops, or FM systems [11]. For operating at high microwave frequencies (millimetric band), an analog divider must be used [12–21] because of the limitations of digital technologies. Analog dividers allow an output frequency of about the maximum oscillation frequency of the active device. Two types of analog divider exist, depending of the self-oscillation or not of the divider circuit in the absence of an input signal. Harmonic injection dividers by the order N [7] behave as free-running oscillators when no external signal is introduced (see Section 5.1). The frequency division is due to the synchronization of the

N th harmonic of the self-oscillation with the input-generator frequency. In contrast with the harmonic injection dividers, the regenerative dividers [12–15] do not exhibit a free-running oscillation in the absence of an input signal. In regenerative dividers by two, the onset of the subharmonic component is due to a direct flip bifurcation versus the input-generator power. For low input-generator power, the regenerative divider behaves in the periodic regime at the input-generator frequency ω_{in} . As the input power increases, the direct flip bifurcation gives rise to the frequency division by two. As can easily be understood, frequency division in harmonic-injection dividers can be achieved from lower input-power values than in regenerative dividers.

When using an FET transistor in the design, the basic divider topology consists of the FET device, with series or parallel feedback, to enable the self-oscillation, and two matching filters (see Figure 5.5), respectively, at the input and output frequency [17–19]. In the case of a frequency divider by two, the input filter is centered at ω_{in} , while the output filter and feedback network are centered at $\frac{\omega_{in}}{2}$. In general, the FET transistor is biased close to pinch-off to take advantage of the quadratic behavior of the drain current versus the gate-

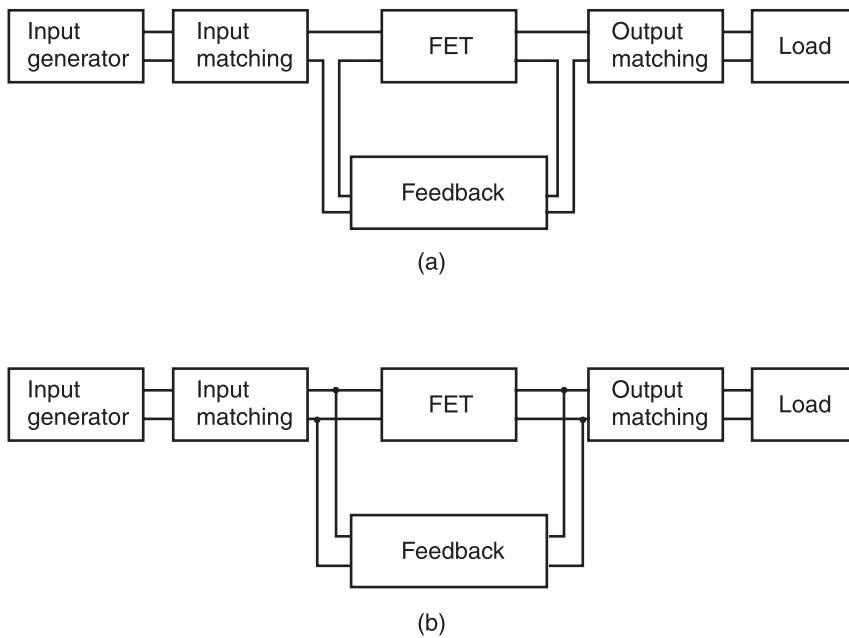


Figure 5.5 Basic configurations of FET-based frequency dividers: (a) series configuration, and (b) parallel configuration.

to-source voltage in this region. In most cases, the practical difference between a regenerative divider (no free-running oscillation) and a harmonic-injection divider simply depends on the value of the gate-bias voltage V_{GS} . For a more negative V_{GS} , the free-running oscillation is quenched and the circuit behaves as a regenerative frequency divider. In the absence of input power, the increase in this voltage leads to the onset of a free-running oscillation at the frequency ω_o with the circuit behaving as a harmonic-injection divider when the input generator is connected.

The analog frequency dividers are typically narrowband. To increase the operation bandwidth, the two-stage configuration of Figure 5.6 can be used [20, 21]. The first stage performs the matching and amplification of the input signal at the generator frequency $\omega_{in} \cong 2\omega_o$. In the second stage, the feedback network ensures the presence of the self-generated frequency ω_a at the transistor input, where it will be mixed with the signal at ω_{in} .

In a similar way to Figure 5.5, two different configurations are possible in the two-stage divider, depending on the series or parallel connection of the feedback network in the second stage. The block diagram shown in Figure 5.6 corresponds to the second type. For broadband operation, the second stage is optimized in small signal to obtain in the operating band a zero value and a minimum frequency variation of the phase difference ϕ between the voltages V_i and V_o at the input and output of the feedback loop [21]:

$$\frac{d\phi}{d\omega} \rightarrow 0 \quad \text{with} \quad \phi = \angle \frac{V_o}{V_i} = 0 \quad (5.5)$$

These conditions ensure the phase locking of the circuit over a frequency band.

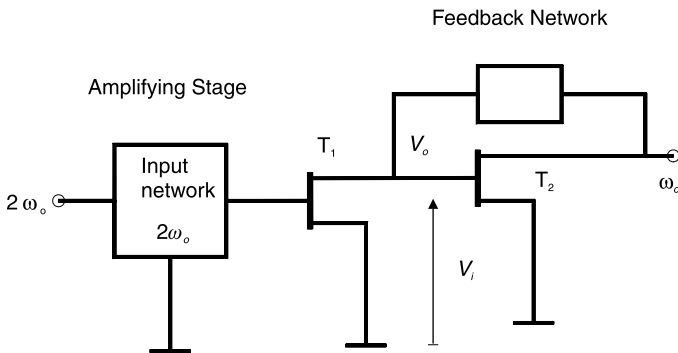


Figure 5.6 Broadband configuration of analog frequency dividers with two FET-transistor stages.

5.3.2 Parametric Stability Analysis of Frequency Dividers by Two

As has already been said, two main mechanisms may lead to the frequency division by two in a divider circuit: the flip-type bifurcation and the synchronization of the second harmonic of the autonomous frequency with the input-generator frequency. Flip-type bifurcations lead to a frequency division by two from a periodic regime at the external generator frequency ω_{in} . When the flip-type bifurcation takes place, the subharmonic $\frac{\omega_{in}}{2}$ arises and, with it,

other harmonic components at $k\omega_{in} \pm \frac{\omega_{in}}{2}$, with k integer. In the case of harmonic synchronization, the divider circuit, prior to synchronization, operates in a self-oscillating mixer regime, having both the input frequency ω_{in} and the autonomous frequency ω_a as fundamentals. The value of the autonomous frequency ω_a is influenced by the input generator, which enables the synchronization $2\omega_a \rightarrow \omega_{in}$. In the following, the different phenomena leading to frequency division by two in a divider circuit are analyzed, using, for illustration, the monolithic circuit of Figure 4.20.

The bifurcation diagram of Figure 5.7, has been obtained by varying the input-generator frequency ω_{in} of the circuit in Figure 4.20 for constant input power $P_{in} = 6$ dBm. The transistor bias point is $V_{GS} = -1.5$ v, $V_{DS} = 3$ v. In a frequency interval about the input frequency $f_{in} = 5$ GHz, the circuit behaves in the periodic regime at the fundamental frequency delivered by the generator. The solution path in this interval is traced in terms of the output power at this fundamental frequency. When increasing the input frequency, a flip-type bifurcation F_1 (from the stable periodic regime at ω_{in}) gives rise to the onset of the subharmonic $\frac{\omega_{in}}{2}$, providing the start of the band of frequency division by two.

The evolution of the frequency-divided solution versus f_{in} is represented by tracing two paths, one providing the output power at the frequency component ω_{in} and the other providing the output power at the subharmonic component $\frac{\omega_{in}}{2}$.

As the input frequency continues to be increased, a second (and inverse) Flip bifurcation takes place at F_2 . However, the end of the frequency-divided regime is not determined by this bifurcation, but by a saddle-node bifurcation in the frequency-divided solution (turning point T_2). It is a saddle-node bifurcation with loss of synchronization, giving rise to a quasiperiodic solution with two fundamental frequencies: the input-generator frequency ω_{in} and the self-oscillation frequency ω_a . The evolution of this solution (for frequencies beyond the turning point T_2) is represented by tracing a path for each of the two

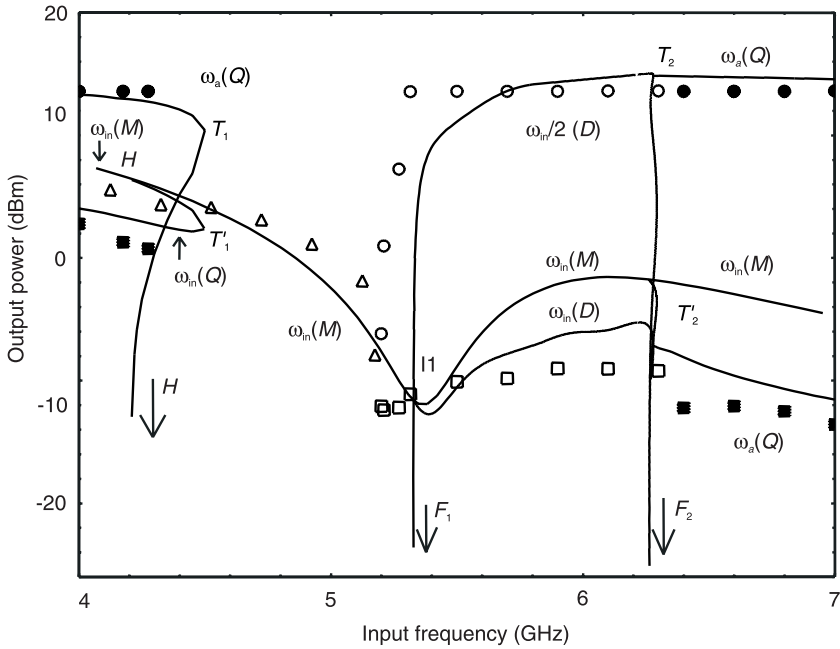


Figure 5.7 Bifurcation diagram of the monolithic frequency divider of Figure 4.22 for constant input power $P_{in} = 6$ dBm and variable input frequency f_{in} . Both periodic and quasiperiodic solutions have been traced with measurement points superimposed. (From: [19]. © 1996 IEEE. Reprinted with permission.)

fundamental frequencies, each path showing the output power at the corresponding fundamental. The turning point T_2 in the path at the autonomous fundamental ω_a has its image T_2' in the path at ω_{in} , as, obviously, all the harmonic components have the same turning points. Global bifurcations are discontinuous, so at the synchronization points, there is always a small discontinuity in the paths. Due to this discontinuity, the output power at $\frac{\omega_{in}}{2}$, at the

turning point T_2 , does not take exactly the same value as the power of ω_a after the loss of synchronization. The same happens at T_2' , in terms of ω_{in} and $2\omega_a$.

In the immediate neighborhood of the synchronization points, the results from the frequency-domain analysis are approximate. As the parameter gets closer to the synchronization value, the rotation number continuously approaches a rational value ($r = \frac{1}{2}$, in a frequency divider by two). See Figure 4.25, as an example of evolution of the rotation number versus the parameter.

The close-to-rational rotation number r gives rise to a great density of spectral lines with relevant power about each frequency component $k\omega_a$. The analysis demands a very high nonlinearity order for good accuracy. To see this more clearly, Figure 5.8 shows the spectrum of the frequency divider close to a synchronization value of the input frequency. When the rotation number approaches $r = \frac{1}{2}$, the frequency component $2\omega_a$ approaches ω_{in} (i.e., $2\omega_a \rightarrow \omega_{in}$), and the spectral lines $k\omega_{in} + l\omega_a$, with k, l integers, take close values. Close to the synchronization points, there is a big sensitivity of the analysis with respect to the nonlinearity order $nl = \max\{|k| + |l|\}$. As has already been said in Section 2.2.1, in any quasiperiodic analysis, there is a nonlinearity order nl_o , such that the increment of nl beyond nl_o gives no appreciable effect. While relatively far from the synchronization point, this order can be $nl_o = 7$ or $nl_o = 8$, close to the synchronization point, this order is very high ($nl_o = 20$ or greater).

The left-hand side of the bifurcation diagram of Figure 5.7 shows the existence of a quasiperiodic solution with paths at both the input frequency ω_{in} and the autonomous frequency ω_a . The point marked H indicates an inverse

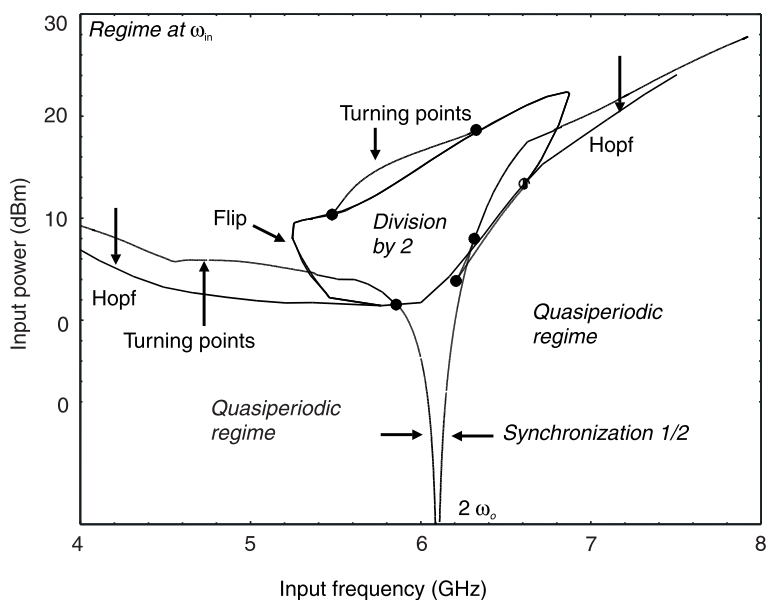


Figure 5.8 Bifurcation loci about the second harmonic of the free-running oscillation $2\omega_a$ of the monolithic frequency divider of Figure 4.20. (From: [19]. © 1996 IEEE. Reprinted with permission.)

Hopf bifurcation, in the increasing sense of the input frequency ω_{in} , of subcritical type. There is a turning point in the quasiperiodic paths, marked T_1 in the path at ω_a and T_1' in the path at ω_a . If the circuit initially behaves in the quasiperiodic regime, the transformation to the periodic regime with increasing input frequency will take place at T_1-T_1' . The only fundamental of this regime is ω_{in} (multiplying regime). From this regime, the direct (and super-critical) flip-type bifurcation F_1 gives rise to a frequency division by two. When decreasing the input frequency from about $f_{in} = 4.5$ GHz, the transformation to the quasiperiodic regime does not take place until the Hopf bifurcation point H is reached. An hysteresis cycle is obtained.

As can be gathered from the above bifurcation diagrams, the analog frequency dividers, although originally intended to behave as such, can also exhibit other operation modes. It would be helpful for the designer to know the circuit operation mode for given input-generator conditions in terms of frequency and power. This requires the tracing of the circuit bifurcation loci in the two-parameter plane (ω_{in}, P_{in}) . In view of the bifurcation diagrams of Figure 5.7, it would be necessary to trace the turning-point locus in the periodic regime (including synchronization points and jump points), the flip-bifurcation locus (giving rise to frequency division by two from periodic regime at ω_{in}), the secondary Hopf-bifurcation locus and the turning point locus in the quasiperiodic regime because of the possibility of jumps from the quasiperiodic regime to the periodic regime. The flip-bifurcation locus is traced using (4.76). This equation is rewritten here for the specific parameters $\bar{\eta} = (\omega_{in}, P_{in})$:

$$\begin{aligned} H_{pr}(\phi_p, \omega_{in}, P_{in}) &= 0 \\ H_{pi}(\phi_p, \omega_{in}, P_{in}) &= 0 \\ A_p &= \varepsilon \end{aligned} \quad (5.6)$$

with the auxiliary generator operating at the subharmonic frequency $\omega_p = \frac{\omega_{in}}{2}$. The above system contains four unknowns in three equations, which gives rise to a solution curve P_{in} versus ω_{in} . A continuation technique with parameter switching between the three variables $P_{in}, \omega_{in}, \phi_p$ has to be applied to pass through the possible turning points of the locus itself.

The locus of turning points in the period-doubled regime (including the synchronization locus) is obtained by applying

$$\begin{aligned}
 H_{pr} (A_p, \phi_p, \omega_{in}, P_{in}) &= 0 \\
 H_{pi} (A_p, \phi_p, \omega_{in}, P_{in}) &= 0 \\
 \det [JH_p (A_p, \phi_p, \omega_{in}, P_{in})] &= 0 \\
 \omega_p &= \frac{\omega_{in}}{2}
 \end{aligned} \tag{5.7}$$

where the Jacobian matrix is given by

$$[JH_p] = \begin{bmatrix} \frac{\partial H_{pr}}{\partial A_p} & \frac{\partial H_{pr}}{\partial \phi_p} \\ \frac{\partial H_{pi}}{\partial A_p} & \frac{\partial H_{pi}}{\partial \phi_p} \end{bmatrix} \tag{5.8}$$

The difference from (5.2) is in the operation frequency ω_p of the auxiliary generator. The relationship $\omega_{in} = 2\omega_p$ in (5.7) enables tracing the Arnold tongue $r = \frac{1}{2}$, in contrast with (5.2), which provided the Arnold tongue $r = 1$. On the other hand, the locus of turning points in the quasiperiodic regime (giving the parameter values for the transformation from the quasiperiodic to the periodic regime) is obtained by applying

$$\begin{aligned}
 H_{pr} (A_p, \omega_p, \omega_{in}, P_{in}) &= 0 \\
 H_{pi} (A_p, \omega_p, \omega_{in}, P_{in}) &= 0 \\
 \det [JH_p (A_p, \omega_p, \omega_{in}, P_{in})] &= 0
 \end{aligned} \tag{5.9}$$

In this case, the Jacobian matrix is given by

$$[JH_p] = \begin{bmatrix} \frac{\partial H_{pr}}{\partial A_p} & \frac{\partial H_{pr}}{\partial \omega_p} \\ \frac{\partial H_{pi}}{\partial A_p} & \frac{\partial H_{pi}}{\partial \omega_p} \end{bmatrix} \tag{5.10}$$

Equation (5.9) must be solved using two-tone harmonic balance at the two fundamental frequencies ω_{in} and ω_a . The third equation of (5.9) is the

condition for turning point (i.e., for singularity of the Jacobian matrix of the auxiliary generator impedance/admittance function).

The flip-bifurcation locus, the Hopf bifurcation locus, the turning-point locus in the periodic regime, and the turning-point locus in the quasiperiodic regime have been represented in the plane (P_{in}, ω_{in}) in Figure 5.9. This representation provides the input power and input frequency for each of the three main operation modes of the circuit: as frequency divider by two, as self-oscillating mixer (quasiperiodic regime at ω_{in} and ω_o) and as band amplifier (periodic regime at ω_{in}). It also shows the input-generator values for the two

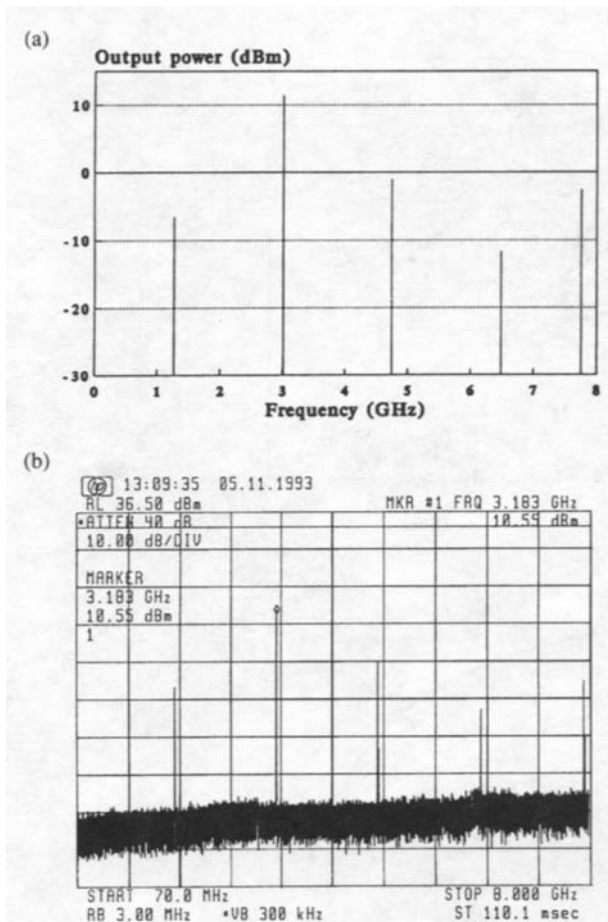


Figure 5.9 Spectrum of the monolithic frequency divider of Figure 4.22 for input frequency $f_{in} = 4.75$ GHz and input power $P_{in} = 5$ dBm: (a) simulated through multitone harmonic balance, and (b) measured.

main mechanisms of frequency division: by second-harmonic synchronization, from the quasiperiodic regime, and by flip bifurcation, from periodic regime at ω_{in} . The V-shaped synchronization locus constitutes the Arnold tongue $r = \frac{1}{2}$.

The internal line separating the flip-bifurcation locus from the synchronization locus has no physical effect, in a similar way to the upper line in the turning-point locus of Figure 5.4(b). The turning-point locus (in the periodic regime) above the upper part of the flip-bifurcation locus gives rise to hysteresis in the transformation from the frequency-divided regime to the periodic regime at ω_{in} (and vice versa). Both this locus and the synchronization locus are obtained as two different solutions of (5.7) isolated from each other.

As seen in Figure 5.7, turning points in the quasiperiodic solution paths cause hysteresis in the transformations from the quasiperiodic regime to the periodic regime at ω_{in} and the periodic regime at ω_{in} to the quasiperiodic regime. The locus of these turning points in the plane (P_{in}, ω_{in}) is obtained from (5.9). The sections of this locus above the flip-bifurcation locus (see Figure 5.8) give rise to hysteresis in the transformations from the quasiperiodic regime to the frequency-divided regime at $\frac{\omega_{in}}{2}$ and the frequency-divided regime at $\frac{\omega_{in}}{2}$ to the quasiperiodic regime.

Although both of them lead to the periodic regime, there is an essential difference between inverse Hopf bifurcations and synchronization from the point of view of the evolution of the state-variable spectra versus the parameter. As has already been said, in the neighborhood of inverse Hopf bifurcation (also called *asynchronous extinction*), the power at autonomous frequency decreases in a continuous fashion. Another characteristic is that, contrary to what happens near synchronization, the rotation number r does not tend to be rational, and the spectral lines are separated when the inverse Hopf bifurcation occurs. An example is shown in Figure 5.10. The input frequency is $f_{in} = 4.75$ GHz, and the input power is $P_{in} = 5$ dBm, so as gathered from Figure 5.9, the circuit is operating in the neighborhood of an inverse Hopf bifurcation. For comparison, take a look at the spectrum for $f_{in} = 6$ GHz and $P_{in} = -2$ dBm with circuit operation close to second-harmonic synchronization (see Figure 5.9) that had been represented in Figure 5.8. The rotation number approaches $r = \frac{1}{2}$, and the frequency distance between the spectral lines is very small, obtaining a dense triangular spectrum [22] typical of the presynchronization stage. As has already been said, for accuracy in the calculation, the nonlinearity order nl to

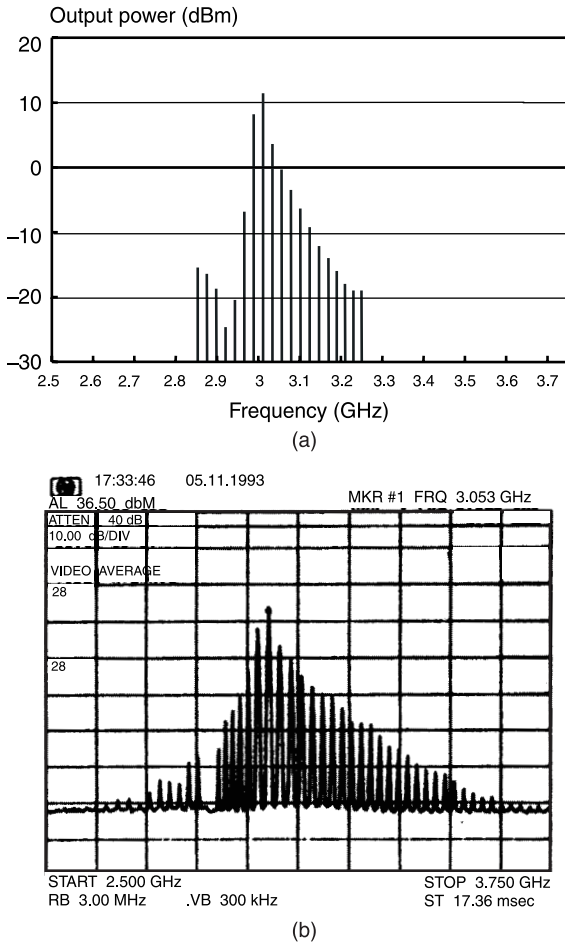


Figure 5.10 Spectrum of the monolithic frequency divider of Figure 4.22 for input frequency $f_{in} = 6$ GHz and input power $P_{in} = -2$ dBm close to synchronization: (a) simulated through multitone harmonic balance with nonlinearity order $N_l = 20$, and (b) measured. (From: [18]. © 1994 IEEE. Reprinted with permission.)

be taken into account in the harmonic-balance calculation of this quasiperiodic solution must be very high (20 or more).

5.3.3 Improvement in the Frequency-Divider Design

The bifurcation loci (see Figure 5.9) of all analog frequency dividers by two by harmonic injection are qualitatively similar. Both the harmonic-synchronization

and flip-bifurcation loci will exist. However, some hysteresis phenomena may be less relevant or even disappear. The width of the second-harmonic synchronization locus may also greatly vary. In the case of regenerative dividers (which do not oscillate in the absence of an input signal), the frequency division is exclusively obtained through flip bifurcations. These dividers are not expected to operate in the quasiperiodic regime outside the division band, and the synchronization locus will not exist.

A monolithic frequency divider by two with input frequency $f_{in} = 28$ GHz and based on the broadband topology of Figure 5.6 has also been analyzed [20, 21]. In the schematic of Figure 5.11, both the amplifying and regenerative stages can be distinguished, as can the autobias network. For the second stage, parallel feedback has been chosen. For 5ν bias voltage, the circuit oscillates in the absence of an input signal at the frequency $f_o = 14.23$ GHz. The bifurcation loci of this frequency divider, obtained applying (5.6) to (5.10), are shown in Figure 5.12.

The comparison with the bifurcation loci of the 6- to 3-GHz frequency divider (Figure 5.9) evidences the broadening of the division band by second-harmonic synchronization. Unlike the diagram in Figure 5.9, there is no turning-point locus in the quasiperiodic regime, so no hysteresis is observed in the transformations from the quasiperiodic regime to the periodic regime and

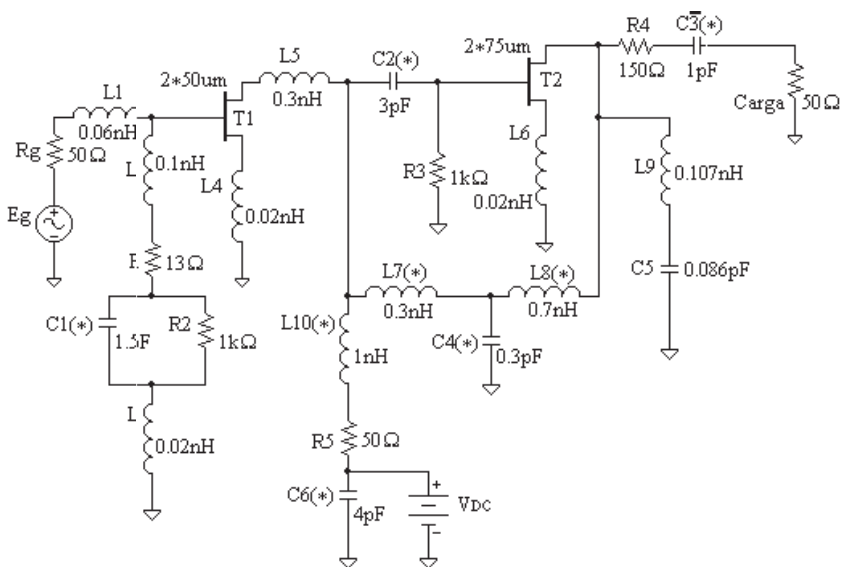


Figure 5.11 Two-stage monolithic frequency divider with 28-GHz input frequency.

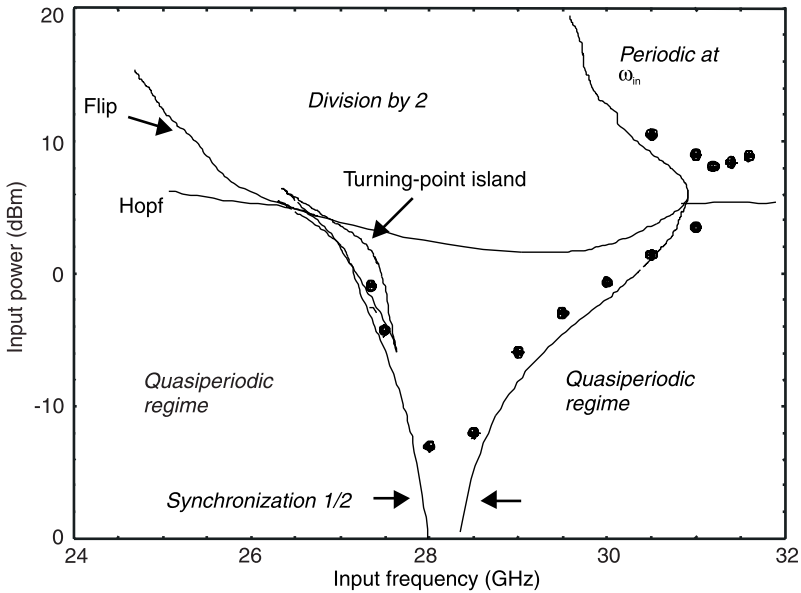


Figure 5.12 Bifurcation loci of the monolithic frequency divider by two of Figure 5.11. There is no turning-point locus in the quasiperiodic regime. The “island” is composed of turning points of the frequency-divided curves. (From: [20]. © 1998 IEEE. Reprinted with permission.)

the periodic regime to the quasiperiodic regime. As seen in Figure 5.12, when solving (5.7) for the 28- to 14-GHz divider, aside from the synchronization locus or Arnold tongue $r = \frac{1}{2}$, a closed curve, looking like an island is obtained.

This “island” is composed of turning points of the solution curves in the frequency-divided regime. The simulations of Figure 5.13 illustrate the influence of the turning-point island over the solution curves. For constant input power $P_{in} = 0$ dBm [see Figures 5.12 and 5.13(a)] and increasing the input frequency from $f_{in} = 26$ GHz, the circuit initially operates in the quasiperiodic regime. However, the synchronization locus (or Arnold tongue $1/2$) is traversed at the point S_1 , and at this point, second-harmonic synchronization takes place, leading to a frequency division by two. As already mentioned, quasiperiodic paths in the immediate neighborhood of the synchronization point always have a certain inaccuracy. There is also a small amplitude jump in the paths at ω_a (becoming $\frac{\omega_{in}}{2}$) and ω_{in} when the synchronization takes place because of the discontinuity of this bifurcation [3].

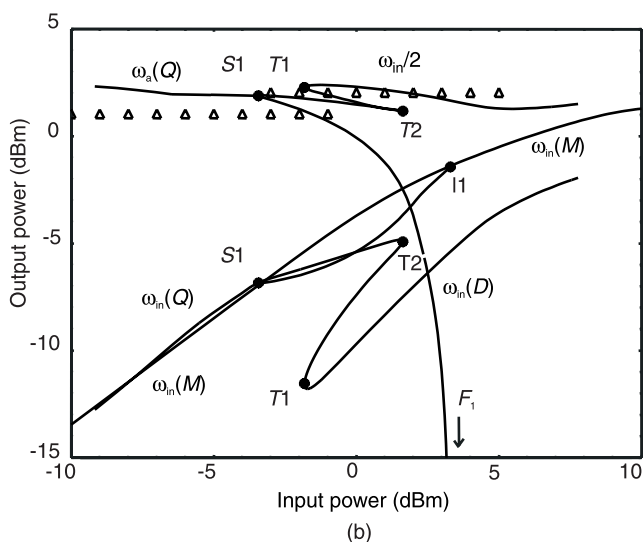
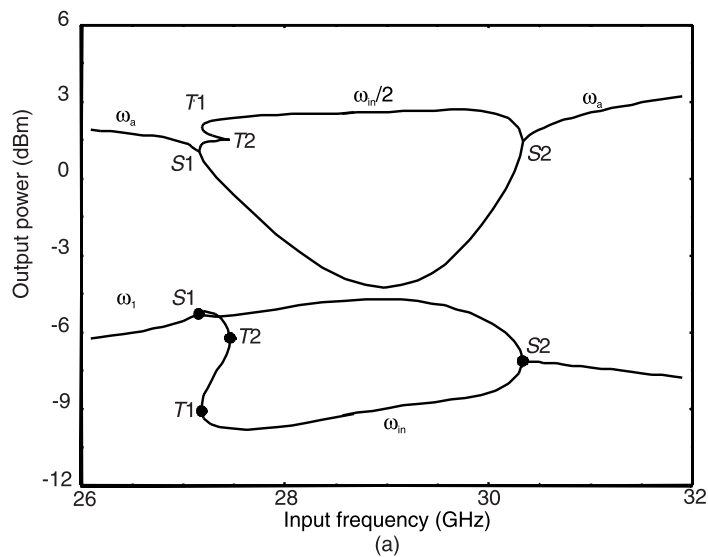


Figure 5.13 Simulations of the monolithic frequency divider by two of Figure 5.11: (a) for constant input power $P_{in} = 0$ dBm, and (b) for constant input frequency $f_{in} = 27.35$ GHz. (From: [20]. © 1998 IEEE. Reprinted with permission.)

The second crossing of the synchronization locus (or Arnold tongue $1/2$) at the point S_2 determines the end of the synchronization band. As has already been seen, constant input-power solution curves for which division by

synchronization takes place are typically closed, like the ones in Figure 5.13(b). The two closed curves are actually part of the same solution, one of them providing the output power at the subharmonic component $\frac{\omega_{in}}{2}$ and the other, the output power at ω_{in} . The crossing for this input-power value of the turning-point island (see Figure 5.12) gives rise to the two turning points T_1 and T_2 . A Nyquist stability analysis indicates that only the sections S_1-T_2 and T_1-S_2 are stable.

The simulation of Figure 5.13(b) shows the evolution of the output power at ω_{in} and $\frac{\omega_{in}}{2}$, versus the input power P_{in} for constant input frequency $f_{in} = 27.35$ GHz. The frequency division is due to second-harmonic synchronization at the point S_1 . Thus, the subcritical flip bifurcation F_1 has actually no effect over the circuit behavior. Note that the point F_1 belongs to the nonphysical line separating division points inside the Arnold tongue from division points inside the flip-bifurcation locus (see Figure 5.12). The branch S_1-F_1 is unstable. The crossing of the turning-point island gives rise to the two turning points in the frequency-divided regime T_1 and T_2 . These points are responsible for an hysteresis phenomenon in the divided regime. In the increasing input-power sense, an upward jump takes place at T_2 . In the decreasing input-power sense, a downward jump takes at T_1 .

5.4 Global Behavior of Self-Oscillating Mixers

5.4.1 Design Concepts and Applications of Self-Oscillating Mixers

Nowadays transmitter/receiver systems require very efficient frequency converters with small size and low-power consumption and compatible with the MMIC technology. Low cost is also a key characteristic for success in the communication market. The *self-oscillating mixer* is a very attractive frequency converter to fulfill these requirements [23].

In conventional downconverters, the input RF signal is mixed with that of a local oscillator, which is external to the mixer circuit. The mixer is usually based on the use of rectifier diodes because of low-cost requirements. In self-oscillating mixers a transistor or any suitable device serves both as a local oscillator and as a mixing element [23–28]. Due to this double function, the circuit design is very compact and simplified. The reduced component number increases reliability and manufacturing yield. Less active components also reduce the power consumption. The self-oscillating mixer approach simplifies the circuitry of the entire receiver system. Another advantage over the

conventional converters (using diode mixers) is the capability to provide conversion gain. Due to this fact, amplifier stages can be eliminated. Low-noise active devices can be used for low-noise designs.

A self-oscillating mixer is basically an oscillator at the frequency ω_o with an input RF signal at the frequency ω_{in} . The circuit oscillates in the absence of an input signal, so the first design step must be to obtain a free-running oscillator at ω_o . This oscillation frequency is tuned varying the bias point of the active element. When the low-power RF signal is introduced at ω_{in} , the mixing between the two fundamental frequencies provides the sum and difference (intermediate frequency) intermodulation products. The oscillator quality factor must be high to reduce the phase noise and the shift in the oscillation frequency due to the influence of the input signal. This influence increases with the input power.

Two terminal devices such as Gunn or IMPATT devices are often used for very compact and simplified receivers, especially at millimeter frequencies [24–27]. The use of waveguide cavities enables designs of high quality factor. MESFET, HEMT, and bipolar oscillators are also commonly employed for the design of self-oscillating mixers, stabilizing the oscillation frequency through a dielectric resonator [23, 28]. The single transistor configurations require an accurate design of the input and intermediate frequency filters to guarantee sufficient input/output isolation.

A self-oscillating mixer, based on a *dielectric-resonator-oscillator* (DRO) configuration, is shown in Figure 5.14. A MESFET transistor has been used [28]. For the design of the free-running oscillator, negative resistance is

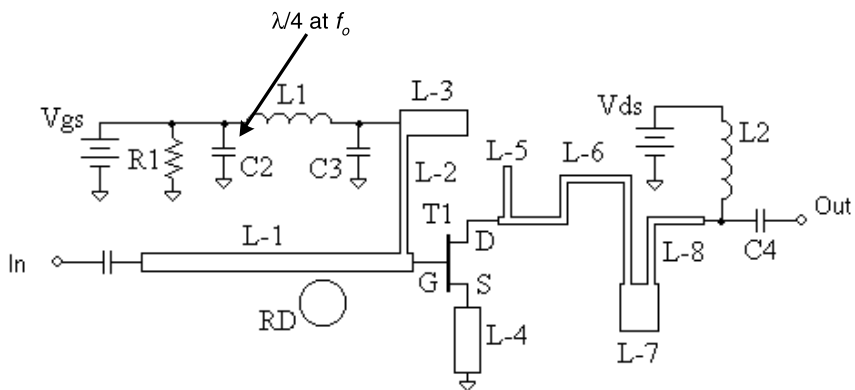


Figure 5.14 FET-based self-oscillating mixer stabilized through a dielectric-resonator-oscillator.

obtained at the transistor input at the desired oscillation frequency ω_o . Series feedback ($L4$) (at the transistor source) is used to get this negative resistance. The transistor output impedance is matched at the intermediate frequency f_{IF} . A dielectric resonator is coupled to the input microstrip line $L1$ and tuned at ω_o . The negative-resistance band must be narrow around ω_o and the output filter at IF must provide a high attenuation at the oscillation frequency to guarantee good input/output isolation. For attenuating the input frequency an open-circuited $\lambda/4$ parallel line at ω_o ($L5$) is introduced at the transistor output. The transistor bias point is $V_{GS} = -1.3v$, $V_{DS} = 3.6v$. For this point, the oscillation frequency is 9.56 GHz, with output power $P_{out} = 14$ dBm. The oscillation-signal isolation at the IF output is about 30 dB. The frequency of the input RF signal varies between $f_{in} = 10.5$ GHz and $f_{in} = 12$ GHz. This example will be continuously referred to in the following sections to illustrate the different aspects of the analysis of self-oscillating mixers.

5.4.2 Steady State of the Self-Oscillating Mixer

The nonlinear analysis of the self-oscillating mixer enables a realistic determination of characteristics, such as the dynamic range, the intermodulation content, and the possible instability. Actually, frequency-conversion techniques [16], based on the circuit linearization around the free-running oscillation (in the absence of an input signal), are only applicable for very small input powers. When this condition is not fulfilled, nonlinear analysis techniques, like harmonic balance must be used [28, 29]. In the case of self-oscillating mixers, there will be two incommensurable fundamental frequencies given respectively by the input-generator frequency ω_{in} and the self-oscillation frequency ω_o , slightly perturbed under the influence of the external generator ω_{in} . Because the two fundamental frequencies are not harmonically related, the resulting regime is quasiperiodic. The two fundamental frequencies give rise to intermodulation products of the form $k\omega_{in} + l\omega_o$ with k, l integers.

The high quality factor of the resonant circuits employed in the design of self-oscillating mixers limits the variations of ω_o . In spite of these small variations, the harmonic-balance analysis requires the inclusion of ω_o in the set of harmonic-balance unknowns, as in any other calculation of an autonomous quasiperiodic regime. Because one of the fundamental frequencies is autonomous, there is an insensitivity of the solution with respect to the phase-origin. The phase of one of the harmonic components of one state variable is set to zero and is replaced, as a system unknown, with the autonomous frequency ω_o .

For the harmonic-balance analysis of this quasiperiodic regime, the Fourier expansions of the circuit variables must be truncated to a finite number of

spectral components. For the self-oscillating mixer of Figure 5.14, the nonlinearity order $nl=5$ has been used, so 31 spectral components have been considered for each circuit variable.

As in any quasiperiodic regime with an autonomous fundamental, the mixing solution of self-oscillating mixer coexists with a generally unstable periodic solution having the input-generator frequency ω_{in} . as only fundamental (see Section 2.3.3). To avoid this solution, an auxiliary generator is introduced at the oscillation frequency $\omega_p = \omega_a$. The presence of this generator (with non-zero value) enables the initialization of the frequency components at ω_a that otherwise would remain at zero value (see Section 2.3.3). When this auxiliary generator fulfills the nonperturbation condition $\bar{H}_p = 0$, the solution of the circuit containing the auxiliary generator is identical to the actual circuit solution.

In the self-oscillating mixer of Figure 5.14, the auxiliary generator is connected in parallel with the transistor gate. The resulting output power spectrum for input power $P_{in} = -18$ dBm and input frequency $f_{in} = 10.6$ GHz is shown in Figure 5.15. The intermediate frequency is, in this case, $f_{IF} = 1$ GHz. This simulated spectrum can be compared with the experimental one in Figure 5.15(b). Note that some further filtering would be necessary to select the intermediate frequency ω_{IF} with good attenuation of ω_{in} and ω_a . Once the harmonic-balance analysis has been performed, the conversion loss of the self-oscillating mixer is directly obtained from the ratio:

$$L = 10 \log \left(\frac{P_{in}}{P_{IF}} \right) \quad (5.11)$$

For $P_{in} = -18$ dBm and $f_{IF} = 1$ GHz, conversion loss of about $L = 2$ dB (Figure 5.15) is obtained.

5.4.3 Parametric Analysis of the Self-Oscillating Mixer

Obtaining the evolution of the conversion gain/loss (or IF output power) of the self-oscillating mixer under variations in a parameter η (such as the device bias, the input power, or the input frequency) will generally be of interest for the designer. Versus the input power, this parametric analysis provides the 1-dB gain compression point. It must also be taken into account that the self-oscillating mixers, although intended to behave as frequency mixers, can also exhibit other undesired operation modes. The parametric analysis will enable an accurate determination of the bands with mixing behavior (in terms of one or two significant parameters) and the optimum operation conditions.

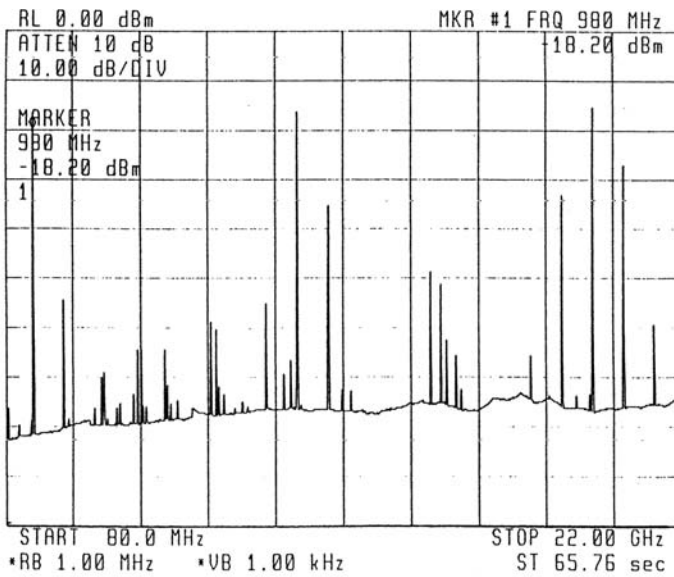
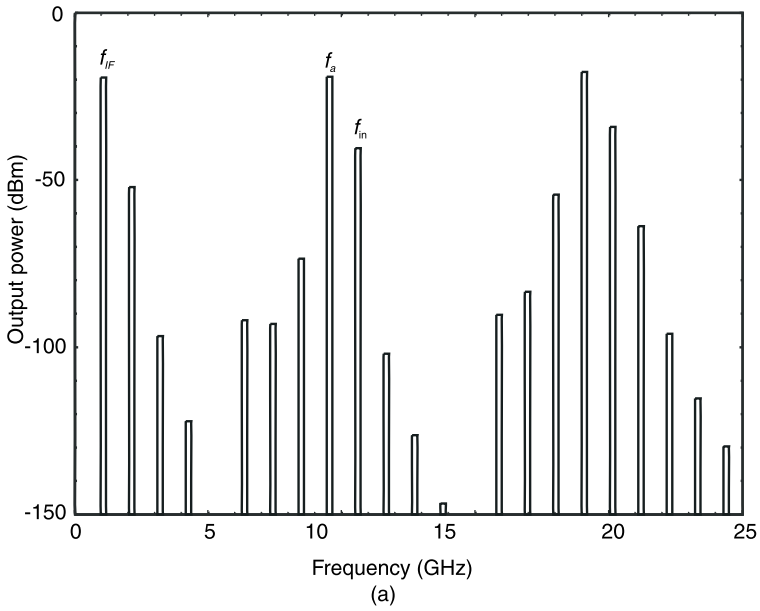


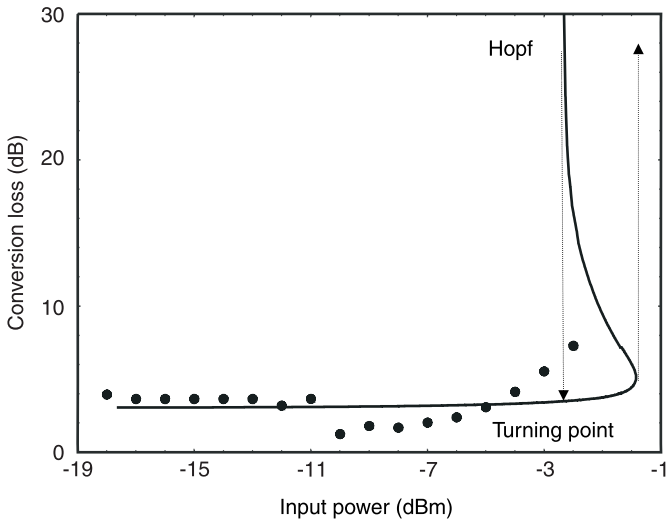
Figure 5.15 Output spectrum of the self-oscillating mixer of Figure 5.14 for $P_{in} = -18$ dBm and $f_{IF} = 1$ GHz: (a) simulated, and (b) experimental.

When varying a parameter η of a self-oscillating mixer, turning points are often encountered in the solution curves. The tracing of these curves requires a prediction/correction continuation technique with parameter switching, like the continuation technique of Section 2.6.3, based on the use of an auxiliary generator. The switching is carried out between the two auxiliary-generator values A_p and ω_p and the parameter η to fulfill the nonperturbation condition $\overline{H}_p = 0$. The application of this technique to the self-oscillating mixer of Figure 5.14 has enabled obtaining the variation of its conversion loss versus the input power [Figure 5.16(a)] and versus the intermediate frequency [Figure 5.16(b)].

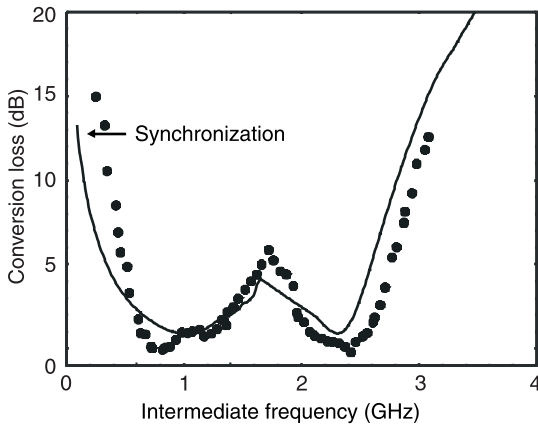
In Figure 5.16(a), the conversion loss, for input power $P_{in} \cong -3$ dBm, tends to infinity. This is due to the extinction for this relatively high input power of the self-oscillation at an inverse Hopf bifurcation of subcritical type at the point H . At this point, the fundamental frequency ω_a disappears as fundamental, together with all the harmonic components involving this frequency, in particular, the intermediate frequency $\omega_{IF} = \omega_{in} - \omega_a$. The amplitude of all the spectral components containing the frequency ω_a tends to zero as the Hopf bifurcation is approached. The output power at P_{IF} tends to zero and the conversion loss, according to (5.11), tends to infinity.

The subcritical nature of the Hopf bifurcation H gives rise to hysteresis in the transformation of the quasiperiodic regime to the periodic regime and the periodic regime to the quasiperiodic regime. The transformation of the quasiperiodic regime to the periodic regime in the increasing input power sense is actually due to the turning point T in the quasiperiodic solution curve. For $P_{in} > P_{inT}$, the circuit operates in a nonautonomous regime with the input-generator frequency ω_{in} as only fundamental. This kind of operation is similar to that of a bad amplifier. Decreasing the input power P_{in} from periodic regime, the self-oscillating mixer operation is not recovered until P_{in} is reduced below P_{inH} . The transformation from the periodic regime to the quasiperiodic regime takes place at point H .

The evolution of the conversion loss of the self-oscillating mixer versus variations in the intermediate frequency is shown in Figure 5.16(b). As in the case of input-power variations, experimental points have been superimposed. For very low values of intermediate frequency, the conversion loss increases quickly. This is due to the synchronization of the two independent fundamentals ω_a , ω_{in} . The synchronization prevents the mixing process because the two frequencies become the same, leading the circuit to a periodic regime similar to that of a synchronized oscillator. Synchronization takes place for an input frequency very close to the self-oscillation one and, in general, will not be relevant because of the usually high value of the resonant-circuit quality factor.



(a)



(b)

Figure 5.16 Conversion loss of the self-oscillating mixer versus (a) input power for constant input frequency $f_{in} = 10$ GHz, and (b) intermediate frequency for constant input power $P_{in} = -18$ dBm.

The self-oscillating-mixer circuit is expected to operate in an autonomous quasiperiodic regime, giving rise to the mixing of the two fundamental frequencies ω_{in} and ω_{ω} . However, as has been shown, other operating regimes are possible because of its intrinsic autonomous nature. The operation regions of the self-oscillating mixer versus two parameters of interest, such as input power and input frequency, can be determined by tracing its bifurcation loci in

the plane defined by the two selected parameters. This has been done in Figure 5.17(a) in the plane (P_{in}, ω_{in}) .

The loci that have been represented are the Hopf bifurcation locus, the turning-point locus in the quasiperiodic regime, and the turning-point locus in the periodic regime, providing the synchronization locus (Arnold tongue 1/1). For parameter variations such that both the turning point and inverse Hopf bifurcation loci are traversed, an hysteresis phenomenon is observed in the transformation between the quasiperiodic regime (self-oscillating-mixer operation) and the periodic regime. There are some input-frequency values for which the input power can be substantially increased without leading the circuit to the uninteresting periodic behavior. For these frequency values, the input generator observes very low impedance. Most of the input power is reflected and no actual mixing takes place.

The synchronization locus has been obtained from the locus of turning points in the periodic regime at ω_{in} [see (5.2)]. It is very narrow due to the high value of the quality factor of the resonant circuit. An expanded view of the bifurcation loci about the synchronization region is shown in Figure 5.17(b).

5.5 Global Behavior of Frequency Doublers

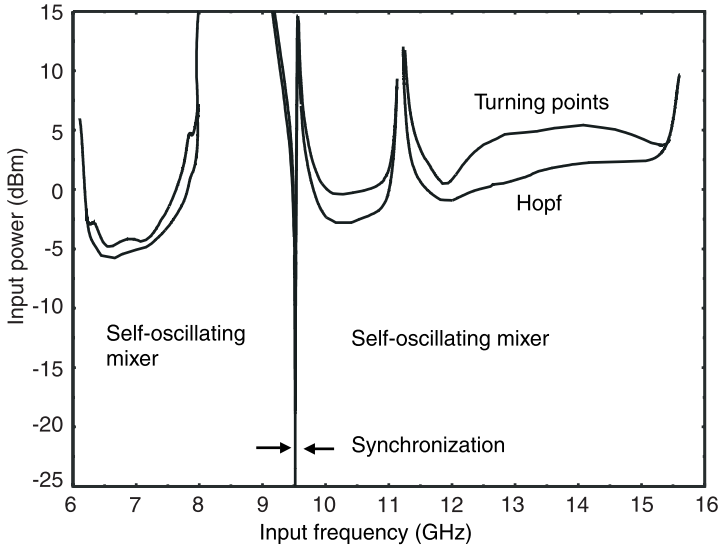
5.5.1 Design Concepts of Frequency Doublers

The circuit in Figure 5.18 is another example of microwave-frequency doublers, based on the use of a long-lifetime varactor diode of PV -type [30–32] similar to the one that has already been studied in Example 4.4. The schematic includes an input bandpass filter, about the input-generator frequency ($f_{in} = 4$ GHz) and an output filter, about the doubled frequency ($f_{out} = 8$ GHz).

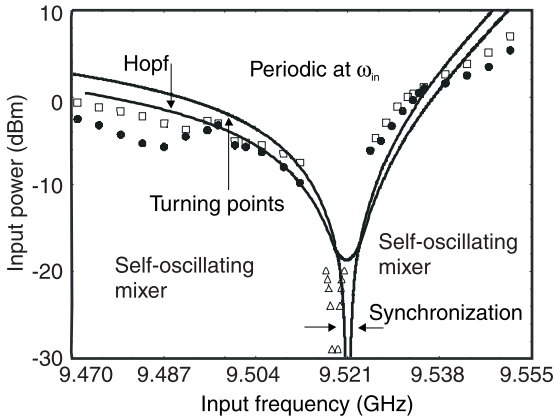
5.5.2 Parametric Analysis of Frequency Doublers

The frequency doubler is expected to operate in the periodic regime at the fundamental frequency f_{in} delivered by the input generator. The high nonlinearity of the capacitance should enable significant power at the second harmonic component. However, this highly nonlinear behavior is also likely to give rise to instability. The frequency doubler of Example 4.4 exhibited flip bifurcations as the input-power increased. In the doubler of Figure 5.18, Hopf-type instabilities are observed.

To detect any possible instability of the frequency doubler of Figure 5.18 as the input-generator power P_{in} is increased, sequential stability analyses by



(a)



(b)

Figure 5.17 (a) Operation modes of the self-oscillating mixer determined from the bifurcation loci; and (b) expanded view of the synchronization zone. Experimental points have been superimposed.

means of the Nyquist plot (see Chapter 2) have been carried out versus this parameter (Figure 5.19). These plots, calculated for constant input frequency $f_{in} = 3.7$ GHz and different input-power values, have been obtained using commercial harmonic balance.

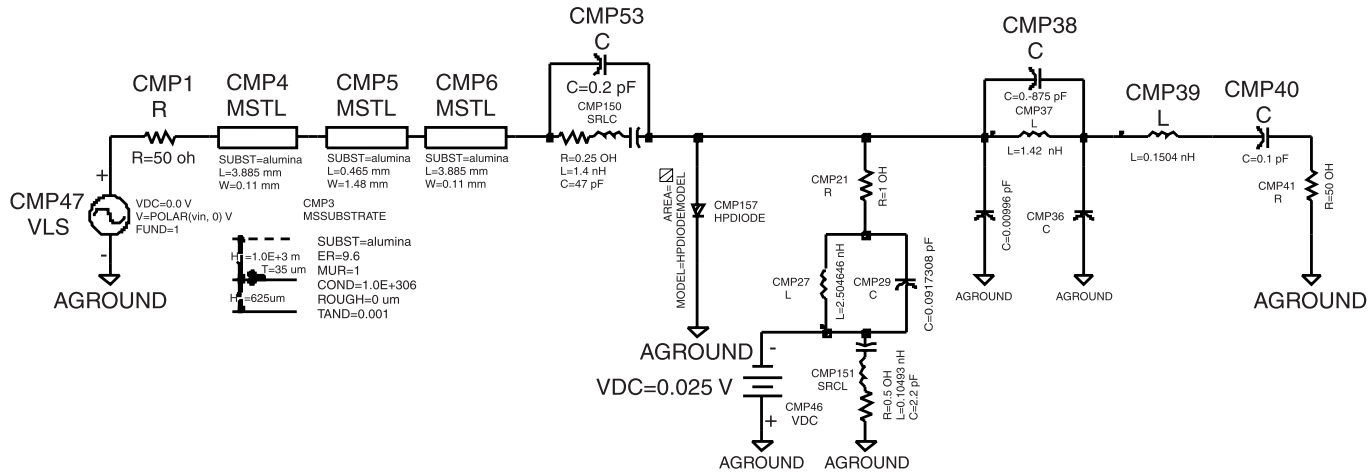


Figure 5.18 Microwave-frequency doubler with input frequency $f_{in} = 4$ GHz.

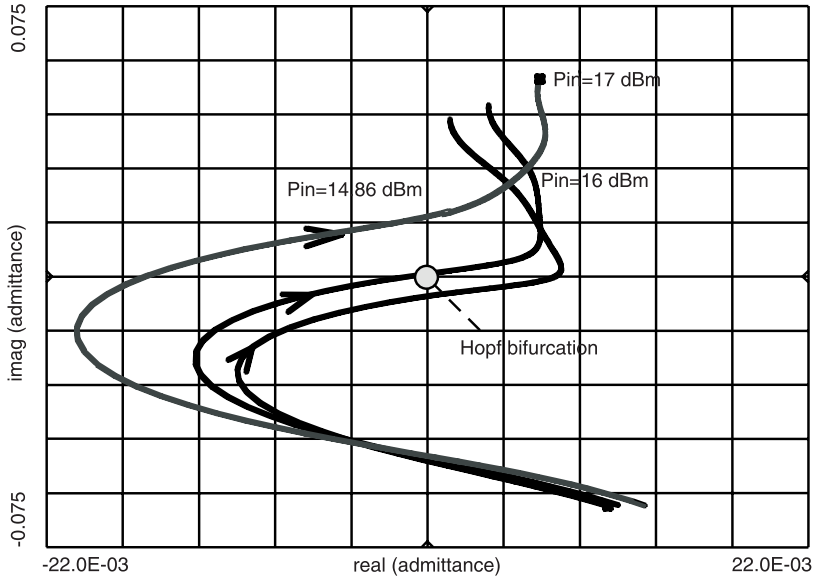


Figure 5.19 Stability analysis of the frequency doubler through Nyquist plots for constant input frequency $f_{in} = 3.7$ GHz. It has been obtained using commercial harmonic balance. A Hopf bifurcation is obtained at the input power $P_{in} = 16$ dBm. (From: [32]. © 1998 IEEE. Reprinted with permission.)

As can be seen in Figure 5.19, for input power below $P_{in} = 16$ dBm, the frequency doubler is stable because the Nyquist stability plot does not encircle the plot origin. Then, the observed solution is periodic (as desired), having the input-generator frequency $f_{in} = 3.7$ GHz as only fundamental. However, for input power above $P_{in} = 16$ dBm, the origin is encircled, thus signaling unstable behavior. This means that the periodic solution at the input-generator frequency, although mathematically correct, is physically unobservable. The input power $P_{in} = 16$ dBm is a critical value at which a direct Hopf bifurcation takes place in the frequency doubler. Associated with this qualitative variation of the solution stability, there is also a qualitative variation of the type of steady-state solution. The Hopf bifurcation gives rise to the onset on an oscillation at the frequency ω_a . The autonomous frequency is $f_a = 1.9$ GHz. This frequency mixes with the existing input-generator frequency ω_{in} to give rise to a quasiperiodic regime and typical mixer spectrum (Figure 5.20). The type of steady-state solution has varied from a limit cycle (for $P_{in} < 16$ dBm) to a 2-torus (for $P_{in} > 16$ dBm).

Figure 5.21 shows the evolution of the output power of the frequency doubler at twice the input frequency $2\omega_a$ for constant input frequency $f_{in} = 3.7$

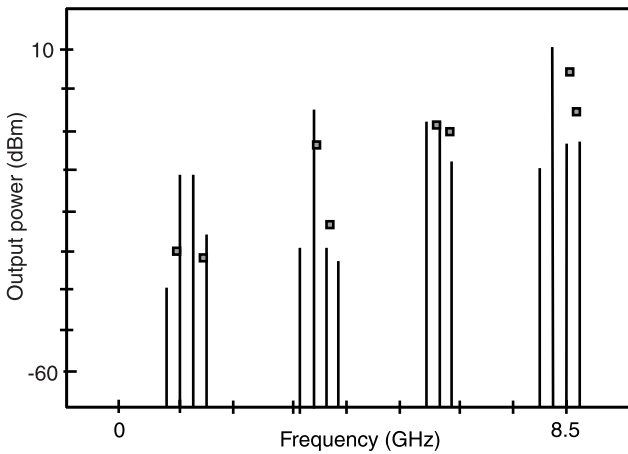


Figure 5.20 Self-oscillating mixer regime of the frequency doubler with experimental points super-imposed. There are two independent fundamentals: one provided by the input generator ($f_{in} = 3.7$ GHz) and the other due to the self-oscillation ($f_a = 1.9$ GHz).

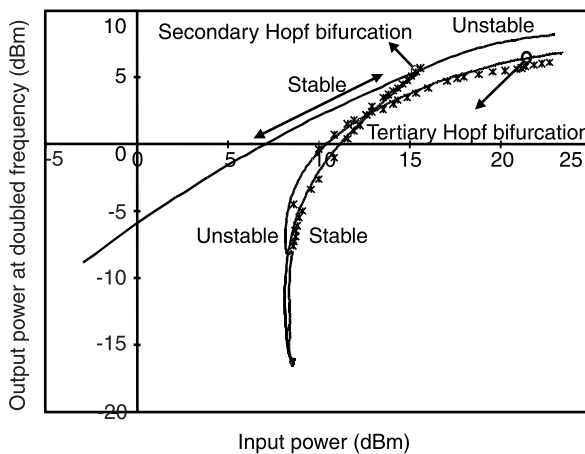


Figure 5.21 Bifurcation diagram of the frequency doubler with input frequency $f_{in} = 3.7$ GHz. The results of in-house (—) and commercial (*) harmonic balance can be compared. The subcritical Hopf bifurcation gives rise to a quasiperiodic regime at the fundamental frequencies $f_{in} = 3.7$ GHz and $f_{in} \cong 1.9$ GHz. An hysteresis phenomenon is observed in the transformation from the periodic regime to the quasiperiodic regime, and vice versa. (From: [32]. © 1998 IEEE. Reprinted with permission.)

GHz. The bifurcation diagram has been traced using the auxiliary-generator technique. Simulations have been performed with in-house and commercial harmonic balance for accuracy comparison. As can be seen, the Hopf bifurcation (taking place for $P_{in} = 16$ dBm) is of subcritical type. The stability of the different regions of the solution paths is indicated in the figure. From the branching point, the path corresponding to the periodic solution is unstable. The subcritical Hopf bifurcation gives rise to an hysteresis phenomenon. When increasing the input power from $P_{in} < 7$ dBm, the self-oscillation appears at $P_{in} = 16$ dBm. However, when decreasing the input power from $P_{in} > 16$ dBm, the oscillation persists until the input power is reduced below $P_{in} = 7$ dBm, where a jump takes place to the periodic-solution path.

To determine the safe operation region of the frequency doubler in terms of input-generator power and frequency, the Hopf-bifurcation locus is traced in the plane defined by these two parameters (ω_{in} , P_{in}). The locus, given by (5.4) has been calculated using commercial software (see Figure 5.22). The amplitude of the auxiliary generator is set to a very small value $A_{AG} = \varepsilon$. Then, the input-generator frequency f_{in} is swept, optimizing for each f_{in} the input-generator amplitude E_{in} and the autonomous frequency $f_{AG} \equiv f_a$ to fulfill the nonperturbation condition $Y = 0$ [see Figure 2.12(b)]. The turning points are circumvented through parameter switching, sweeping in the regions of difficult convergence the input-generator amplitude E_{in} and optimizing f_{in} and $f_{AG} \equiv f_a$. It is also possible to sweep f_{AG} and optimize E_{in} and f_{in} .

The Hopf locus provides the border between the region of stable operation as frequency doubler and the region with self-oscillating behavior (quasi-periodic regime). Although it has not been analyzed here, similar kinds of behavior can be expected in other forced circuits, with parametric instability, such as power amplifiers. The term parametric refers to the fact that the circuit does not oscillate in the absence of input power (see Figure 5.21). Instead, the self-oscillation starts in the nonlinear regime obtained through the increment of the input-generator power (circuit parameter). The linearization of the circuit equations about this nonlinear regime may show the existence of a frequency interval with negative resistance giving rise to a possible onset of a subharmonic (see Example 4.4) or autonomous frequency if the necessary instability conditions are fulfilled. See the Nyquist plots of Figure 5.19.

5.6 Global Behavior of Phase-Locked Loops

Systems containing several individual circuits, such as phase-locked loops [33–35], can also exhibit bifurcations when one or more parameters vary [36].

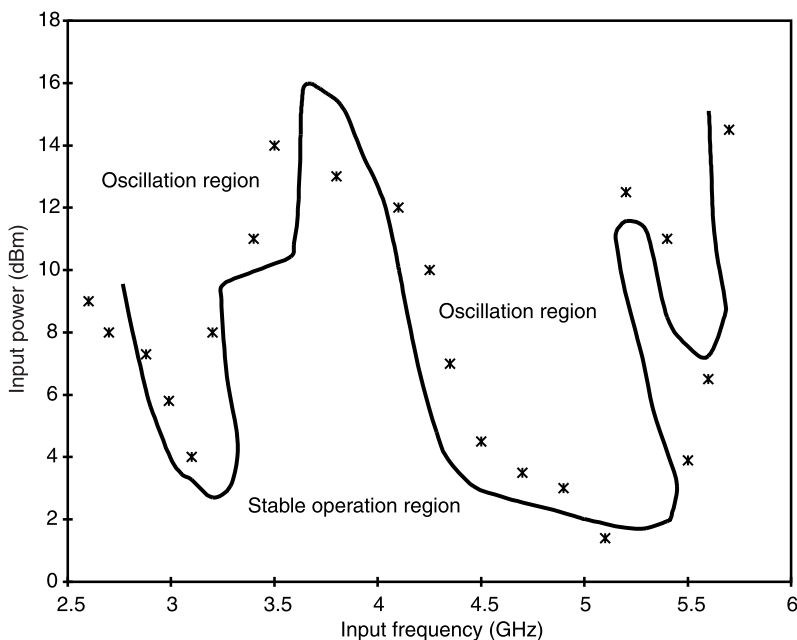


Figure 5.22 Hopf bifurcation locus delimiting the stable and unstable operation regions of the frequency doubler of Figure 5.19. It has been obtained using commercial harmonic balance. Experimental points have been superimposed. (From: [32]. © 1998 IEEE. Reprinted with permission.)

As in the case of circuits, these bifurcations delimit their operation ranges. As an example, the global stability of phase-locked loops is analyzed in this section.

5.6.1 General Equations of the Phase-Locked Loop

As shown in Figure 5.23, a general phase-locked loop is made up of a nonlinear phase detector, a loop filter, a VCO and a frequency divider [34]. Using normalized variables, the input voltage $v_i(t)$ is assumed to be a sinusoidal waveform, given by

$$v_i(t) = \cos(\theta_i(t)), \text{ with } \theta_i(t) \in S^1 \text{ and } \frac{d\theta_i}{dt} = \omega_i \quad (5.12)$$

while the VCO output voltage has the form:

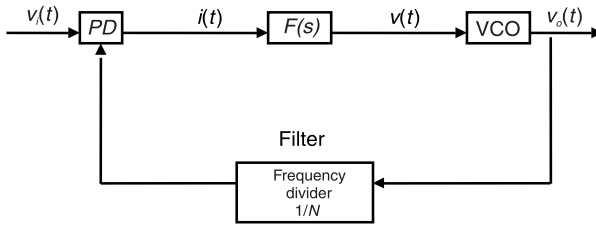


Figure 5.23 General schematic of the phase-locked loop.

$$v_o(t) = \cos(\theta_o(t)), \quad \theta_o(t) \in S^1 \quad (5.13)$$

The output signal of the phase detector $p(t)$ (either a current or a voltage) is a nonlinear function of the input-signal phase θ_i and the output-signal phase θ_o , divided by N :

$$p(t) = p\left(\theta_i(t), \frac{\theta_o(t)}{N}\right) \quad (5.14)$$

On the other hand, the VCO oscillates at a frequency depending on the control voltage $v(t)$:

$$\dot{\theta}_o(t) = f_{VCO}(v(t)) \quad (5.15)$$

This frequency is often assumed to be a linear function of the control voltage $v(t)$. However, in a more realistic analysis, the saturation of the VCO frequency must be taken into account. The phase-detector output signal $p(t)$ and the control voltage $v(t)$ are related by the filter transfer function $F(s)$:

$$V(s) = F(s)P(s) \quad (5.16)$$

The combination of (5.14) to (5.16) provides the Laplace form of the general equation governing the dynamics of the phase-locked loop:

$$s\theta_o = f_{VCO}\left(F(s)P\left(\theta_i, \frac{\theta_o}{N}\right)\right) \quad (5.17)$$

The resolution of (5.14) to (5.17) through time-domain integration provides the transient and steady-state behavior of the phase-locked loop.

5.6.2 Parametric Analysis of the Phase-Locked Loop

The parametric analysis of phase-locked loops is usually carried out in terms of the reference frequency ω_i and the loop gain k . This analysis is particularized here to two different kinds of loops: the type I loop, with one pole at the origin in the closed-loop transfer function of the linearized system, and the type II loop, with two poles at the origin in this transfer function of the linearized system [29–31]. This particularization is convenient because of the qualitative differences in the behavior of each type of phase-locked loop.

5.6.2.1 Type I Phase-Locked Loop with a Sinusoidal Phase Detector

In this section, (5.14) to (5.17) are particularized to the case of a type I phase-locked loop with a sinusoidal phase detector and division order $N=1$. The filter transfer function is

$$F(s) = \frac{1 + \tau_2 s}{1 + \tau_1 s} \quad (5.18)$$

with τ_1 and τ_2 being constants. As has already been said, the output voltage of the phase detector is modeled with a sinusoidal function of the phase error ϕ :

$$v_d = k_d \sin(\phi) \quad (5.19)$$

with

$$\phi(t) = \theta_o(t) - \theta_i(t) \quad (5.20)$$

The VCO has a linear characteristic, given by

$$\frac{d\theta_o(t)}{dt} = \omega_o + k_v y(t) \quad (5.21)$$

where ω_o is the free-running oscillation frequency and $y(t)$ is the VCO control voltage. The output phase θ_o of the VCO can be expressed as a function of the phase error $\phi(t)$ and the reference frequency ω_i as $\theta_o(t) = \omega_i t + \phi(t)$. The

equation ruling the behavior of the phase-locked loop is easily obtained combining (5.18) to (5.21):

$$\frac{d^2\phi}{dt^2} + \frac{(k\tau_2 \cos(\phi) + 1)}{\tau_1} \frac{d\phi}{dt} + \frac{k \sin(\phi)}{\tau_1} + \frac{\omega_o - \omega_i}{\tau_1} = 0 \quad (5.22)$$

where $k = k_v \cdot k_d$. It is a nonlinear differential equation of second order in ϕ . For phase-locked operation, the phase error must have a constant value ϕ_o . Thus, the phase-locked solutions of (5.22) are obtained from

$$\sin(\phi_o) = \frac{\omega_i - \omega_o}{k} \quad (5.23)$$

Provided that the right-hand side of the above equation has magnitude smaller than unity, there are two possible solutions, given by

$$\phi_o = \arcsin\left(\frac{\omega_i - \omega_o}{k}\right) \quad (5.24)$$

$$\phi'_o = \pi - \phi_o \quad (5.25)$$

Each of the two solutions ϕ_o and ϕ'_o constitutes an equilibrium point of (5.22). For the stability analysis of each equilibrium point, it is convenient to split the second-order differential equation (5.22) into two first-order equations through the variable change $z = \frac{d\phi}{dt}$. Then the Jacobian matrix of the linearized system is given by

$$[Df]_o = \begin{bmatrix} 0 & 1 \\ \frac{-k}{\tau_1} \cos(\phi_o) & \frac{-k\tau_2}{\tau_1} \cos(\phi_o) - \frac{1}{\tau_1} \end{bmatrix} \quad (5.26)$$

The phase error ϕ_o in (5.26) is alternatively particularized to each of the two equilibrium points ϕ_o and ϕ'_o . For a stable equilibrium point, the two eigenvalues of the above Jacobian matrix must have a negative sign. Due to (5.25) and the form of dependence on ϕ_o of (5.26), one of the equilibrium points will be stable while the other will be unstable. In [36–38], the stable phase-locked

solution is called *node* and will be denoted here as ϕ_{oN} . The unstable phase-locked solution is a saddle and will be denoted here as ϕ_{oS} .

Equation (5.24) is not always solvable due to the bounded value of the sinus function $-1 \leq \sin(\phi_o) \leq 1$. The limit condition of existence of phase-locked solutions is given by

$$\sin(\phi_o) = \frac{\omega_i - \omega_o}{k} = \pm 1 \quad (5.27)$$

with $k = k_v \cdot k_d$.

In this limit situation, the two phase-locked solutions take the same value $\phi_{oN} = \phi_{oS} = \pm \frac{\pi}{2}$. Thus, the existence of phase-locked solutions will depend on the values of the reference frequency ω_i , the free-running oscillation frequency ω_o and the loop gain k . Actually, in the two-parameter plane (ω_i, k) , the phase-locked solutions will be located inside the locus defined by the straight line:

$$1 = \frac{\omega_i - \omega_o}{k} \Rightarrow k = \omega_i - \omega_o \quad (5.28)$$

where it is assumed that the VCO can only have oscillation frequencies above its free-running value ω_o . The straight line defines the border at which the node- and saddle-type equilibrium points collide, taking the same value $\phi_{oN} = \phi_{oS} = \frac{\pi}{2}$. The straight line constitutes the locus of saddle-node bifurcations [see Figure 5.24(a)]. It is equivalent to the Arnold tongue of synchronized circuits. However, because it has been assumed that the VCO can only have oscillation frequencies above its free-running value ω_o , only one half of the Arnold tongue, split by a vertical axis at $\omega_i = \omega_o$, will exist. Outside the saddle-node bifurcation locus, there is no phase-locked behavior because of the inexistence of solutions of (5.23) and the steady state is given by a time-varying phase error $\phi(t)$.

The steady-state solutions of the phase-locked loop can be represented in the phase space defined by ϕ and $\dot{\phi}$ (see Figure 5.25). The phase-locked solutions (ϕ_{oN} and $\phi_{oS} = \pi - \phi_{oN}$), fulfilling $\dot{\phi} = 0$, lie on the horizontal axis $\dot{\phi} = 0$. The saddle solution ϕ_{oS} is not represented in the figure. Due to its instability, solutions obtained through time-domain integration never evolve to it. The unlocked solutions exhibit big variations of $\dot{\phi}$ versus ϕ and are not bounded in terms of $\dot{\phi}$ when an unbounded phase axis is considered (

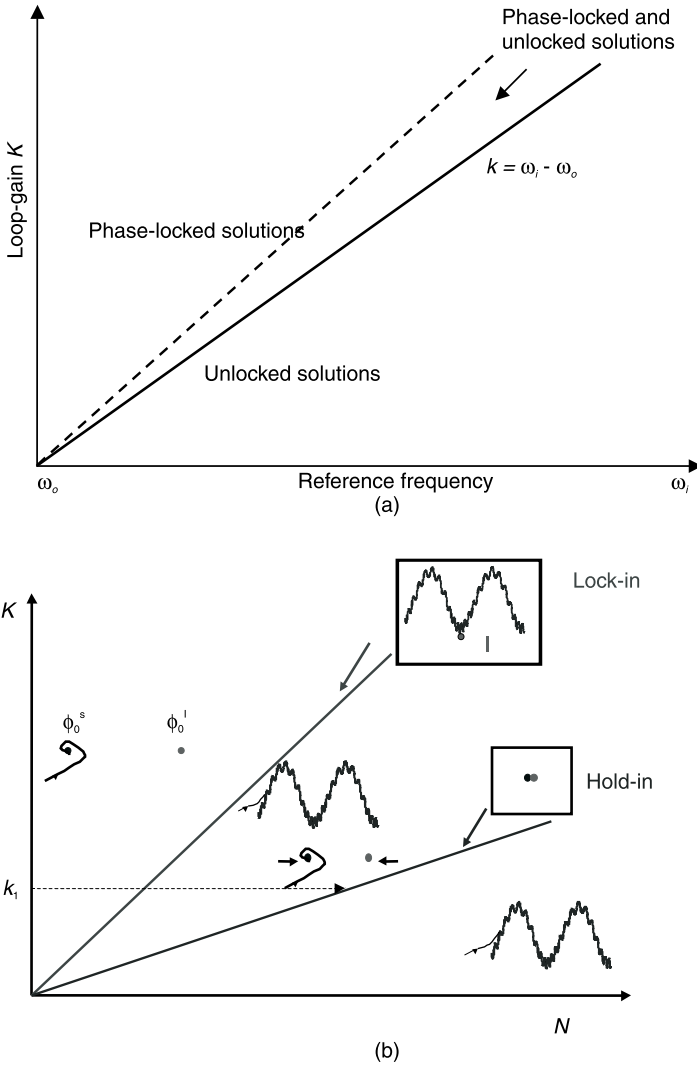


Figure 5.24 Region of phase-locked solutions of a type I PLL in the plane $k - \omega_r$. (a) Bifurcation loci. The saddle-node bifurcation locus provides the hold-in border, while the saddle-connection locus (dashed line) provides the lock-in border. Between the two loci, locked and unlocked solutions coexist, which gives rise to hysteresis. (b) Sketch of the different solutions and general bifurcation behavior.

$-\infty \leq \phi \leq \infty$). These time-varying solutions become, however, bounded in the cylindrical space in which the phase variation is restricted to the interval

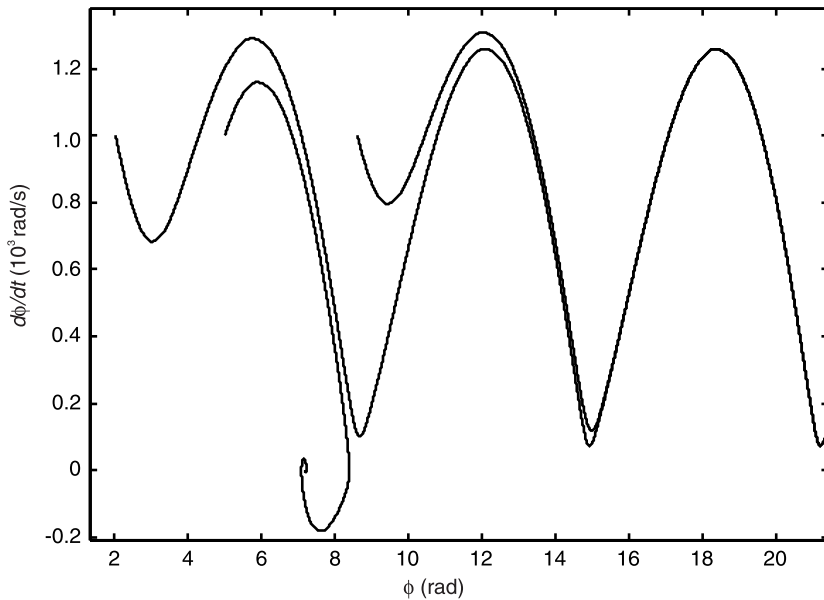


Figure 5.25 Coexistence of rotations and phase-locked solutions in a type I PLL for given parameter values (ω_p, k) . The phase-locked solutions lie on the horizontal axis $\dot{\phi} = 0$. (From: [39]. © 2001 IEEE. Reprinted with permission.)

$[0, 2\pi]$. This is equivalent to considering the folding of the phase plane $(\phi, \dot{\phi})$ over itself to give rise to a cylinder. The unlocked solutions (periodic in ϕ with period 2π) are called rotations $\phi_r(t)$ [36–38].

Outside the saddle-node bifurcation locus of Figure 5.24(a), only rotations $\phi_r(t)$ are possible. However, inside the locus, there is a region in which both phase-locked solutions and rotations coexist. This is, in fact, the case of Figure 5.25, where, as has already been said, the phase-locked solutions $(\phi_{oN}$ and $\phi_{oS} = \pi - \phi_{oN})$ lie on the horizontal axis. Depending on the initial conditions, the system will converge to either the stable phase-locked solution ϕ_{oN} or the stable rotation $\phi_r(t)$ (see Figure 5.25). Explanation for this comes from the fact that the rotation solutions are actually generated inside the region delimited by the saddle-node bifurcation locus. The rotation solutions appear at saddle connections (see Section 4.3.1), occurring at the saddle equilibrium points ϕ_{oS} [36–38]. As studied in Chapter 4, saddle connections are a particular type of global bifurcation. Global bifurcations do not only depend on the local stability properties of a given steady-state solution, but also on the global configuration of its stable and unstable manifolds. In the case of saddle connections, the stable or unstable manifolds intersect, which may give rise to a limit

cycle or to a rotation solution (in systems described in terms of phase, like in the phase-locked loop).

In the parameter plane (ω_i, k) , a second bifurcation locus exists (in addition to the saddle-node bifurcation locus) providing the parameter values at which saddle connections take place. This is sketched in Figure 5.24(a). Let parameter values in the plane region close to the vertical axis, in which only phase-locked solutions exist ϕ_{oNS} , be considered initially. As the input frequency ω_i is increased, for constant gain value [see Figure 5.24(b)], the saddle-connection locus is traversed for a certain value of this frequency. The global bifurcation gives rise to the generation at the saddle solution of a stable rotation solution $\phi_r(t)$. Both solutions coexist from this input frequency value. However, the system will remain phase-locked in spite of the crossing of the saddle-connection locus. The observation of one stable solution or another depends on the initial conditions, and these conditions in the increasing frequency sense are in the neighborhood of the phase-locked solution. As the input frequency continues to increase, the crossing of the saddle-node bifurcation locus in Figure 5.24 indicates the collision and subsequent destruction of the node solution and the saddle solution. Thus, no phase-locked solutions can exist beyond the saddle-node bifurcation locus.

Decreasing the frequency increment $\Delta\omega = \omega_i - \omega_o$ from a value beyond the saddle-node bifurcation locus (or increasing the loop gain k), rotation solutions $\phi_r(t)$ continue to exist when the saddle-node bifurcation locus is traversed [see Figure 5.24(b)]. In fact, the saddle-node bifurcation is (in this system) a bifurcation from dc regime, so it does not affect the rotation. Again, between the saddle-connection locus and the saddle-node bifurcation locus, phase-locked and unlocked stable solutions coexist. However, in the decreasing frequency sense, the system evolution is conditioned by initial values in the neighborhood of the unlocked rotation solution $\phi_r(t)$. The reduction of the input frequency alters and displaces this rotation solution until it collides with the saddle equilibrium point $\phi_r(t)$ [see Figure 5.24(b)]. When this collision takes place, the rotation solution vanishes. For frequencies below this value, only phase-locked solutions are possible, so the system locks. This hysteresis phenomenon is well known to phase-locked loop designers. In fact, for constant loop gain k , the saddle-node bifurcation provides the limit of hold-in or synchronization. The saddle connection provides the limit of lock-in or capture.

The analysis carried out in the above example has been particularized to the case of a type I loop (containing one pole at the origin in closed-loop equations) with idealized components (a sinusoidal phase detector and linear model of the VCO). To continue with the study, the case of the commonly employed type II loops (containing two poles at the origin in the closed-loop transfer

function) and more realistic models for the loop components will be considered.

5.6.2.2 Type II Phase-Locked Loop with Realistic Models for the Loop Elements

In this section, the parametric behavior of type II phase-locked loops is analyzed. The study will start with simplified models for the loop elements, increasing, as the section advances, the accuracy of the models and, correspondingly, the accuracy of the results. Initially, the simple case of a loop filter with the transference function $F(s) = \frac{\tau_2 s + 1}{\tau_1 s}$ will be considered. The particularization of (5.22) to this transfer function, provides the result:

$$\frac{d^2\phi}{dt^2} + \frac{k\tau_2 \cos(\phi)}{\tau_1} \frac{d\phi}{dt} + \frac{k \sin(\phi)}{\tau_1} = 0 \quad (5.29)$$

In this case, phase-locked solutions must simply fulfill $\sin(\phi) = 0$. Thus, the phase-locked solutions are given by $\phi_o = 0$ and $\phi'_o = \pi$. In most cases, the solution $\phi_o = 0$ will be the node one (i.e., $\phi_{oN} = 0$). Because whatever the parameter values, the equation to be fulfilled by the phase-locked solutions is $\sin(\phi) = 0$ (and this can always be solved), phase-locked solutions exist all over the two-parameter plane (ω_i, k) and the saddle-node bifurcation locus lies on the horizontal axis $k = 0$. This should be true for type II phase-locked loops of any order. However, the practical observations of PLL designers contradict this result. In fact, the location at the origin of a pole of the loop filter $F(s)$ is an over-simplification of the system. In practice, limitations in the gain of the active filter (which cannot be infinite at dc) and parasitics give rise to a slight shift of the pole to the left-hand side of the complex plane. On the other hand, the saturation effects in the VCO frequency versus the control voltage will make phase locking impossible beyond a certain frequency increment $\Delta\omega = \omega_i - \omega_o$. Actually, (5.21) is only valid for a certain frequency interval because of the limitation in the possible oscillation frequencies of the VCO.

Coming back to the ideal case of a pole located at the origin, phase-locked solutions of (5.29) will exist all over the parameter plane (ω_i, k) . However, unlocked solutions of rotation type $\phi_r(t)$ will also coexist with them in a certain parameter region relatively close to the saddle-node bifurcation locus in similar way to the loci of Figure 5.24(a). In this region, convergence to rotation solutions can be obtained for some initial conditions. Another physical problem arises here because these rotation solutions for a filter pole located at the origin behave as stability centers with their amplitude depending on

the initial conditions. This nonphysical situation is also due to the filter idealization.

In all the above analysis [Section 5.6.2.1 and (5.29)], the output voltage of the phase detector has been modeled with a sinusoidal function of the phase error [see (5.19)]. When using this model for the phase detector, no harmonic components of the reference frequency ω_i are present in the loop in phase-locked conditions. However, in a more accurate model of the frequency mixer commonly employed as phase detector, both the phase-difference and the phase-addition terms must be considered; that is,

$$v_d = k_d [\sin(\theta_i - \theta_o) + \sin(\theta_i + \theta_o)] \quad (5.30)$$

When using (5.30), the output of the phase detector in phase locked conditions will be

$$v_d(t) = k_d [\sin(\phi_o) + \sin(2\omega_i t - \phi_o)] \quad (5.31)$$

where ϕ_o is a constant phase shift. Thus, in phase-locked conditions, the phase-detector output is not a constant voltage, but a periodic voltage at twice the reference frequency $2\omega_i$. This time-varying signal passes through the loop filter, which provides attenuation of harmonic component $2\omega_i$. However, this frequency component cannot be completely eliminated and is responsible for the frequency modulation of the VCO output signal [see (5.21)]. This frequency modulation is called incidental FM [33]. Thus, when considering the presence of spurious frequency components in the PLL, the phase-locked solutions are no longer given by equilibrium points. Instead, they become limit cycles with very small amplitudes.

To illustrate this, the simulation of a type II third-order phase-locked loop with variable division order from $N=2,100$ to $N=3,000$ is presented in the following. It is a 2–3-GHz frequency synthesizer. The loop-filter transfer function given by

$$F(s) = \frac{\tau_2 s + 1}{\tau_1 s (\tau_3 s + 1)} \quad (5.32)$$

For a realistic simulation [39], a small shift to the left-hand side of the complex plane of the pole ideally located at the origin [see (5.32)] will be considered. The shift is in correspondence with the limited filter gain at dc and the parasitics of the filter elements. As in the case of type I loops (see Figures 5.24 and

5.25), there is a region of coexistence of phase-locked solutions and rotations. The two types of solution can be appreciated in the simulation of Figure 5.26, where the model (5.30) has been used for the phase detector. As can be seen, the phase-locked solutions become small-amplitude limit cycles and the rotation solutions (periodic in the sinusoidal model) become quasiperiodic for (5.30). Although there is a qualitative change in the steady-state solutions, the bifurcation behavior is, in general terms, the same as the one already studied.

In the parametric analysis of a phase-locked loop (as the one studied here) containing a frequency divider in the feedback branch, the reference frequency ω_i can be replaced with the division order N . Thus, the bifurcation diagram of the realistic type II loop in the two-parameter plane (N, k) is shown in Figure 5.27. The hold-in border, given by the saddle-node bifurcation locus, is close to the horizontal axis $k = 0$ because of the proximity to the origin of one of the filter poles. The almost vertical section of this locus is due to the saturation effects in the VCO. The saddle-connection curve, providing the lock-in border, has also been traced. In the region between the two loci, both phase locked and unlocked solutions can be obtained, depending on the initial conditions.

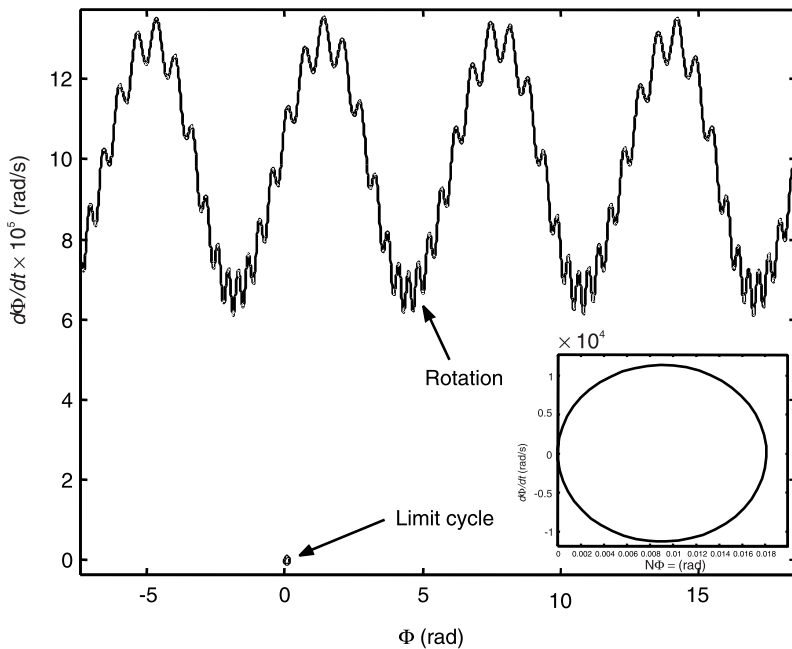


Figure 5.26 Coexistence of phase-locked solutions and rotations in a phase-locked loop with incidental FM. The phase detector model is given by (5.30). (From: [39]. © 2001 IEEE. Reprinted with permission.)

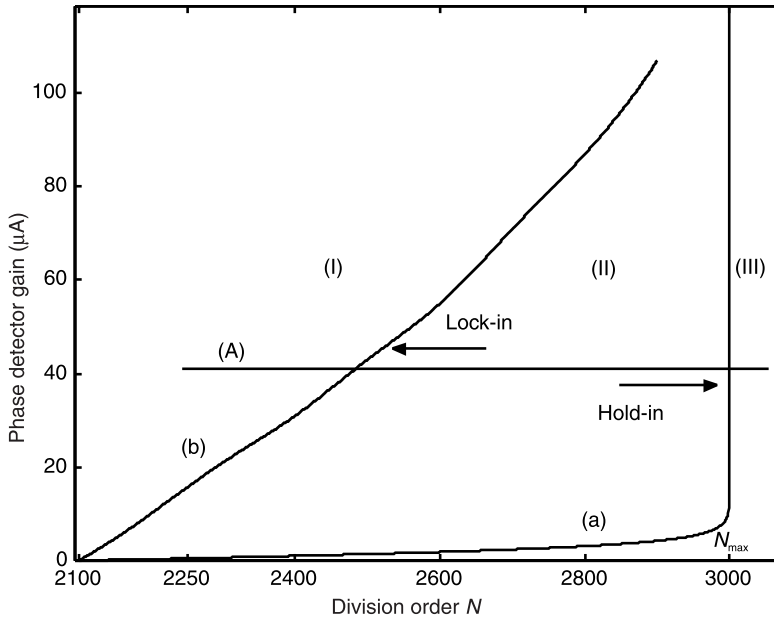


Figure 5.27 Bifurcation loci of a type II phase-locked loop.

5.6.3 Use of the Poincaré Map to Determine the Operating Bands of the Phase-Locked Loop

A convenient tool for the bifurcation detection in phase-locked loops is the Poincaré map. For its application, the steady-state solution is sampled at integer multiples of the period of the reference frequency $T_i = 1/f_i$. As the parameter varies, the system evolution is followed by using each solution as the initial condition for the next parameter value. The map is traced in terms of the rotation number given by the ratio between the loop output frequency $\theta_o(t)$ and the reference frequency ω_i (i.e., $r = \frac{\theta_o(t)}{\omega_i}$). For phase-locked behavior, this

number must take a constant value.

The simulation of Figure 5.28 corresponds to a phase-locked loop based on the use of a sampling phase detector [40, 41]. The step-recovery diode in this detector enables the multiplication of the crystal-oscillator frequency ω_x by a very high order M . The output frequency $M\omega_x$, acting like the reference frequency, mixes at a Schottky diode with the divider output frequency. The increase in the value of the reference frequency allows reducing the order N of

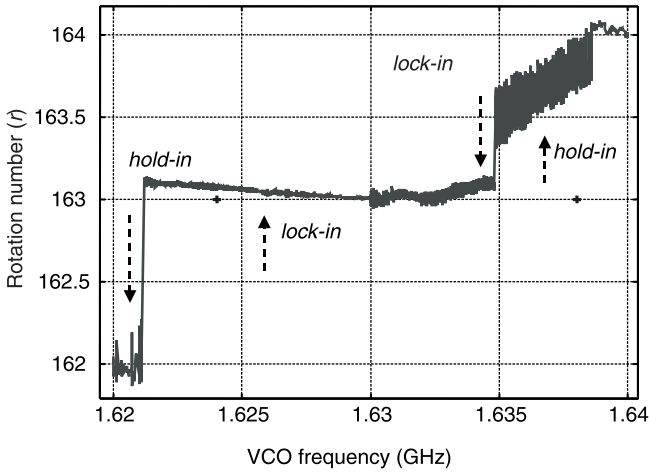


Figure 5.28 Application of the Poincaré map for bifurcation calculation in a phase-locked loop. The solution for a given value of the parameter is employed as the initial condition for the next value of the parameter.

the frequency divider, and thus better phase-noise performance can be obtained [40]. The high spurious content at the output of the phase detector requires narrowband filtering. The aim of the simulation of Figure 5.28 is to determine the VCO frequency range for which phase-locking about the harmonic component $M = 163$ of the crystal-oscillator frequency can be achieved. The rotation number has been defined as

$$r = \frac{\theta_o(t)}{\omega_i} \quad (5.33)$$

As can be seen, the rotation number takes the constant value $r = 163$ in a frequency interval, limited at each side by two different bifurcations. One of them is a saddle-node bifurcation, while the other is a saddle connection, in agreement with Figure 5.24. The two bifurcations give rise to hysteresis. When starting from an unlocked solution, at the left-hand side of the diagram, phase-locking is due to a saddle connection (indicated in the figure as lock-in). Using the final solution for a given VCO frequency as the initial condition for the next frequency value, the phase-locked solution is maintained until, at the right-hand side of the diagram, a saddle-node bifurcation occurs (indicated in the figure as hold-in). Starting now from the unlocked solution at the right-hand side of the diagram and decreasing the VCO frequency, phase

locking will be due to a saddle connection. As shown in the diagram, the existence of the two different bifurcations gives rise to hysteresis between the transformations from the phase-locked regime to the unlocked regime and the unlocked regime to the phase-locked regime. If the frequency continues to be decreased, the unlocking will not take place until the saddle-node bifurcation, at the left-hand side of the diagram, is encountered. Thus, hysteresis is observed at both ends of the frequency interval with phase-locked behavior.

References

- [1] Wiggins, S., *Introduction to Applied Nonlinear Dynamical Systems and Chaos*, New York: Springer-Verlag, 1990.
- [2] Ioos, G., and D. D. Joseph, *Elementary Stability and Bifurcation Theory*, 2nd ed., New York: Springer-Verlag, 1990.
- [3] Thompson, J. M. T., and H. B. Stewart, *Nonlinear Dynamics and Chaos*, New York: John Wiley & Sons, 1986.
- [4] Parker, T. S., and L. O. Chua, *Practical Algorithms for Chaotic Systems*, Berlin, Germany: Springer-Verlag, 1989.
- [5] Palazuelos, E., et al., "Hysteresis Prediction in Autonomous Microwave Circuits Using Commercial Software. Application to a Ku Band MMIC VCO," *IEEE J. Solid-State Circuits*, Vol. 33, No. 8, Aug. 1998, pp. 1239–1243.
- [6] Kurokawa, K., "Some Basic Characteristics of Broadband Negative Resistance Oscillator Circuits," *Bell Syst. Tech. J.*, July–Aug. 1969, pp. 1937–1955.
- [7] Sierra, F., and J. Perez, "Analysis of Harmonic Injection Dividers with Three Terminal Dividers," *IEE Proc.*, Vol. 135, Pt. H, No. 2, April, 1988, pp. 70–74.
- [8] Zhang, X., et al., "A Study of Subharmonic Injection for Local Oscillators," *IEEE Microwave Guided Wave Lett.*, Vol. 2, No. 3, March 1992, pp. 97–99.
- [9] Quéré, R., et al., "Large Signal Design of Broadband Monolithic Frequency Dividers and Phase-Locked Oscillators," *IEEE Trans. Microwave Theory Tech.*, Vol. 41, No. 11, Nov. 1993, pp. 1928–1938.
- [10] Ngoya, E., et al., "Steady State Analysis of Free or Forced Oscillators by Harmonic Balance and Stability Investigation of Periodic and Quasiperiodic Regimes," *Int. J. Microwave Millimetric-Wave Computer Aided Eng.*, Vol. 5, No. 3, March 1995, pp. 210–223.
- [11] Bomford, M., "Selection of Frequency Dividers for Microwave PLL Applications," *Microwave J.*, Nov. 1990, pp. 159–167.
- [12] Rauscher, C., "Regenerative Frequency Division with a GaAs FET," *IEEE Trans. Microwave Theory Tech.*, Vol. 32, No. 11, Nov. 1984, pp. 1461–1468.

-
- [13] Kudszus, S., et al., "94/47-GHz Regenerative Frequency Divider MMIC with Low Conversion Loss," *IEEE J. Solid-State Circuits*, Vol. 35, No. 9, Sept. 2000, pp. 1312–1317.
- [14] Mullrich, J., et al., "SiGe Regenerative Frequency Divider Operating Up to 63 GHz," *Elec. Lett.*, Vol. 35, No. 20, Sept. 1999, pp. 1730–1731.
- [15] Angelov, I., et al., "48/24 GHz and 20/10 GHz Regenerative Frequency Dividers," *Microwave Symp. Digest, 1996, IEEE MTT-S*, Vol. 2, 1996, pp. 971–974.
- [16] Rizzoli, V., and A. Neri, "State of the Art and Present Trends in Non-Linear Microwave CAD Techniques," *IEEE Trans. Microwave Theory Tech.*, Vol. 36, No. 2, Feb. 1988, pp. 343–365.
- [17] Suárez, A., et al., "Large Signal Design of Broadband Monolithic Frequency Dividers," *IEEE MTT Symp.*, Albuquerque, NM, June 1992, pp. 1595–1598.
- [18] Suárez, A., et al., "Stability Analysis of Analog Frequency Dividers in the Quasiperiodic Regime," *IEEE Microwave Guided Wave Lett.*, Vol. 4, No. 5, May 1994, pp. 138–140.
- [19] Morales, J., A. Suárez, and R. Quéré, "Accurate Determination of Frequency Dividers Operating Bands," *IEEE Microwave Guided Wave Lett.*, Vol. 6, No. 1, Jan. 1996, pp. 46–48.
- [20] Suárez, A., J. Morales, and R. Quéré, "Synchronization Analysis of Autonomous Microwave Circuits Using New Global Stability Analysis Tools," *IEEE Trans. Microwave Theory Tech.*, Vol. 46, No. 5, May 1998, pp. 494–504.
- [21] Suárez, A., et al., "Broadband Design and Simulation of Frequency Dividers in the Millimetric Band," *European Microwave Conf.*, Madrid, Spain, Sept. 1993, pp. 777–780.
- [22] Adler, R., "A Study of Locking Phenomena in Oscillators," *Proc. IRE*, June 1946; *IEEE Trans. Microwave Theory Tech.*, Vol. 21, No. 10, Oct. 1973, pp. 1380–1385.
- [23] Wang, G. C., et al., "A Low Cost DBS Low Noise Block Downconverter with a DR Stabilized MESFET Self-Oscillating Mixer," *IEEE MTT-S Digest*, 1994, pp. 1447–1450.
- [24] Förg, P. N., and J. Freyer, "Ka-Band Self-Oscillating Mixers with Schottky Baritt Diodes," *Elec. Lett.*, Vol. 16, Oct. 23, 1980, pp. 827–829.
- [25] Dixon, S., and H. Jacobs, "Millimeter-Wave InP Image Line Self-Mixing Gunn Oscillator," *IEEE Trans. Microwave Theory Tech.*, Vol. 29, No. 9, Sept. 1981, pp. 404–407.
- [26] Claassen, M., and U. Güttich, "Conversion Matrix and Gain of Self-Oscillating Mixers," *IEEE Trans. Microwave Theory Tech.*, Vol. 39, No. 1, Jan. 1991, pp. 25–30.
- [27] Sironen, M., Y. Qian, and T. Itoh, "A Dielectric Resonator Second Harmonic Quasi-optical Self-Oscillating Mixer for 60 GHz Applications," *IEEE MTT-S Digest*, Vol. 1, 1999, pp. 139–142.
- [28] Morales, J., et al., "Global Stability Analysis of Self-Oscillating Mixers," *European Microwave Conf.*, Bologna, Italy, Vol. 2, 1994, pp. 139–142.
- [29] Rizzoli, V., D. Masotti, and F. Mastri, "Computer-Aided Noise Analysis of Integrated Microwave Front-Ends," *IEEE MTT-S Digest*, Orlando, FL, May 1995, pp. 1561–1564.

- [30] Basu, S., S. A. Maas, and T. Itoh, "Stability Analysis of a Microwave Frequency Doubler," *IEEE Trans. Microwave Theory Tech.*, Vol. 43, No. 12, Dec. 1995.
- [31] Sandberg, I. W., and G. J. J. van Zyl, "Designing Periodically Driven Varactor Circuits with Guaranteed Stability," *IEEE Microwave Guided Wave Lett.*, Vol. 9, No. 6, June 1999, pp. 230–232.
- [32] Iglesias, V., A. Suárez, and J. L. García, "New Technique for the Determination Through Commercial Software of the Stable-Operation Parameter Ranges in Nonlinear Microwave Circuits," *IEEE Microwave and Guided Wave Lett.*, Vol. 8, No. 12, Dec. 1998, pp. 424–426.
- [33] Rohde, U. L., *Microwave and Wireless Synthesizers*, New York, John Wiley & Sons, 1997.
- [34] Gardner, F. M., *Phaselock Techniques*, New York: John Wiley & Sons, 1966.
- [35] Manassewitsch, V., *Frequency Synthesizers: Theory and Design*, New York: John Wiley & Sons, 1987.
- [36] Endo, T., and L. O. Chua, "Chaos from Phase-Locked Loops," *IEEE Trans. Circuits Syst.*, Vol. 35, No. 8, Aug. 1988, pp. 987–1003.
- [37] Salam, F. M. A., and S. S. Sastry, "Dynamics of the Forced Josephson-Junction Circuit: The Regions of Chaos," *IEEE Trans. Circuits Syst.*, Vol. 32, No. 8, Aug. 1985, pp. 784–796.
- [38] Odyniec, M., and L. O. Chua, "Josephson-Junction Circuit Analysis Via Integral Manifolds," *IEEE Trans. Circuits Syst.*, Vol. 30, No. 5, May 1983, pp. 308–320.
- [39] Sancho, S., A. Suárez, and T. Fernández, "Nonlinear Dynamics of Microwave Synthesizers: Stability and Noise," *IEEE Trans. Microwave Theory Tech.*, Vol. 49, No. 10, Oct. 2001, pp. 1792–1803.
- [40] Sancho, S., et al., "Nonlinear Analysis of Microwave Synthesizer Based on a Sampling Phase Detector," *IEEE MTT-S Digest*, Phoenix, AZ, May 2001.
- [41] Gismoero, J., and J. Grajal, "9 GHz Phase Locked Oscillator Using a Sampling Phase Detector. Application to VSAT Local Oscillators (18–27 GHz)," 23rd European Microwave Conf., Madrid, Spain, Oct. 1983, pp. 784–786.

6

Bifurcation Routes to Chaos

Chapter 4 presented the most common types of bifurcations and illustrated them with examples. Chapter 5 showed how these bifurcations delimit the stable operation regions, in terms of the circuit parameters, of circuits such as VCOs, frequency dividers, and phase-locked loops. This chapter analyzes how the qualitative variations of the stability of the solutions, associated with bifurcations, may also lead to chaotic behavior. As has already been shown in Section 1.3.3.4, chaos is a particular kind of steady-state solution of nonlinear circuits, which is neither periodic, nor quasiperiodic [1–8]. Thus, it has a continuous spectrum, at least for some frequency intervals. The sensitive dependence on the initial conditions makes the time-evolution of the circuit solution unpredictable because solution starting from arbitrarily close points diverge exponentially (see Figure 1.12). When representing the chaotic steady-state solution in the space defined by the circuit state variables a fractal-dimension figure is obtained, which constitutes another characteristic of these solutions.

The particular sequence of bifurcations that precedes the chaotic behavior when a circuit parameter η is continuously modified constitutes a *route to chaos* [1, 5, 8]. This chapter will present the most usual routes to chaos. As will be seen, the onset of chaos may be the result of an infinite sequence of flip bifurcations. It may also be the result of two or more consecutive Hopf bifurcations. In other cases, the bifurcations leading to chaos are of global type, involving collisions in the phase space of stable solutions with unstable solutions of saddle type.

Due to the continuity of the spectrum of chaotic solutions, these solutions can only be simulated in time domain or through the transient-envelop

technique. Although some applications of chaotic solutions have been recently proposed in the bibliography, based on chaotic synchronization [9, 10] or on chaos control [11, 12], the main interest of the microwave circuit designer is usually in avoiding chaotic behavior. Harmonic balance, although unapplicable for the simulation of chaotic solutions, can be used to predict the circuit parameter values for the onset of chaos. This harmonic-balance prediction of chaotic behavior is mainly based on the detection of the initial bifurcations taking place in each route to chaos.

The aim of the chapter is to give some explanation for the formation of chaotic solutions in common microwave circuits and provide tools for chaos detection in harmonic-balance. The analyzed circuits are free-running oscillators, frequency dividers, frequency doublers, and self-oscillating mixers.

6.1 Homoclinicity

The constant (dc) solutions of a nonlinear circuit are given by the equilibrium points of the nonlinear differential equations, describing its behavior (see Section 1.1). For a saddle equilibrium point, the linearized circuit equations have eigenvalues with negative real parts and eigenvalues with positive real parts (Section 1.4.2), respectively associated with its stable and unstable manifolds (nonlinear equivalents of the eigenspaces). As shown in Section 4.3.1, under some circumstances, the stable and unstable manifolds may intersect (Section 4.3.1). Then a trajectory leaving the equilibrium point through the unstable manifold will return to it through the stable one, giving rise to a *homoclinic* orbit [1, 2, 4]. In a *transversal* intersection, the vectors tangent to the manifold at each point of the intersection can generate through linear combination all possible directions in the phase space [1]. The transversal intersection gives rise to a countable number of Smale horseshoes (stretching and folding in the Poincaré map, as shown in Section 1.5.3) and, thus, to chaotic behavior.

Homoclinic orbits may form through the collision of a limit cycle with a saddle equilibrium point as a parameter is modified. The formation of a transversal homoclinic orbit is often preceded by period doubling bifurcations [13]. In the case of a third-order system (in R^3), the theorem of Shil'nikov [14] establishes the conditions for the formation of a transversal homoclinic orbit (i.e., for the generation of chaos). The saddle equilibrium point (at which the homoclinic orbit is formed) must have a real eigenvalue $\gamma > 0$ and a pair of complex-conjugate eigenvalues $\sigma \pm j\omega$ with $\sigma < 0$. According to the theorem of Shil'nikov, the collision of a stable limit cycle with this equilibrium point gives rise to a transversal homoclinic orbit if the eigenvalues of the saddle equilibrium point fulfill $\gamma > |\sigma| > 0$.

Homoclinic chaos is often encountered in circuits exhibiting more than one equilibrium point, as in the case of using active elements with *N*-shape nonlinearity like Gunn and tunnel diodes. Homoclinic chaos has also been reported in type I phase-locked loops with a frequency-modulated input [15]. Example 6.1 shows the process of formation of a transverse homoclinic orbit in Chua's circuit with fulfillment of the theorem of Shil'nikov. It also presents the capabilities of harmonic balance for the detection of homoclinic chaos.

Example 6.1 Detection of a homoclinic orbit through harmonic balance

Homoclinic chaos has been thoroughly studied in Chua's circuit [4, 5]. Here a cubic nonlinearity implementation of this circuit has been used (Figure 6.1). It is a three-dimensional system, with the following nonlinear differential equations:

$$\begin{aligned} \frac{dv_{C1}}{dt} &= -\frac{v_{C1}}{C_1R} + \frac{v_{C2}}{C_1R} - \frac{i_{nl}(v_{C1})}{C_1R} = -\frac{v_{C1}}{C_1R} + \frac{v_{C2}}{C_1R} - \frac{av_{C1} + bv_{C1}^3}{C_1} \\ \frac{dv_{C2}}{dt} &= \frac{v_{C1}}{C_2R} - \frac{v_{C2}}{C_2R} - \frac{i_L}{C_2} \\ \frac{di_L}{dt} &= \frac{v_{C2}}{L} \end{aligned} \tag{6.1}$$

One of the equilibrium point of the above system is given by $v_{C1} = 0$, $v_{C2} = 0$ and $i_L = 0$. The other two are obtained by solving the following:

$$-\frac{v_{C1}}{R} = i_{nl}(v_{C1}) = av_{C1} + bv_{C1}^3 \Rightarrow v_{C1} = \pm \sqrt{\frac{-a - \frac{1}{R}}{b}} = \pm 1.5v \tag{6.2}$$

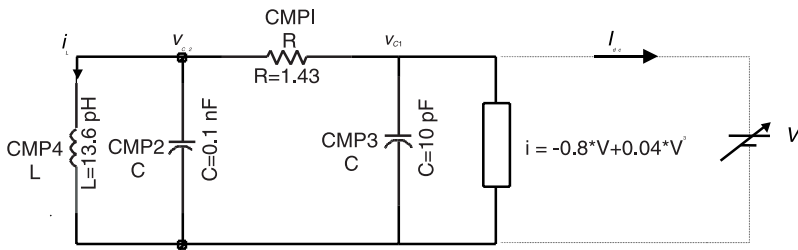


Figure 6.1 Chua's circuit with cubic nonlinearity. A dc auxiliary generator of voltage type has been introduced in the circuit for the calculation of the equilibrium points.

The three equilibrium points are thus $EP_1 = (v_{C1}, v_{C2}, i_L) = (0,0,0)$, $EP_2 = (15,0,-1.065)$, and $EP_3 = (-15,0,1.065)$. Chua's circuit is commonly analyzed as a function of two parameters, depending on the linear element values: $\alpha = \frac{C_2}{C_1}$ and $\beta = \frac{C_2}{LG^2}$. The value of the three equilibrium points does not change versus variations in the parameters (α, β) because these equilibrium points only depend on the nonlinear-element parameters a and b and the resistance R .

The stability of the equilibrium points is analyzed by linearizing (6.1) around each of these points and calculating the eigenvalues of the corresponding Jacobian matrix. For any couple (α, β) of parameter values in region (a) of Figure 6.2, the points $EP_2 = (15,0,-1.065)$ and $EP_3 = (-15,0,1.065)$ are stable, while the point $EP_1 = (0,0,0)$ is an unstable point of the saddle type. As an example, for particular (α, β) , the point $EP_1 = (0,0,0)$ has the three eigenvalues: $\gamma = 1.7408 \cdot 10^{10}$ and $\sigma \pm j\omega = (-10.7166 \pm j1.9339) \cdot 10^{10}$. The points EP_2 and EP_3 have the same three eigenvalues: $\gamma = -2.7282 \cdot 10^{10}$ and $\sigma \pm j\omega = (-0.16797 \pm j 2.1295) \cdot 10^{10}$. Either the constant solution of EP_2 or EP_3 will be observed, depending on the initial condition.

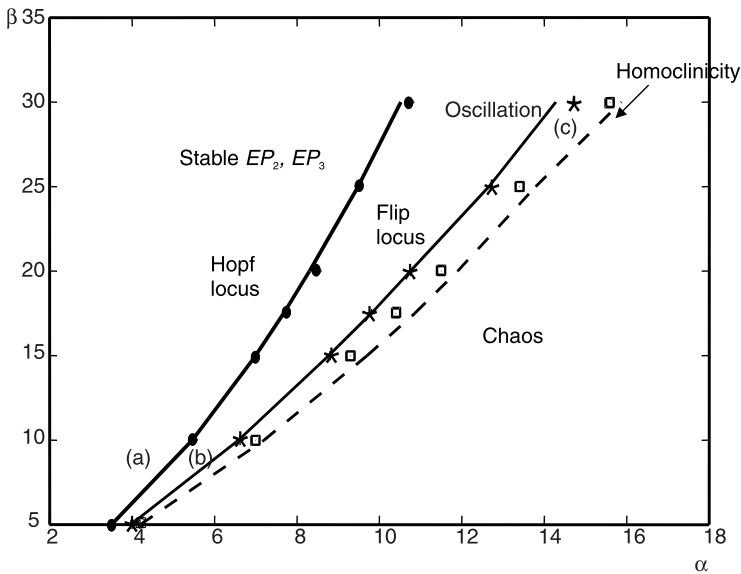


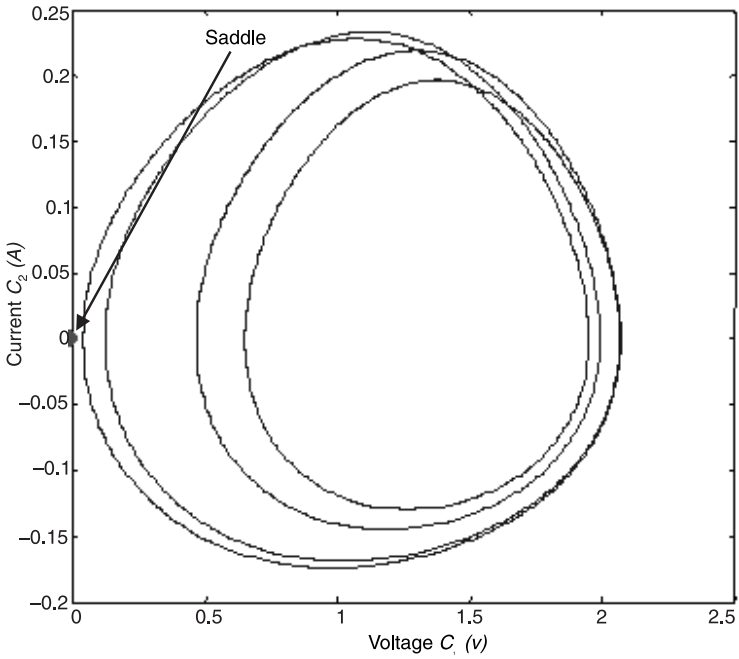
Figure 6.2 Bifurcation diagram of Chua's circuit versus variations of the two parameters α and β . The diagram has been obtained using commercial harmonic balance. The superimposed points are results from time-domain simulation included for comparison. (From: [16]. © 1998 IEEE. Reprinted with permission.)

In region (b), the points EP_2 and EP_3 are unstable foci ($\sigma > 0$). Depending on the initial condition, a limit cycle about either EP_2 or EP_3 will be observed. The Hopf locus provides the border between regions (a) and (b). When crossing this locus, an oscillation starts at points EP_1 and EP_2 , through a Hopf bifurcation. As said earlier, depending on the initial condition, either one or another limit cycle will be observed.

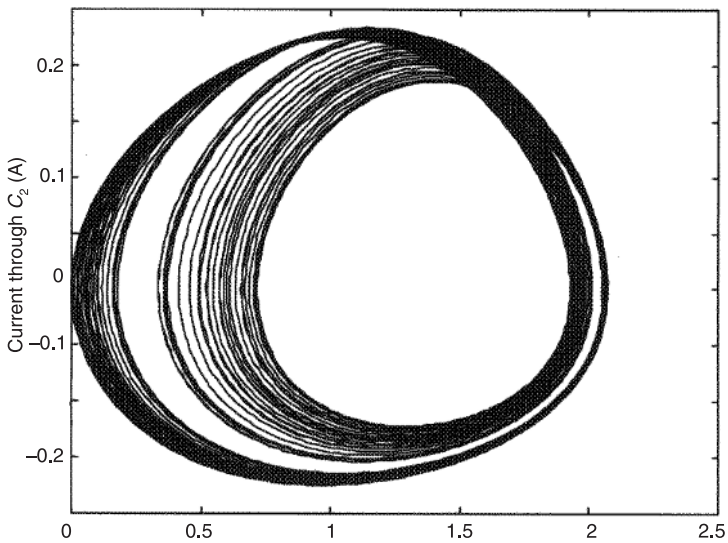
For some parameter values, a flip bifurcation takes place in the limit cycles (see Figure 6.2). The flip bifurcation gives rise to period doubling in each limit cycle, and the set of values (α, β) for which this doubling takes place is given by the flip-bifurcation locus. After this first doubling of the limit cycle, some other doublings take place (see Figure 6.3), until it collides with the saddle equilibrium point EP_1 at the locus labeled “Homoclinicity” in Figure 6.2. Figure 6.3 shows the period-4 cycle (just before the collision with the saddle equilibrium point) and the chaotic attractor, resulting from the formation of the transversal homoclinic orbit. It can easily be verified through calculation of the eigenvalues of (6.1) that, for all the locus points (α, β) , the saddle equilibrium point EP_3 fulfills the Shil’nikov condition for transversality $\gamma > |\sigma| > 0$. Thus, the locus named Homoclinicity provides the parameter values for the onset of chaos. The different bifurcation loci on Figure 6.2 have been obtained using commercial harmonic balance, with the technique that will be described in the following.

The availability of an efficient tool for the determination of multiple equilibrium points is of major importance in the analysis of homoclinic chaos because of its characteristic equilibrium point-limit cycle interaction. Here a specific technique has been developed that is very well suited for commercial simulators [16, 17]. It is based on the use of an auxiliary dc voltage generator, which is connected in parallel with the nonlinear element, as shown in Figure 6.1. A large-interval sweep is performed in the voltage of this generator, calculating the dc current I_{dc} flowing through this generator, as shown in Figure 6.4. The equilibrium points are given by the voltage values v_{C1} for which I_{dc} is equal to zero. Note that for zero current value, the dc generator has no influence over the circuit solution. In this way, it has been possible to obtain, using commercial harmonic balance, three equilibrium points with respective v_{C1} values $v_{C1} = \pm 15v$ and $v_{C1} = 0v$. The result is in agreement with the equilibrium points obtained from (6.1).

Considering a constant value $\beta = 15$, the two asymmetric equilibrium points EP_2 and EP_3 become unstable at $\alpha = 7$, which can be detected through a simple Nyquist stability plot. The resulting limit cycle undergoes a first period doubling for $\alpha \cong 9$ that can easily be detected in harmonic balance through the use of an auxiliary generator at the divided-by-two frequency (see Section



(a)



(b)

Figure 6.3 Onset of chaos in Chua's circuit owing to the formation of a transversal homoclinic orbit: (a) period-4 solution, just before the collision, and (b) chaotic attractor. (From: [16]. © 1998 IEEE. Reprinted with permission.)

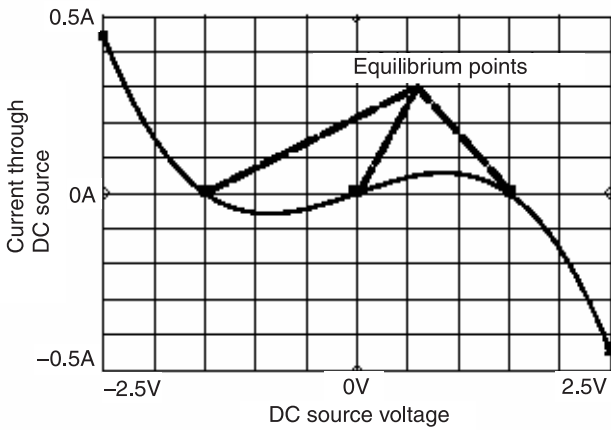


Figure 6.4 Calculation in commercial harmonic balance of the equilibrium points of the circuit in Figure 6.1. A voltage sweep in the dc auxiliary generator is carried out. (From: [16]. © 1998 IEEE. Reprinted with permission.)

2.6.2). For $\alpha \cong 10$, the cycle collides with the saddle equilibrium point EP_1 . In harmonic balance, this collision can be graphically verified. Figure 6.5 shows the harmonic-balance prediction of the collision between the limit cycle and the saddle equilibrium point that gives rise to the homoclinic orbit. The collision of Figure 6.5 has been simulated using commercial harmonic balance. Greater accuracy is obtained when the parameter values for the occurrence of the collision are determined using the period-2 steady-state solution [6].

6.2 Quasiperiodic Route to Chaos

The quasiperiodic route to chaos is observed in systems having a transition from a quasiperiodic state with two incommensurate frequencies (a flow on a 2-torus) to a quasiperiodic state with three incommensurate frequencies (a flow on a 3-torus). It can be shown [1, 8] that a system with a 3-torus generally evolves under any small perturbation to a system with a chaotic solution. Thus, chaos can arise from any small perturbation, and three-fundamental quasiperiodic states have seldom been observed [18]. They require special symmetry conditions that are relatively rare in physical systems.

Accordingly, in the quasiperiodic route to chaos two successive Hopf bifurcations (onset of an autonomous frequency) are observed as a parameter η is continuously modified. In the case of a circuit with input-generator

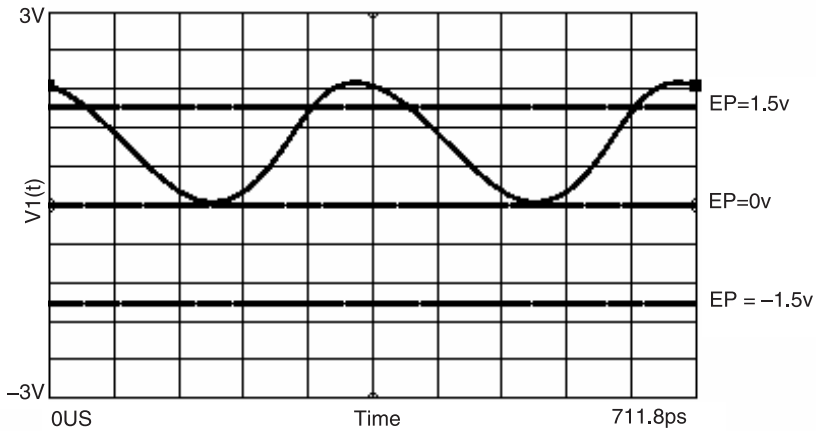


Figure 6.5 Chua's circuit. Harmonic-balance prediction of the collision between the limit cycle and the saddle equilibrium point. (From: [16]. © 1998 IEEE. Reprinted with permission.)

frequency ω_{in} , the first Hopf bifurcation, for $\eta = \eta_{o1}$, gives rise to the onset of a natural frequency ω_{a1} . Beyond this parameter value, the solution is quasiperiodic, corresponding to a 2-torus in the state space. This quasiperiodic regime may be the standard circuit solution, as in a self-oscillating mixer, or it may be undesired, as in a frequency doubler or a frequency divider. If the parameter continues to be modified, a second Hopf bifurcation at $\eta = \eta_{o2}$ would give rise to a 3-torus through the onset of a second autonomous frequency ω_{a2} and, thus, very likely to chaos. In Example 6.2, the example of a quasiperiodic route to chaos in a frequency divider [19] is presented.

Example 6.2 Quasiperiodic route to chaos in a MMIC frequency divider

A quasiperiodic route to chaos has been observed in the MMIC frequency of divider by two with $f_{in} = 28$ GHz in Section 5.3.3. In standard operation, the frequency divider by two exhibits a period-doubled cycle. However, other operation modes are possible. Outside the synchronization region at both sides of the Arnold tongue (see the bifurcation loci of Figure 5.12), the circuit behaves as a self-oscillating mixer. This regime is obtained for the input frequency $f_{in} = 31.5$ GHz and the input power $P_{in} = 1$ dBm. It is a quasiperiodic solution that gives rise to a 2-torus in the phase space (see Figure 6.6). The two incommensurable fundamentals are $f_{in} = 31.5$ GHz and $f_a \cong 14$ GHz. The operation as a self-oscillation mixer for this input power has been

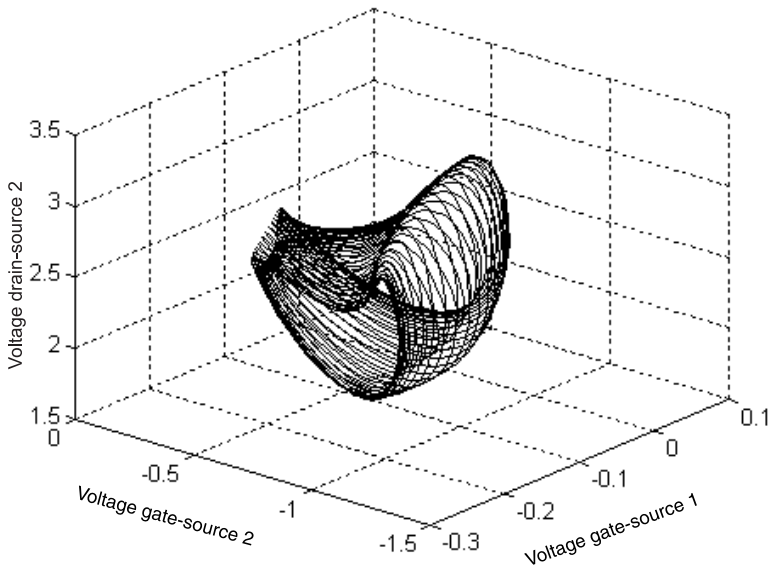


Figure 6.6 Quasiperiodic regime of MMIC frequency divider by two: input-generator conditions $f_{in} = 31.5$ GHz and $P_{in} = 1$ dBm. (From: [19]. © 1998 IEEE. Reprinted with permission.)

experimentally verified. However, when the input power is increased, a chaotic spectrum (Figure 6.7) is experimentally observed from a certain P_{in} value. The spectrum in the figure has been obtained for $P_{in} = 4.2$ dBm.

To find out about the bifurcation sequence that leads the MMIC frequency divider to the chaotic behavior of Figure 6.7, the variations of the quasiperiodic solution of Figure 6.6 versus the input power have been analyzed. The corresponding bifurcation diagram is shown in Figure 6.8. As usual, each path corresponds to one of the two independent fundamentals of the 2-torus. The input-generator frequency has been kept constant at the value $f_{in} = 31.5$ GHz. With increased input power, the possible onset of a second autonomous frequency ω_{a2} is checked through recursive application of the Nyquist criterion to the 2-torus solution. This requires a linearization of the harmonic-balance equation about the 2-torus steady-state solution. The onset of a second autonomous fundamental ω_{a2} would make the spectrum denser, giving rise to new spectral lines between the frequency components of the unstable two-fundamental regime. Thus, the sweeping interval can be reduced to $[0, f_l]$ with f_l being the lowest intermodulation frequency of the two fundamental regime.

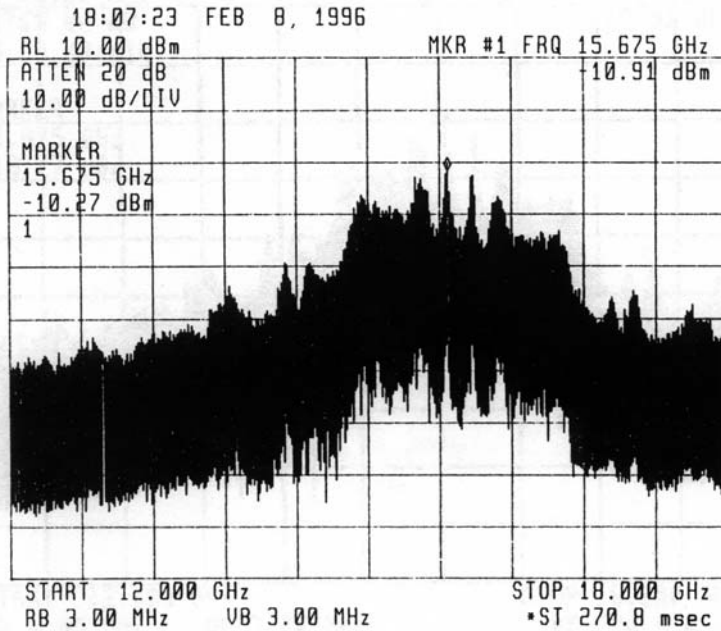


Figure 6.7 Experimental spectrum of the MMIC frequency divider by two for $f_{in} = 31.5$ GHz and $P_{in} = 4.2$ dBm. (From: [19]. © 1998 IEEE. Reprinted with permission.)

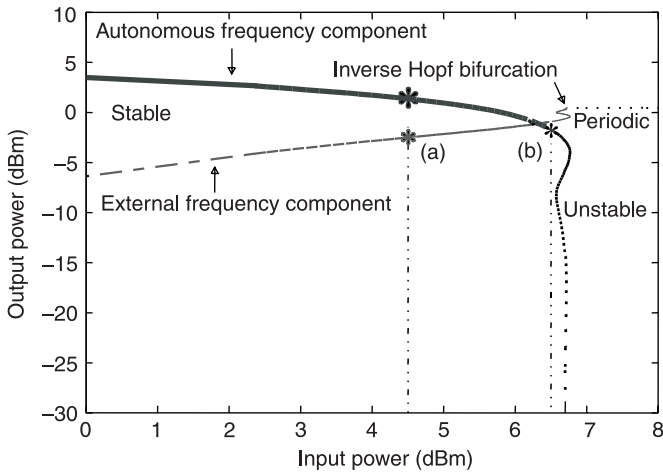


Figure 6.8 Bifurcation diagram of the MMIC frequency divider by two in the quasiperiodic regime versus the input power for $f_{in} = 31.5$ GHz. (From: [19]. © 1998 IEEE. Reprinted with permission.)

For $P_{in} = 6.5$ dBm, the resulting Nyquist plot is shown in Figure 6.9. The unstable plot intersects the negative real axis for $f_c = 1.74$ GHz. The autonomous fundamental of the 2-torus flow is $f_a = 14.98$ GHz, so the second autonomous fundamental must be $f_{a2} = 14.98 \pm 17$ GHz. This frequency is not rationally related with the two existing fundamentals $\omega_{a2} \neq m\omega_{in} + n\omega_a$. This should give rise to a 3-torus steady state. However, because of the inherent instability of 3-torus steady state, a chaotic solution will generally be observed.

6.3 Period-Doubling Route to Chaos

In the period-doubling route to chaos, as a parameter η is varied, a succession of period doublings (or flip bifurcations) is obtained at the parameter values $\eta_1, \eta_2, \dots, \eta_n, \dots$. The length of the parameter intervals (η_n, η_{n+1}) of $2^n T$ period decrease with n . At a certain parameter value η_∞ , the period doubles ad infinitum, giving a nonperiodic chaotic solution. Feigenbaum [1, 5, 8] has shown that the series of flip-bifurcation parameter values $\{\eta_n\}$ converges fast to η_∞ . He defined the following ratio:

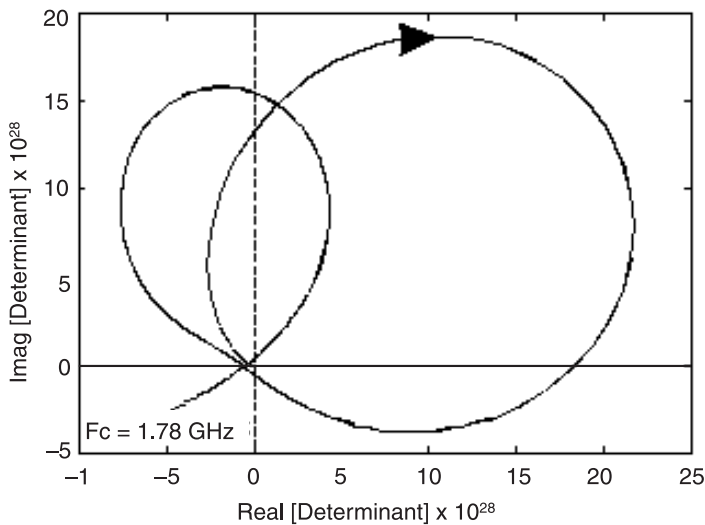


Figure 6.9 Stability analysis of the quasiperiodic solution of the MMIC frequency divider. Nyquist plot for $f_{in} = 31.5$ GHz and $P_{in} = 6.5$ dBm. (From: [19]. © 1998 IEEE. Reprinted with permission.)

$$\delta_n = \frac{\eta_{n+1} - \eta_n}{\eta_{n+2} - \eta_{n+1}} \quad (6.3)$$

with δ_n converging to the value $\delta = 4.6692016$ after just a few period doublings. There are many examples of circuits exhibiting a period-doubling route to chaos.

For the study of the period-doubling route to chaos, the Poincaré-map technique can be employed. As is already known, in the case of a nonautonomous circuit, for each parameter value, the steady-state solution is sampled at integer multiples of the input-generator period $x(nT)$. Clearly, for periodic solutions of the same period T as the input generator, the map will provide a single point, while for periodic solutions of period nT , it will provide n different points. An example of the use of the Poincaré map for the analysis of a period-doubling route to chaos in an IMPATT-based circuit [8, 9, 20] is shown in Example 6.3.

Example 6.3: Period-doubling route to chaos in an IMPATT-based circuit

As an example of a period-doubling route to chaos, an IMPATT diode, loaded by 50 Ohm, is analyzed here versus variations of the RF input current [21]. This circuit was already considered in Example 1.8. The IMPATT model [21, 22] is mainly a circuit implementation of the diode transport equations with each element in direct correspondence with a physical mechanism. P-I-N doping profile, low current bias, and negligible diffusion effects are assumed. The model is composed of two equivalent circuits [22], one for the avalanche region and the other for the drift region, in a series connection.

The constant input frequency is $f_{in} = 50$ GHz. The resulting Poincaré map versus the RF input current was shown in Figure 1.21. This map evidences, as the input power increases, a period-doubling route to chaotic behavior. A flip bifurcation, leading to a period-2 regime, takes place for the input current $I_g = 0.17A$. A second flip bifurcation, leading to a period-4 regime, takes place for $I_g = 0.35A$. The third flip bifurcation, more difficult to appreciate, takes place for $I_g \cong 0.42A$. The calculation of the two first iterations of the Feigenbaum ratio (6.3) gives $\delta_1 = 2.57$, $\delta_2 = 4.68$, which constitutes a good approach to the theoretical value. Chaos can be recognized from the characteristic cloud of points in the Poincaré diagram because of the loss of periodicity of the circuit response. The chaotic attractor, obtained for the input-current $I_g = 0.5A$, is shown in Figure 6.10.

As is already known, time-domain integration may be difficult to apply in circuits operating at microwave frequencies because of the long duration of the transient, compared with the solution period. When the time-domain analysis

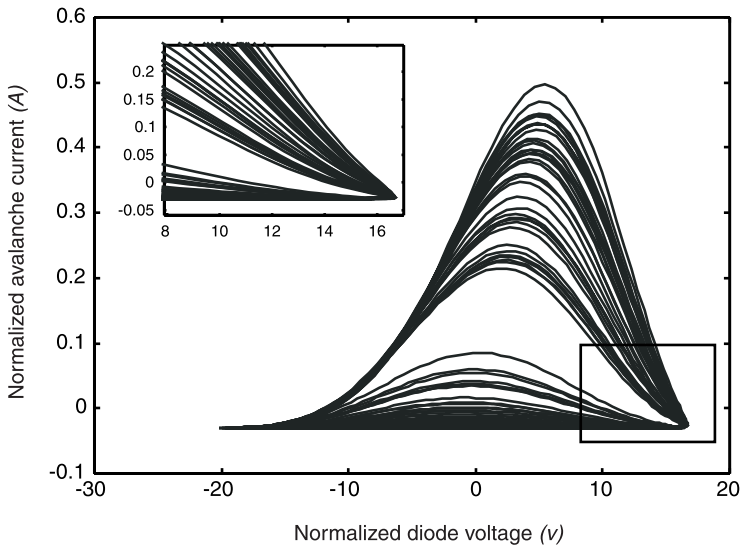


Figure 6.10 Chaotic attractor of the IMPATT-based circuit for input current $I_g = 0.5A$.

is not applicable, harmonic balance can be used to detect the initial flip bifurcations of the period-doubling route to chaos. The technique is a generalization of the auxiliary-generator techniques employed in Chapters 4 and 5 for the analysis of flip bifurcations and period-doubled solutions. It will be presented in the following.

The stability analysis of a period- T regime in the presence of period-doubling perturbations can be carried out by introducing a period-2 auxiliary generator AG_1 (with $2T$ period) with very small amplitude $A_1 = \varepsilon$ and variable phase ϕ_1 [see Figure 6.11(a)]. Let Y_1 be the input admittance from the AG_1 terminals. The period-1 regime will be unstable if the conditions for the startup of a frequency division by two, $\text{Re}(Y_1) < 0$, $\text{Im}(Y_1) = 0$, are satisfied for a certain phase value of AG_1 . This is verified through a phase sweep from $\phi_1 = 0^\circ$ to $\phi_1 = 180^\circ$. Figure 6.11(b) shows an example of period-doubling detection through this technique, using commercial harmonic balance. To obtain the period-2 steady state, the amplitude A_1 and phase ϕ_1 of the AG_1 are optimized (or solved through a Newton-Raphson algorithm) to fulfill the nonperturbation condition $|Y_1| = 0$.

For the prediction of a second period doubling, the period-2 AG_1 is kept at its steady-state value, amplitude A_{1o} and phase ϕ_{1o} , introducing an additional AG_2 of period $4T$ (see Figure 6.11) with amplitude A_2 and phase ϕ_2 . For the

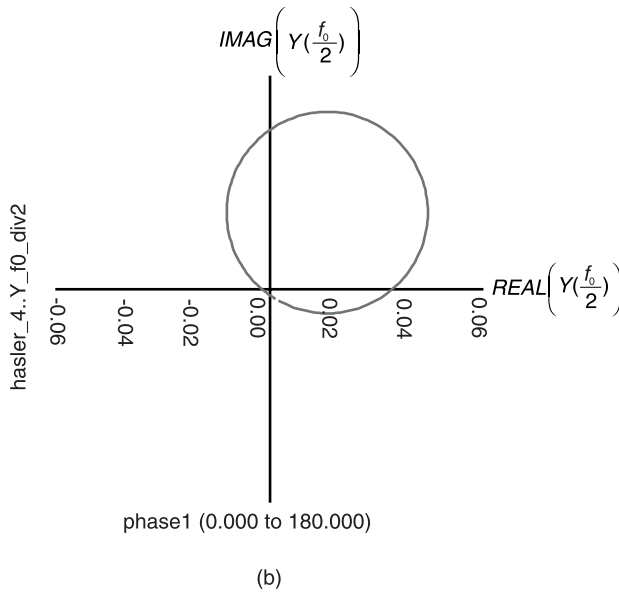
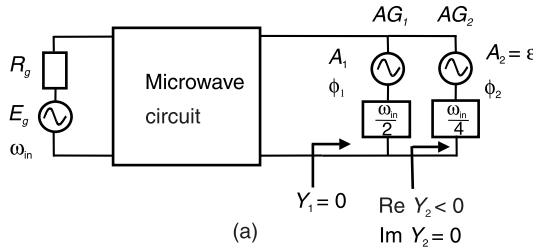


Figure 6.11 Use of auxiliary generators for the detection of the two initial period doublings in a period-doubling route to chaos: (a) connection of the auxiliary generators, and (b) prediction of a period-doubling instability.

stability analysis of the period-2 regime in the presence of period-doubling perturbations, the amplitude the AG_2 is set to a very small value $A_2 = \epsilon$, performing a phase sweep from $\phi_2 = 0^\circ$ to $\phi_2 = 90^\circ$. A new period doubling will be obtained if, for a certain ϕ_2 , the conditions $\text{Re}(Y_2) < 0$, $\text{Im}(Y_2) = 0$ are fulfilled. The steady-state period-4 regime is obtained through the optimization of the two auxiliary generators AG_1 and AG_2 , in the variables A_1 , ϕ_1 , A_2 , and ϕ_2 , to fulfill $|Y_1| = 0$ and $|Y_2| = 0$.

For the prediction of a frequency division by eight, a third auxiliary generator AG_3 , at the input-generator frequency divided by eight, with a very small amplitude $A_3 = \varepsilon$ and variable phase ϕ , would be introduced. After prediction of this third period-doubling, the steady-state period-8 solution would be calculated through optimization of the amplitude and phase values of the three auxiliary generators AG_1 , AG_2 , and AG_3 . This technique can be recursively applied to obtain period-doubled solutions of higher order. However, the parameter accumulation properties shown by Feigenbaum make the prediction of these high-order divisions unnecessary in practice. The parameter values for the onset of chaos may be estimated after only a few bifurcations.

The chaotic IMPATT-based circuit of Example 6.3 was relatively well behaved in the sense that the sequence of flip bifurcations, leading to chaotic behavior, were of supercritical type (with no associated hysteresis). In other cases, the flip bifurcations are subcritical, which gives rise to hysteresis and broken paths in the Poincaré map. An example of a period-doubling route to chaos with subcritical flip bifurcations has been obtained in the varactor-based frequency doubler of Figure 4.11 and Example 4.4 [23]. Example 6.4 presents the parametric analysis of this circuit in a wider range of input-generator amplitudes. The circuit is analyzed through the Poincaré map and with the harmonic-balance technique. The latter technique enables a detailed analysis of the subcritical bifurcations.

Example 6.4 Period-doubling route in a varactor-based frequency doubler

The second example of a circuit with a period-doubling route to chaos is the varactor-based frequency doubler of Figure 4.11. The calculation of the Poincaré map versus variations in the input-generator amplitude provides the bifurcation diagram of Figure 6.12(a). The broken branches indicate hysteresis phenomena. Two consecutive flip bifurcations give rise to a period-4 solution, extending from $E_g = 2.3v$ to $E_g = 3.4v$. The extinction of this solution through an inverse flip bifurcation leads the system back to a period-2 solution, extending up to $E_g = 3.9v$. From this value, a period-doubling route to chaos is obtained.

The doubler circuit has also been analyzed through harmonic balance in Figure 6.12(b). To obtain this bifurcation diagram, use has been made of the auxiliary generator technique of Figure 6.11. The amplitude of the most representative subharmonic components has been represented. The multivalued solution curves are in perfect agreement with the hysteresis phenomena of Figure 6.12(a). Between $E_g = 1.8v$ and $E_g = 2.8v$, the period-1 solution coexists with the period-2 solution with the convergence to one or another depending on the initial conditions. A similar situation is obtained for input-generator amplitudes about $E_g = 3.8v$.

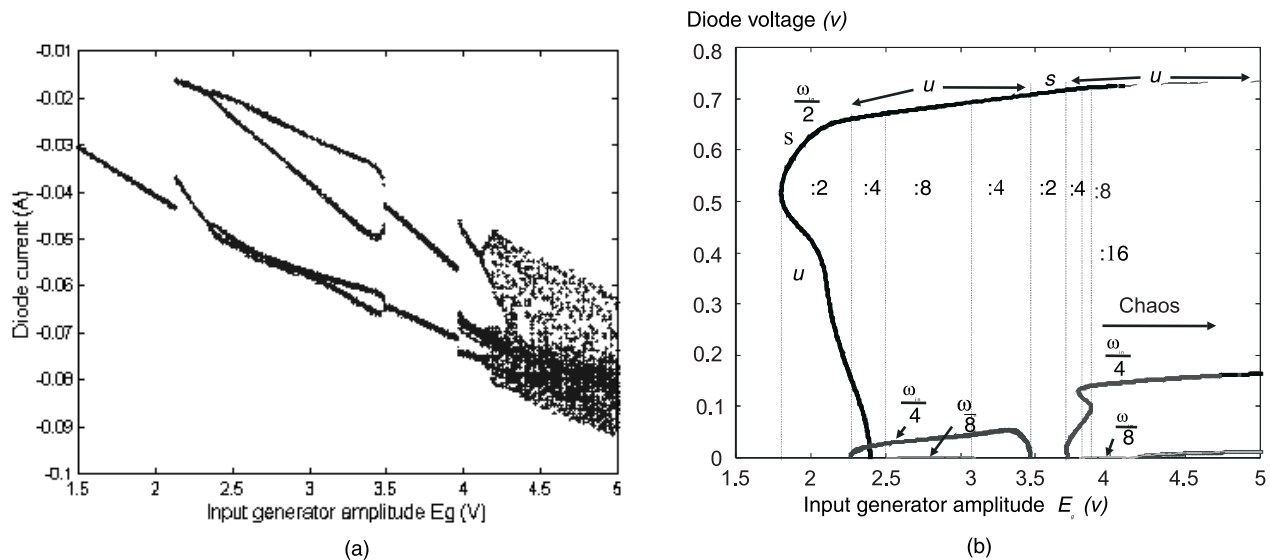


Figure 6.12 Period-doubling route to chaos in the varactor-based frequency doubler: (a) Poincaré map, and (b) harmonic balance using the auxiliary generator technique of Figure 6.11. For the detection of the frequency division by 16, five auxiliary generators in parallel connection have been used. (From: [23]. © 1999 IEEE. Reprinted with permission.)

For the detection of the period-16 solution, four auxiliary generators, fulfilling the nonperturbation condition $Y_i = 0$ have been used, together with a fifth auxiliary generator of very small amplitude, fulfilling the instability condition $\text{Re}(Y_5) < 0$, $\text{Im}(Y_5) = 0$ for a certain phase value.

6.4 Torus-Doubling Route to Chaos

In the torus-doubling route to chaos, the circuit initially operates in a quasiperiodic regime with two incommensurate fundamental frequencies ω_1, ω_2 , giving rise to a 2-torus in the phase space. This regime may be the standard operation regime of the circuit (as in the case of a self-oscillating mixer [21]) or it may be an undesired regime [24]. Under variations of a parameter, the torus undergoes a succession of doublings until it becomes a chaotic attractor (see Figure 6.13).

The doubling of a torus in the phase space is due to the division by two of one of its fundamental frequencies. This leads to the regime at the frequencies ω_1, ω_2 and the subharmonic frequency $\frac{\omega_1}{2}$. If the parameter continues to vary, a new division by two of the same fundamental frequency, giving the subharmonic frequency $\frac{\omega_1}{4}$, will lead to a new doubling of the torus. The doublings generally take place for decreasing parameter intervals and may continue ad infinitum. Actually, the torus-doubling route to chaos is closely related with the period-doubling route to chaos of Section 6.3.

The consecutive divisions by two of one of the fundamental frequencies of the torus can be detected through the use of auxiliary generators, in similar way to the technique given in Section 6.3 for the analysis of period doubling. Assuming a fundamental delivered by the input generator and an autonomous fundamental, respectively denoted ω_{in} and ω_a , for the detection of the first torus doubling, two auxiliary generators are necessary (see Figure 6.14). The first generator AG_1 is employed to obtain the steady-state quasiperiodic solution at ω_{in} and ω_a . The generator frequency is $\omega_p = \omega_a$. The frequency and amplitude A_1 of this generator are optimized to fulfill the nonperturbation condition $Y_1 = 0$, obtaining the steady-state values A_{1o}, ω_{ao} . Then, a second auxiliary generator AG_2 is introduced at the autonomous frequency divided by two $\frac{\omega_a}{2}$. Due to the harmonic relationship between this frequency and the autonomous frequency ω_a , a phase relationship must exist between the two auxiliary generators, so the variables of the generator AG_2 will be the amplitude A_2 and the phase ϕ .

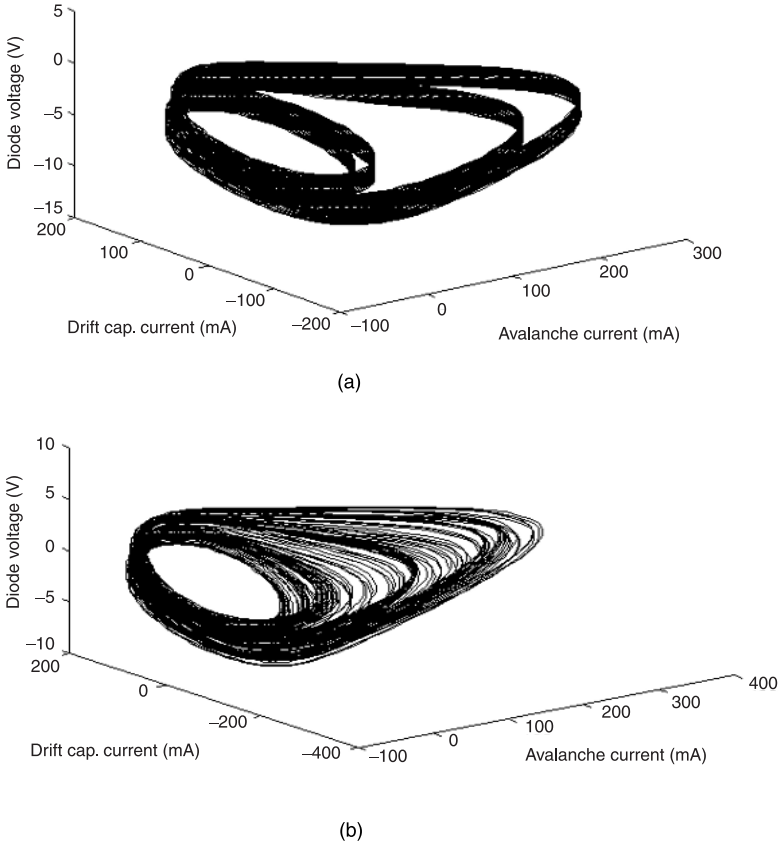


Figure 6.13 Auxiliary-generator technique for the detection of torus doubling. One generator enables obtaining the steady-state quasiperiodic solution. The second generator enables detecting the division by two of the autonomous frequency ω_a .

For the prediction of the torus doubling, the amplitude of the generator AG_2 is set to a very small value $A_2 = \varepsilon$. Keeping the AG_1 at its steady-state values $A_{1,ss}, \omega_{a,ss}$, a sweep in the phase of AG_2 is carried out from $\phi_2 = 0^\circ$ to $\phi_2 = 180^\circ$. In this sweep, the input admittance Y_2 is calculated, checking for the possible fulfillment of the instability conditions $\text{Re}(Y_2) < 0, \text{Im}(Y_2) = 0$. To obtain the steady-state doubled torus, the four variables of the two auxiliary generators, that is the frequency ω_a , the phase ϕ , and the two amplitudes generator A_1 and A_2 , must be calculated to fulfill the nonperturbation conditions $Y_1 = 0$ and $Y_2 =$

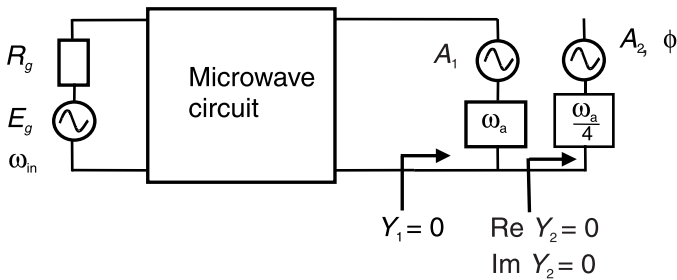


Figure 6.14 Doubled torus obtained when decreasing the resistance r_1 of the linear network in the self-oscillating mixer of Figure 1.24: (a) harmonic-balance calculation (note the different sampling rates at each of the two fundamental frequencies), and (b) result of the time-domain integration. (From: [25]. © 1999 IEEE. Reprinted with permission.)

0. A second doubling in the torus would be detected in a similar manner, introducing a third auxiliary generator AG_3 with very small amplitude $A_3 = \epsilon$ and performing a phase sweep from $\phi_3 = 0^\circ$ to $\phi_3 = 90^\circ$.

The IMPATT-based self-oscillating mixer of Figure 1.24 exhibits a torus-doubling route to chaos [25] versus variations in the resistance of the load circuit. Example 6.5 shows how the steady-state doubled torus is calculated through harmonic balance and compared with the result of time-domain integration.

Example 6.5: Torus-doubling route to chaos in an IMPATT based self-oscillating mixer

The circuit of Figure 1.24, based on an IMPATT diode, operates both as oscillator and mixer and provides RF to IF downconversion through the mixing of the external frequency ω_{in} with the autonomous one ω_a . Because there are two incommensurable fundamentals, the solution is quasiperiodic, giving rise to a 2-torus in the phase space. When decreasing the resistance r_1 of the linear circuit (see Figure 1.24), the torus undergoes a doubling (see Figure 6.15).

In the harmonic-balance calculation of the doubled torus, a two-dimensional Fourier-series expansion of the state variables is used with a different time variable for each dimension. For an efficient resolution, the number of time samples is $2(2nl + 2)$ per dimension, with nl being the nonlinearity order. When calculating the inverse Fourier transform, this provides a different sampling step for each dimension, respectively given by Δt_{in} and Δt_a . The resulting doubled torus is shown in Figure 6.15(a). For constant $t_{in} = n_1 \Delta t_{in}$ (with n_1 integer), the sampling at Δt_a (longitudinal) shows the period doubling already observed in the Poincaré map. The small circles, without period doubling, are

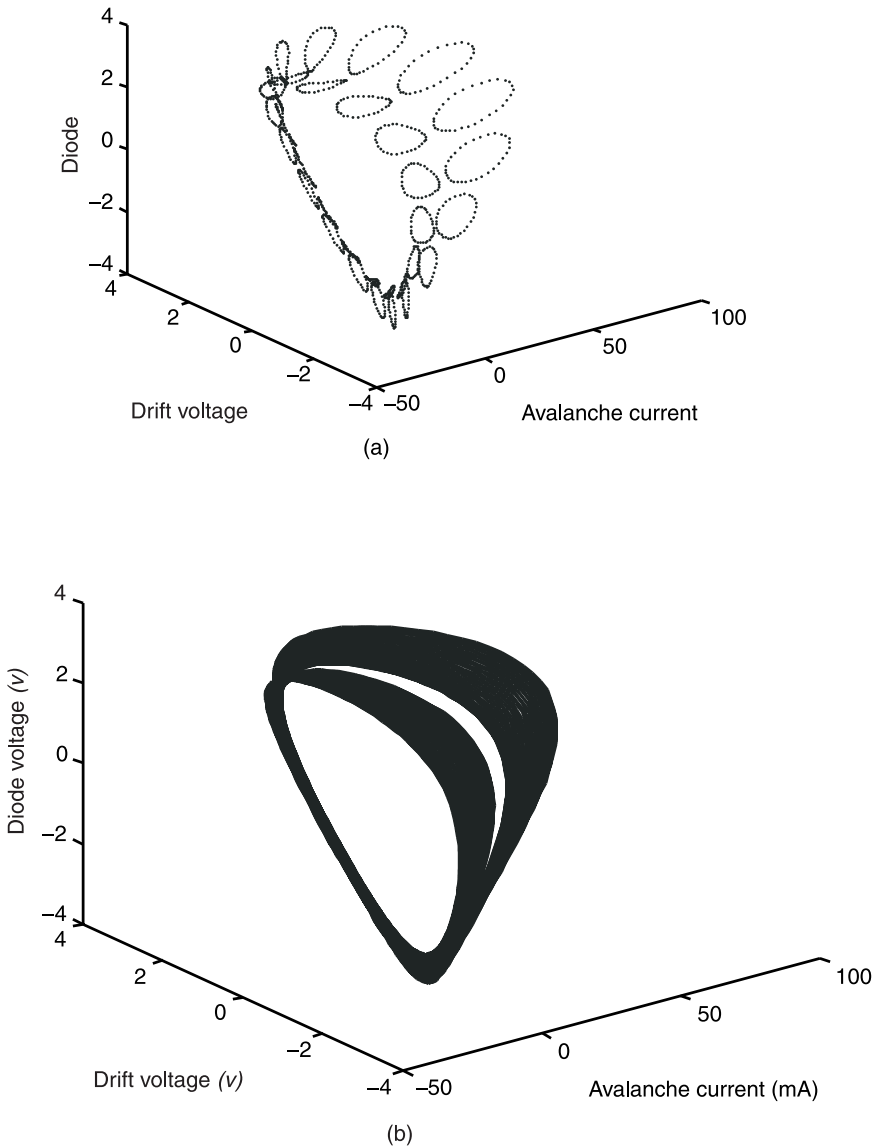


Figure 6.15 Torus-doubling to chaos in the IMPATT-based self-oscillating mixer: (a) torus after two consecutive doublings, and (b) chaotic attractor.

due to the sampling at the smaller rate Δt_{in} (transversal). In Figure 6.15(b), this attractor can be compared with the doubled torus obtained from time-domain simulations.

If the value of the resistance r_1 continues to be reduced, the torus of Figure 6.15 undergoes more doublings. The resistance intervals for each doubling decrease with the order of the doubling, in similar way to the period-doubling route to chaos. Figure 6.13(a) shows the torus after a second division by two of the autonomous frequency $\frac{\omega_a}{2} \rightarrow \frac{\omega_a}{4}$ and Figure 6.13(b) shows the chaotic attractor.

6.5 Intermittence

For the description of the intermittence route to chaos, a periodic solution is initially assumed and the continuous variation of a parameter η is considered. From a certain value $\eta = \eta_o$, the formerly periodic waveform starts to be interrupted by bursts of irregular behavior. These bursts of irregular behavior become longer in time and more frequent as the parameter continues to evolve. Eventually an entirely chaotic waveform is observed. This constitutes an intermittence route to chaos. This route has been obtained in a particular implementation of Chua's circuit (Figure 6.16), for two different values of the capacitance C_2 [26] exhibit the waveforms of Figure 6.17. Similar routes to chaos have been obtained in power systems [27] and coupled phase-locked loops [28, 29].

Two things can be gathered from the time-domain behavior in Figure 6.17. Obviously, at the parameter value $\eta = \eta_o$ that determines the start of the intermittence process, the periodic solution becomes unstable. This is necessarily due to a bifurcation taking place at $\eta = \eta_o$. On the other hand, the solution with the irregular bursts is neither periodic nor quasiperiodic. It is a chaotic solution.

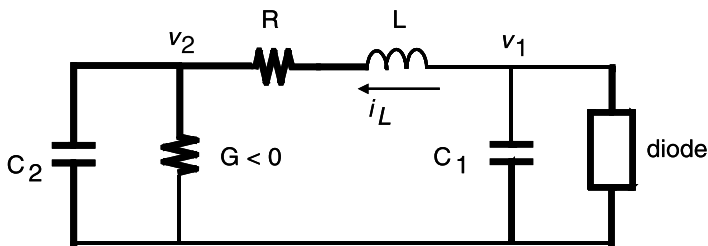
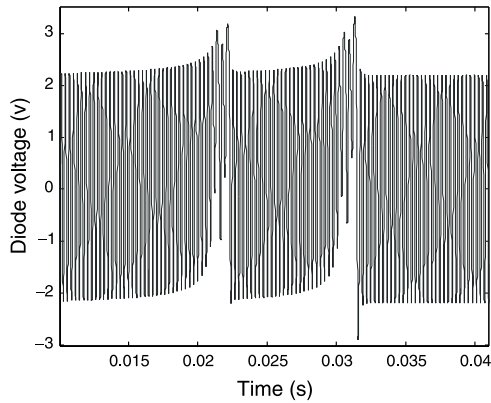
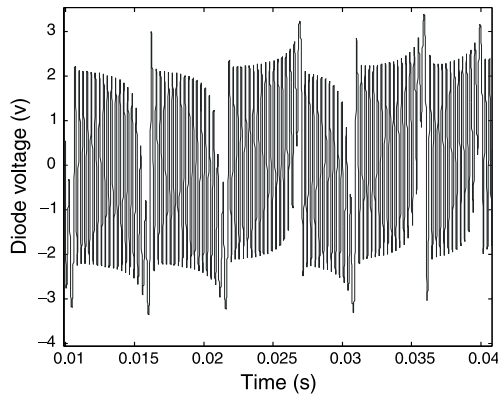


Figure 6.16 Chua's circuit with an intermittence route to chaos. The linear element values are $C_1 = 33$ nF, $R = 200$ Ohm, $L = 100$ mH and $R1 = -2,000$ Ohm. The cubic non-linearity of the diode is $j_n(v) = -10^{-4}v + 10^{-4}v^3$.



(a)



(b)

Figure 6.17 Intermittence in Chua's circuit of Figure 6.16. Two different values of the capacitance C_2 have been considered: (a) $C_2 = 33.8$ pF, and (b) $C_2 = 34$ pF.

The sketch of Figure 6.18 enables a general explanation of intermittence [27]. The one-dimensional map $x_{n+1} = F(x_n)$ has been considered. This map enables obtaining the iteration point x_{n+1} from the preceding point x_n . In the case of the Poincaré map, the succession $\{x_n\}$ is given by the consecutive intersections of the solution trajectory with a transversal surface. In Figure 6.18(a), the mapping function F has been represented, together with the unity-slope line (identity map) $x_{n+1} = x_n$, which helps in obtaining the sequence of points that constitute the map. The fixed points x_o of the map satisfy $x_o = F(x_o)$. These points will be stable for $|F'(x_o)| < 1$. In Figure 6.19, three different steady-state solutions are obtained around the unstable equilibrium point: the

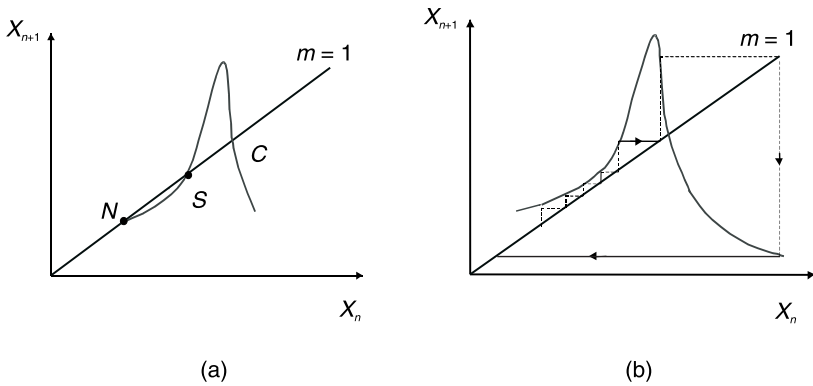


Figure 6.18 An explanation of intermittence: (a) stable node, and (b) intermittence.

stable equilibrium point N , the saddle equilibrium point S and a chaotic solution C . Note that the fixed points of the Poincaré map correspond to time-periodic solutions of the circuit.

While the stable node exists, a periodic solution is observed because the trajectory from the chaotic attractor will eventually come to the node and stay there. However, under variations of a parameter η , the situation depicted in Figure 6.18(b) is obtained. The system has undergone a saddle-node bifurcation (collision of the node and saddle point, giving rise to their annihilation). The stable node does not exist any more and the chaotic solution is the only stable solution. However, a laminar region has formed between the curve $F(x)$ and the unity-slope straight line $x_{n+1} = x_n$. Then the trajectory remains for a long time where the stable node used to be (see the big number of iterations of the Poincaré map in this region) and gives rise to an apparently periodic solution for a certain time interval. Then the trajectory leaves the region between the curve and the straight line, undergoing the big variations that correspond to the chaotic solution and returning to the gap region after some time. This gives rise again to an apparently periodic behavior. As the parameter evolves, the distance between the curve $F(x)$ and the straight line increases, and the time intervals with apparent periodic behavior become shorter and less frequent. It must be noted that the saddle-node bifurcation has not given rise to the chaotic attractor, which was already present when this bifurcation took place. The bifurcation determines the extinction of the periodic solution and the transition to the chaotic attractor. Different kinds of bifurcation may start the intermittence process [30]. In Example 6.6, the start of intermittence is due to a pitchfork bifurcation (Section 4.4.2).

Example 6.6 Intermittence in Chua's circuit

Chua's circuit of Figure 6.16 exhibits an intermittence route to chaos [26–31], as shown in the simulations of Figure 6.17, obtained for two different values of the capacitance C_2 . The rest of the element values are given in the figure caption.

The sequence of bifurcations leading to this behavior has been investigated through the harmonic-balance technique. The bifurcation diagram versus C_2 is shown in Figure 6.19. Different paths can be observed. Each point of Path 1 corresponds, in the phase space, to a periodic orbit that is symmetric with respect to the origin. This path exhibits a turning point T_1 , separating the subpaths 1a and 1b. The recursive application of the Nyquist stability analysis shows that the only stable section of Path 1 is the section between the turning

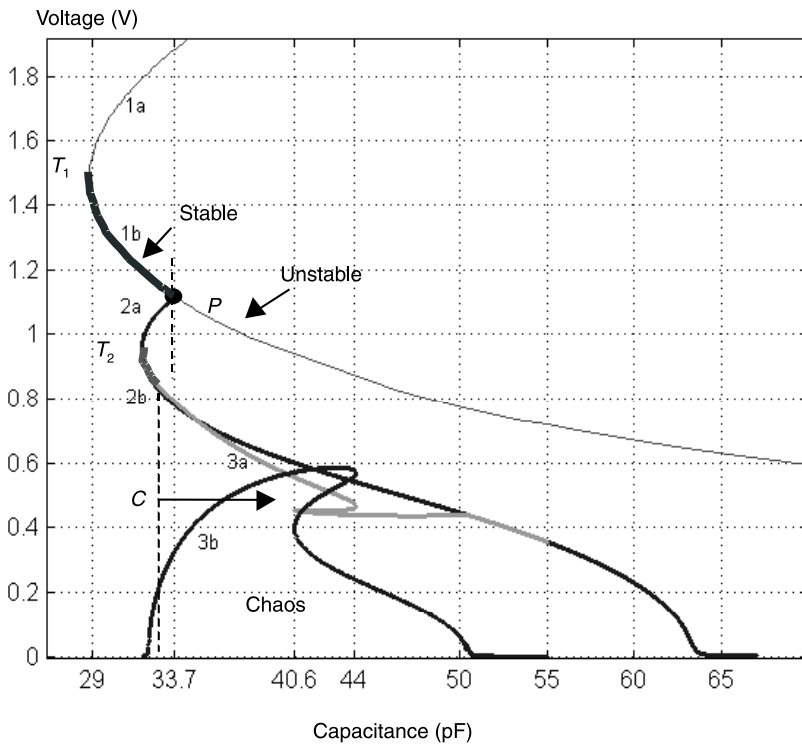


Figure 6.19 Intermittence in Chua's circuit: a bifurcation diagram obtained through the harmonic-balance technique. At the pitchfork bifurcation, the periodic orbit $1b$ becomes unstable, and the solution moves to the chaotic attractor. (From: [31].©2001 IEEE.)

point T_1 and the bifurcation point P . One of these stable periodic orbits has been represented in Figure 6.20(a).

At the point P , Path 2 is generated, through a pitchfork bifurcation (see Section 4.1.2.2). Each point of this path represents, in fact, two periodic orbits that are asymmetric with respect to the origin. The pitchfork bifurcation is sub-critical, and only the section between the turning point T_2 and the flip

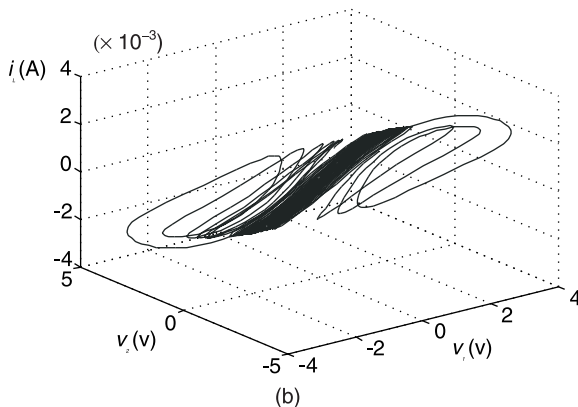
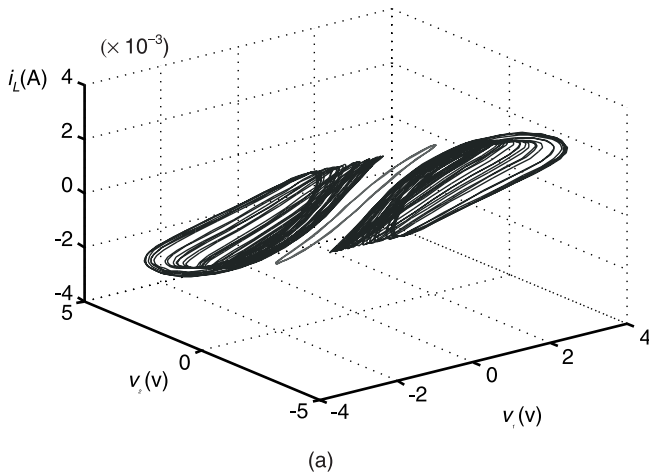


Figure 6.20 Intermittence in Chua's circuit: (a) coexistence of a stable periodic orbit with two chaotic attractors generated through a period-doubling route in the Path 3b of Figure 6.19, and (b) chaotic attractor with intermittency. The trajectory spends a long time where the formerly stable period orbit used to be. (From: [31].©2001 IEEE.)

bifurcation F is stable. From point F , a period-doubling cascade starts in the asymmetric orbits, giving rise to chaotic behavior from the border C . In view of the bifurcation diagram, the increase of the capacitance C_2 gives rise to the following situations in the phase space:

- *Interval T_2-F* : A symmetric period-1 orbit and two asymmetric period-1 orbits coexist for each capacitance value in T_2-F .
- *Interval $F-C$* : A symmetric period-1 orbit coexists with two period-2 asymmetric orbits for each capacitance value in $F-C$.
- *Interval $C-P$* : A symmetric period-1 orbit coexists with two chaotic asymmetric orbits for each capacitance value in $C-P$. An example is shown in Figure 6.20(a).

At the bifurcation point P , the central symmetric orbit becomes unstable and the chaotic solution becomes the only stable solution (compare with the sketch of Figure 6.19). For the capacitor value at which the pitchfork bifurcation takes place, the two asymmetric chaotic attractors merge, giving rise to one single chaotic attractor. For the value of C_2 at which the pitchfork bifurcation occurs, the chaotic attractor geometrically contains the periodic orbit in the phase space [see Figure 6.20(b)]. As a result, for C_2 values slightly larger than the bifurcation value, the solution spends a long time in the neighborhood of the formerly stable periodic orbit. This gives rise to the apparently periodic behavior of Figure 6.16. The solution is actually chaotic, which explains the irregular bursts.

The observation of intermittence has been related [1] with the geometrical location, at the bifurcation point, of the formerly stable solution inside the solution that persists after the bifurcation. The system tends to spend a long time in the neighborhood of the formerly stable solution. This is actually the case of Figure 6.20(b).

References

- [1] Thomson, J. M. T., and H. B. Stewart, *Nonlinear Dynamics and Chaos*, New York: John Wiley & Sons, 1997.
- [2] Guckenheimer, J., and P. Holmes, *Nonlinear Oscillations, Dynamical Systems and Bifurcations of Vector Fields*, Berlin, Germany: Springer-Verlag, 1990.
- [3] Wiggins, S., *Introduction to Applied Nonlinear Dynamical Systems and Chaos*, Berlin, Germany: Springer-Verlag, 1990.

-
- [4] Parker, T. S., and L. O. Chua, *Practical Algorithms for Chaotic Systems*, Berlin, Germany: Springer-Verlag, 1989.
 - [5] Special Issue on Chaotic Systems, *IEEE Trans. Circuits Syst.*, Aug. 1987.
 - [6] Lichtenberg, A. J., and M. A. Lieberman, *Regular and Chaotic Dynamics*, Berlin, Germany: Springer-Verlag, 1991.
 - [7] Cvitanovic, P., *Universality in Chaos*, Philadelphia, PA: Institute of Physics Publishing, 1996.
 - [8] Swinney, H. L., "Observations of Order and Chaos in Nonlinear Systems," *Int. Conf. Order Chaos*, Los Alamos, NM, May 24–28, 1982.
 - [9] Pecora, L. M., and T. L. Carroll, "Synchronization in Chaotic Systems," *Phys. Rev. Lett.*, Vol. 64, 1990, pp. 821–824.
 - [10] Silva, C. P., and A. M. Young, "Implementing RF Broadband Chaotic Oscillators: Design Issues and Results," *Proc. IEEE Int. Symp. Circuits Syst.*, Vol. 4, Monterey, CA, May 1998, pp. 489–493.
 - [11] Ott, E., C. Grebogi, and J. A. Yorke, "Controlling Chaos," *Phys. Rev. Lett.*, Vol. 64, 1990, pp. 1196–1199.
 - [12] Special Issue on Chaos Synchronization and Control, *IEEE Trans. Circuits Syst.*, Vol. 44, No. 10, Oct. 1997.
 - [13] Genesisio, R., and A. Tesi, "A Harmonic Balance Approach for Chaos Prediction: Chua's Circuit," *Int. J. Bifurcation Chaos*, Vol. 2, No. 1, Jan. 1992, pp. 61–79.
 - [14] Silva, C. P., "Shil'nikov Theorem—A Tutorial," *IEEE Trans. Circuits Syst.*, Vol. 40, No. 10, Oct. 1993, pp. 675–682.
 - [15] Endo, T., and L. O. Chua, "Chaos from Phase-Locked Loops," *IEEE Trans. Circuits Syst.*, Vol. 35, No. 8, Aug. 1988, pp. 987–1003.
 - [16] Suárez, A., and J. M. Collantes, "Chaos Detection in Microwave Circuits Using Harmonic Balance Commercial Simulators," *IEEE Int. Microwave Symp., MTT-S*, Baltimore, MD, June 1998, pp. 271–274.
 - [17] Collantes, J. M., and A. Suárez, "Period Doubling Analysis and Chaos Detection Using Commercial Harmonic Balance Simulators," *IEEE Trans. Microwave Theory Tech.*, Vol. 48, No. 4, Apr. 2000, pp. 578–581.
 - [18] Basu, S., S. A. Maas, and T. Itoh, "Stability Analysis for Large Signal Design of a Microwave Frequency Doubler," *IEEE Trans. Microwave Theory Tech.*, Vol. 43, No. 12, Dec. 1995, pp. 2890–2898.
 - [19] Suárez, A., J. Morales, and R. Quéré, "Chaos Prediction in a MMIC Frequency Divider in Millimetric Band," *IEEE Microwave Guided Wave Lett.*, Vol. 8, No. 1, Jan. 1998, pp. 21–23.
 - [20] Hasler, M. J., "Electrical Circuits with Chaotic Behavior," *IEEE Special Issue on Chaotic Systems, IEEE Trans. Circuits Syst.*, Aug. 1997, pp. 1009–1021.

-
- [21] Suárez, A., A. Mediavilla, and J. Luy, "Period Doubling Route to Chaos in SiGe IMPATT Diodes," *IEEE Microwave Guided Wave Lett.*, Vol. 8, No. 4, April 1998, pp.170–172.
- [22] Gannett, J., and L. Chua, "A Nonlinear Circuit Model for IMPATT Diodes," *IEEE Trans. Circuits Syst.*, Vol. 25, No. 5, May 1978, pp. 299–307.
- [23] Suárez, A., and J. M. Collantes, "Harmonic Balance Analysis of Two Bifurcation Routes to Chaos," *IEEE Int. Microwave Symp., MTT-S*, Anaheim, CA, June 1999, pp. 767–770.
- [24] Iglesias, V., A. Suárez, and J. L. García, "New Technique for the Determination Through Commercial Software of the Stable-Operation Parameter Ranges in Nonlinear Microwave Circuits," *IEEE Microwave Guided Wave Lett.*, Vol. 8, No. 12, Dec. 1998, pp. 424–426.
- [25] Suárez, A., et al., "Chaos Analysis in a Millimeter-Wave Self-Oscillating Mixer," *IEEE Microwave Guided Wave Lett.*, Vol. 9, No. 10, Oct. 1999, pp. 422–424.
- [26] Chua, L.O., and G. Lin, "Intermittency in a Piecewise-Linear Circuit," *IEEE Trans. Circuits Syst.*, Vol. 38, May 1991, pp. 510–520.
- [27] Venkatasubramanian, V., and W. Ji, "Chaotic Motions from Intermittency Mechanisms in a Simple Power System Model," *Int. Symp. Circuits Syst., ISCAS'96*, Atlanta, GA, May 1996 pp. 641–644.
- [28] Ohno, W., and T. Endo, "A Double Crisis-Induced Intermittency in a Forced PLL Equation," *Proc. Circuits Syst., ISCAS 2000*, Geneva, Switzerland, Vol. 1, 2000, pp. 731–734.
- [29] Hasegawa, A., et al, "A New Type of Intermittency from a Ring of Four Coupled Phase-Locked loops," *IEEE Trans. Circuits Syst.-I: Fundamental Theory and Applications*, Vol. 45, No. 6, June 1998, pp. 623–633.
- [30] Bergé, P., Y. Pomeau, and C. Vidal, *Order Within Chaos: Towards a Deterministic Approach to Turbulence*, New York: John Wiley & Sons, 1984.
- [31] Sancho, S., A. Suárez, and P. San Román, "Floquet Analysis of an Intermittence Route to Chaos Through a Pitchfork Bifurcation," *IEEE Trans. Circuits Syst.-I: Fundamental Theory and Applications*, Vol. 11, No. 3, March 2001, pp. 374–376.

About the Authors

Almudena Suárez received a degree in electronic physics from the University of Cantabria (Spain) in 1987. She received a Ph.D. from the same University in 1992 and a Ph.D. in electronics from the University of Limoges in 1993. Since 1995 Dr. Suárez has been an associate professor at the University of Cantabria and a member of its Communications Engineering Department (DICOM). She is a senior member of IEEE. Her areas of interest include the nonlinear design of microwave circuits and, especially, nonlinear stability analysis, phase-noise analysis, and the investigation of chaotic regimes. Dr. Suárez has been the project manager of a two Spanish national research and development projects and has taken part in a number of Spanish and European projects in collaboration with industries.

Raymond Quéré earned a degree in electrical engineering from ENSEEIHT, Toulouse, France, in 1976, the French “agrégation” in applied physics in 1978, and a Ph.D. from the University of Limoges in 1989. In 1992 he was appointed full professor at the University of Limoges, where he leads the nonlinear circuits group at IRCOM, a laboratory of the French CNRS. He is involved in research into high-frequency nonlinear device modeling and circuit design. He is also involved in nonlinear phenomena analysis, such as stability in high-frequency circuits like power amplifiers and oscillators, as well as the use of chaos in communication systems. He is a senior member of the IEEE and serves as a referee for several transactions and conferences. He is a member of the TPC of the European GaAs Conference as well as the French Microwave Conference.

Index

- Admittance
 - equation, 84
 - Jacobian matrix, 107
 - matrix, 155
- Admittance diagrams
 - of HEMT frequency divider, 105
 - tracing, auxiliary generator for, 101
- Arnold tongue, 251, 264
- Asynchronous extinction, 261
- Attractors, 31
 - chaotic, 307, 318, 319
 - defined, 31
 - limit sets as, 31
- Autonomous period regime, 230–31
 - primary Hopf bifurcation, 230
 - turning points, 231
- Autonomous quasiperiodic regime, 233–40
 - synchronization, 233–34
 - tertiary Hopf bifurcation, 234–39
- Autonomous systems, 2–10
 - in closed harmonic-balance programs, 100–104
 - continuation technique for, 100
 - equilibrium points of, 22
 - flow in, 21
 - frequency-domain simulation of, 76
 - harmonic balance for, 75–91
 - immittance diagrams, 100–103
 - optimization, 103–4
 - phase space, 18
 - solutions of, 5
 - time origin, 14–15
 - vector field, 4, 5
- Auxiliary generators
 - amplitude, 90–91
 - for analyzing self-oscillating mixer, 90–91
 - for analyzing synchronized regime of cubic nonlinearity oscillator, 88–89
 - continuation method based on, 106–11
 - for detection of initial period doublings, 308
 - free-running oscillator convergence
 - process using, 86
 - frequency, 88, 90–91
 - illustrated, 80
 - immittance function, 81
 - introduction into cubic nonlinearity oscillator, 82
 - for Newton-Raphson algorithm, 85
 - self-oscillating mixer, 269
 - small-signal amplitude of, 85
 - for steady-state analysis, 228
 - for tracing admittance diagrams, 101
 - types, 79

- Auxiliary generators (continued)
 - use of, 82–86
- Basin of attraction, 42
 - defined, 130
 - of equilibrium points, 43, 130
 - of stable limit cycle, 43
- Bifurcation analysis, 177–240
 - direct-type bifurcation, 204–5
 - from harmonic characteristic system, 216–28
 - Poincaré map, 196–97
 - stability solution magnitudes, 179
- Bifurcation diagrams
 - Chua's circuit, 298
 - direct-type bifurcation, 205
 - of frequency divider, 147
 - of frequency doubler, 277
 - as function of input frequency, 237
 - Hopf bifurcation, 188
 - intermittence in Chua's circuit, 318
 - MMIC frequency divider, 304
 - monolithic frequency divider, 256
 - varactor-based frequency doubler, 208
- Bifurcation loci
 - analog frequency dividers by two, 262
 - comparison, 263–64
 - Hopf, 238, 244, 246, 249, 250
 - monolithic frequency dividers, 264
 - phase-locked loops, 290
 - saddle-node, 285
 - second harmonic of free-running oscillation, 257
 - in synchronized oscillator, 251
 - tracing, 258
- Bifurcation points, 182, 220
- Bifurcations
 - in analog frequency divider by two, 226–28
 - branching, 229–30
 - of codimension one, 178
 - of codimension two, 178
 - from dc regime, 178
 - defined, 177
 - direct-type, 194–95, 204–9
 - example, 43–44, 177
 - fixed point, 200
 - flip-type, 201–4
 - fold-type, 181, 183
 - global, 178, 211–16
 - Hopf, 181, 185–88, 209–11
 - indirect-type, 195
 - local, 178–96
 - Naimark, 196
 - from periodic regime, 178
 - phase portrait before/after, 182
 - of Poincaré map, 196–211
 - from quasiperiodic regime, 178
 - routes to chaos, 295–320
 - saddle-node, 183
 - turning-point, 182–85, 229
 - types of, 177–78
- Bode, Platzker approach, 153–60
 - instabilities and, 153
 - multitransistor case, 156–57
 - one-transistor case, 153–55
 - practical measurement of RR, 156–57
 - remarks, 158–60
 - See also* Open-loop approach
- Branching bifurcations, 229–30
- Canonical fundamental matrix, 190, 191
- Capacitance matrix, 136
- Capacitive oscillator, 136–37
- Cauchy theorem, 123
- Chaos, 27–29
 - homoclinic, 296–302
 - limit set, 28, 29
 - routes to, 295–320
 - solutions, 27–28
 - spectrum, 28–29
 - waveform illustration, 27
- Chaotic solutions, 295
 - applications of, 296
 - simulation of, 296
- Characteristic equation
 - time-domain, 132
 - zeros, having negative real part, 135
- Characteristic loci, 147–49
- Characteristic matrix, 217
- Characteristic system
 - bifurcation analysis from, 216–28
 - derivation, in harmonic-balance formulation, 131–52

- eigenvalues of, 141
- expression, 132–35
- of harmonic-balance equation, 144
- remarks, 136
- Chua's circuit
 - bifurcation diagram, 298
 - with cubic nonlinearity, 297
 - harmonic-balance prediction, 301
 - intermittence in, 315–20
 - onset of chaos, 299
- Circuits
 - autonomous, 75–91, 99–100
 - Chua's, 297–98, 299, 301, 315–20
 - defined, 2
 - distributed, 142–47
 - IMPATT-based, 47, 51, 202–4, 306–9, 314
 - inductor-capacitor resonant, 12
 - linear, 10–16, 119–28
 - lumped, 119–22, 135–42
 - microwave, 121, 243–92
 - multibias, 160–61
 - nonautonomous, 66–75
 - nonlinear, 1–57, 128–31, 177–240
 - synchronized, 75–91, 104–6
- Closed-loop transfer function, 151, 152
- Codimension-one systems, 180
- Complex-conjugate eigenvalues, 180
- Continuation technique
 - for autonomous and synchronized circuits, 100
 - based on auxiliary generators, 106–11
 - defined, 73–74
 - for high amplitude of RF generators, 73–75
 - initially applied to dc generators, 74
 - for tracing solution curves, 96–99
 - turning points and, 98
- Convolution product, 124
- Cramer's rule, 154
- Cubic nonlinear oscillators, 9
 - for approximate analysis, 76
 - auxiliary generators and, 82–86
 - bifurcation loci for, 236
 - envelope-transient analysis of, 94–96
 - harmonic-balance analysis of
 - bifurcations in, 239–40
 - Hopf bifurcation, 186–88, 210–11
 - with ideal transmission line, 65
 - loss of synchronization in, 214–16
 - nonlinear differential-difference equations of, 64–66
 - phase-locked solutions, 55
 - Poincaré map, 215
 - quasiperiodic solution of, 25
 - self-oscillating mixer regime, 90–91
 - solution curves, 77
 - spectrum, 92
 - stability of equilibrium point in, 39–42
 - synchronized regime of, 88–89
 - synchronized solutions, 54–57
- Current generators, 79
 - in cubic nonlinearity oscillator, 82
 - filter connection, 81
 - illustrated, 80
 - See also* Auxiliary generators
- Damped oscillators, 183–85
- Damping
 - linear oscillator with/without, 11–13
 - nonlinear, 13–14
 - term, 12, 13
- dc generators, 86
- dc regime
 - codimension-one systems, 180
 - harmonic-balance analysis of
 - bifurcations from, 217–19
 - local bifurcations from, 179–88
- dc solutions, 22, 179
- Dielectric-resonator-oscillator (DRO), 267–68
- Difference-differential equations, 65
- Differential algebraic equation (DAE), 119
- Differential equations
 - difference, 65
 - isocline, 3
 - linear, solution, 12
 - nonlinear, of cubic nonlinearity oscillator, 7–10
 - ordinary (ODEs), 118
- Diode oscillators, 7
- Direct-integration methods, 63
 - calculation time, 66
 - problems, 63

- Direct-type bifurcations, 194–95
 - bifurcation diagram, 205
 - defined, 204
 - Floquet multiplier and, 204
 - period-1 solutions, 207
 - phase portrait after, 205
 - pitchfork type, 206
 - subcritical, 219
 - turning points, 206
 - See also* Bifurcations
- Discrete Fourier transform (DFT), 71
- Distributed circuits, 142–47
- Drain voltage, 244
- Eigenvalues
 - of characteristic system, 141
 - complex-conjugate, 180
 - Jacobian matrix, 186
 - of monodromy matrix, 192
 - negative, 185
- Entrainment, 52–57
- Envelope transient, 91–96
 - analysis of cubic nonlinearity oscillator, 94–96
 - formulations, 93
- Equilibrium points, 32
 - of autonomous system, 22
 - basin of attraction, 43, 130
 - classification, 34
 - constant, 33
 - defined, 6
 - focus, 35, 37–38
 - hyperbolic, 34
 - inflected node, 38–39
 - local annihilation of, 182
 - node equilibrium, 34
 - nonhyperbolic, 34
 - outset, 37
 - Poincaré maps and, 48
 - saddle, 35, 36–37, 211
 - stability, 298
 - stability, in cubic nonlinearity oscillator, 39–42
 - stability center, 38
 - stable node, 35, 36
 - stable/unstable manifolds, 212
 - undesired convergence to, 79
 - unstable, 41
 - by voltage values, 300
- Existence-Uniqueness theorem, 8, 20
- Feedback system
 - general, 152
 - SISO, 153
- Field effect transistor (FET), 143
 - Colpitts oscillator, 150
 - equivalent circuit of, modification, 158
 - frequency dividers, 252–254
 - self-oscillating mixer, 266–67
 - two-stage, power amplifier, 159
- Fixed point(s)
 - bifurcations, 199
 - classifications, 200
 - direct, 199
 - hyperbolic, 198
 - indexes, 201
 - indirect, 199
 - negative, 200
 - positive, 200
 - stability, 209
- Flip-type bifurcations, 201–204
 - bifurcation equation, 222
 - continuity characteristic, 211
 - defined, 201
 - frequency-division by two, 231, 253
 - illustrated, 202
 - in IMPATT-based circuit, 202–204
 - locus, 254, 261
 - from period-1 solutions, 204
 - period doubling, 299
 - in Poincaré map, 202
 - subcritical, 203
 - supercritical, 203, 223
 - See also* Bifurcations
- Floquet multipliers, 179, 188–93, 194, 195
 - defined, 192
 - in direct-type bifurcations, 204
 - exponential expression, 193
 - hyperbolic fixed point, 199
 - representation, 193
 - stability and, 194
- Focus point
 - defined, 37–38
 - illustrated, 35

- See also* Equilibrium points
- Fold-type bifurcation, 181
in damped oscillator, 183–85
of dc regime, 183
illustrated, 181, 183
- Fourier basis, 70
- Fourier coefficients, 134
- Fourier-series expansions
for circuit variables, 89
of nonlinear-function derivatives, 73
- Fourier transforms, 71
discrete (DFT), 71
inverse, 314
- Free-running oscillators, 44
analysis of, 78–86, 244
convergence process, 86
evolution of, 245
global behavior, 244–46
solution, 81
start of, 230–31
- Frequency dividers, 145–47
admittance diagram, 105
analog, 252, 254
applications, 252–54
bifurcation diagram of, 147
broadband configuration, 254
defined, 252
design concepts, 252–54
design improvement, 262–66
FET-based, 143, 253
harmonic injection, 252
MMIC, quasiperiodic route to chaos,
302–5
MMIC, schematic, 146
monolithic, 256, 257, 260
parallel configuration, 253
parametric analysis of, 273–78
regenerative, 145, 253
series configuration, 253
two-stage, 263
- Frequency dividers by two
with 6-GHz input frequency, 224
bifurcation loci, 262–63
flip-type bifurcations, 231, 253
global behavior, 252–66
monolithic, 262
parametric stability analysis, 255–62
- Frequency division
for fractional rotation number, 87
prediction of, 308
- Frequency-domain simulation, 76
- Frequency doublers
bifurcation diagram of, 277
design concepts, 273
global behavior of, 273–78
illustrated, 275
input frequency, 275
instability detection, 273–74
nonlinear behavior, 273
operation, 273, 274
output power, 276
safe operation region, 278
self-oscillating mixer regime of, 277
stable/unstable operation regions of,
278
varactor-based, 309–11
- Generalized eigenvalues search algorithms,
136
- Global bifurcations, 211–16
defined, 178
invariant cycle formation and, 248
manifold configuration changes, 211
with qualitative changes, 211
saddle connection, 178, 211–13
saddle-node local/global, 178, 213–16
types of, 178, 211
See also Bifurcations
- Globally asymptotically stable, 42
- Global stability, 243–92
free-running oscillators, 244–46
frequency dividers by two, 252–66
frequency doublers, 273–78
injected oscillators, 243
phase-locked loops, 278–92
self-oscillating mixers, 266–73
synchronized oscillators, 247–52
See also Stability
- Harmonic balance
for autonomous and synchronized
circuits, 75–91
convergence, 67
convergence, avoiding, 89
fundamental frequencies, 68

- Harmonic balance (continued)
 - for nonautonomous circuits, 66–75
 - representation of nonlinear circuit, 68
 - simulation, 73
 - two-tone, 259
- Harmonic-balance analysis
 - bifurcations from dc regime, 217–19
 - bifurcations from periodic regime, 219–28
 - bifurcations in cubic nonlinearity oscillator, 239–40
 - bifurcations with aid of auxiliary generator, 228–40
 - stability analysis and, 132
- Harmonic-balance equations, 67–71, 83
 - characteristic system of, 144–45
 - convergence, 75
 - forced nature of, 79
 - general, obtaining, 84
 - matrix formulation, 67
 - numerical resolution of, 71–73
 - obtaining, 67
 - resolution process, 72
 - solution, 71
- Harmonic coefficients, 93
- Harmonic components, sampling rate, 94
- Harmonic injection dividers, 252–53
- Homoclinic orbits, 296–302
 - defined, 211–12
 - detection of, 297–302
 - formation, 296
- Hopf bifurcations, 181, 185–88
 - bifurcation diagram, 188
 - of branching type, 224–26
 - change of sign association, 186
 - continuity characteristic, 211, 219
 - in cubic nonlinearity oscillator, 186–88, 210–11
 - defined, 185
 - illustrated, 181, 185
 - inverse, 186, 244, 261
 - in Ku-band VCO, 218–19
 - locus, 238, 244, 246, 249, 250, 278
 - new fundamental frequency, 224
 - in Poincaré map, 210
 - primary, 230, 250
 - quasiperiodic route to chaos, 302
 - secondary, 196, 232, 250
 - subcritical, 185, 187–88, 210, 271
 - supercritical, 185, 187, 210
 - tertiary, 234–40
 - types, 187
 - See also* Bifurcations
- Hyperbolic fixed points, 198–99
 - defined, 34
 - Floquet multipliers, 199
 - See also* Fixed point(s)
- Hypertorus, 24
- Hysteresis
 - phase-locked loops and, 286
 - stable solutions coexistence and, 42–43
 - subcritical Hopf bifurcation and, 271
 - turning points and, 221
- Immittance diagrams, 100–102
- Immittance function, 81
- IMPATT-based circuits, 47
 - chaotic attractor of, 307
 - with chaotic behavior, 51, 309
 - flip-type bifurcations in, 202–204
 - period-doubling route to chaos in, 306–9
 - self-oscillating mixer, 314
- Impedance-function analysis, 100
- Indirect-type bifurcation, 195
- Inductor-capacitor resonant circuits, 12
- Inflected node, 38
- Injected oscillators
 - bifurcations, in periodic regime, 238
 - global behavior of, 247
 - low input-power solutions in, 247
- Intermittence in Chua's circuit, 315–20
 - bifurcation diagram, 318
 - capacitance values, 316
 - chaotic attractor, 319
 - coexistence of periodic orbit and, 319
 - example, 318–20
 - illustrated, 315
- Intermittence route to chaos, 315–20
 - defined, 315
 - obtaining, 316–17
 - See also* Routes to chaos
- Invariant sets, 21–29
- Isoclines, 3

- Jacobian matrix, 21, 38, 72, 179, 250, 259
 admittance, 106–7, 238
 eigenvalues, 186
 harmonic-balance, 98–99
 of harmonic components, 72
 of linearized system, 282
 of nonlinear system of equations, 136
 periodic, 188, 189
 of Poincaré map, 198
 singular, 97, 107
- Kirchoff's equations
 linear, 143
 projection of, 132
 system of, 135
- Kirchoff's laws, 15, 64
 applying, 70, 83
 applying, at frequency, 85
- Krylov subspace methods, 73
- Ku-band MMIC power amplifier, 167
 experimental data, 168
 input frequency, 167
- Ku-band VCOs, 102–3, 104
 admittance function, 103
 Hopf bifurcation in, 218–19
 oscillation frequency, 108
 output power, 108
 output power evolution, 108
 simulation, 102
 solution curves, 108–10
 tuning voltage vs., 108–10
 voltage auxiliary generator, 102
- Kurokawa stability function, 231
- Laplace analysis, 119
- Laplace domain, 119–20
 circuit equation in, 120
 solution definition in, 119
- Laplace transform, 121, 127
- Large-signal steady-state regimes
 open-loop approach, 161–68
 stability, 165
 stability analysis, 168–71
- Limit cycles, 19–20
 basin of attraction, 42
 collision with saddle point, 212
 defined, 18, 22
 Poincaré maps and, 48
 trajectory behavior, 19
- Limit sets
 as attractor, 31
 chaotic, 28, 29
 defined, 17
 Poincaré maps and, 48–50
 repeller, 31
 saddle-type, 31
 stability of, 29–44
 types of, 21
- Limit torus, 22–27
- Linear circuits
 lumped, 119–22
 oscillations in, 10–16
 stability of, 119–28
- Linear flow, 33
- Linear matrixes, 70–71
- Linear oscillator, 10
 with nonlinear damping, 13–14
 with/without damping, 11–13
- Local bifurcations, 178–96
 analysis basis, 188
 of dc regime, 179–88
 defined, 178
 direct-type, 194–95
 fold, 181, 183
 Hopf, 181, 185–88
 indirect-type, 195
 Naimark, 196
 of periodic regime, 188–96, 221–26
 stability properties, 179
 turning-point, 182–85
See also Bifurcations
- Local stability, 128–30
 concept, 128–30
 condition for, 130–31
- Local stability analysis, 117–71
 character system derivation, 131–52
 open-loop approach, 152–71
 stability concept and, 118–31
- Loop filter, 279
- Lumped circuits
 characterization, 121
 stability, 119–22
 stability analysis of, 135–42
- Lyapunov exponents, 179

- Microwave circuits
 - characterization, 121
 - global stability of, 243–92
- MMIC frequency divider
 - analysis, 226
 - bifurcation diagram, 304
 - experimental spectrum, 304
 - quasiperiodic regime of, 303
 - quasiperiodic route to chaos in, 302–5
 - schematic, 146
 - simulations, 225
 - by two, bifurcations, 226–28
 - by two, with 6-GHz input frequency, 224
 - See also* Frequency dividers
- Monodromy matrix
 - defined, 192
 - eigenvalues of, 192
- Monolithic frequency dividers
 - bifurcation diagram, 255
 - bifurcation loci, 264
 - simulations, 265
 - spectrum, 260, 262
 - two-stage, 263
 - See also* Frequency dividers; Frequency dividers by two
- Multibias circuits, 160–61
- Naimark bifurcation, 196
- Negative impedance approach, 151–52
 - advantage, 151
 - defined, 151
 - injection circuit, 151, 152
- Newton-Raphson algorithm, 66, 72, 85
 - auxiliary generator for, 85
 - efficiency, 73
 - very large circuits and, 73
- Node equilibrium points, 34
- Nonautonomous systems, 2–10
 - expressing, as autonomous system, 6
 - harmonic balance for, 66–75
 - independent generators, 68
 - Poincaré map, 197
 - solution curve, 5
- Nonlinear analysis techniques, 61–111
 - analysis in closed harmonic-balance programs, 99–111
 - continuation technique, 96–99
 - envelope transient, 91–96
 - harmonic balance (autonomous/synchronized circuits), 75–91
 - harmonic balance (nonautonomous circuits), 66–75
 - time-domain simulation, 62–66
- Nonlinear circuits
 - bifurcation analysis, 177–240
 - description of, 1
 - with nonlinear damping, 13–14
 - oscillations in, 10–16
 - with periodic forcing, 24
 - stability of, 128–31
 - steady-state solutions, 1–57
 - synchronization phenomenon, 53
- Normalized determinant function (NDF), 155, 157
 - calculating, 158
 - characteristic function equivalence, 155
 - of circuit, 159
 - evaluation of, 157
 - Nyquist analysis, 155
 - Nyquist plot, 163, 164
 - plot, 161
 - recursive method of calculation, 165
 - total, 159
 - two-stage heterojunction bipolar transistor power amplifier, 161
 - unstable zero of, 159
- Nyquist criterion, 122–28
- Nyquist locus, 128
 - complex behavior, 171
 - plots, 129
- Nyquist plots, 147
 - case inspection of, 124
 - contour of, 123
 - interpretation of, 127
 - of NDF, 163, 164
 - periodic steady-state regimes, 148
 - stability, 300
- Open-loop approach, 152–71
 - Bode, Platzker, 153–60
 - defined, 152
 - general circuit configuration, 154

- for large-signal periodic steady-state regimes, 161–68
- for linear circuits, 153–60
- for multibias circuits, 160–61
- sequential testing and, 160
- Open-loop gain, 169
- Optimization
 - admittance magnitude, 103
 - autonomous circuits, 103–4
- Ordinary differential equations (ODEs), 118
- Oscillations, 10–16
 - frequency, 87
 - self-sustained, 11
 - start-up conditions, verification of, 14
 - steady-state, 11, 14
- Oscillators
 - capacitive, 137–38
 - circuit solution variations, 45
 - cubic nonlinear, 54–57, 64–66, 82–86, 88–89, 94–96
 - damped, 183–85
 - diode, 7
 - FET Colpitts, 150
 - free-running, 44, 78–86, 244–46
 - injected, 238, 247
 - synchronized, 247–52
 - van der Pol, 124–28, 247
 - voltage-controlled (VCOs), 102–3, 280–82, 288
- Period-doubling cascade, 320
- Period-doubling route to chaos, 305–11
 - defined, 305
 - in IMPATT-based circuit, 306–9
 - Poincaré-map technique and, 306
 - with subcritical flip bifurcations, 309
 - in varactor-based frequency doubler, 309–11
 - See also* Routes to chaos
- Periodic regime
 - autonomous, 230–31
 - with external excitation, 231–33
 - harmonic-balance analysis of
 - bifurcations from, 219–28
 - injected oscillators in, 238
 - local bifurcations from, 188–96
- Periodic solutions, 22
 - phase-locked, 53
 - stability, 189, 197
- Perturbation
 - amplitude, 180
 - equation, 132
 - evolution, 41
 - signal, 132
 - stability and, 32
- Phase detector, 279, 280
 - output signal, 280
 - output voltage, 281
 - sinusoidal, 281–87
- Phase error, 282
- Phase-locked loops
 - bifurcation detection in, 290
 - bifurcation loci, 290
 - filter transfer function, 281
 - general equations, 279–81
 - global behavior of, 278–92
 - hysteresis and, 286
 - parametric analysis, 281–90
 - phase-locked solutions, 289
 - Poincaré maps and, 290–92
 - with realistic models for loop elements, 287–90
 - rotations, 289
 - saddle solution, 283
 - schematic, 280
 - with sinusoidal phase detector, 281–87
 - steady-state solutions, 283
- Phase-locked solutions, 52–57
 - for cubic nonlinearity oscillator, 55
 - defined, 52
 - existence of, 283
- Phase space
 - autonomous system, 18
 - chaotic solutions, 28
 - defined, 16
 - nesting cycles, 20
 - representation, 16–29
 - representation of quasiperiodic solution, 26
 - trajectory in, 17
- Pitchfork bifurcation, 206
- Poincaré maps, 44–52
 - application of, 48

- Poincaré maps (continued)
- bifurcations of, 196–211
 - chaotic behavior and, 50–52
 - of chaotic solution, 53
 - cubic nonlinear oscillator, 215
 - defined, 44
 - definition of, 44–48
 - equilibrium point, 48
 - first iteration, 197
 - fixed point of, 45–46
 - Hopf bifurcation in, 210
 - hyperbolic, 198–99
 - Jacobian matrix, 198
 - limit cycle, 48–49
 - limit sets and, 48–50
 - linearization, 46
 - of nonautonomous circuit, 197
 - perturbation implications, 197
 - phase-locked loops and, 290–92
 - qualitative variations in, 47–48
 - quasiperiodic solutions, 49–50
 - succession of points of, 46
 - Taylor-series expansion, 198
 - transversal intersection, 46
- Pole-zero cancellation, 147, 149
- Power harmonic amplifier layout, 162
- Prediction-correction algorithm, 97
- Quasiperiodic regime
- autonomous, 233–40
 - harmonic-balance analysis of, 268–69
 - locus of turning points, 258–59
 - mixing solution of self-oscillating mixer, 269
 - of MMIC frequency divider, 302
 - turning point locus and, 264
- Quasiperiodic routes to chaos, 302–5
- Hopf bifurcations, 302
 - in MMIC frequency divider, 302–5
 - observation, 302
 - See also* Routes to chaos
- Quasiperiodic solutions, 22–27
- of cubic nonlinearity oscillator, 25
 - of MMIC frequency divider, 305
 - phase-space representation of, 27
 - Poincaré maps, 48–50
- Regenerative dividers, 145, 253
- Repellor, as limit set, 31
- Return difference
- determinant of, 176
 - equation, 174–75
 - function, 175
 - matrix, 175
- Return matrix, 173
- Return ratio, 155, 157
- defined, 152
 - matrixes, 165, 175
 - for multidevice ratio, evaluation of, 157
 - Nyquist analysis, 155
 - practical measurement of, 157–58
- Rollet Factor Calculation, 152
- Rotation number, 23
- defined, 23
 - fractional, 87
- Routes to chaos, 295–320
- defined, 295
 - homoclinicity, 296–302
 - intermittence, 315–20
 - period-doubling, 305–11
 - quasiperiodic, 302–5
 - torus-doubling, 311–15
- Saddle connection, 178, 212–13
- homoclinic orbit, 211–12
 - illustrated, 212
 - See also* Global bifurcations
- Saddle-node bifurcation, 183
- chaotic attractor and, 317
 - from dc regime, 286
 - in frequency-divided solution, 255
 - loci, 285
- Saddle-node global local/global bifurcation, 178, 213–16
- defined, 213
 - with mode locking, 214
 - See also* Global bifurcations
- Saddle point, 36–37
- collision with limit cycle, 212
 - defined, 36
 - illustrated, 35
 - outset, 37
 - stable/unstable manifolds, 37
 - unstable, 211
 - See also* Equilibrium points

- Self-oscillating mixers
 - analysis of, 89–91
 - applications, 266–68
 - auxiliary generator, 269
 - circuit operation, 272–73
 - conversion loss, 272
 - defined, 266, 267
 - design concepts, 266–68
 - global behavior of, 266–73
 - illustrated, 51
 - IMPATT-based, 314
 - non-linear analysis, 268
 - operation, 271
 - operation modes, 274
 - output spectrum, 270
 - parametric analysis, 269–73
 - Poincaré map of chaotic solution, 53
 - solution, 52
 - steady state of, 268–69
 - synchronization, 273
- Self-oscillating mixing regime, 26
- Self-oscillation
 - amplitude, 246
 - extinguished, 244
 - frequency, 247
 - onset, 244
- Self-sustained oscillations, 11
- Shil'nikov condition for transversality, 299
- Simulation Program with Integrated Circuits Emphasis (SPICE), 1
- Single-input-single-output (SISO) feedback system, 153
- Solution curves
 - defined, 96
 - folding over itself, 98
 - Ku-band VCO vs. tuning voltage, 108–10
 - tracing, continuation technique for, 96–99
 - turning point of, 221–22
- Solution paths
 - defined, 179
 - quasiperiodic, 261
 - tracing, 223
 - turning points of, 221
- Solution trajectory, 16
- Stability
 - center, 38
 - concept, 29–31
 - concept for linear/nonlinear circuits, 118–31
 - equilibrium points, 298
 - fixed points, 209–10
 - Floquet multipliers and, 193
 - general nonlinear equation, 128
 - global, 128–30, 243–92
 - of large-signal steady-state regime, 165
 - of limit sets, 29–44
 - of linear circuits, 119–28
 - local, 128–31
 - of lumped circuits, 119–22
 - of nonlinear circuits, 128–31
 - perturbation and, 32–33
 - properties, qualitative variations in, 43–44
 - structural, 178
 - types, 31–42
 - verification, 30
- Stability analysis, 32
 - characteristic system derivation, 131–52
 - of distributed circuits, 142–47
 - fixed point, 197–98
 - frequency dividers by two, 255–62
 - in frequency domain, 122–28
 - of frequency doublers, 273–78
 - harmonic-balance analysis and, 132
 - large-signal, using simplified filter, 168–71
 - local, 117–71
 - of lumped circuits, 135–42
 - multitransistor circuit for, 156
 - Nyquist, 122–28, 250, 266
 - open-loop approach, 152–71
 - phase-locked loop, 281–90
 - quasiperiodic solution of MMIC
 - frequency divider, 305
 - self-oscillating mixer, 269–73
 - stability concept and, 118–31
- Stable solutions coexistence, 42–43
 - hysteresis phenomena and, 42–43
 - illustrated, 42
- State variables, 2
- Steady state
 - oscillations, 11, 14

- Steady state (continued)
 - of self-oscillating mixer, 268–69
- Structural stability, 178
- Subcritical flip bifurcation, 203
 - period-doubling route to chaos with, 309–11
 - turning points and, 207–8
 - in varactor-based frequency doubler, 208–9
 - See also* Flip-type bifurcations
- Subcritical Hopf bifurcation, 185, 187–88, 209–11
 - hysteresis, 271
 - turning points and, 207
 - See also* Hopf bifurcations
- Subharmonic synchronization, 86–87
 - extension to, 87
 - oscillation frequency, 87
 - See also* Synchronization
- Supercritical flip bifurcation
 - defined, 203
 - illustrated, 223
 - See also* Flip-type bifurcations
- Supercritical Hopf bifurcation, 185, 187, 210
- Sweep plan, 166
- Synchronization
 - autonomous quasiperiodic regime, 233–40
 - locus, 265, 273
 - loss of, in cubic nonlinearity oscillator, 214–16
 - self-oscillating mixers, 271
 - subharmonic, 86–87
 - turning point, 248
- Synchronization phenomenon, 53
 - applications of, 57
 - bands, schematic representation, 54
 - for generator frequencies, 54
 - in nonlinear systems, 53
- Synchronized circuits, 104–6
 - analysis of, 86–89
 - in closed harmonic-balance programs, 104–6
 - continuation technique for, 100
 - frequency-domain simulation of, 76
 - harmonic balance for, 75–91
- Synchronized oscillators
 - behavior, 248
 - bifurcation loci in, 251
 - global behavior, 247–52
- System flow, 21
- Taylor-series expansion, 198
- Time-domain simulation, 62–66
- Time-frequency techniques, 62
- Torus-doubling route to chaos, 311–15
 - auxiliary-generator technique, 312
 - defined, 311
 - in IMPATT-based self-oscillating mixer, 314
 - prediction, 313–14
 - See also* Routes to chaos
- Tracking filter
 - configurations, 161
 - connexion of, 166
 - structure, 166
- Trajectories
 - behavior of, 19
 - homoclinic orbit, 213
 - isolated closed, 19
 - nonlinear, 35–36
 - ordinary, 17
 - perturbed, 39
 - singular, 17
 - solution, 16, 19
 - transient, 16–19
- Transconductance matrix, 155, 176
 - decomposition, 173
 - general, 156
- Transient-envelope technique, 91–96
 - analysis through, 93–96
 - harmonic-balance system, 93
- Turning-point bifurcations, 182–85, 229
 - defined, 229
 - singularity condition, 238
- Turning points, 74
 - calculating, 232–33
 - in closed curves, 248–49
 - conditions fulfilled by, 107
 - continuation algorithm and, 98
 - direct-type bifurcations, 206
 - harmonic-balance detection of, 235
 - hysteresis phenomena, 221

- island, 264
 - locus, 258, 259, 264, 273
 - singular Jacobian matrix, 107
 - of solution curve, 221–22
 - of solution path, 221
 - solution point as, 107
 - subcritical Hopf and flip bifurcations, 207
 - in synchronized oscillators, 89
 - tangential condition at, 109
- Unitary matrix, 173
- van der Pol oscillator, 124–28, 247
- Varactor-based frequency doubler
 - bifurcation diagram, 208
 - subcritical flip bifurcation in, 208–9
- Vector fields
 - autonomous system, 4, 5
 - defined, 2, 3
- Voltage-controlled oscillators (VCOs), xii
 - control voltage, 281
 - frequency oscillation, 280
 - Ku-band, 102–3, 104
 - linear characteristic, 281
 - output phase, 281
 - output signal, 288
 - output voltage, 280
- Voltage generators, 79
 - in cubic nonlinearity oscillator, 82
 - in harmonic-balance software, 100
 - illustrated, 80
 - See also* Auxiliary generators
- Zero-input solution, 120–21